Hydrothermal synthesis of molybdenum based oxides for the application in catalysis

Zur Erlangung des akademischen Grades eines

DOKTORS DER NATURWISSENSCHAFTEN

(Dr. rer. nat.)

Fakultät für Chemie und Biowissenschaften

Karlsruher Institut für Technologie (KIT) - Universitätsbereich

genehmigte

DISSERTATION

von

Dipl.-Ing. (FH) Kirsten Schuh

aus

Mainz

Dekan: Prof. Dr. Peter Roesky

Referent: Prof. Dr. Jan-Dierk Grunwaldt

Korreferent: Prof. Dr. Anker Degn Jensen

Tag der mündlichen Prüfung: 17. April 2014

Acknowledgements

I owe many thanks to a lot of people who have helped, supported and encouraged me during my doctoral studies, not just scientifically but also personally.

First I would like to thank my supervisor Prof. Dr. Jan-Dierk Grunwaldt for the opportunity to complete my doctoral studies in his group and for providing me with a very interesting and diversified topic. I am grateful for the scientific freedom he gave me, the possibility to spend several months at the Technical University of Denmark as well as University of Zurich and for the opportunity to attend international conferences.

I am grateful to Dr. Wolfgang Kleist for his scientific help especially with presentations and publications making the manuscripts reader friendly.

I would also like to thank Prof. Dr. Anker Degn Jensen for agreeing to be my co-supervisor, for very helpful corrections and suggestions of abstracts, manuscripts and presentations and for giving me the opportunity to spend four months in his group at the Technical University of Denmark (DTU), where I felt very welcome.

I am especially grateful for the help of Dr. Martin Høj, who put the selective oxidation set-up at DTU into operation, tested several of my samples for selective oxidation of propylene and performed TEM measurements of my FSP samples. I would like to thank him for the fruitful discussions and for making the start at DTU very easy and the time in Denmark such a positive experience. I also would like to thank Maya, Christina, Amalie, Xiao, Tanja and Christel for the good time in Copenhagen / Lyngby.

I would like to thank Prof. Dr. Greta R. Patzke for the possibility to stay one month in her group at the University of Zurich, for getting me started with hydrothermal synthesis and for helpful suggestions especially relating inorganic chemistry. I am grateful to Dr. Franziska Conrad, Dr. Ying Zhou, Min Sheng, Roman Olivier Kontic and Debora Ressnig for their help during my time at University of Zurich and for making it such a good experience.

I am very grateful to Dr. Michael Brorson at Haldor Topsøe A/S for the hydrotreating activity measurements, TEM measurements of the spent catalysts and for the scientific

input. I would like to thank Dr. Pablo Beato at Haldor Topsøe A/S for the possibility to measure Raman spectroscopy, for his interest in my study, for discussing my results and for directing me to literature. I would also like to thank Randi Hansen for Raman spectroscopy measurements.

I am very grateful to Vanessa Trouillet at the IAM-ESS at KIT who performed and analyzed the XPS measurements and discussed the results with me. I kindly acknowledge Hermann Köhler at IKFT at KIT for the ICP-OES measurements and Dr. Thomas Bergfeldt at the Institute for Applied Materials in the Chemical Analysis group (IAM-AWP) at KIT for the quantitative nitrogen analysis. The European Synchrotron Radiation Facility (ESRF) in Grenoble is acknowledged for providing XAS beamtime at beamline BM01B. I thank Dr. Dmitry Doronkin and Dr. Hudson Carvalho for the XAS measurements and Dr. Wouter van Beek for help and support during the beamtime. I gratefully acknowledge ANKA at KIT for providing PDIFF beamtime, HASYLAB at DESY in Hamburg for providing XAS beamtime and the Center for Electron Nanoscopy (CEN) at DTU for providing microscopy time (SEM and TEM) as well as the help and support during the measurements. I gratefully acknowledge the Danish Council for Strategic Research for financial support in the framework of the DSF proposal "Nanoparticle synthesis for catalysis" and the Karlsruhe House of Young Scientist (KHYS) for financial support during my stay in Denmark (foreign exchange scholarship).

I would like to thank Angela Beilmann for performing most of the BET measurements and for good collaboration during my time at KIT. I also owe special thanks to Hans Weickenmeier who keeps everything in building 11.23 running and therefore made working so much easier. I would like to thank Jan Pesek for advices and help with technical problems.

During my PhD I met many inspiring people and nice colleagues and definitively made some new friends. I would like to thank Dr. Changbo Lu for the good times sharing an office, for interesting conversations and for making the first year at KIT less lonely. Thanks to Dr. Maria Casapu, who listened to me when I needed it and for the entertaining nightshifts at ANKA. I would like to thank Dr. Henning Lichtenberg for reading some sections of this thesis, for diverting dinners and for the good times in Karlsruhe. Special thanks goes to "the girls" Marina, Melanie, Denise, Karin, Gülperi and Meike for entertaining weekend trips, fun nights out, amusing conversations and for being there. Nice

colleagues and friends make rainy days less grey… It was a pleasure to work in this group and I am grateful for the good work atmosphere.

I would like to express my gratitude to my parents, who believed in me, who let me follow my own path and always supported me, no matter what. I am very lucky to have my sister Friederike, my brother Manuel and my friends who listen to me, support me but can also give honest feedback. Family and friends make life so much easier and more enjoyable.

Abstract

Shape and structure of a material strongly influences some of its physical and chemical properties and also plays an important role in catalysis. Hence, strong research effort has recently been spent on the preparation of advanced materials with controlled size, shape and composition. Molybdenum oxide based materials find a large variety of applications in catalysis. Hydrothermal synthesis is a typical soft chemistry method giving access to advanced metal oxides with high crystallinity, controlled morphology and good reproducibility. Flame spray pyrolysis is a one-step method leading to homogeneous nanoparticles which are non-porous, have a defined crystallinity and typically a high surface area.

In the present work hydrothermal synthesis was applied to prepare MoO_3 and mixed molybdenum oxides for the application in catalysis. The influence of the synthesis parameters on the product properties and their catalytic activity was studied in detail. Additionally, flame spray pyrolysis was applied for comparison. The synthesized materials were used for selective oxidation of propylene, hydrodesulfurization and related hydrotreating reactions as target reactions.

Orthorhombic molybdenum trioxide (α-MoO_3) with various morphologies has been successfully synthesized under hydrothermal conditions using $MoO_3 \cdot 2H_2O$ and ammonium heptamolybdate as molybdenum precursors, varying the pH value and adding different acids (nitric or acetic acid) to the initial solution. The ammonium containing molybdenumoxide-phase resulting from ammonium heptamolybdate and nitric acid at pH = 1 – 2 was completely transformed into α-MoO_3 after calcination at 550 °C. Direct hydrothermal synthesis of α-MoO_3-rods from $MoO_3 \cdot 2H_2O$ was achieved in the presence of acetic or nitric acid and from ammonium heptamolybdate with nitric acid at low pH values at 180 °C. After calcination all samples consisted of α-MoO_3. By applying nitric acid during synthesis, the rod-like morphology of the samples could be stabilized during calcination and catalytic activity tests, which was beneficial for the catalytic performance in propylene oxidation. Those samples, which retained their rod-like morphology during the activity tests, yielded the highest propylene conversion, probably due to the large exposure of the (100) facets.

Although MoO_3 is an easy model system, correlation of the particle morphology and the catalytic activity and selectivity in propylene oxidation already requires a detailed characterization of the materials before and after the catalytic test reaction. Extension of the preparation method to mixed transition metal molybdates resulted in a large variety of phases and thus direct correlation between the morphology and the catalytic activity was not possible. Hydrothermal synthesis and flame spray pyrolysis have been used to prepare bismuth molybdate catalysts for the selective oxidation of propylene to acrolein. Application of a high Bi/Mo ratio during hydrothermal synthesis afforded γ-Bi_2MoO_6 as the main phase, whereas lower initial bismuth contents led to the formation of α-$Bi_2Mo_3O_{12}$. The product phase was strongly influenced by the pH value of the initial solution using Bi/Mo = 1:1 but formation of β-$Bi_2Mo_2O_9$ could not be detected. At low pH values α-$Bi_2Mo_3O_{12}$ was the dominant phase, whereas at high pH values γ-Bi_2MoO_6 was formed. All samples displayed a plate-like morphology but their individual aspect ratios varied with the reaction conditions. Generally, the catalytic performance in propylene oxidation of the samples decreased notably after calcination at 550 °C. The use of nitric acid during hydrothermal synthesis enhanced both propylene conversion and acrolein yield, possibly due to a change in morphology. Flame spray pyrolysis led to phase pure bismuth molybdates with a relatively high surface area, which, however, did not exert a positive influence on the catalytic performance of these samples. In contrast to hydrothermal synthesis, which led to a phase mixture of α- and γ-bismuth molybdate, flame spray pyrolysis provided a single step access to β-$Bi_2Mo_2O_9$ without thermal post-treatment. This sample showed high catalytic activity in the oxidation of propylene to acrolein at temperatures up to 400 °C. However, deactivation at higher temperatures started due to the decomposition into α-$Bi_2Mo_3O_{12}$ and γ-Bi_2MoO_6. The sample synthesized with Bi/Mo = 1:1 at pH = 6 under hydrothermal conditions consisted of γ-Bi_2MoO_6 with a relatively high specific surface area and a Bi/Mo ratio of two in the bulk and on the surface exhibited the highest propylene conversion (up to 55%) with acrolein selectivities of 80 – 90% (360 – 400 °C).

Cobalt molybdates were prepared by hydrothermal synthesis and flame spray pyrolysis as oxide precursors for Co-Mo-S by sulfidation and subsequent application in hydrotreating. Hydrothermal synthesis from two different molybdenum precursors (ammonium heptamolybdate and sodium molybdate) at various pH values and with different Co/Mo ratios gave access to a large variety of phases. The pH value of the initial solution had a

stronger influence on the product composition than the Co/Mo ratio due to the dependence of the solubility of the precursors on the pH value of the solution and the stability of the different polymolybdate species in the aqueous solution. Under acidic conditions molybdenum rich phases of high crystallinity were obtained and part of the cobalt remained in solution. At high pH values the products contained relatively high Co concentration in combination with relatively large surface areas. Flame spray pyrolysis resulted in the formation of β-$CoMoO_4$ and MoO_3 if an excess of molybdenum was applied. Characterization of the spent samples, i.e. after sulfidation and subsequent application in hydrotreating, by powder X-ray diffraction showed only the presence of Co_9S_8 and no evidence of crystalline MoS_2. The hydrothermally synthesized samples at high pH value containing relatively high amounts of cobalt along with a relatively large surface area exhibited high catalytic activity for hydrodesulfurization, hydrodenitrogenation and hydrogenation as well as a high ratio for the pre-hydrogenation pathway compared to a commercial reference catalyst. The activity for hydrodesulfurization of the most active hydrothermally synthesized catalyst resembled the activity of the commercial catalyst whereas the activity for hydrodenitrogenation was higher in relation to the reference catalyst. The active samples showed curved MoS_2 slabs in the transmission electron microscopy images. Variation of the Co/Mo ratio for the flame made materials suggested that the optimum activity was achieved with Co/Mo = 1:2.

In conclusion hydrothermal synthesis is an attractive preparation method for model catalyst systems, which gives access to crystalline phases without the application of high temperatures (T > 200 °C) and enables the preparation of a large variety of phases with a defined morphology. Flame spray pyrolysis resulted in unsupported oxide materials exhibiting large surface areas and allows the formation of phases which are stable at high temperature and metastable at room temperature (e.g. β-$Bi_2Mo_2O_9$). The combination of hydrothermal synthesis, flame spray pyrolysis and conventional preparation methods is well-suited to study structure-activity-relationships. This can be further exploited by *in situ* spectroscopy (e.g. Raman or X-ray absorption spectroscopy) applied during the catalytic activity measurements or during catalyst synthesis.

Kurzfassung

Die physikalischen, chemischen und katalytischen Eigenschaften von Materialien werden sowohl durch ihre Form als auch ihre Struktur beeinflusst. Aus diesem Grund wurden in den letzten Jahren im Bereich der gezielten Präparation neuer Materialien mit definierter Partikelgröße, Morphologie und Zusammensetzung viele neue Forschungsansätze entwickelt. Materialien auf der Basis von Molybdänoxid werden in einer Vielzahl katalytischer Prozesse angewendet. Hydrothermale Synthese ist eine typische Methode der „sanften Chemie“ („chimie douce“), die zu Materialien mit hoher Kristallinität, definierter Morphologie sowie guter Reproduzierbarkeit führt. Mit Hilfe von Flammensprühpyrolyse lassen sich weiterhin in nur einem Arbeitsschritt nanokristalline homogene Partikel und typischerweise hohe Oberflächen herstellen.

In der vorliegenden Arbeit wurden MoO_3 und gemischte Molybdänoxide mit Hilfe von hydrothermaler Synthese dargestellt, die erhaltenen Materialien wurden als Katalysatoren eingesetzt. Der Einfluss der Parameter während der Synthese auf die Eigenschaften der Oxide und ihre katalytische Aktivität wurden im Detail untersucht. Zum Vergleich wurden entsprechende Katalysatoren mit Flammensprühpyrolyse hergestellt. Die synthetisierten Proben wurden in der selektiven Oxidation von Propen zu Acrolein, in der Entschwefelung sowie vergleichbaren „Hydrotreating“ Reaktionen getestet.

Mit Hilfe hydrothermaler Synthese war es möglich, orthorhombisches Molybdäntrioxid (α-MoO_3) mit variierender Morphologie herzustellen. Dabei wurden $MoO_3 \cdot 2H_2O$ und Ammoniumheptamolybdat als Molybdänpräkusoren eingesetzt und der pH-Wert variiert. Weiterhin wurden verschiedene Säuren (Salpetersäure oder Essigsäure) zur Anfangslösung hinzu gegeben. Die ammoniumhaltige Molybdänoxidphase, die sich aus Ammoniumheptamolybdat und Salpetersäure bei pH = 1 – 2 bildete, konnte durch Kalzinierung bei 550 °C vollständig zu α-MoO_3 umgewandelt werden. Stäbchenförmige α-MoO_3-Partikel wurden durch hydrothermale Synthese bei 180 °C aus $MoO_3 \cdot 2H_2O$ in der Gegenwart von Essig- oder Salpetersäure oder aus Ammoniumheptamolybdat mit Salpetersäure bei niedrigem pH-Wert hergestellt. Nach der Kalzinierung bestanden alle Proben ausschließlich aus α-MoO_3. Die Anwendung von Salpetersäure in der hydrothermalen Synthese stabilisierte die stäbchenförmige Morphologie der Proben während der Kalzinierung und der katalytischen Messungen. Dies steigerte die katalytische

Aktivität in der Propenoxidation. Daraus folgt, dass höhere Propenumsätze erzielt werden können, wenn die stäbchenförmige Morphologie der Partikel während der Aktivitätstests beibehalten wird. Ein relativ hoher Anteil der (100) Flächen der nadelförmigen Partikel führt voraussichtlich zu höheren Propenumsätzen.

Wenngleich es sich bei MoO_3 um ein einfaches Modellsystem handelt, erforderte die Korrelation der Partikelmorphologie und der katalytischen Aktivität sowie Selektivität in der Propenoxidation bereits eine detaillierte Charakterisierung der Materialien - sowohl vor als auch nach den Aktivitätsmessungen. Die Erweiterung der Strategie auf gemischte Übergangsmetallmolybdate resultierte in einer Vielzahl von Phasen und erschwerte die direkte Korrelation der Morphologie und der katalytischen Aktivität. Verschiedene Bismutmolybdate wurden mit Hilfe von hydrothermaler Synthese und Flammensprühpyrolyse synthetisiert und in der katalytischen Oxidation von Propen zu Acrolein eingesetzt. Die Anwendung hoher Bi/Mo-Verhältnisse während der hydrothermalen Synthese führte hauptsächlich zu γ-Bi_2MoO_6, während bei niedrigeren Bi/Mo-Verhältnissen bevorzugt α-$Bi_2Mo_3O_{12}$ entstand. Der pH-Wert der Anfangslösung hatte einen großen Einfluss auf die Phase des Produkts, das mit einer Ausgangsverhältnis von Bi/Mo = 1:1 synthetisiert wurde. Die Bildung von β-$Bi_2Mo_2O_9$ wurde nicht beobachtet. Bei niedrigem pH-Wert dominierte α-$Bi_2Mo_3O_{12}$, während hohe pH-Werte zur Ausprägung von γ-Bi_2MoO_6 führten. Alle hydrothermal synthetisierten Proben wiesen eine plättchenartige Morphologie auf, jedoch mit unterschiedlichen Längenverhältnissen, die von den Reaktionsbedingungen abhingen. Nach Kalzinierung der Proben bei 550 °C nahm die katalytische Aktivität im Allgemeinen ab. Die Anwendung von Salpetersäure während der hydrothermalen Synthese führte zu einer Verbesserung des Propenumsatzes und der Acroleinausbeute, was vermutlich auf die geänderte Morphologie zurück zu führen ist. Während der Flammensprühpyrolyse entstanden phasenreine Bismutmolybdate mit relativ hoher Oberfläche. Die erhöhte Oberfläche alleine hatte jedoch keinen positiven Einfluss auf die katalytischen Eigenschaften der Proben. Im Gegensatz zur hydrothermalen Synthese, die zu einer Mischung aus α- und γ-Bismutmolybdat führte, ermöglichte die Flammensprühpyrolyse bei einem Bi/Mo-Verhältnis von 1:1 den direkten Zugang zu β-$Bi_2Mo_2O_9$ ohne thermische Nachbehandlung. Diese Probe zeigte eine hohe katalytische Aktivität bis 400 °C. Bei höheren Temperaturen trat eine Deaktivierung aufgrund der Zersetzung zu α-$Bi_2Mo_3O_{12}$ und γ-Bi_2MoO_6 auf. Den höchsten Propenumsatz mit bis zu 55% bei Acroleinselektivitäten von 80-90% (360 – 400 °C) erzielte die Probe, die mit

einem Bi/Mo-Verhältnis von 1:1 bei pH = 6 unter hydrothermalen Bedingungen hergestellt wurde. Diese Probe enthielt ausschließlich γ-Bi_2MoO_6 und hatte eine vergleichsweise hohe Oberfläche.

Kobaltmolybdate wurden ebenfalls mit Hilfe von hydrothermaler Synthese und Flammensprühpyrolyse präpariert. Die resultierenden Kobaltmolybdänoxide wurden sulfidiert und anschließend in der Entschwefelung sowie weiteren „Hydrotreating"-Reaktionen getestet. Ausgehend von zwei verschiedenen Molybdänverbindungen (Ammoniumheptamolybdat und Natriummolybdat) bei unterschiedlichem pH-Wert und verschiedenen Co/Mo-Verhältnissen konnte eine Vielzahl von Phasen durch hydrothermale Synthese hergestellt werden. Der pH-Wert der Anfangslösung beeinflusste die Produktzusammensetzung stärker als das angewandte Co/Mo-Verhältnis, da die Löslichkeit der Vorläuferverbindungen in wässriger Lösung stark vom pH-Wert abhängt. Saure Bedingungen führten zu kristallinen molybdänreichen Phasen und ein Teil des Kobalts verblieb in der Lösung. Bei hohen pH-Werten hingegen wiesen die Produkte hohe Kobaltkonzentrationen in Kombination mit hohen Oberflächen auf. Flammensprühpyrolyse resultierte in β-$CoMoO_4$ und MoO_3 im Falle von hohen Mo-Anteilen. Die Charakterisierung der verwendeten Katalysatoren mit Hilfe von Pulver-Röntgendiffraktometrie deutete nur auf die Gegenwart von Co_9S_8 hin, jedoch nicht auf kristallines MoS_2. Die Proben, die bei hohen pH Werten durch hydrothermale Synthese hergestellt wurden und einen hohen Kobaltanteil sowie hohe Oberflächen aufwiesen, zeigten die beste katalytische Aktivität in der Hydrodesulfurierung, Hydrodenitrogenierung und Hydrierung. Außerdem wurde im Vergleich zum kommerziellen Referenzkatalysator ein relativ hoher Anteil an Dibenzothiophen durch indirekte Entschwefelung über vorhergehende Hydrierung umgesetzt und nicht durch direkte Entschwefelung. Die Leistung des aktivsten Katalysators in Bezug auf Hydrodesulfurierung ähnelte dem kommerziellen Referenzkatalysator, während für die Hydrodenitrogenierung eine höhere Aktivität im Vergleich zum Referenzkatalysator erzielt wurde. Die aktiven Katalysatoren zeigen eine gekrümmte MoS_2-Schichtstruktur im Elektronentransmissionsmikroskop. Maximale Aktivität wurde im Falle der Flammensprühpyrolyse für den Katalysator, der mit einem Co/Mo-Verhältnis von 1:2 synthetisiert wurde, erreicht.

Im Rahmen der vorliegenden Arbeit konnte gezeigt werden, dass die hydrothermale Synthese eine attraktive Methode für die Präparation von Modellkatalysatorsystemen ist.

Sie ermöglicht die Herstellung kristalliner Phasen ohne Nachbehandlung bei hohen Temperaturen (T > 200 °C). Mit Hilfe der hydrothermalen Synthese kann eine Vielzahl von Phasen mit definierter Morphologie dargestellt werden. Flammensprühpyrolyse führt zu ungeträgerten, oxidischen Materialien mit hoher Oberfläche. Sie ermöglicht die Synthese von Phasen, die bei hohen Temperaturen stabil sind, bei Raumtemperatur jedoch metastabil. Die Kombination von hydrothermaler Synthese, Flammensprühpyrolyse und konventionellen Präparationsmethoden hat ein hohes Potential, um Struktur-Aktivitäts-Korrelationen zu untersuchen. *In situ* Messungen z. B. mit Hilfe von Raman oder Röntgenabsorptionsspektroskopie sowohl während der katalytischen Messungen als auch während der Synthese können einen tieferen Aufschluss über die aktiven Phasen unter Reaktionsbedingungen und die Entstehung der aktiven Zentren geben.

Table of Contents

Acknowledgements ..... **I**

Abstract ..... **IV**

Kurzfassung ..... **VII**

Table of Contents ..... **XI**

1 Introduction **1**
1.1. Catalyst synthesis 1
1.1.1. Hydrothermal synthesis 2
1.1.2. Flame spray pyrolysis (FSP) 13
1.2. Target reactions 18
1.2.1. Selective oxidation of propylene 18
1.2.2. Hydrotreating 27
1.3. Motivation 31

2 Materials and methods **33**
2.1. Catalyst synthesis 33
2.1.1. Hydrothermal synthesis 33
2.1.2. Flame spray pyrolysis (FSP) 34
2.2. Characterization 35
2.2.1. X-ray diffraction (XRD) 35
2.2.2. Raman spectroscopy 36
2.2.3. X-ray absorption spectroscopy (XAS) 37
2.2.4. Physisorption 37
2.2.5. Electron microscopy 38
2.2.6. X-ray photoelectron spectroscopy (XPS) 39
2.2.7. Analysis of bulk composition 40
2.2.8. Temperature programmed reaction methods 40
2.3. Catalytic activity measurements 41
2.3.1. Selective oxidation of propylene 41
2.3.2. Hydrotreating 45

3 MoO_3 as model catalyst in the selective oxidation of propylene **48**
3.1. Introduction 48
3.2. Catalyst preparation 49
3.3. Results and Discussion 50
3.3.1. Structural characterization and composition 50
3.3.2. Reducibility and acidity of α-MoO_3 samples 59
3.3.3. Effect of morphology on the catalytic activity and selectivity 61
3.3.4. Effect of nitrogen incorporation on the catalytic activity and selectivity 67
3.3.5. Catalyst deactivation 69
3.4. Conclusions 71

4 Bismuth molybdates for selective oxidation of propylene **73**
4.1. Introduction 73
4.2. Catalyst preparation 74
4.3. Results and Discussion 75
4.3.1. Hydrothermal synthesis in water with Bi/Mo = 0.5 – 3 75

4.3.1.1. Characterization of the as-prepared bismuth molybdates 75
4.3.1.2. Catalytic performance of the as-prepared bismuth molybdates 80
4.3.2. Influence of the calcination procedure on catalyst properties and activity 83
4.3.2.1. Characterization of the calcined samples 83
4.3.2.2. Catalytic performance before and after calcination 87
4.3.3. Comparison of hydrothermally synthesized catalysts with flame made materials 89
4.3.3.1. Characterization of the samples synthesized by different preparation methods 89
4.3.3.2. Catalytic performance of differently synthesized bismuth molybdates 96
4.3.4. Hydrothermally synthesized bismuth molybdates at various pH values 100
4.3.4.1. Characterization of the samples synthesized with Bi/Mo = 1:1 100
4.3.4.2. Influence of the pH at lower and higher Bi/Mo ratio 105
4.3.4.3. Catalytic performance in propylene oxidation to acrolein 107
4.4. Conclusions 113

5 Cobalt molybdates as hydrotreating catalysts 116
5.1. Introduction 116
5.2. Catalyst precursor preparation 118
5.3. Results and Discussion 121
5.3.1. Influence of the pH value during hydrothermal synthesis using two different Mo precursors 121
5.3.2. Effect of synthesis time during hydrothermal synthesis 128
5.3.3. Influence of the Co/Mo ratio and synthesis procedure 130
5.3.4. Characterization of the samples prepared by flame spray pyrolysis and co-precipitation 135
5.3.5. Performance in hydrotreating and characterization of the spent catalysts 137
5.4. Conclusions 146

6 Final remarks and Outlook 148

References 151

List of Abbreviations i

List of Symbols iii

List of Publications iv

1 Introduction

Molybdenum oxides find a large variety of applications in catalysis. Transition metal molybdates are important components of industrial catalysts for selective oxidation of hydrocarbons and oxidative dehydrogenation. In their sulfided form they are also applied in hydrotreating. The most common method to prepare supported transition metal molybdates is impregnation and for unsupported materials solid state reactions at temperatures up to 1000 °C, co-precipitation or sol-gel synthesis. In the first part of this chapter (1.1) two alternative methods for the preparation of molybdates are introduced, namely hydrothermal synthesis and flame spray synthesis, and an overview of different aspects and preparation routes from the literature is given. Selective oxidation of propylene and hydrotreating reactions are well suited test reactions, their state of the art and current trends are described in 1.2.

1.1. Catalyst synthesis

Over the past decades, material science research focused amongst others on the controlled synthesis of nano- and bulk materials with specific structure and properties paving the way for rational design of solid materials. Two methods which have been applied in a large variety of applications are hydrothermal synthesis, a typical soft chemical method (‘chimie douce’), and flame spray pyrolysis, using rather harsh conditions but only for a short time.

1.1.1. Hydrothermal synthesis

Yoshimura and Byrappa [1] described hydrothermal synthesis as a homogeneous or heterogeneous reaction in the presence of an aqueous solvent at temperatures higher than room temperature and pressure higher than 1 bar in a closed system. The aqueous precursor solutions or suspensions are heated in a sealed vessel to temperatures often above 100 °C, so that the solvent (water) evaporates and autogeneous pressure arises in the vessel. Under these conditions water can dissolve materials that would be insoluble under ordinary conditions and enables crystallization of the product phase. Addition of mineralizing agents and templating molecules changes the reaction path and therefore hydrothermal synthesis offers a wide flexibility of product phases with different structures and morphologies. [2-3] Gopalakrishnan [4] defined hydrothermal synthesis as a nontopotactic / nontopochemical method i.e. according to him there is no explicit and reproducible crystallographic relationship between the precursor and the product phases.

In 1845 the first hydrothermal synthesis was conducted by E.T. Schafthual who prepared fine quartz in a papin´s digester. Since then mainly silicates, clays, hydroxides and oxides were prepared. Commercial application began in 1908, when bauxite mineral was leached under hydrothermal conditions to obtain aluminum. [3] Hydrothermal synthesis is used in material science to grow single crystals [5] or for the preparation of open frameworks e.g. zeolites [2]. Zeolites are synthesized from alumosilicate gels under hydrothermal conditions at temperatures of 100 – 200 °C at appropriate pH and in the presence of certain organic additives. [4] Application of templating agents gives access to a range of pore sizes. [2] Nowadays mild hydrothermal synthesis is also used to prepare new metastable transition metal oxide structures which cannot be synthesized by conventional methods. Cations in solution, which act as templating ions, and the pH of the solution were found to have dramatic effects on the product phases and structures. [6] Hydrothermal synthesis enables the preparation of advanced metal oxides of high purity with controlled morphology and good reproducibility. The particle size distribution of the products is relatively narrow and crystallinity is high. The drawback of this preparation method is that the crystallization and growth mechanisms of the crystals are complex and not well understood yet. [3] Therefore several studies have been performed to gain further knowledge and understanding of the nucleation, crystallization and growth of the particles under hydrothermal conditions e.g. by using *in situ* cells and observation of the hydrothermal process under reaction condition

by energy dispersive X-ray diffraction (EDXRD) and extended X-ray absorption spectroscopy (EXAFS). [2, 7-8] Information on the influence of various process parameters on the product phase and the formation of the products and intermediates is essential for predictive preparation and rational design of hydrothermally synthesized materials with specific properties. In 1995 Gopalakrishnan [4] reported that rational design of microporous solids by hydrothermal synthesis is becoming possible, however for transition metal oxides it still remains challenging. Future trends with reference to hydrothermal synthesis are alternative soft hydrothermal technologies e.g. microwave assisted hydrothermal synthesis, which leads to a reduction in reaction time and cost, combined sol-gel synthesis / hydrothermal synthesis and hydrothermal synthesis for nanotechnology. [3]

In literature a large variety of transition metal oxides were prepared by hydrothermal synthesis and also (mixed) molybdenum oxides are accessible by this preparation route. The easiest molybdenum oxide is MoO_3, which has several polymorphs: the thermodynamically stable orthorhombic α-MoO_3 (space group Pbmn), metastable monoclinic β-MoO_3 ($P2_1/c$), the metastable high-pressure phase ε-MoO_3 ($P2_1/m$) and hexagonal metastable h-MoO_3 ($P6_3/m$). [9] Various preparation routes are known for the hydrothermal synthesis of α-MoO_3 [7, 10-17] and h-MoO_3 [13, 18-20] from different precursors and under different reaction conditions. In the present work the focus is on the preparation of orthorhombic α-MoO_3. In the α-type highly asymmetrical MoO_6 octahedra are interconnected with their edges along [001] and interlinked with their corners along [100] to form a double-layer planar structure. [10] Lou and Zeng [10] described the synthesis of MoO_3 from ammonium heptamolybdate (AHM; $(NH_4)_6Mo_7O_{24} \cdot 4\ H_2O$) and nitric acid. Isopolymolybdate anions ($Mo_7O_{24}^{6-}$) can react to Mo_7O_{21} (or α-MoO_3) in the presence of protons (see following equation) and the equilibrium can be shifted to α-MoO_3 by high concentrations of $Mo_7O_{24}^{6-}$ or H^+.

$$Mo_7O_{24}^{6-} + 6\ H^+ \rightarrow Mo_7O_{21} + 3\ H_2O \qquad (1.1)$$

The products containing a mixture of MoO_3 and ammonium molybdates showed a hexagonal prismatic morphology. These ammonium molybdates were completely converted to α-MoO_3 at 420 °C under nitrogen, but the effect of the heating procedure on the product properties was not analyzed. An aged ammonium heptamolybdate solution gave access to pure α-MoO_3 with rod morphology and a width of about 200 nm after 40 h

at 180 °C under hydrothermal conditions. According to the authors, the product distribution was strongly dependent on acid concentration (pH value) and reaction time. The α-MoO_3 rods were transformed to 2H-MoS_2 in an H_2S/H_2 flow at 600 °C and the rod-morphology could be preserved. [10] In a similar approach the influence of the addition of the surfactant cetyltrimethylammonium bromide (CTAB) to ammonium heptamolybdate and nitric acid during hydrothermal synthesis was studied, resulting in α-MoO_3 with spherical or flower like hierarchical structures. [17] Formation of α-MoO_3 instead of h-MoO_3 depends on the temperature: at 90 °C h-MoO_3 was obtained from hydrothermal synthesis with ammonium heptamolybdate and nitric acid, whereas at 150 °C a mixture of orthorhombic and hexagonal MoO_3 was formed. Synthesis at 210 °C led to α-MoO_3. [13] Xia et al. [21] added different inorganic salts such as KNO_3, $NaNO_3$, $La(NO_3)_3$ to control the morphology of α-MoO_3 and investigated the growth mechanism under the applied conditions from ammonium heptamolybdate at pH = 1 - 3. They suggest the formation of $MoO_3 \cdot 2H_2O$, which is then subsequently dehydrated to α-MoO_3:

$$Mo_7O_{24}^{6-} + 6\ H^+ + 11\ H_2O \rightarrow 7\ MoO_3 \cdot 2H_2O \qquad (1.2)$$

$$MoO_3 \cdot 2H_2O \rightarrow \alpha\text{-}MoO_3 \cdot H_2O + H_2O \qquad (1.3)$$

$$\alpha\text{-}MoO_3 \cdot H_2O \rightarrow \alpha\text{-}MoO_3 + H_2O \qquad (1.4)$$

Figure 1.1 depicts the structural change of $MoO_3 \cdot 2H_2O$ (monoclinic symmetry) during hydrothermal transformation to α-MoO_3 which exhibits two different sorts of chains along the a and the c axis and grows preferentially into rods under hydrothermal conditions. [21] This agrees well with the process described by Dewangan et al. [14], who used a nitrosyl-complex of molybdenum synthesized from molybdic acid, NaOH and $NH_2OH \cdot Cl$ as the Mo precursor and tested the resulting α-MoO_3 for their electrochemical properties. They suggest that the product phase strongly depends on the pH value due to the different stable molybdenum species in solution, which are summarized as:

$$[MoO_4]^{2-} \xrightarrow{\text{pH 6}} [Mo_7O_{24}]^{6-} \xrightarrow{\text{pH 1.5-2.9}} [Mo_8O_{26}]^{4-} \xrightarrow{\text{pH < 1}} MoO_3 \cdot 2H_2O$$

Patzke et al. [11] described the one-step synthesis of MoO_3 fibers from bright yellow $MoO_3 \cdot 2\ H_2O$ by dehydration in stainless steel autoclaves with Teflon liners and found that rod formation takes place either in water (neutral media) or under acidic conditions. The influence of various acids on the rod-morphology was investigated: weak organic acids

like acetic acid led to diameters in the nanometer range, whereas in strong inorganic acids e.g. HNO_3, HCl, H_2SO_4 rods with dimensions in the micrometer range were formed. The thickness of the MoO_3-rods can be further controlled by temperature variation. The nanorods had an average diameter of 100 – 150 nm. Investigation of the effect of alkali / alkaline earth halides as additives on the morphology and particle size showed, that LiBr, LiCl, $CaCl_2$ and $MgCl_2$ just changed the aspect ratio in the rod-shaped products, whereas MX (with M = Na – Cs, X = Cl, Br) participated actively in the reaction with $MoO_3 \cdot 2H_2O$ and led to the formation of hexagonal molybdates forming bundle-like ordered arrangements. The structure of these hexagonal molybdates is closely related to the structure of $AH_{6x-1}Mo_{6-x}O_{18}$ (A = Na, K, NH_4). In comparison addition of RbBr resulted in flower-like hexagonal molybdate particles. [11]

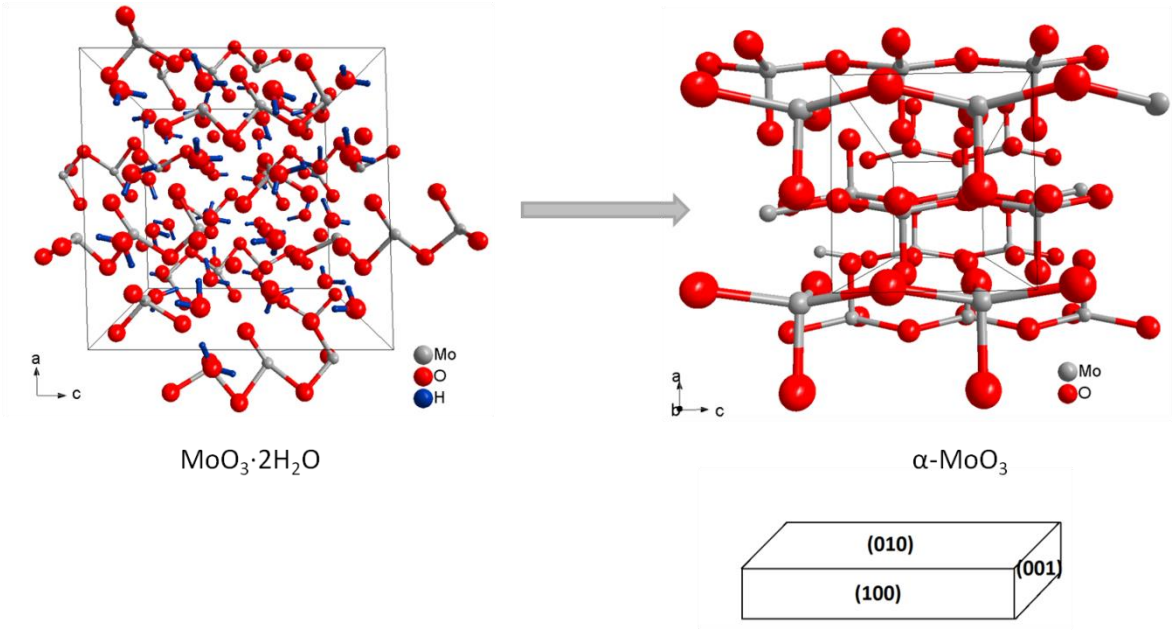

Figure 1.1: Crystal structures of $MoO_3 \cdot 2H_2O$ and α-MoO_3, indicating the tendency toward the formation of one-dimensional structure including the preferred orientation of the resulting α-MoO_3 nanorods.

The crystallization mechanism of $MoO_3 \cdot 2H_2O$ to MoO_3 in water was studied by *in situ* X-ray absorption spectroscopy (XAS) in a specially designed batch reactor. [7] The experimental results suggest a quick dissolution-precipitation mechanism without a crystalline intermediate phase. The yellow starting material was transferred into a grey-blue product, which indicates a partial reduction of MoO_3.

Most of the hydrothermally synthesized α-MoO_3 samples were tested for their electrochemical properties, but hardly any catalytic activity studies were described. Li et

al. [16] tested their synthesized nanobelts and microflowers in ethanol oxidation. They used $Na_2MoO_4 \cdot 2H_2O$ and HCl at pH values < 1 and added P123 ($EO_{20}PO_{70}EO_{20}$, MW = 5800) as a surfactant, which directed the assembly of α-MoO_3 nanobelts into microflowers. The nanobelts yielded higher ethanol conversion at slightly lower acetaldehyde selectivity compared to the microflowers. Hydrothermally synthesized molybdenum trioxide was also used as precursors for hydrodesulfurization (HDS) catalysts and their morphology (nanoribbons) could be preserved during transformation of α-MoO_3 to MoS_2 with H_2S. [22] Direct synthesis of MoS_2 under hydrothermal conditions was reported using ammonium tetrathiomolybdate (ATTM; $(NH_4)_2MoS_4$), but relatively high temperatures (260 – 350 °C) were required and the autoclave needed to be purged with nitrogen, hydrogen or H_2S. [23-24]

With respect to γ-Bi_2MoO_6 hydrothermal synthesis was mainly used for photocatalytic applications [25-30] and not yet for the preparation of oxidation catalysts. Bismuth nitrate ($Bi(NO_3)_3 \cdot 5H_2O$) and either ammonium heptamolybdate or sodium molybdate were applied as precursors. The low-temperature γ-phase is the naturally occurring mineral koechlinite. It does not show any cation vacancies and is an example for an Aurivillius structure type, which consists of alternating $[Bi_2O_2]^{2+}$ slabs and layers of corner sharing MoO_6 octahedra. At temperatures higher than 570 °C the metastable γ”-phase is formed and is further transferred to the high-temperature stable γ’-phase at 640 °C. [31] The α- and the β-phase can be regarded as a defect fluorite structure. α-$Bi_2Mo_3O_{12}$ contains elongated columns of MoO_4 tetrahedra which enclose rectangular tunnels filled with two columns composed of Bi^{3+} ions and cation vacancies. In the metastable β-$Bi_2Mo_2O_9$ columns of isolated MoO_4 units enclose two types of square tunnels: the smaller one contains only one column of Bi^{3+} cations, the larger tunnel incorporates four columns of Bi^{3+}, with every second site vacant in two of the columns. [32] The structures of the three different low temperature phases are depicted in Figure 1.2.

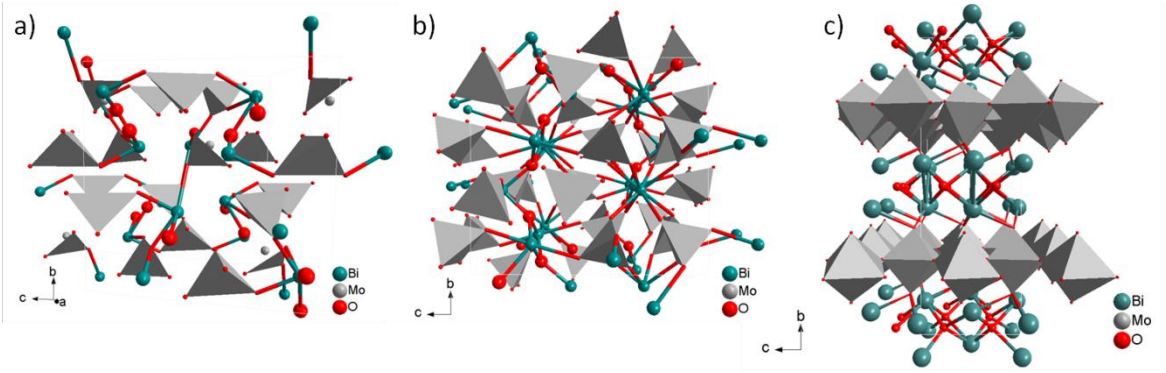

Figure 1.2: Crystalline structures of (a) α-$Bi_2Mo_3O_{12}$, (b) β-$Bi_2Mo_2O_9$ and (c) γ-Bi_2MoO_6 projected along the a axes.

Pure γ-Bi_2MoO_6 could be prepared from $BiCl_3$ and ammonium heptamolybdate with NaOH or from $Bi(NO_3)_3 \cdot 5H_2O$ and H_2MoO_4 at 180 °C for 24 h, whereas preparation with ammonium heptamolybdate and bismuth nitrate as precursors led to additional phases in the hydrothermal product. [25] Maczka et al. [27] obtained differently sized γ-Bi_2MoO_6 nanoplates using bismuth nitrate and sodium molybdate by variation of the temperatures between 120 °C and 300 °C. Increasing the temperature from 155 to 205 °C only slightly influenced the thickness of the platelets whereas the lateral dimensions increased significantly. In a similar approach the morphology of hydrothermally synthesized γ-Bi_2MoO_6 could be controlled by adjustment of the pH with concentrated ammonia solution at 180 °C for 24 h. [28] A decrease of the preparation temperature to 160 °C for 12 h led to the formation of $Bi_{3.64}Mo_{0.36}O_{6.55}$ from bismuth nitrate, ammonium heptamolybdate and NaOH at basic conditions (pH ≥ 9), whereas at neutral conditions (pH = 6.6 – 7) mixtures of $Bi_{3.64}Mo_{0.36}O_{6.55}$ and γ-Bi_2MoO_6 were found. [33] The application of surfactants such as cetyltrimethyl ammonium bromide (CTAB) [29] or poly(vinyl pyrrolidone) (PVP) [26] resulted also in the formation of nanoplates under the applied conditions. In all these cases a Bi/Mo ratio of 2:1 was used corresponding to γ-Bi_2MoO_6. Li et al. [34] synthesized different bismuth molybdate phases and phase mixtures using different initial Bi/Mo ratios (Bi/Mo = 2:3, 2:2 and 2:1) from acidic bismuth nitrate solution and ammonium heptamolybdate by variation of the pH value. γ-Bi_2MoO_6 was formed throughout the entire pH range at low molybdenum concentration (Bi/Mo = 2:1). At higher molybdenum concentration (Bi/Mo = 2:2 and 2:3) the product phase was dependent on the pH value, due to the formation of different polymolybdate species in solution. The molybdate anion can polymerize forming various isopoly derivatives and the extent of polymerization is dependent on the molybdate concentration, the pH value and the temperature of the

solution. High pH values led to the formation of γ-Bi_2MoO_6, under acidic conditions α-$Bi_2Mo_3O_{12}$ was obtained. This can be explained by the following equations: [34]

$$2\ BiO^+ + MoO_4^{2-} \rightarrow (BiO)_2(MoO_4)\downarrow \quad (1.5)$$

$$3\ MoO_4^{2-} + 4\ H^+ \leftrightarrow Mo_3O_{10}^{2-} + 2\ H_2O \quad (1.6)$$

$$2\ BiO^+ + Mo_3O_{10}^{2-} \rightarrow Bi_2(MoO_4)_3\downarrow \quad (1.7)$$

At high pH values MoO_4^{2-} is present in solution which reacts with 2 BiO^+ to the γ-phase (1.5), whereas with increasing H^+ concentration $Mo_3O_{10}^{2-}$ forms (1.6) resulting in precipitation of α-$Bi_2Mo_3O_{12}$ (1.7) at pH = 1 - 3. β-$Bi_2Mo_2O_9$ could not be prepared directly by hydrothermal synthesis but a pure phase was obtained after calcination at 560 °C. The resulting non-calcined samples exhibited surface areas of 39 m²/g to 57 m²/g, which is relatively high for unsupported bismuth molybdates. [34] Beale and Sankar [8] also prepared all three phases with $Bi_2O_3 \cdot nMoO_3$ (n = 1, 2, 3) mixing stoichiometric amounts of acidified bismuth nitrate solution (Bi_2O_3 dissolved in HNO_3) with ammonium heptamolybdate dissolved in ammonium hydroxide. α-$Bi_2Mo_3O_{12}$ and γ-Bi_2MoO_6 could be produced in one step, whereas for β-$Bi_2Mo_2O_9$ calcination at 560 °C was required. *In situ* time resolved energy dispersive X-ray diffraction (EDXRD) during hydrothermal synthesis at temperatures between 110 and 140 °C suggested that α-$Bi_2Mo_3O_{12}$ and γ-Bi_2MoO_6 formed directly from the precursor gel without intermediate phases present. The overall reaction rate increases with increasing temperature. Different growth mechanisms for α- and γ-bismuth molybdate were observed: α-$Bi_2Mo_3O_{12}$ grows 3-dimensionally, whereas γ-Bi_2MoO_6 initially grows in 2-dimensions. [8] A similar study was performed by Kongmark et al. [35], who applied combined *in situ* high-resolution powder diffraction (HRPD), X-ray absorption spectroscopy (XAS) and Raman spectroscopy to observe the formation of γ-Bi_2MoO_6 under hydrothermal conditions at 160, 170 and 180 °C. They found that independent of the temperature a two step reaction occurs and an intermediate fluorite structure was observed. From the precursor gel containing $BiO_2(NO_3)_2$ and $(NH_4)_4Mo_7O_{24}$ a distorted fluorite structure was formed in which MoO_4-species were randomly distributed [$(Bi_{1-x}Mo_x)_2O_{3+\delta}$]. With increasing reaction time [Bi_2O_2]-type and [MoO_4] self-organize in a structure related to L-$Bi_{2n+4}Mo_nO_{6(n+1)}$ [36] consisting of stacked $[Bi_{2n+4}O_{2n+6}]^{2n+}$ layers parallel to the (001) plane with n isolated [MoO_4] tetrahedra in the interspaces. This fluorite structure will be transformed into γ-Bi_2MoO_6 and the spherical particles observed

in the beginning will change into plates. The monomeric molybdate species $[MoO_4]^{2-}$ in the precursor is needed to form γ-Bi_2MoO_6, attesting that the pH of the precursor solution plays an important role. [35] In agreement with Beale and Sankar [8] they also found a 2-D growth process determined by diffusion limitations.

All these preparations were performed in batch reactors, but also continuous hydrothermal synthesis of α-$Bi_2Mo_3O_{12}$ and γ-Bi_2MoO_6 was reported. [37] An acidified bismuth nitrate solution and a basic solution of molybdic acid were mixed in a reactor using supercritical water at 375 – 450 °C and a pressure of 24.1 MPa as a crystallizing medium. The resulting materials were highly crystalline and exhibited high surface areas (8 and 11m^2/g respectively). With respect to hydrothermal synthesis catalytic studies are rare and bismuth molybdates have not yet been synthesized under hydrothermal conditions for the application in selective oxidation reactions.

Cobalt and nickel molybdates were synthesized by hydrothermal synthesis mainly for the preparation and detailed characterization of new phases. The group of Eda synthesized the hydrate phases of $CoMoO_4$ [38] and $NiMoO_4$ [39] to analyze the structure and the amount of coordinated water. In both cases the formula was determined to be $MMoO_4 \cdot 0.75H_2O$. $NiMoO_4 \cdot 0.75H_2O$ revealed a rod-like morphology and turned into α-$NiMoO_4$ at temperatures above 210 °C. [39] They also synthesized $MMo_4O_{13} \cdot 2H_2O$ (M = Co, Ni) with a novel pillared structure from MCl_2 and insoluble MoO_3 or soluble $MoO_3 \cdot nH_2O$ with M/Mo ratios of 1, 5 and 10. For the preparation of $CoMo_4O_{13} \cdot 2H_2O$ an excess of cobalt was required (Co/Mo = 5 or 10) at initial pH values < 4. The usage of the soluble precursor reduced the hydrothermal treatment time from three to one day. [40] In another study Eda et al. [41] used various soluble and insoluble Mo and Co precursors to investigate the effects of the solubility on the resulting materials. They reported that pH plays a key role in the synthesis of $CoMo_4O_{13} \cdot 2H_2O$ and suggested that it was formed via a hydrothermal dissolution-precipitation process. The formation of the high pressure hp-$CoMoO_4$ was dependent on the pH and the nature of the starting material. Strong structural resemblance between $CoMo_4O_{13} \cdot 0.75H_2O$ and hp-$CoMoO_4$ indicated that solid state transformation occurred during hydrothermal synthesis. Hence, Eda et al. [41] suggested that some hydrothermal solution reactions may in fact take place in the solid state, so that the structure of the product phase is inherited by the solid intermediate formed under hydrothermal conditions. Figure 1.3 displays the crystal structures of low temperature α-

$CoMoO_4$ (space group C2/m), hp-$CoMoO_4$ (P2/c), $CoMoO_4 \cdot 0.75H_2O$ and $CoMo_4O_{13} \cdot 0.75H_2O$. For the high temperature β-$CoMoO_4$ the atomic positions have not been presented yet. [38] For nickel analogue isomorphs exist. Here, Co and Ni are always in octahedral sites, whereas the coordination of Mo^{6+} varies from octahedral in the α-phases, high pressure phases as well as in $MMo_4O_{13} \cdot 0.75H_2O$ and tetrahedral in the β-phases and the hydrates. [42]

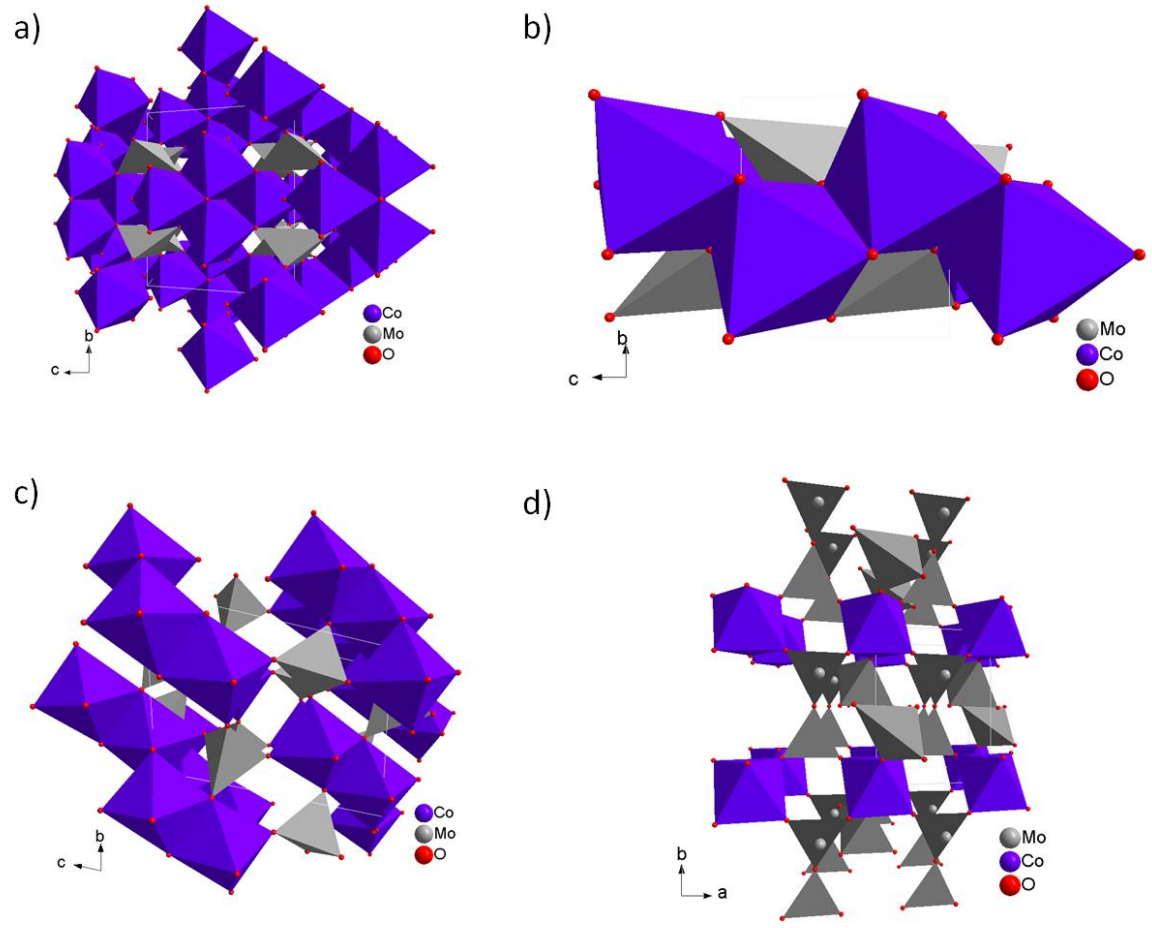

Figure 1.3: Polyhedral crystal structures of the different cobalt molybdate phases: (a) α-$CoMoO_4$, (b) hp-$CoMoO_4$, (c) $CoMoO_4 \cdot 0.75H_2O$ and (d) $CoMo_4O_{13} \cdot 2H_2O$.

The influence of the synthesis temperature (40 – 200 °C) on the phase, specific surface area and particle size of the hydrothermally prepared materials from $Na_2MoO_4 \cdot 2H_2O$ and $Co(NO_3)_2 \cdot 6H_2O$ was investigated after calcination at 500 °C showing that a mixture of α-$CoMoO_4$ and β-$CoMoO_4$ was obtained at synthesis temperatures < 160 °C, whereas at higher temperatures β-$CoMoO_4$ was favored. [43] Furthermore, the effect of the addition of polyethylene glycol (PEG-400, Mw = 380-430) during hydrothermal synthesis at 160 °C for 6 h was studied leading to $NiMoO_4 \cdot nH_2O$ microflowers and $CoMoO_4 \cdot nH_2O$ rods. [44]

The corresponding rods emerged due to added ethanol as co-solvent and the particle size could be controlled by variation of the ethanol concentration. [45] α-$CoMoO_4$ nanorods or nanowhiskers were obtained applying different molar ratios of H_2O/CTAB with cobalt nitrate and sodium molybdate as Co and Mo precursor at 120 °C for 24 h. [46]

Despite most of the materials described above were not tested in catalytic reactions, Palacio et al. [47] synthesized various Cu, Mn, and Co molybdates for the oxidative dehydrogenation (ODH) of propane by hydrothermal synthesis. The hydrothermally synthesized cobalt molybdate catalyst from Na_2MoO_4 and $Co(NO_3)_2$ with $H_2N(NH_2)_2NH_2$ provided reasonable propylene yield and showed the highest stability during the catalytic tests at 600 °C. The same group tested hydrothermally synthesized wolframite type Ni-Mo-W-O and Co-Mo-W-O in the ODH of propane. [48]

By analogy with MoS_2 (see p. 6), unsupported $CoMoS_2$ and $NiMoS_2$ were prepared by one step hydrothermal synthesis from ammonium tetrathiomolybdate (ATTM) and cobalt or nickel nitrate adding decalin as organic solvent. The reactor was purged, filled with hydrogen and heated to 350 °C for 2 h with subsequent cooling. The samples exhibited surface areas of 300 m²/g and higher catalytic activity in the hydrodesulfurization (HDS) of dibenzothiophene (DBT) and 4,6-dimethyldibenzothiophene (4,6-DMDBT) under the applied test conditions compared to commercial supported Co-Mo/Al_2O_3 and Ni-Mo/Al_2O_3 catalysts. [24] Furthermore, the effects of the preparation conditions on the activity and selectivity of this Ni-Mo sulfide catalyst were studied in detail. [49] Catalysts prepared at higher temperature (variation between 300 – 375 °C) showed higher surface area (121 m²/g at 300 °C, 249 m²/g at 375 °C), larger pore volume (0.19 cm³/g at 300 °C, 0.30 cm³/g at 375 °C) and higher catalytic activity. Similar to the effect of preparation temperature an increase in hydrogen pressure (variation between 1.4 MPa and 3.4 MPa) had a positive effect on 4,6-DMDBT and DBT conversion and increased the surface area (83 m²/g at 1.4 MPa, 231 m²/g at 3.4 MPa) and the pore volume (0.17 cm³/g at 1,4 MPa, 0,37 cm³/g at 3.4 MPa) of the products synthesized at 350 °C. Hydrogen was needed in the decomposition of ATTM for the formation of the catalytically active bimetallic sulfide. Application of hydrothermal synthesis at suitable conditions led to formation of nanosized Mo sulfide clusters and more Ni atoms could be incorporated into smaller Mo sulfide nanocrystallites to form more active Ni-Mo-S catalysts. [49]

Transition metal oxides based on molybdenum and vanadium are interesting materials for partial oxidation reactions, which have been extensively studied in the literature. Amongst other preparation methods they were also synthesized hydrothermally. Ueda and Oshihara [50] prepared Mo-V-M-O (M = Al, Ga, Bi, Sb and Te) catalysts and tested their catalytic performance in the selective oxidation of ethane to ethene and acetic acid as well as in the selective oxidation of propane to acrylic acid. For Mo-V-Al-O they first synthesized an Anderson-type heteropolymolybdate $(NH_4)_3AlMo_6H_6O \cdot 7H_2O$ from ammonium heptamolybdate and aluminium sulfate and converted it with $VOSO_4$ at 175 °C for 24 h under hydrothermal conditions. The other samples were prepared from an aqueous solution of ammonium heptamolybdate with bismuth sulfate, antimony sulfate or TeO_2 and an aqueous solution of $VOSO_4$ mixed in an autoclave at 175 °C for 24 h. The samples with the composition $Mo_6V_2Sb_1O_x$ and $Mo_6V_2Te_1O_x$ yielded high ethane conversions at high ethene selectivities. Several groups studied the effect of composition and preparation procedure of hydrothermally synthesized Mo-V-Nb-Te-O on the structure and morphology of the product and on the resulting catalytic activity in selective oxidation of propane and propene to acrylic acid. [51-55] The M1 phase corresponding to $Mo_{6.24}V_{1.41}Te_{1.76}Nb_{2.35}O_x$ is considered to be the active phase in light alkane oxidation and is accessible via mild hydrothermal synthesis. Furthermore, orthorhombic and trigonal Mo_3VO_x were successfully synthesized at different pH values under hydrothermal conditions and were applied in selective oxidation of acrolein to acrylic acid. [56]

Recently $Fe_2(MoO_4)_3/MoO_3$ nanostructured catalysts were prepared and applied in the oxidation of methanol to formaldehyde. [57] MoO_3 nanorods were synthesized from commercial MoO_3 and H_2O_2 in a Teflon-lined autoclave at pH = 0 - 1 (adjustment by nitric acid) and subsequently impregnated with $Fe(NO_3)_3 \cdot 9H_2O$. The influence of calcination at various temperatures on the product phase and the structure was investigated. Calcination at 400 °C resulted in MoO_3 nanorods with $Fe_2(MoO_4)_3$ islands on the surface formed via a solid state diffusion mechanism. [57] Pure $Fe_2(MoO_4)_3$ could be obtained by one step hydrothermal synthesis using iron nitrate nonahydrate and ammonium heptamolybdate tetrahydrate with Mo/Fe ~ 1.5 without other additives at 150 °C. If the molybdenum content was increased and a ratio of Mo/Fe ~ 3 was applied, a mixed phase iron molybdate material resulted and a high surface area was reached compared to surface areas of similar materials. The groups discovered that crystalline $Fe_2(MoO_4)_3$ is required for an active catalyst for selective oxidation of methanol and that the high selectivity to formaldehyde is

influenced by the presence of octahedral Mo^{6+} containing oxide phases. [58] These examples show that hydrothermal synthesis is an attractive method in catalysis especially because nanoparticles with special morphologies can be formed and products with controlled compositions and structure can be obtained.

1.1.2. Flame spray pyrolysis (FSP)

An alternative preparation method for catalysts is flame aerosol technology that even allows large scale production of nanoparticles. [59] A detailed overview of the development of flame aerosol technology and in particular flame spray pyrolysis is given in [59], whereas [60] summarizes the use of aerosol flame technology in catalysis. According to the precursor state (aqueous-based, solvent-based or vapor-based) and the combustion condition three different techniques are distinguished: vapor-fed aerosol flame synthesis (VAFS), flame assisted spray pyrolysis (FASP) and flame spray pyrolysis (FSP). [60] FSP has a self-sustaining flame in comparison with VAFS and FASP, which use an evaporator or external flame respectively. [59] Industrially flame aerosol techniques are already applied and industry leaders such as Cabot, Cristal, DuPont, Evonik and Ishihara manufacture materials in millions of tons with a value of more than $ 15 billion/year. [61] Mainly pigments (TiO_2), reinforcement materials for polymers (carbon black, SiO_2) and other ceramic nanoparticles are produced by these techniques. Johnson Mattey Co. a major manufacturer of catalysts operates a pilot plant for flame spray pyrolysis of catalysts at its Research Center in the UK. [59]

In flame spray pyrolysis (FSP) a liquid precursor is used, which has a high combustion enthalpy and needs to deliver more than 50% of the total combustion enthalpy. [62] Hence, organic solvents are used and the resulting organic precursor solution is dispersed either ultrasonically [62] or by gas convection through a nozzle [63-64] Due to the fact, that the enthalpy to operate the flame is generated by combusting the liquid precursor, control of the particle size is feasible by controlling the rate of combustion enthalpy and the metal concentration in the precursor solution. [64] Flame spray pyrolysis enables rapid and scalable synthesis of nanomaterials and upscaling of the production can be achieved preserving the tailored properties. [59] The resulting materials are non-porous and exhibit a defined crystallinity as well as high thermal stability. [60] In Figure 1.4 the experimental set-up of FSP according to [64] is depicted, which was used for preparation of fumed silica.

The precursor solution is injected with a syringe pump in a capillary placed in the centre of a nozzle assisted with high velocity air or oxygen. A pressure drop of at least 1.5 bar over the nozzle arises leading to fast, turbulent spray flames. The sprayed precursor droplets are ignited with supporting CH_4/O_2 flamelets and the particles are collected on a vacuum-assisted filter above the flame.

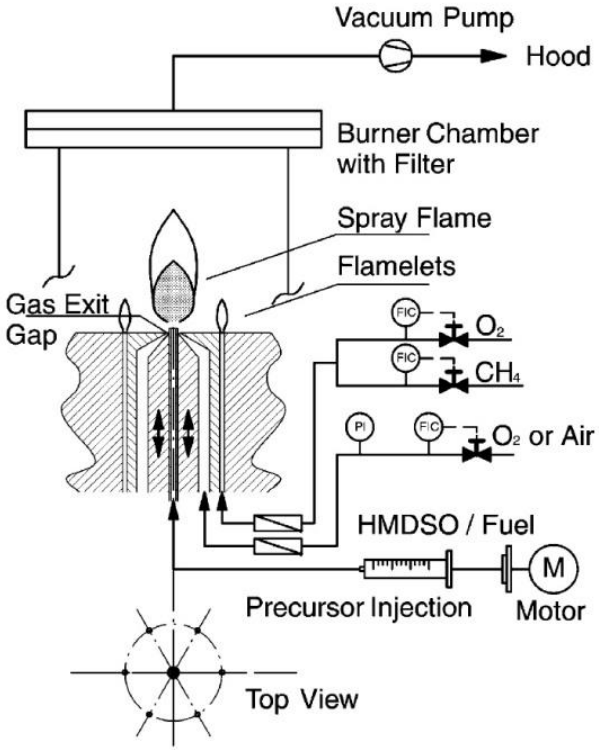

Figure 1.4: Experimental FSP set-up using an air-assisted nozzle and CH_4/O_2 for the supporting flames, collecting the particles on a filter with the aid of a vacuum pump; with permission from [64].

The maximum flame temperature is affected by the composition of the oxidant and the dispersion gas. The application of oxygen instead of air led to higher flame temperatures of about 1000 K. [65] Temperatures of up to 2600 – 2700 K have been measured and the residence time in the flame is in the millisecond range with a high temperature gradient (170 K/min) along the flame axis. [59] These high temperatures allow the formation of homogeneous and crystalline particles; the short residence time generates particles in the nanoscale. Due to the rapid quenching, metastable phases can be formed which was demonstrated for the example of tetragonal γ-Fe_2O_3. [66] In Figure 1.5 the principles of particle formation and growth in the flame are illustrated. The particles can form via the droplet-to-particle or gas-to-particles route, albeit the gas-to-particle route gives access to homogeneous morphologies and particle sizes. The sprayed precursor evaporates and / or

decomposes forming metal vapor. Nucleation takes place due to supersaturation and coalescence and condensation let the particles grow. They are further aggregated and agglomerated and subsequently collected on the filter.

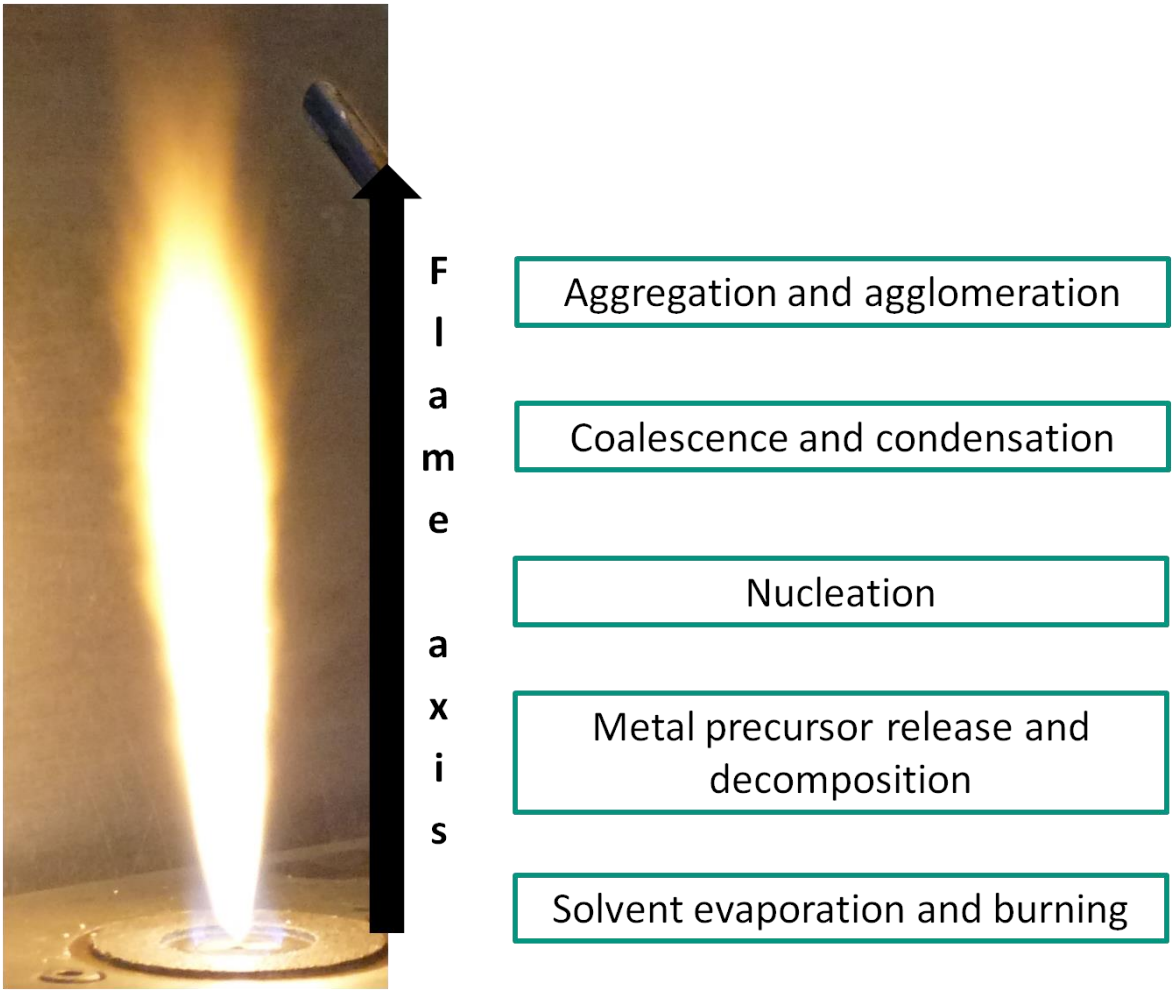

Figure 1.5: Scheme of particle formation and growth according to [67].

These steps are influenced by the characteristics of the metal precursor and the solvent. Hence, a very important aspect in flame spray pyrolysis is the formulation of the liquid precursors. [59] Properties of the metal precursor and the solvent such as combustion enthalpy, melting/decomposition temperature, miscibility and chemical stability determine the properties of the resulting particles. Nitrates, acetates and acetylacetonates, which are frequently used as metal precursors based on conventional preparation methods, often do not provide homogeneous morphologies. Dense and homogeneous fine particles can be obtained when the melting temperature of the precursor is below the boiling point of the solvent and sufficient heat for the evaporation of the precursor is supplied. Metal alkoxides offer high volatilities, high combustion enthalpy, low viscosity and commercial

availability. They are also soluble in many organic solvents, but expensive and moisture sensitive. A summary of precursors used in the open literature for the preparation of various materials is given in [59].

Multicomponent materials can be produced with a higher flexibility using more than one nozzle (in case of two nozzles: twin nozzle or double flame reactor). Thereby separation of the phases can be achieved, core-shell or supported materials can be prepared. Each nozzle is controlled independently and the properties of the resulting particles depend on the properties of the precursor solutions and the interface angle of the separate nozzles. [59] This preparation route was successfully applied for the production of $BaCO_3/Al_2O_3$ for NO_x storage catalysts. [68]

Sokolowski et al. [62] were the first who applied flame spray pyrolysis. They used it for the preparation of γ-Al_2O_3 from aluminum acetylacetonate and suggested a formation mechanism. Later, the rapid insertion and retraction of a transmission electron microscopy (TEM) grid made it possible to observe the evolution of particle morphology along the flame axis. [69] The effects of the flame configuration, i.e. fuel and oxidant flow rate as well as the position of the flame, on the surface area of titania and the composition of rutile and anatase was investigated in detail. Fine anatase titania powder formed at low precursor concentration, low residence time in the flame and low flame temperature. [70] Mädler et al. [64] synthesized nanostructured silica particles and calculated the droplet lifetime in the flame for air or oxygen as dispersion gas. Oxygen led to lower surface areas, due to the rapid burning of the droplets and the resulting longer residence time at high temperatures compared to air. The temperatures measured in the flame were 2440 K at 5 mm above the nozzle and 2000 K at 12 mm above the nozzle for air as dispersion gas and 2620 K at 7 mm above the nozzle and 2340 K at 12 mm above the nozzle for oxygen as dispersion gas. At low oxidant flow rates the specific surface area of the product was increased with increasing flow rate. For high oxidant flow rates (turbulent regime) the flame length was reduced and the particles had less time to grow and agglomerate. The specific surface area of the flame made materials could be controlled systematically through the oxidant flow rate and the precursor/fuel composition. [64] Pratsinis et al. [71] studied continuous flame spray pyrolysis of nanostructured silica particles at high production rates. The oxidant flow rate as well as the precursor supply rate influenced the particle size of silica, whereas oxygen as the dispersion gas allowed a larger variation of particle size compared to air.

Co_3O_4 and Ru-doped cobalt zirconia applied for Fischer-Tropsch reaction were synthesized from Co-2-ethylhexanoate in xylene. [72] The same group prepared $BiVO_4$ from a Bi precursor obtained from bismuth acetate and 2-ethylhexanoic acid mixed with vanadium oxytripropoxide in xylene. They observed that the crystallinity of $BiVO_4$ is a function of the filter temperature and concluded that the short flame residence time is insufficient to cause crystallization within the flame. [73] Dissolution of bismuth nitrate in a mixture of ethanol and nitric acid resulted in hollow particles and sintered dense particles of Bi_2O_3. When glacial acetic acid was used as a solvent homogeneous solid nanoparticles were formed. [74] For the preparation route in acetic acid the influence of the flow rate of the dispersion gas and the precursor feed was studied in detail and the results match the results found for silica [64]. The flame height and accordingly the residence time in the flame was a function of the precursor feed rate and the oxygen flow rate. Shorter residence time in the hot zone of the flame resulted in smaller particles and accordingly in higher surface area (range 20 – 80 m^2/g). [74] Generally, it can be concluded, that the concentration of the precursor, the precursor flow rate and the flow rate of the dispersion gas affects the particles size of the flame made products. Suitable precursors need to be applied.

For the application in catalysis and in sensors, noble metals or alloys were deposited on various metal oxides (Al_2O_3, TiO_2, SiO_2, etc.). The preparation of these materials is possible by flame spray pyrolysis but is limited to thermodynamic properties, i.e. the deposits have to nucleate at high temperature (low boiling point). Noble metals have a low boiling/sublimation point relative to the oxide support materials and therefore sequential nucleation is possible. At higher temperatures the support metal nucleates, whereas the noble metals nucleate at cooler temperatures. The particles grow along the concentration gradient of the spray flame. Double FSP offers a higher flexibility in the preparation of complex oxides. [59] Debecker et al. [75] synthesized MoO_3 supported on SiO_2-Al_2O_3 for the metathesis of propene to ethene and butene in a single flame reactor. At low loadings (1 - 5 wt.% Mo) amorphous molybdates were formed, whereas at high loading (5 - 15 wt.% Mo) crystalline MoO_3 was detected in the X-ray diffraction pattern. Flame spray pyrolysis led to highly dispersed monomeric molybdates on the support, which was beneficial for olefin metathesis. Supported and unsupported cobalt molybdate catalysts for hydrotreating were synthesized using a single flame [76] and double flame [77] approach. Aluminum acetylacetonate, molybdenum 2-ethylhexanoate and cobalt 2-ethylhexanoate in toluene were used as precursor. Preparation of the unsupported catalyst resulted in formation of

MoO_3 and β-$CoMoO_4$. The supported catalysts prepared with one nozzle contained γ-Al_2O_3 with unwanted $CoAl_2O_4$ and well dispersed MoO_3 and the surface area decreased with increasing loading (surface areas 90 – 221 m^2/g), due to particle sintering and aggregation. [76] Double flame spray pyrolysis allowed reducing the amount of $CoAl_2O_4$ by variation of the angle between the two nozzles and the mixing distance between the nozzle and the mixing point. [77]

1.2. Target reactions

1.2.1. Selective oxidation of propylene

Today 25% of the most important chemicals and intermediates are produced via partial oxidation reactions. [78] Most of the catalysts used in selective oxidation are transition metal oxides due to the potential of transition metals to slightly change their oxidation state or store oxygen reversible. Oxidation of hydrocarbons on a metallic surface is a dynamic process and the catalyst needs to perform multiple functions, thus structural and / or phase complexity is required. [78-79] The organic substrate needs to be activated and therefore hydrogen abstraction is required. The resulting intermediate has to be adsorbed on the surface followed by oxygen insertion and subsequent desorption of the product from the catalyst surface. Medium reducibility, weak Lewis-acid centers and oxygen mobility are important properties for a selective oxidation catalyst. [79] Bettahar et al. [80] stated, that the redox properties and acid-base properties of the catalyst surface need to be in equilibrium to permit controlled selective oxidation. Partial oxidation on a metal oxide catalyst proceeds via a Mars-van-Krevelen mechanism, where the oxygen source for selective oxidation is the oxygen of the catalyst, which is reoxidized by gaseous oxygen [81] (illustrated schematically in Figure 1.6). After adsorption of the hydrocarbon molecule on the surface, the hydrocarbon is oxidized while the metal cations in the lattice are reduced and oxygen vacancies form. The oxygen of the bulk migrates and fills the anion vacancy at the surface, while the vacancy moves to another site. Oxygen vacancies are reoxidized by gaseous oxygen to regenerate the catalyst closing the catalytic cycle. It is important, that the catalyst enables lattice oxygen diffusion and facile flow of electrons. [78] Several kinds

of active oxygen (O^-, O_2^- and O^{2-}) were detected on the catalyst surface. The role of these surface oxygen species in partial versus total oxidation need to be further elucidated. [79]

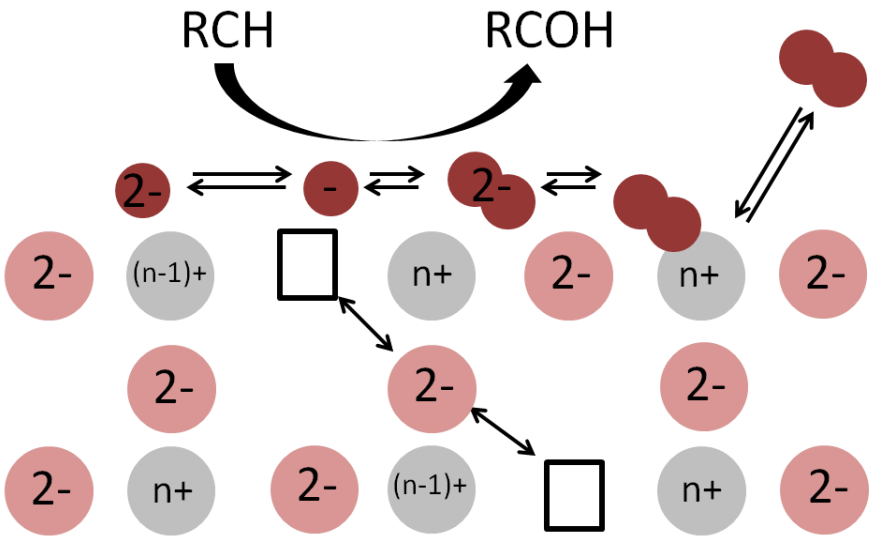

Figure 1.6: Schematic of a Mars-van-Krevelen mechanism, where the squares represent the anion vacancies, the red balls are oxygen and the grey balls the metal.

Grasselli [78] summarized seven fundamental principles, which are important for selective heterogeneous catalysis in general.

- **Lattice oxygen:** The lattice oxygen of a reducible metal oxide may be more selective than gaseous oxygen. [82]
- **Metal-oxygen bond:** The metal-oxygen bond must be of medium strength under reaction conditions e.g. it has to be weak enough to activate the organic substrate molecule but strong enough not to cause over oxidation.
- **Host structure:** The desired lattice oxygen has to be provided, rapid electron transfer and oxygen diffusion through the bulk is required and the structure must be stable also after formation of oxygen vacancies in the lattice.
- **Redox:** The removal of oxygen from the lattice and the re-oxidation of the catalyst by gaseous oxygen are essential.
- **Multifunctionality of active sites:** The catalyst needs to perform various functions mentioned before.
- **Site isolation:** The products are more active than the substrate and therefore re-adsorption has to be avoided. A selective catalyst provides finite sites and isolated oxygen (groupings).

- **Cooperation of phases:** Multifunctionality of the catalyst can be achieved by combining different catalyst phases, each offering one function and bringing them in intimate contact.

These principles were also summarized by other authors in a similar manner [83-84]. Most of industrial oxidation catalysts consist of more than one phase and each phase fulfills several functions. Delmon and Ruiz [85] studied the interaction of two separate oxide phases in the oxidation of isobutylene to methacrolein. They explained the improved catalytic activity of these well defined metal oxide phases (A and B), where each phase may already be active on its own in the catalytic reaction, by a continuous activation of potential centers on A by spill-over oxygen from B (remote control theory). That means an acceptor phase activates the hydrocarbon and a donor phase produces activated oxygen at a high rate, which spills over to the acceptor phase and accelerates the oxidation reaction. [85] Some principles such as the importance of oxygen mobility are discussed controversially and for example according to Wachs and Routry [86] a correlation between oxygen mobility or the ability of oxygen removal from the catalyst lattice and the reaction rates in catalytic selective oxidation is missing. They consider the chemical properties of the specific active sites to be essential and find that the catalytic performance has to be related to the surface characteristics of the catalyst.

$$CH_3CH{=}CH_2 + O_2 \rightarrow CH_2{=}CHCHO + H_2O \qquad (1.8)$$

The selective oxidation of propylene to acrolein (Eq. 1.8) and the ammoxidation of propylene to acrylonitrile are important industrial processes. In 1948 Hearns and Adams [87] patented a process for direct oxidation of propylene to acrolein over a cuprous oxide catalyst. Shell applied this process on an industrial scale. The catalyst operated at 370 – 400 °C albeit low conversion was achieved and a high recycling stream was required. In 1959 Sohio established bismuth molybdate catalysts for the direct oxidation of propylene to acrolein. These bismuth molybdates showed a higher tolerance toward varying reaction conditions and provided higher acrolein yields compared with the cuprous oxide catalysts. [88-89] Nowadays the industrial catalysts consist of at least four transition metals and yield more than 90% acrolein. [90] In industrial practice 5 - 10% propylene in a mixture of air and steam or off-gas are applied at 300 – 400 °C and 1.5 – 2.5 kPa. Under reaction conditions Bi-Mo-O catalysts are quite stable in the sense that their selectivity and activity remain constant. [91] In the industrial application the oxygen/propylene molar ratio needs to be

around 1.6 due to reduction of the catalyst at lower values. Acrolein is mainly oxidized to acrylic acid on a catalyst based on Mo and V and acrylic acid or acrylates (esters of acrylic acid) are polymerized.

Since the discovery of these bismuth molybdate catalysts, this type of materials have received large attention and several researchers have studied their catalytic properties in considerable detail [91-100]. Adams and Jennings [101] discovered that the first step contains a hydrogen abstraction from the methyl group and formation of a symmetric allyl species. The fact that 1,5-hexadiene forms in high yield over Bi_2O_3 and not at all over MoO_3 indicates that the initial α-hydrogen abstraction in the partial oxidation of propylene over bismuth molybdates proceeds via oxygen atoms associated with bismuth. The insertion of oxygen in the allylic species is associated with molybdenum. [92, 102] Investigations of α-$Bi_2Mo_3O_{12}$ showed, that the oxygen exchange occurred preferentially on Mo polyhedra having neighboring bismuth ions. Ono and Ogata [103] concluded that oxygen anions bridging bismuth and molybdenum are active for hydrogen abstraction. Ueda et al. [104] found that two different oxygen species are involved in hydrogen abstraction by the application of $^{18}O_2$ tracer studies. The first hydrogen abstraction from propylene occurs on Mo^{6+}-O-Bi^{3+}, whereas oxygen doubly bonded to Mo^{6+} is incorporated into the activated allyl species to form acrolein. [100, 105]

Byproducts mostly reported are acrylic acid, CO, CO_2, acetaldehyde, formaldehyde and acetic acid, but the formation mechanism of these products is still under investigation and there are several speculations. [106-107]

Based on structural considerations, *in situ* infrared (IR) and Raman pulsed reduction as well as $^{18}O_2$ reoxidation studies, Grasselli and Burrington [92, 108] proposed a reaction mechanism for oxidation and ammoxidation of propylene over bismuth molybdate catalysts. It was modified on the basis of *ab initio* calculations by Jang and Goddard [109], who reported that the first hydrogen abstraction from propylene to form the allylic intermediate is most favorable on Bi(V) according to their calculation. Oxygen insertion and second hydrogen abstraction occur on two separate but adjacent Mo^{6+} di-oxo sites, rather than only one Mo site. Figure 1.7 shows the modified mechanistic cycle of the selective oxidation of propylene to acrolein adapted from Grasselli et al. [110]. Instead of Bi(V) they suggested that Bi(III) is involved in the first hydrogen abstraction.

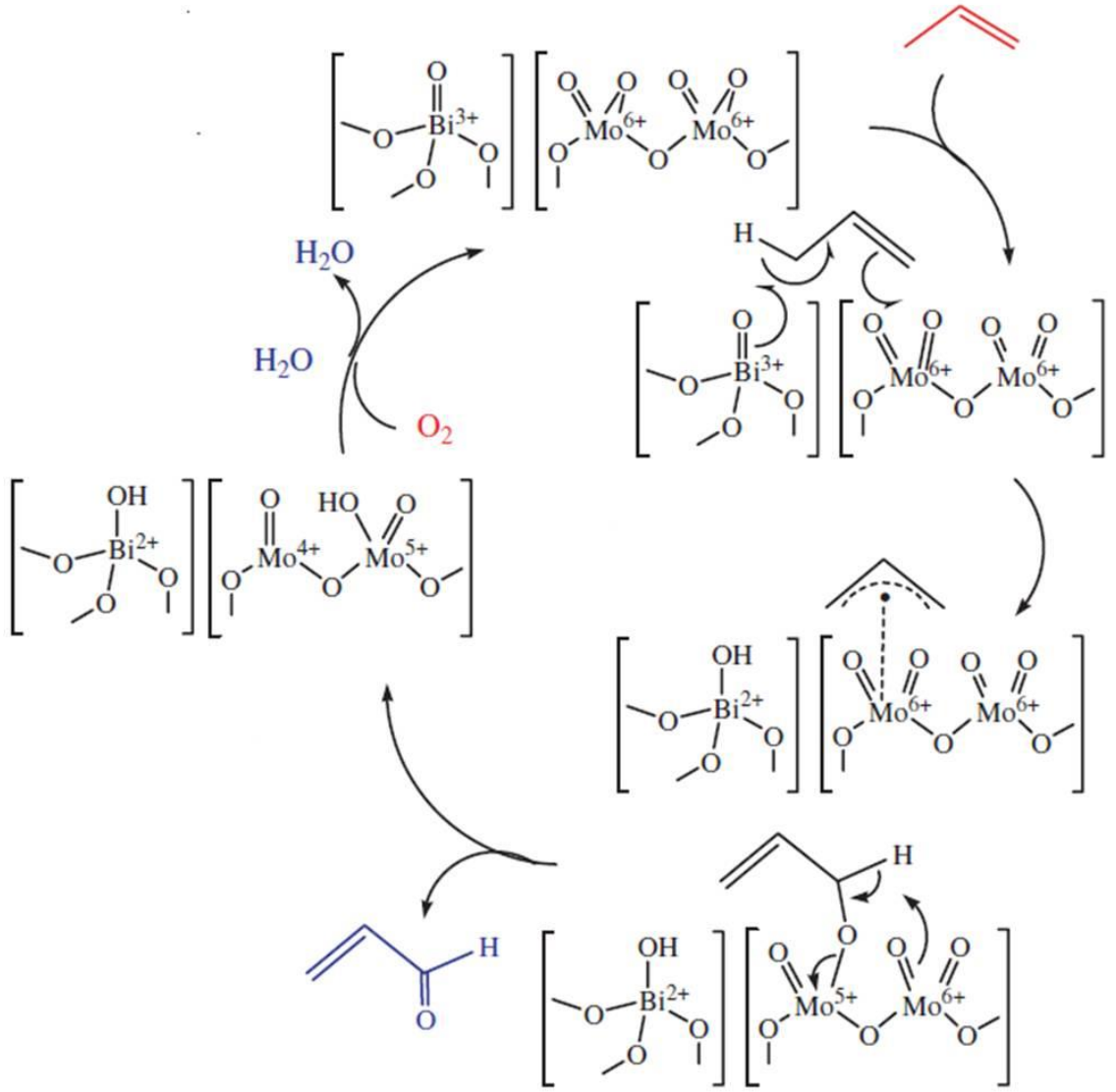

Figure 1.7: Propylene oxidation mechanism over bismuth molybdate catalysts with permission from [110]. The reagents are marked in red, the products in blue.

The allylic H-abstraction, which is the rate-determining step, occurs on a bismuth site and the resulting π-allyl intermediate is adsorbed on a neighboring Mo center. Oxygen attached to Mo is inserted into the π-allyl complex, resulting in σ-O-allyl species and formation of a Mo-O-C bond. Subsequently the second hydrogen is abstracted by an adjacent Mo=O, acrolein is formed and desorbed from the catalyst surface. Water is eliminated from the surface and the reduced site is regenerated by gaseous oxygen. Desorption of the oxygenated product from the catalyst surface leaves an oxygen vacancy, which is reoxidized via oxygen diffusion through either the near surface layer (nucleophilic surface lattice oxygen $[O^{2-}]_{SL}$) or the bulk ($[O^{2-}]_{L}$). The diffusion kinetics of oxygen are strongly

affected by the elemental composition of the catalyst and the geometric structure of the catalyst phases. [111]

According to Krenzke and Keulks [96] the abstraction of the α-hydrogen to form the allylic intermediate is the rate determining step at higher temperature (450 °C), whereas at lower temperature (350 °C) re-oxidation of the catalyst is rate determining. This agrees well with the observation, that above 400 °C and with $p(O_2)$ = 0.1atm the reaction order is zero with respect to oxygen for all bismuth molybdates. Below 400 °C the reaction order is dependent on oxygen and ranges from 0 to 0.5. [112-113] The reaction orders determined for temperatures < 400 °C with respect to propylene and oxygen are influenced by the rate limiting step involving the transfer of oxygen between the different functional groups within the bismuth molybdates catalyst. [91] Recently it has been reported that on $Bi_2Mo_3O_{12}$ catalysts the reaction order in oxygen is zero at 340 °C and 400 °C, i.e. the reaction rate for acrolein formation is independent of oxygen partial pressure, indicating that the re-oxidation of the catalyst is not the rate determining step at temperatures below 400 °C. [114] The influence of the partial pressure of oxygen on the reaction rate may also depend on the exact properties of the catalysts

The bismuth molybdates which are of significance for selective oxidation of propylene to acrolein have the general chemical formula $Bi_2O_3 \cdot nMoO_3$ with n = 3, 2, 1, corresponding to α-$Bi_2Mo_3O_{12}$, β-$Bi_2Mo_2O_9$ and γ-Bi_2MoO_6. They show different crystal structure (see Figure 1.2 in section 1.1.1) and are supposed to have different catalytic activity. [34]

Despite the large number of studies there is still a debate in literature about the relative activity of these model catalyst phases. [98, 113] Krenzke and Keulks [112] and Monnier and Keulks [113] found the γ-Bi_2MoO_6-phase to be most active, whereas Brazdil, Suresh and Grasselli [115] stated that the β-phase is the most active phase for propylene oxidation. After several reduction-reoxidation cycles there is a phase separation into MoO_{3-y} + Bi_2MoO_{6-x} and finally to α-$Bi_2Mo_3O_{12}$ + γ-Bi_2MoO_6 showing lower catalytic activity.

In contrast, Carson et al. [116] who prepared the different bismuth molybdate phases by co-precipitation at pH = 7 found that the catalytic activity for propylene oxidation decreases in the following order: α > γ > β. They also discovered that a mechanical mixture of α-$Bi_2Mo_3O_{12}$ and γ-Bi_2MoO_6 is more active and selective in propylene oxidation to acrolein than the according pure phases. This synergetic effect could be increased by a close contact

of the two phases. Calcination of the α+γ-phase catalyst at temperatures > 555 °C led to the formation of the β-phase and a loss in activity. [97] Le et al. [99] found that the γ-phase is essential for the existence of the synergy effect, due to its outstanding ability to transport oxygen based on its layered structure. The replenishment of lattice oxygen seems to play an important role in the oxidation process. The rate of oxygen transport is increased when the γ-phase is in close contact with the α- or the β-phase. This synergy effect was confirmed by Bing et al. [98], who suggested that the γ-phase produces the active oxygen species and the α-phase delivers the selective sites for acrolein formation (analogue remote control theory [85]). Soares et al. [117] investigated the existence of a synergy effect between the β- and the γ-phase for selective catalytic oxidation of 1-butene. They found that the surface composition is always close to the β-phase, but the γ-phase grows around β-$Bi_2Mo_2O_9$. Mixed phases always led to higher activity and lower selectivity to CO_2 than pure phases. They also ascribed the enhanced activity to the high oxygen mobility in the γ-Bi_2MoO_6, allowing the migration of the active oxygen species from the γ- to the α-phase.

Snyder and Hill [118] studied the stability of bismuth molybdate catalysts under reaction conditions normally employed for selective oxidation of propylene to acrolein by *in situ* Raman spectroscopy in a special reactor cell. α-, β- and γ- bismuth molybdate were all stable in a gas mixture containing 20% oxygen and 10% propylene in helium at 400 °C.

The most common method to prepare these catalysts includes co-precipitation at a specific pH and thermal treatment at 400 to 700 °C to obtain the crystalline phase. [119] Aleshina et al. [120] prepared bismuth molybdates by co-precipitation with Bi/Mo = 2 at pH values between 0 and 7 and with surface areas of 1 – 3 m²/g and tested them in propylene oxidation in the presence of steam. Co-precipitation at pH = 2 – 5 resulted only in γ-Bi_2MoO_6 according to X-ray diffraction and the Bi/Mo ratio determined in the product was 2.0. γ-Bi_2MoO_6 synthesized at pH = 3 yielded the highest propylene conversion (86%). In the sample prepared at pH = 7 they detected Bi_2O_3 and concluded that with increasing pH value molybdenum dissolves and the resulting product is rich in bismuth. This sample showed lower propylene conversion (73%) and very low acrolein selectivity. Le et al. [99, 121] studied the influence of the phase composition on the activity in propylene oxidation and the selectivity for acrolein on catalysts synthesized by spray drying of aqueous solutions. [99, 121] Also solid-state reaction of Bi_2O_3 and MoO_3 [122] at temperatures up to 1000 °C and sol-gel synthesis [123] was applied. Studying the influence of the calcination

temperature on the catalytic activity of γ-Bi_2MoO_6 revealed that calcination strongly deactivates the catalyst due to bismuth enrichment on the surface. [124]

The multicomponent catalyst used in the industrial process, which is highly active and selective in propylene oxidation to acrolein, shows a complex structure and therefore determination of the role of the various components in oxidation of propylene remains challenging. The composition of the multicomponent bismuth molybdate catalyst is given in Figure 1.8. The alkali promoters alter the oxidation/reduction behavior of the catalyst, affect surface acidity and / or cause a synergism between alkali and transition metal oxide phase. [79]

	Atomic %	
Mo^{VI}	50 – 55	
Bi^{III}	3 – 7	
M^{II}	30 – 35	Co, Ni, Fe, Mg, Mn, ….
M^{III}	8 – 15	**Fe**, Cr, Al
M^{I}	small	K, Na, Cs, Tl, ….
X		Sb, Nb, V, W, Te, …
Y		P, B

Figure 1.8: Composition of multicomponent bismuth molybdate catalyst according to [90].

The multicomponent metal oxides exhibit higher surface areas than the pure bismuth molybdates. [90] In the presence of iron the surface related activity outperform pure bismuth molybdates. [125] Marooka and Ueda [90] reported that $Mo_{12}Bi_{0-1}Co_8Fe_3O_x$ is enriched in bismuth and molybdenum on the surface, whereas iron and cobalt are situated in the bulk. Oxygen dissociatively adsorbed on Fe-doped cobalt molybdate phases and dissociated into the lattice. The replacement of the divalent ions by Fe^{3+} results in anion vacancies which facilitates oxygen transport. [125] Also for the multicomponent propylene oxidation catalysts spillover of oxygen was observed (remote control theory): the adsorbed oxygen moves from the activating molecular oxygen phase to the second phase, which is responsible for the oxidation of hydrocarbons. [126] Co^{2+} and Fe^{3+} activate molecular oxygen more effectively than bismuth molybdate. Thus on supported $Bi_2Mo_3O_{12}$ catalysts it could be demonstrated that the active oxygen migrates from cobalt or iron molybdate to $Bi_2Mo_3O_{12}$ by bulk diffusion through lattice vacancies. [127] A comparison of the Mo-Bi-Co^{2+}-O and the Mo-Bi-Co^{2+}-Fe^{3+}-O system showed that for both systems lattice oxygen

from bismuth molybdate participated in propylene oxidation, whereas the lattice oxide ions from the other transition metal molybdate participate only for iron containing systems. [104]

MoO_3 was applied as a model catalyst to study the structure-activity relationships of molybdenum based catalysts. It was stated that α-MoO_3 is not active in selective propylene oxidation and that bulk nanostructuring and complex surface termination, which is only detectable in transition electron microscopy examinations, are required for efficient catalysts. [128] Ressler et al. [129] demonstrated by *in situ* X-ray absorption spectroscopy (XAS) that under reaction conditions (0 – 500 °C, C_3H_6/O_2 from 1:1 to 1:5) α-MoO_3 was partially reduced and defects similar to "$Mo_{18}O_{52}$" were formed. The original layered α-MoO_3 structure was not disturbed and α-MoO_3 remained the only crystalline phase detected in the XRD. The presence of a number of these defects is essential to make orthorhombic MoO_3 an active catalyst. The weakening of the Mo-O bonds, the sufficient mobility of oxygen ions and the formation of defects was suggested to be crucial for the reduction of MoO_3 and for its catalytic activity. [129] During the creation of these defects steps, point defects and new sites can be created by the removal of oxygen atoms from the catalyst surface as examined by Smith and Rohrer [130-131] by atomic force microscopy, which can influence the catalytic activity. [79]

Furthermore surface sensitivity of α-MoO_3 with regard to catalytic activity and selectivity in propylene oxidation was investigated by several groups. Volta and coworkers [132-134] applied graphite supported MoO_3 prepared from $MoCl_5$ at different temperatures in propylene oxidation and claimed the (100) plane to be active for acrolein formation and the (010) plane for CO_2 production. Hence, they concluded that hydrogen abstraction occurs on the (001) and (100) facets, whereas nucleophilic addition of oxygen into the allylic species takes place on (010). Testing the catalytic performance of oxidized Mo foils in the oxidation of propylene confirmed that total oxidation occurred on the basal (010) planes. [135-136] In contrast, Ziolkowski [137] concluded from a theoretical study that acrolein can be formed on (101) facets containing isolated oxygen. When oxygen groups were present like on the (001) or (100) facets, further oxidation or undesired total combustion, respectively, occurred. Brückman et al. [138] reported the (100) and (101) facets to be responsible for the activation of propylene, while oxygen was subsequently inserted into activated propylene on the (010) facet.

1.2.2. Hydrotreating

Hydrotreating describes the catalytic removal of heteroatoms from organic compounds with hydrogen, whereby the removal of sulfur is called hydrodesulfurization (HDS) and the removal of nitrogen hydrodenitrogenation (HDN). Besides the removal of sulfur and nitrogen, hydroprocessing leads to partial hydrogenation (HYD) of unsaturated hydrocarbons, mainly aromatics. The hydrotreating process is important in the petroleum refining industry and has been applied for over 50 years. All fractions of the distillation except for the light ends are treated in hydrogen for purification. This treatment is important to avoid NO_x and SO_x emissions, protect the catalyst used in following stages of the refining process as well as to improve the properties of the refined product. [139] Recently, new legislations regarding the sulfur content of support fuels has resulted in the demand for ultra low sulfur diesel (ULSD). Additionally the availability of light crude oil decreases and increasingly heavy feedstocks have to be refined, leading to new challenges for the refining industry and for catalyst design. [140-141]

The commercial hydroprocessing catalyst typically used is alumina supported molybdenum sulfide promoted with Ni or Co. [141-143] A pre-shaped alumina support is simultaneously impregnated with Mo and Co or Ni. Calcination delivers the oxide form. The oxidic catalyst is subsequently activated by *in situ* sulfidation with H_2S/H_2 and transformed into the sulfide form Co/Ni-Mo-S. The catalyst of choice depends on the reaction conditions e.g. temperature, feedstock, space velocity. [141] Co-Mo-S catalysts are more active in hydrodesulfurization, whereas Ni-Mo-S shows better activity for hydrodenitrogenation and hydrodeoxygenation. Ni-W-S is highly active in aromatic or olefin hydrogenation but is more expensive than the Mo based materials and therefore rarely used. [139]

For further improvement of the catalytic performance it is important to control the preparation and activation of the catalyst and to understand the characteristics of the active site. By application of various techniques such as extended X-ray absorption fine structure (EXAFS), transmission electron (TEM) and scanning tunneling microscopy (STM), electron paramagnetic resonance (EPR), X-ray photoelectron spectroscopy (XPS) and infrared (IR) it was demonstrated that the structure of the Co-Mo-S catalyst was identical to sulfided Mo/Al_2O_3, i.e. the active phase consists of slabs of hexagonal MoS_2 layers (crystal structure depicted in Figure 1.9). The cobalt was analyzed to exist as Co in the

alumina subsurface and bulk Co_9S_8, depending on the catalyst composition and preparation conditions. [144-149] Delmon [150-152] proposed and developed the "remote control mechanism" based on unsupported catalysts, which proceeds analogue to the remote control mechanism in selective oxidation reaction. The donor phase produces activated hydrogen 'H_{SO}', which spills over to the acceptor phase, where it can react with a heterocyclic compound and e.g. remove the sulfur. Co_9S_8 can activate hydrogen and subsequently this spilled over hydrogen partially reduces the molybdenum sulfide phase. Chu and Schmidt [153] observed by scanning tunneling microscopy (STM) and atomic force microscopy (AFM) that the surface of MoS_2 is partially destroyed by hydrogen especially on the edges of the hexagonal crystallites and sulfur is removed. This effect is strongly increased by the presence of Co or Ni. When sulfur is removed an unsaturated coordination site (CUS) is created which acts as a hydrogenation (HYD) center. The proposed mechanism for hydrodesulfurization of thiophene is depicted in the literature [142]. Generally, it is assumed that the sulfur containing heterocyclic compound and hydrogen react with different catalytic sites. The heterocyclic compound is adsorbed on a reduced metal center (e.g. Mo^{4+}), whereas hydrogen is activated by a sulfur site. [142]

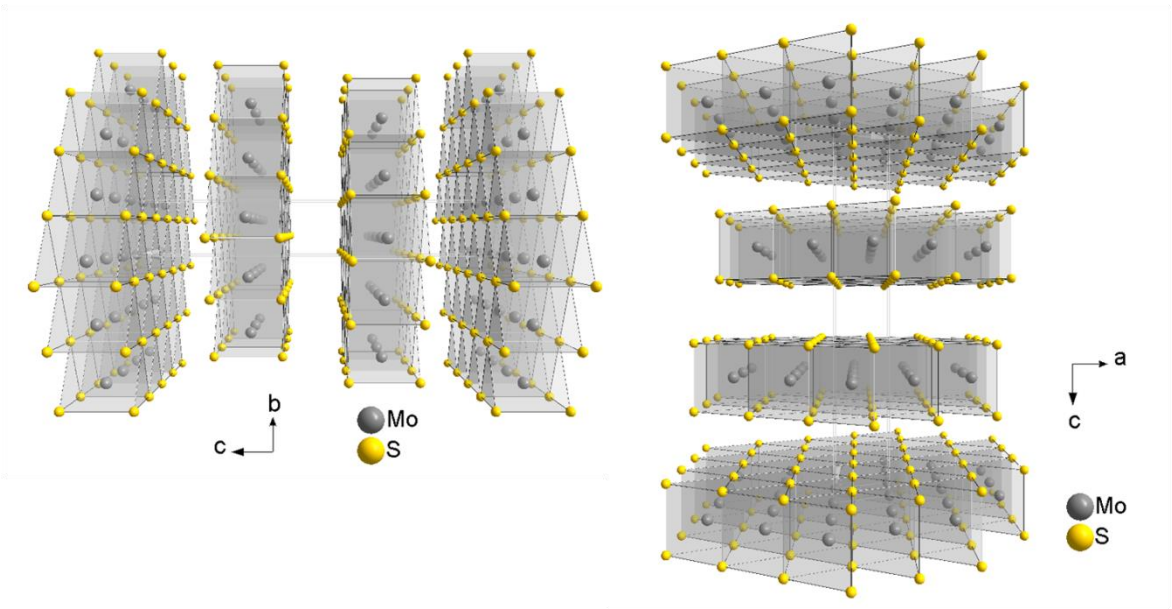

Figure 1.9: Crystal structure of layered MoS_2 projected along the a or the b axis.

Investigation of the influence of the Co concentration in Co/MoS_2 catalysts on the activity for HDS of thiophene showed that there were two increases in activity: At low cobalt content the edges of MoS_2 are decorated with cobalt ions and the activity increases until saturation of the molybdenum sulfide with Co. At higher Co content they suggested the

increase in activity could be attributed to formation of Co_9S_8, which was detected in the X-ray diffraction pattern. [154]

It can be concluded that Ni or Co increases the structural disorder of MoS_2 or WS_2 leading to the formation of non-stoichiometric highly active MoS_2. The promoter segregates from the Co/Ni-Mo/W-S mixed metal sulfide phase creating separated crystals of MoS_2 stacks and Co_9S_8. The MoS_2 stacking and the promoter segregation play important roles in supported industrial catalysts and unsupported model catalysts. [155-156]

This was not only demonstrated for Co- and Ni-promoted catalysts but also for the Fe-Mo-S system. Mixed Fe-Mo and Fe-W sulfides indicated similar structural and morphological properties to Co/Ni-Mo/W-S. [155, 157-159] Introduction of a second promoter (Co or Ni) to the Fe-Mo/W-S catalyst increased the catalytic activity, which was attributed to contact synergy (remote control model): the segregated promoter sulfide (Co_9S_8, FeS_2 or Ni_3S_2) provided spill over hydrogen to the active sites on the edges of the MoS_2 structures. [160-161]

Recently it was demonstrated that the active sites for key catalytic steps are not sulfur vacancies but fully sulfur-coordinated sites with metallic character, so called brim sites. Application of density functional theory (DFT) and atom-resolved scanning tunneling microscopy (STM) provided insight in the electronic structure of promoted and unpromoted MoS_2 showing that small molybdenum sulfide nanocrystals may have special sites at the edges with metallic properties. [162-163] Model studies using MoS_2 supported on Au(111) suggested that MoS_2 forms triangular platelets of S-Mo-S slabs stacked to different degrees. [140, 162] High-resolution transmission electron microscopy (HRTEM) measurements on carbon supported industrial type MoS_2 prepared by incipient wetness impregnation of high surface area graphitic carbon support confirmed the structure estimated for the model systems by STM. Additionally it was possible to determine the type (Mo or S) and the concentration of the edge sites. Shortly this structural information may be combined with catalytic activity data. [164-165] Addition of cobalt to MoS_2 strongly influences the morphology which changes from triangular to hexagonal (cf. Figure 1.10a) due to the preference of the promoter atoms to substitute certain sites. [140, 166] The Co-Mo-S clusters are terminated by (1010) edges and (1010) edges (see Figure 1.10b), where the promoter atoms exclusively occupy the so called S edges [(1010) edges] (see Figure 1.10d) as a result of the slightly higher stability which can be calculated for the different edges from the surface free energies. [163, 166]

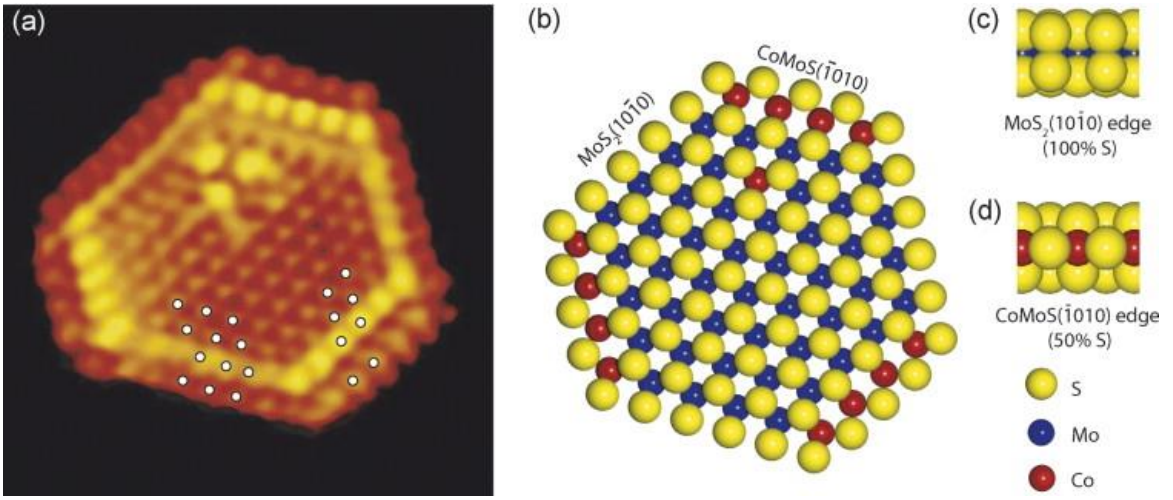

Figure 1.10: (a) Atom-resolved STM image of single layer Co-promoted MoS_2 demonstrating the metallic-like sites which look brighter; (b) Ball model of Co-Mo-S: top view; (c) Side view of MoS_2 $(10\bar{1}0)$ edge; (d) Side view of Co substituted MoS_2, the Co-Mo-S $(\bar{1}010)$ edge; with permission from **[166]**.

Promoter atoms may also be present in the support or as separate promoter sulfide structures (see Figure 1.11) but these species are not active and it is important to avoid their formation during catalyst preparation and activation. [167] Generally, preparation conditions of the Co-Mo-S materials significantly influence their catalytic activity.

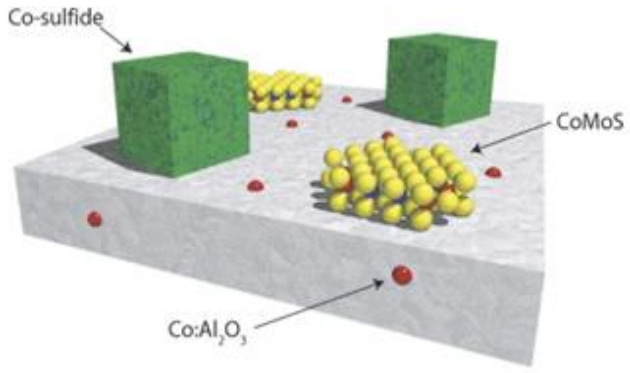

Figure 1.11: Illustration of the various phases in a Co-Mo catalyst after sulfidation. The CoMoS phase is required whereas formation of the other phases should be prevented. Adapted with permission from [166].

During *in situ* STM studies reaction intermediates associated with brim sites could directly be observed. Due to their metallic character brim sites may bind sulfur containing reactants and adjacent edge sites in the form of SH-groups may transfer hydrogen, resulting in hydrogenation of a C=C double bond and breakage of C-S bonds. [168] The brim sites located on the top of multi-stacked MoS_2 structures are considered "open" sites which enable the adsorption of sterically hindered molecules such as dialkylated

dibenzothiophene (DBT) which are considered the least reactive sulfur compounds in the diesel range but need to be removed for ultra low sulfur diesel (ULSD) production. [167] These sterically hindered DBTs mainly proceed via pre-hydrogenation (HYD) route rather than direct desulfurization (DDS), which dominates for molecules like DBT. After pre-hydrogenation the alkylated DBTs are not planar anymore and sulfur can be easier removed. [169] H_2S inhibits hydrodesulfurization but it mainly inhibits the DDS and not HYD pathway, due to the fact that brim sites are not poisoned by H_2S. [142] Basic nitrogen compounds are strong inhibitors to the HYD pathway, because these N-containing molecules strongly interact with brim sites as well as with their neighboring acidic protons. [140]

1.3. Motivation

Over the past decades, the synthesis of inorganic nanomaterials with novel structures and designed morphology [11, 21] as well as a reliable and predictable production has attracted considerable interest. It is well known that shape and structure of materials determine their properties such as electrochemical activity. [170-171] They also play a decisive role in catalysis [172-175] and especially selective oxidation reactions are known to be strongly structure sensitive [134, 176-178]. Therefore the ability to control particle size, shape and composition of transition metal oxides has become an important topic. A detailed understanding of the effect of the preparation conditions on the properties of the product and the resulting effect on the catalytic activity is essential in rational design of catalysts. Conventional preparation methods like co-precipitation or wet impregnation have been optimized in the past but they may have drawbacks like the requirement of calcination to obtain the desired crystalline phase. Hydrothermal synthesis, which is in catalysis usually applied to synthesize zeolites, can give access to a large variety of transition metal oxide materials, metastable or novel phases as well as known phases with defined morphologies. The aim of this work was to synthesize materials under mild hydrothermal conditions as a typical soft chemistry route and to compare them to catalysts prepared by flame spray pyrolysis, a novel preparation method giving access to nanostructured materials. Nanomaterials exhibit different properties compared to the according bulk materials and should be beneficial for catalysis due to the small ratio of bulk material to exposed surface. In the present work, molybdenum based catalysts are prepared by hydrothermal synthesis and flame spray pyrolysis, the resulting properties are studied in detail and compared to

materials synthesized by conventional co-precipitation. Starting from rather simple α-MoO_3, in the next step more complex Bi-Mo-O and Co-Mo-O systems are prepared. The catalysts are applied in selective oxidation of propylene and hydrotreating: Two industrial relevant processes which have been applied for over 50 years, but always have to face new challenges.

2 Materials and methods

In this chapter the general experimental procedures and methods are described with focus on the experimental set-ups and characterization methods. A detailed description of the catalyst synthesis is given in the different chapters.

2.1. Catalyst synthesis

All chemicals applied in this work were analytical grade and used without further purification.

2.1.1. Hydrothermal synthesis

The precursors were dissolved or suspended in water, a diluted acid or base and the pH value was adjusted with the aid of a titrator (TitroLine easy, Schott Instruments). After homogenization through magnetic stirring for a certain time the Teflon-Inlays were transferred in the 250 ml stainless steel autoclaves (see Figure 2.1) from Berghof, sealed and put in a drying cabinet (Binder) for the required time. The autoclaves were taken out of the oven, cooled down to room temperature and the resulting solid was filtrated and washed. Afterwards, the product was dried at room temperature and ambient pressure for several days.

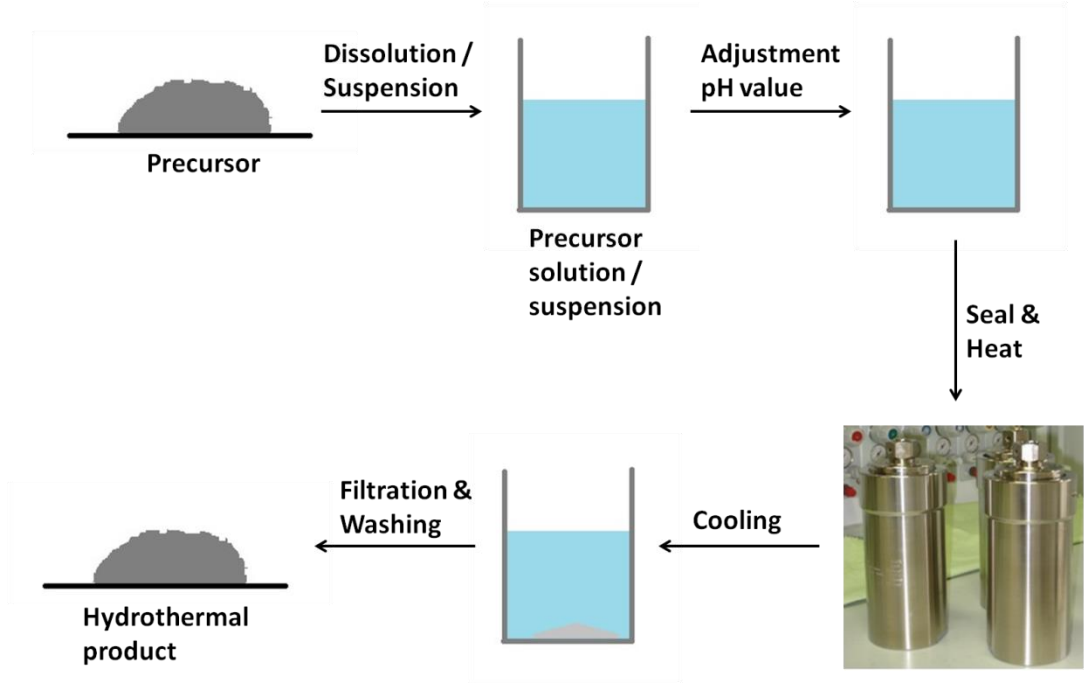

Figure 2.1: Schematic presentation of hydrothermal synthesis steps.

2.1.2. Flame spray pyrolysis (FSP)

The FSP set up at the Institute for Chemical Technology and Polymer Chemistry, KIT is based on previous designs by Mädler and Pratsinis [64, 179-181] depicted in Figure 1.4 corresponding to a set-up at DTU [76, 182]. A photograph of the set up with description of the various components is shown in Figure 2.2. The capillary has a diameter of 0.413 mm (Hamilton KF6 gauge 22) and can be placed in the capillary holder in the nozzle. The precursor solution is loaded in a 50 ml syringe, which is placed in a syringe pump (World Precision Instruments) and the precursor solution was fed to the capillary tube at 5 ml/min. The gas flows of oxygen and methane are controlled by mass flow controllers (Bronkhorst) and typically 5 Nl/min of oxygen as well as a mixture of 1.6 Nl/min of oxygen and 750 Nml/min methane were used as dispersion and supporting gas, respectively. The flame was ignited by the oxygen/methane mixture and the product particles were collected on water cooled glass fiber filter (Ø 240 mm; Whatman GF6) by means of a vacuum pump (R5, Busch).

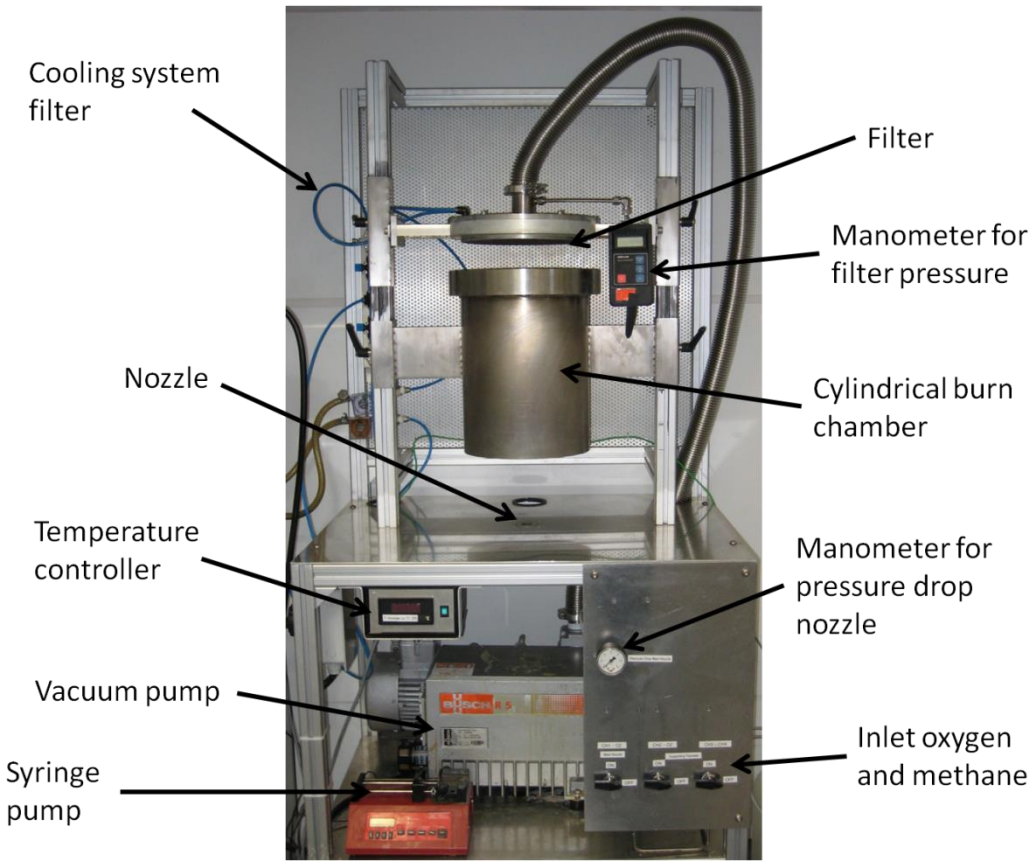

Figure 2.2: Photograph of the FSP set-up at Karlsruhe Institute of Technology (KIT) with description of the different components. The whole set-up is placed in a fume hood.

Typically, after 100 ml solution i.e. two syringe loadings the filter was changed and about 500 mg of catalyst is recovered from the filter by careful scraping with a spatula. The recovered powder is sieved to remove large pieces of filter material from the product. Smaller filter pieces remaining in the FSP product should be catalytically inactive but could influence the weight measurements e.g. for the analysis of the surface area or catalytic activity measurements.

2.2. Characterization

2.2.1. X-ray diffraction (XRD)

X-rays are partly scattered on the surface of a crystal and part of the X-rays can pass through to the next layer of atoms. For obtaining characteristic X-ray pattern, the sample must have a long range order and the spacing between the atoms must be close to the

radiation wavelength. If diffracted beams of atoms in a periodic lattice are in phase, constructive interference occurs and the diffraction pattern shows a reflection. [183] Hence, reflections in the diffraction pattern only occur if the Bragg equation (2.1) is satisfied:

$$n \lambda = 2 d \sin\theta \qquad (2.1)$$

n	integer
λ	wavelength
d	spacing between atom layers
θ	angle of incidence of the X-rays

In this work the structure of the different samples was determined by powder X-ray diffraction (PXRD) using a Bruker D8 Advance diffractometer in the range 2θ = 8 - 80° (step size 0.016 °) with Cu K_α radiation (Ni-filter, 45 mA, 35 kV) in Bragg-Brentano geometry on rotating sample holders. In the case of Bragg-Brentano geometry the detector is always at 2θ of the incident beam, whereas the sample holder is always at θ of the incident beam. For characterization of the sulfided cobalt molybdates a PANalytical X´Pert PRO was used with Cu K_α radiation (Ni-filter, 40 mA, 45 kV) on rotating sample holders in the same 2θ range as the oxidic materials.

2.2.2. Raman spectroscopy

Raman spectroscopy relies on inelastic scattering of monochromatic light, usually from a laser, which can interact with a molecule. [184] When energy is transferred between a photon and a molecule, the molecule is excited from the ground state to a virtual state. After relaxation the molecule returns to a different energy state, not the ground state. The difference in the emitted photon energy leads to the Raman shift. This Raman shift is independent of the laser used in the measurements. [185] The resulting Raman bands can be assigned to vibrations of different bonds in the molecule, whereas the shortest bonds vibrate at the highest energies resulting in high wave numbers for the Raman shift. In this work Raman spectra were recorded at Haldor Topsøe A/S with a Horiba Jobin Yvon spectrometer (LabRam) attached to an Olympus microscope (BX 40) using a HeNe laser with 632.8 nm excitation. Spectra were measured in the 100 - 1100 cm^{-1} range with the sample on an object slide without pretreatment. Several spectra from section 4.3.4.1 were recorded by Randi Hansen and Dr. Pablo Beato.

2.2.3. X-ray absorption spectroscopy (XAS)

X-ray absorption spectroscopy can provide information about the local atomic structure of a material, amorphous phases can be studied and information about promoters as well as local distortions of crystal lattices can be obtained. [186] Monochromatic X-rays are used to excite an electron to an unoccupied molecular orbital (MO); the absorbed energy can be determined by comparing the intensity of the beam in front of the sample and behind it. X-ray absorption spectra are measured at an element specific energy edge to provide enough energy to excite the electron close to the core on a higher energy level. The excited electron can interact with neighboring atoms, leading to backscattering effects. The resulting spectra can be divided into two regions: The X-ray absorption near edge structure (XANES) and the extended X-ray absorption fine structure (EXAFS). XANES gives information about the electronic structure and the oxidation state of the absorber atom, the electronegativity of the neighboring atoms and the symmetry of the atomic environment, whereas by EXAFS analysis the coordination number, the bond length and the short range order can be determined. [186-187]

XAS was performed at the SNBL beamline (BM01B) at the ESRF synchrotron radiation source (Grenoble, France). The samples were diluted with cellulose or boron nitride and pressed as a pellet for *ex situ* measurement in transmission mode at the Mo K edge (20.0 keV). The spectra were recorded by Dr. Hudson Carvalho and Dr. Dmitry Doronkin. XAS data were processed using the IFFEFIT software package. [188]

2.2.4. Physisorption

Nitrogen physisorption at the boiling point of nitrogen was used to determine the specific surface area (SSA) of the various samples with a Belsorp II mini (BEL Japan Inc.) using multipoint BET theory in the $p/p_0 = 0.05 – 0.3$ range. The model according to Brunauer, Emmett and Teller (BET) considers multilayer adsorption and the surface area can be calculated from the linear part of the adsorption/desorption-isotherm with the following equation [183]:

$$\frac{\frac{p}{p_0}}{n_{ads}\,\frac{1-p}{p_0}} = \frac{1}{n_m C} + \frac{C-1}{n_m C} \cdot \frac{p}{p_0} \qquad (2.2)$$

p	equilibrium pressure of adsorbate
p_0	saturation pressure of adsorbate
n_{ads}	quantity of adsorbed gas
n_m	quantity of a monolayer adsorbed gas
C	BET constant

2.2.5. Electron microscopy

Electrons give access to microscopic images with a higher resolution than visible light microscopes. Different modes of electron microscopy were used in the present work namely scanning electron microscopy (SEM) and transmission electron microscopy (TEM). SEM is a straight forward method to determine the size and morphology of particles. A narrow electron beam is scanned over the surface of a sample and either secondary (low energy) or backscattered electrons in relation to the primary beam are detected. Resolutions of 50 – 100 nm can be reached. TEM can be applied for the examination of particles in the size range 1 nm – 5 µm. A homogeneous and parallel electron beam accelerated with high voltage of 50 - 100 kV penetrates the thin sample leading to elastically scattered electrons which provide information about the inner structure and morphology of the particles. Energy dispersive X-ray (EDX) spectroscopy was used to determine the elemental composition at various spots of the samples. Element characteristic X-radiation is generated by the interaction of electrons and matter giving information on the composition. [183, 186]

For scanning electron microscopy (SEM), performed on a Quanta 200 ESEM (FEG) microscope at the Centre of Electron Nanoscopy (CEN) at the Technical University of Denmark (DTU), samples were deposited on a carbon foil on aluminum stubs and coated with carbon to improve the conductivity.

Bright field transmission electron microscopy (Tecnai T20, DTU-CEN) was measured on the as-prepared powders supported on lacey carbon copper grids by Dr. Martin Høj. The oxidic catalyst powder was transferred to the grid by dipping it several times in the powder

and removing loosely bound excess. Transmission electron microscopy (TEM) was also used to examine the spent, sulfided cobalt molybdate catalysts, i.e. the samples after their application in the hydrotreating test reaction, using a CM 200 FEG from Philips/FEI at Haldor Topsøe A/S. For this purpose, a small amount of the sample was dispersed in ethanol in an ultrasonic bath and a drop of the suspension was placed on a Cu-grid coated with carbon.

2.2.6. X-ray photoelectron spectroscopy (XPS)

XPS was used for the analysis of the surface composition. A sample is irradiated by X-rays and surface atoms adsorb photons leading to the ejection of core or valence electrons, which have a certain binding energy (E_b) and kinetic energy (E_{kin}). The number of photoelectrons escaping from the surface is continuously detected as a function of the kinetic energy, which is translated in the binding energy characteristic for an element. [184]

$$E_B = h\nu - E_{kin} - \varphi \qquad (2.3)$$

φ	work function of the spectrometer
h	Planck´s constant
ν	frequency of excitation radiation

XPS measurements require high vacuum and are surface sensitive because the photons have only sufficient energy to penetrate the surface layers. [186] In this work XPS was performed by Vanessa Trouillet at IAM-ESS at KIT with a K-Alpha spectrometer (ThermoFisher Scientific) using a microfocused Al K_α X-ray source (400 µm spot size). Details of the data acquisition and processing using the Thermo Avantage software is described elsewhere. [189] Charge compensation during analysis was achieved using electrons of 8 eV energy and low energy argon ions to prevent any localized charging. Spectra were fitted with one or more Voigt profiles (binding energy uncertainty: ±0.2 eV). [100, 190] Scofield sensitivity factors were applied for quantification. [191] The energy scale was shifted to the binding energy of C 1s (C-C, C-H) at 285.0 eV and was calibrated by means of the photoelectron peaks of metallic Cu, Ag and Au, respectively.

2.2.7. Analysis of bulk composition

The bulk composition of the catalysts was determined by optical emission spectrometry with inductively coupled plasma (ICP-OES, Agilent 720/725-ES) by Herrmann Köhler, IKFT at KIT. The plasma was created by a 40 MHz high-frequency generator and argon was applied as the plasma gas. For the ICP-OES each sample was dissolved in 6 ml concentrated HNO_3, 2 ml concentrated HCl and 0.5 ml H_2O_2 in a microwave (at 600 Watt for 45 minutes). Quantitative nitrogen analysis was carried out using hot gas extraction method (LECO TC 600) by Dr. Thomas Bergfeldt, IAM-AWP at KIT. The samples were heated in a graphite crucible under flowing helium and thermally decomposed. The amount of N_2 gas was determined by a heat conductivity detector. Each measurement was repeated twice and a standard deviation was calculated.

2.2.8. Temperature programmed reaction methods

Temperature programmed reduction

Temperature programmed reduction (H_2-TPR) was conducted in a tubular reactor using 100 mg of sample and a flow of 96 ml/min with a gas composition of 5% H_2 in argon. Crushing and sieving of the sample did not change the results and TPR was performed using the as-prepared powder. The reactor was heated with 5 K/min from room temperature to 1000 °C. Reduction led to a decrease in hydrogen concentration which was detected by a thermal conductivity detector. The condensation of the produced water in the tubes was avoided by using a cold trap, which was cooled with liquid nitrogen.

Temperature programmed desorption

The amount of acidic sites on the surface was estimated using temperature programmed desorption of ammonia (NH_3-TPD) by heating up to 600 °C with 10 K/min and on-line gas analysis by FTIR (MultiGas™ Analyzer, MKS instruments). For this purpose 400 mg of catalyst (without crushing and sieving) were fixed with glass wool in a tubular glass reactor. The reactor was heated up with a rate of 10 K/min and the catalyst was pretreated in synthetic air (500 ml/min) at 500 °C for 1 h. After cooling down to room temperature, the gas was changed to pure nitrogen and the tubes were flushed to remove oxygen. After saturation with ammonia at 50 - 60 °C using 500 ml/min with a composition of 1000 ppm NH_3 in N_2, the excess amount of NH_3 was removed (flushing with N_2 until steady minimum of NH_3 in the exit gas).

2.3. Catalytic activity measurements

2.3.1. Selective oxidation of propylene

Propylene conversion and acrolein / CO_x selectivity was measured in a continuous flow fixed bed micro reactor established at the Technical University of Denmark (DTU) at the Department of Chemical and Biochemical Engineering [192]. The test unit was commercially built (ChimneyLab Europe) and enabled measurements for 50 - 500 mg of sieved catalyst, total gas flow of 30 - 300 Nml/min at 200 - 850 °C near ambient pressure. A photograph of the set-up is shown in Figure 2.3 and Figure 2.4 presents a photograph of the U-shaped quartz reactor. Gas mixing is performed by four calibrated mass flow controllers (MFC, Brooks) and dry air can be supplied by a single MFC for oxidative pretreatment of the catalyst (see PI-diagram in Figure 2.5). Three U-shaped quartz reactors with 4 mm inner diameter are connected in series configuration and each reactor is placed in a 50 mm diameter tubular furnace with individual temperature control (Watlow). A thermocouple was placed inside each reactor just touching the catalyst bed to measure the reaction temperature and a pressure transducer placed upstream of the reactor monitored the actual reaction pressure. Gas analysis was performed using a dual channel GC–MS (Thermo Fisher) with a TCD detector to quantify N_2, O_2, CO and CO_2 using Hayesep Q and Molsieve 5A packed columns and a FID detector parallel with the MS to identify and quantify light hydrocarbons and oxygenated products.

Figure 2.3: Photograph of the activity test set-up for selective oxidation reactions at DTU, Department of Chemical and Biochemical Engineering. On the left the mass flow controllers can be seen and on the right is the GC-MS. On the picture all ovens are lifted up and the reactors are covered.

Figure 2.4: Photograph of the quartz reactor loaded with a catalyst connected to the test set-up.

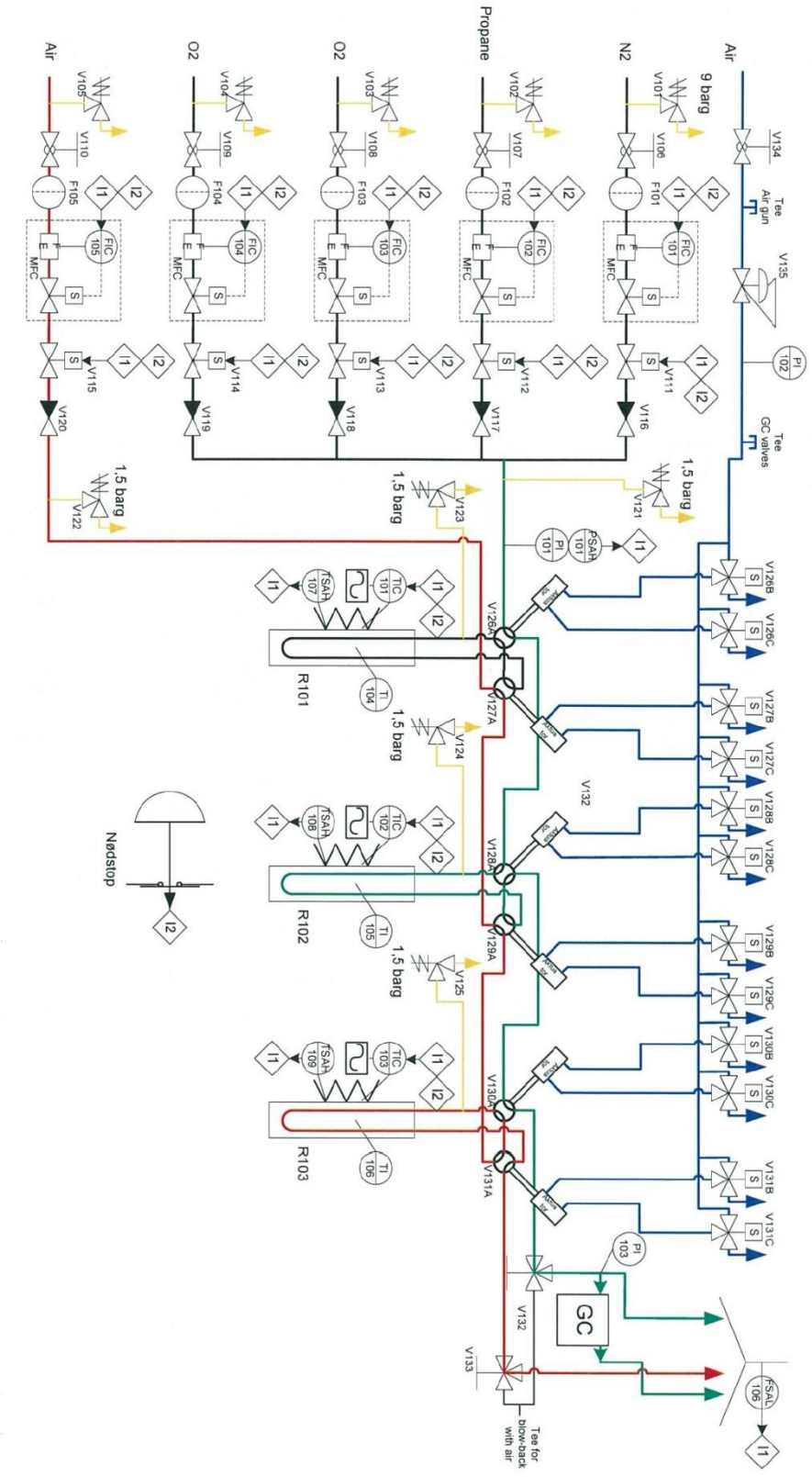

Figure 2.5: PI-diagram of the set-up for selective oxidation. The first reactor is disconnected to the gases e.g. for loading or unloading of the catalyst, whereas the test gas mixture is running through the second reactor and the third reactor has the flow of air for oxidative pre-treatment of the loaded catalyst. Propylene can replace propane.

The measured concentrations were corrected for expansion of the gas due to combustion using the nitrogen signal as internal standard, before calculating the conversion of propylene ($X_{Propylene}$), the selectivity to acrolein ($S_{Acrolein}$) and the acrolein yield ($Y_{Acrolein}$).

$$X_{Propylene} = 1 - \frac{c_{C_3H_6}}{c_{C_3H_6}^{bypass}} \tag{2.4}$$

$c_{C_3H_6}$ propylene concentration detected in the product stream [vol.%]

$c_{C_3H_6}^{bypass}$ propylene concentration detected in the bypass [vol.%]

$$S_{Acrolein} = \frac{c_{C_3H_4O}}{c_{C_3H_6}^{bypass} - c_{C_3H_6}} \tag{2.5}$$

$c_{C_3H_4O}$ propylene concentration detected in the product stream [vol.%]

$$Y_{Acrolein} = X_{Propylene} \cdot S_{Acrolein} = \frac{c_{C_3H_4O}}{c_{C_3H_6}^{bypass}} \tag{2.6}$$

In a typical activity test the catalyst powders were crushed and sieved to 150 – 300 µm sized particles, 500 mg of sample was loaded in the reactor without dilution and stabilized with quartz wool. The catalysts were pre-oxidized in dry air at 550 °C for calcined samples and 300 °C for as-prepared samples in the reactor. Activity tests were performed using a gas composition of $C_3H_6/O_2/N_2$ = 5/25/70 and flows of 50, 80, 120, 180, 260 Nml/min. Part of the activity measurements was performed by Dr. Martin Høj, others during a research stay at DTU.

A blank test without catalyst using a total flow of 100 Nml/min with $C_3H_6/O_2/N_2$ = 5/25/70 showed that no propylene was converted at temperatures from 400 – 540 °C. The values determined for propylene and oxygen conversion varied between 0 – 0.6% indicating that the error is below 1%. Repetition of the activity measurement for sample Bi1Mo1_pH8 (chapter 4.3.4) suggested that the relative error is smaller than 6% for propylene oxidation and 10% for acrolein selectivity. Limitations through mass transfer can be neglected according to [192], where higher rates were achieved.

2.3.2. Hydrotreating

The activity measurements were performed at Haldor Topsøe A/S in a vertical fixed-bed reactor with 7.5 mm inner diameter (see Figure 2.6). The as-prepared catalyst powder was pressed into pellets by means of a hydraulic press with subsequent mechanical granulation to achieve the 600 – 850 µm sieve fraction. 300 mg of catalyst were diluted with 200 µm Ballotini glass beads and the mixture was loaded into the reactor. Below and above the catalyst bed glass beads were placed to secure steady mass and heat transfer. [192-193]

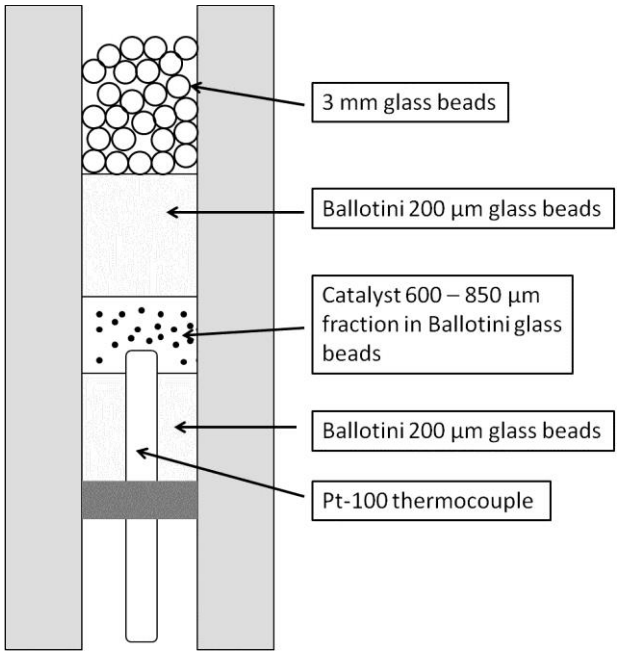

Figure 2.6: Cross section of high pressure reactor for hydrotreating test reaction according to [193].

Upon entry into the hot reactor the liquid feed was evaporated and mixed with a hydrogen stream. The oxidic precursor was sulfided *in situ* for 4 h at 350 °C in a feed flow containing dimethyldisulfide (DMDS) dissolved in n-heptane with hydrogen at a partial pressure of $p(H_2)$ = 42 atm resulting in a total pressure of 50 atm. Under these conditions all components were in the gas phase and DMDS decomposes to hydrogen sulfide and methane. After this activation the liquid feed was switched to a model oil composed of 3.0 wt.% dibenzothiophene (DBT), 0.5 wt.% indole, 1.0 wt.% naphthalene, 2.5 wt.% DMDS and 0.5 wt.% n-nonane in n-heptane. The test was performed at 50 atm ($p(H_2)$ = 38 atm) at 350 °C with a liquid feed rate of 0.5 ml/min and a gaseous hydrogen feed rate of 250 Nml/min. DMDS decomposed in the presence of H_2 and the resulting partial pressure of H_2S ensured that the catalyst remained fully sulfided. [192-194] Note that this mixture

allowed determination of hydrodesulfurization (HDS), hydrodenitrogenation (HDN) and hydrogenation (HYD) activity since DBT is a representative sulfur compound, indole represents nitrogen containing diesel compounds and naphthalene is a representative aromatic compound. The product stream was continuously analyzed by GC-FID analysis and n-nonane was added as an internal standard for the gas chromatographic (GC) analysis. The conversion was calculated by integration of the peaks in the chromatogram. The results were related to a commercial reference catalyst. DBT can be desulfurized via two different routes: direct desulfurization to biphenyl (BP) or pre-hydrogenation to cyclohexyl benzene (CHB) (see Figure 2.7). Indole was hydrodenitrogenated to ethylbenzene and ethylhexane and naphthalene was hydrogenated to tetralene.

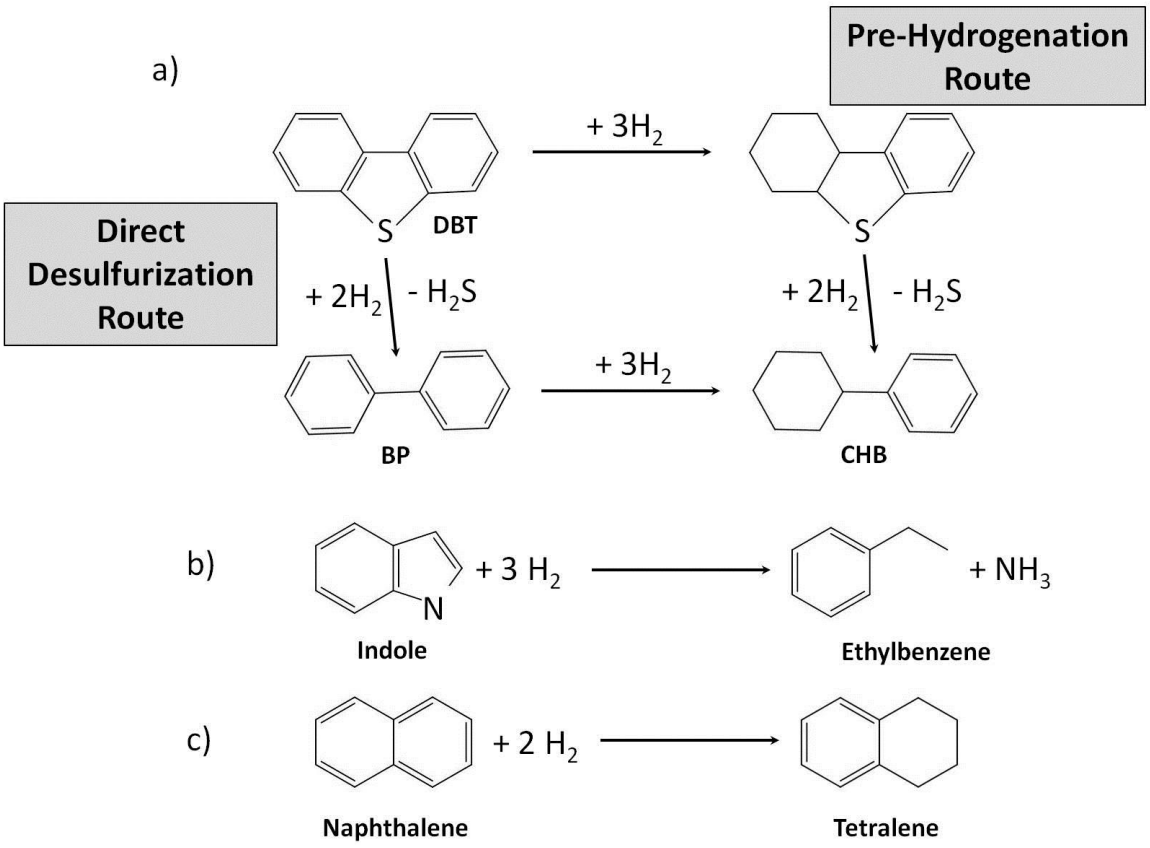

Figure 2.7: The reaction pathways of the three model compounds for hydrodesulfurization (a) by direct desulfurization or pre-hydrogenation of DBT, hydrodenitrogenation of indole (b) and hydrogenation of naphthalene (c).

For desulfurization, denitrogenation and hydrogenation the pseudo first order rate constants were calculated according to the following equation [192-193]:

$$k = -WHSV \cdot \ln(1 - X) \quad (2.7)$$

$$WHSV = (F_{feed} \cdot \rho_{feed})/w_{catalyst} \quad (2.8)$$

X	conversion
WHSV	weight hourly space velocity
F_{feed}	volumetric flow rate
ρ_{feed}	density of the feed
$w_{catalyst}$	catalyst mass

3 MoO_3 as model catalyst in the selective oxidation of propylene[1]

3.1. Introduction

As already mentioned in 1.1.1, hydrothermal synthesis is an ideal method to obtain fine powders of controlled morphology, high crystallinity with narrow particle size distribution. For the hydrothermal synthesis of molybdenum trioxide in the shape of ribbons, rods or nanobelts various preparation routes are known [10-13, 15, 21, 171] and these MoO_3 nanorods tolerate temperatures up to 400 °C. [11]

MoO_3 is known to be a structure sensitive catalyst in the oxidation of olefins [132-134, 138] and alcohols [178, 195-196] as well as the reduction of nitric oxide [197]. However, there is still no general agreement on the role of the different facets of MoO_3 crystals (cf. 1.2.1) and this discussion in the literature corroborates the need for further studies on well characterized molybdenum trioxide materials using hydrothermal synthesis for the design of MoO_3 with various morphologies and thus different preferentially exposed crystal facets. Hence, α-MoO_3 was synthesized under hydrothermal conditions to rationally vary the morphology using e.g. different precursors, acids and pH values and to test them in selective propylene oxidation. In addition, one-step flame spray pyrolysis [75] was applied for comparison. Beside the structure of the prepared MoO_3, also its morphology, acidity, surface area and nitrogen content were studied in detail. Finally, the catalysts were also characterized after their application in selective oxidation of propylene, to analyze possible changes of the applied materials during time on stream.

[1] Part of this chapter will be published as: Systematic study on the influence of particle size and morphology of α-MoO_3 on the selective oxidation of propylene by Kirsten Schuh, Wolfgang Kleist, Martin Høj, Anker Degn Jensen, Pablo Beato, Greta R. Patzke and Jan-Dierk Grunwaldt.

3.2. Catalyst preparation

For the synthesis of pure molybdenum trioxide (MoO_3) by hydrothermal synthesis different precursors and acids were used. The names are given based on the precursor, the acid (HNO_3 and HOAc for acetic acid), pH value (adjusted by HNO_3), additional calcination (at 550 °C) and special methods e.g. FSP for flame spray pyrolysis (detailed denotation see further below). The preparation was performed as follows.

Ammonium heptamolybdate tetrahydrate (AHM; $(NH_4)_6Mo_7O_{24} \cdot 4H_2O$, VWR AnalaR NORMAPUR) was dissolved in 100 ml deionized water under continuous stirring at room temperature. The pH value was adjusted to 0 - 2 by using 2.2 M nitric acid (prepared from nitric acid 65%, VWR AnalaR NORMAPUR), the resulting colorless solution was stirred for 30 minutes and subsequently heated in sealed autoclaves with Teflon inlays (cf. chapter 2.1.1) at 180 °C for 24 h in an oven.

$MoO_3 \cdot 2H_2O$ (synthesized according to a literature procedure [198]) and diluted nitric acid (2.2 M) or acetic acid (25 vol.%; prepared from 100% glacial acetic acid, Merck p.a.) were added to the Teflon liners as reported in literature [11] and the resulting suspensions were heated in the autoclaves at 180 °C for 48 h in an oven (details see chapter 2.1.1).

After the autoclaves were cooled down to room temperature, the solid product was separated by filtration, washed with water, ethanol and finally acetone. The resulting powder was dried at room temperature and ambient pressure. Afterwards all samples were calcined at 550 °C for 4 h, to exclude a possible influence of the temperature treatment on the catalyst performance [124]. These samples are denoted here as followed: Precursor_pH_synthesis time or Precursor_acid.

In addition, MoO_3 was prepared by one-step flame spray pyrolysis (FSP). The precursor solution was prepared by dissolving 9.6 g Mo(VI)-2-ethylhexanoate (15% Mo; Strem Chemicals) in 100 ml xylene. The sample collected from the filter was calcined at 550 °C for 4 h (FSP_MoO3). Details of the preparation by FSP were already described in chapter 2.1.2.

1 g of the non-calcined flame made MoO_3 was also treated hydrothermally in 2.2 M nitric acid for 24 h at 180 °C (FSP_MoO3_HNO3). For comparison with the hydrothermally synthesized and flame made samples ammonium heptamolybdate was calcined for 10 h at 550 °C to prepare pure α-MoO_3 (AHM_calcined).

3 MoO_3 as model catalyst in the selective oxidation of propylene

To analyze the influence of nitrogen incorporation into α-MoO_3 on the catalytic performance of the hydrothermally synthesized materials, the sample prepared from $MoO_3 \cdot 2H_2O$ and acetic acid was also treated in ammonia. The sample was dried in synthetic air at 110 °C for 2 h and then treated in 5% NH_3 in N_2 for 10 h using a flow of 500 ml/min at 250 °C. This resembles the procedure described by Kuehn et al. [199] Afterwards the resulting material was calcined at 550 °C for 4 h like all the other samples.

The synthesized samples were characterized by powder X-ray diffraction (PXRD), Raman spectroscopy, H_2-TPR and NH_3-TPD as described in chapter 2.2. The surface area was determined by nitrogen physisorption, the nitrogen content of the samples was analyzed (see 2.2.7) and the particle morphology was determined by SEM for the hydrothermally synthesized samples and TEM in case of the flame made samples. *Ex situ* XAS measurements were performed using pellets of the samples diluted with cellulose. Details of the characterization are described in chapter 2.2. Catalytic activity measurements for selective oxidation of propylene were performed according to chapter 2.3.1.

3.3. Results and Discussion

3.3.1. Structural characterization and composition

Ammonium heptamolybdate was treated with nitric acid under hydrothermal conditions at 180 °C for 24 h. The product phases and morphologies were strongly dependent on the pH value, which is shown in Figure 3.1a and Figure 3.2. At pH = 2 a phase corresponding to hexagonal $(NH_4)_{0.944}H_{3.304}Mo_{5.292}O_{18}$ [200] (JCPDS no. 83-1175), showing a hexagonal prismatic morphology, was formed. Decreasing the pH value to 1 resulted mainly in $(NH_4)_{0.944}H_{3.304}Mo_{5.292}O_{18}$ but also traces of α-MoO_3 were found in the diffraction pattern as indicated by the diffraction reflections at 23.3, 27.3 and 39.0 °. The particles were also prismatic and hexagonal but more agglomerated and additionally some needles were present, according to SEM (Figure 3.2). Synthesis at pH = 0 led to the formation of pure α-MoO_3 [201] (JCPDS no. 5-508) with rod-like morphology. After calcination at 550 °C for 4 h the diffraction pattern of all three samples (see Figure 3.1b) showed solely α-MoO_3 but the relative intensities of the reflections characteristic for orthorhombic molybdenum

trioxide were different, indicating different morphologies. This is confirmed by the SEM images shown in Figure 3.2. The hexagonal prismatic particles obtained from ammonium heptamolybdate and HNO_3 at pH = 2 were transformed into randomly shaped particles, proving that the morphology could not be conserved after calcination. The sample prepared at pH = 1 still showed a hexagonal prismatic morphology and the sample prepared at pH = 0 maintained its rod-like morphology after calcination.

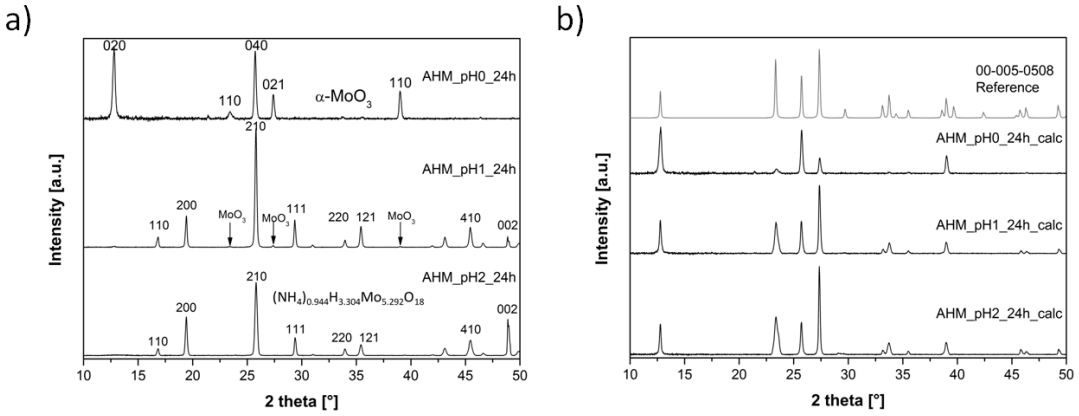

Figure 3.1: X-ray diffraction pattern of differently prepared samples from ammonium heptamolybdate and nitric acid by variation of the pH value before (a) and after calcination (b). Note that $(NH_4)_{0.944}H_{3.304}Mo_{5.292}O_{18}$ is one of the possible ammonia-containing Mo-phases that may be formed.

The different phases of the hydrothermally synthesized products can be explained by the various polymolybdate species present in the solution depending strongly on the pH value. In an acidic solution $[Mo_7O_{24}]^{6-}$ and $[Mo_8O_{26}]^{4-}$ can be found, while at very low pH (< 1) $[Mo_{36}O_{112}]^{8-}$, $[HMoO_3]^{+}$, $[H_2Mo_2O_6]^{2+}$ and $[H_3Mo_2O_6]^{3+}$ are formed. Further decrease of the pH value leads to $MoO_3 \cdot 2H_2O$ (cf. 1.1.1). [14] The isopolymolybdate anions $[Mo_7O_{24}]^{6-}$ are transformed to neutral Mo_7O_{21} (α-MoO_3).

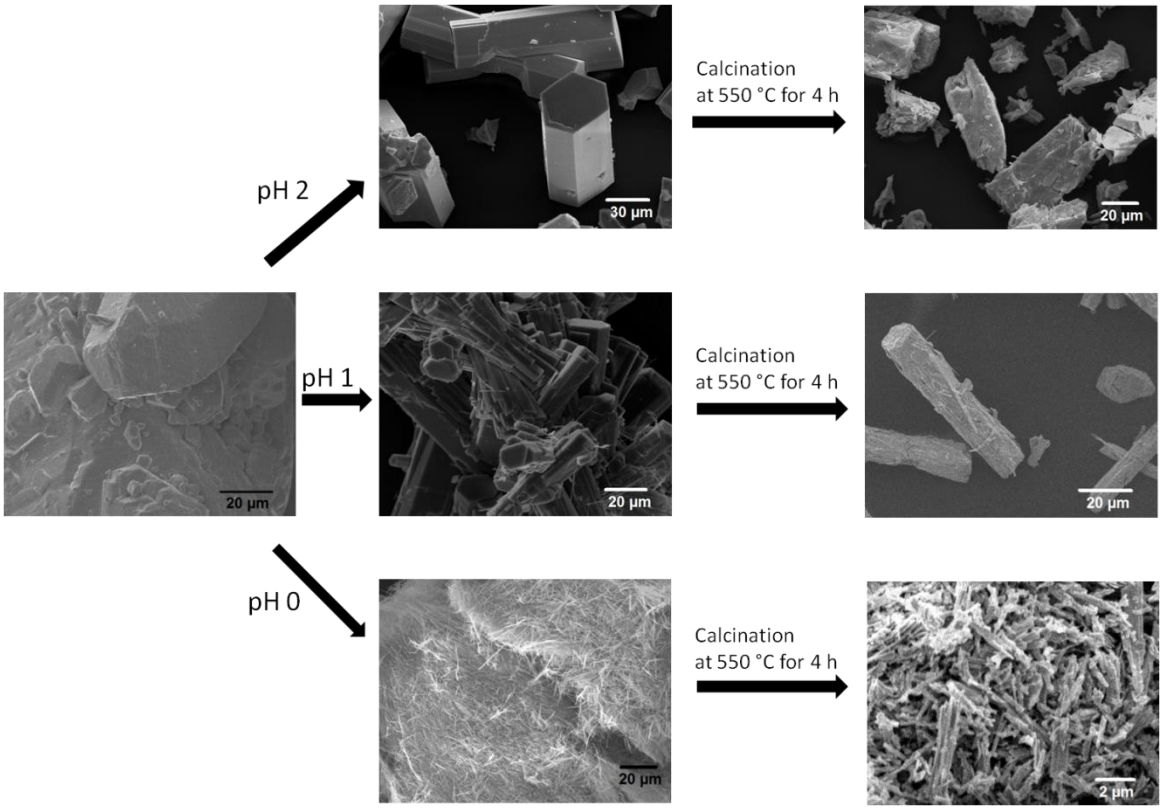

Figure 3.2: Morphology represented by SEM images of different samples from ammonium heptamolybdate and nitric acid by variation of the pH value and after calcination at 550 °C.

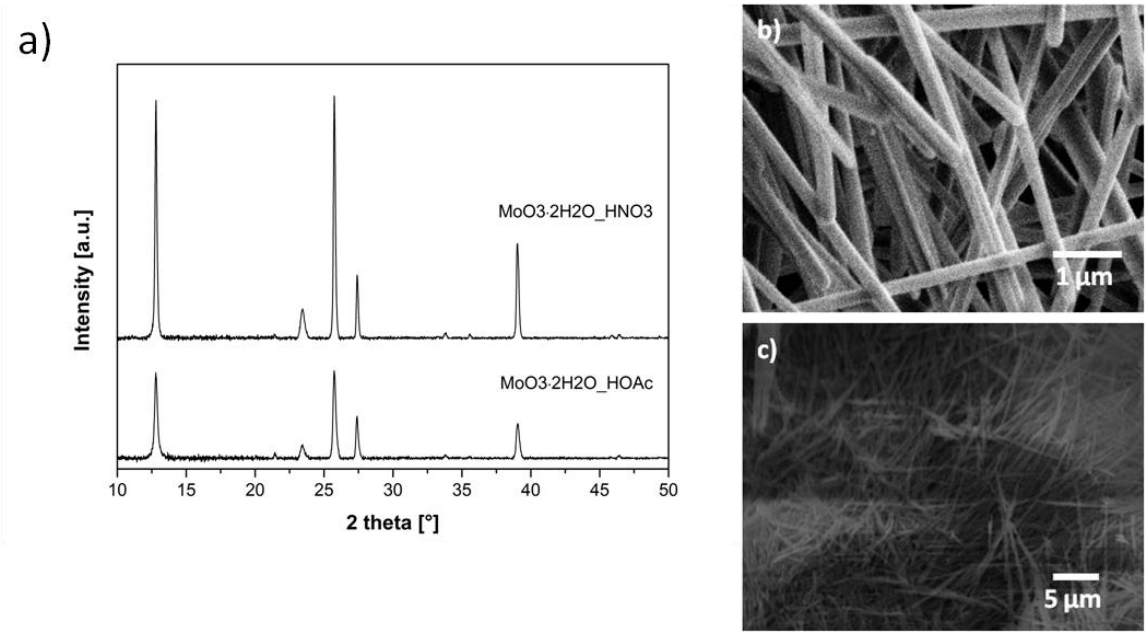

Figure 3.3: Preparation of different samples from $MoO_3 \cdot 2H_2O$ by variation of the acid. X-ray diffraction pattern indicating α-MoO_3 (a), SEM images of MoO3·2H2O_HNO3 (b) and MoO3·2H2O_HOAc (c).

In an alternative preparation route, $MoO_3 \cdot 2H_2O$ was prepared according to a literature procedure [198] and then hydrothermally treated with nitric and acetic acid, respectively at 180 °C for 48 h. The X-ray diffraction pattern of the two obtained products showed the characteristic reflections of α-MoO_3 (see Figure 3.3a). They both also exhibited a rod-like morphology, as can be seen in Figure 3.3b and c. Using nitric acid led to longer and thicker rods than preparation with acetic acid and consequently MoO3·2H2O_HNO3 had a smaller surface area than MoO3·2H2O_HOAc (7 m²/g and 11 m²/g respectively, cf. Table 3-1).

Table 3-1: Characterization of the as-prepared, calcined and used samples by BET, NH_3-TPD, H_2-TPR and quantitative nitrogen analysis.

Sample	Specific surface area (BET) [m² / g]			NH_3-TPD [µmol NH_3 / g_{cat}]			H_2 consumption during H_2-TPR [mmol H_2 / g_{cat}]		Amount of N [wt.%]
	as-prep.	calc.	used	as-prep.	calc.	used	as-prep.	calc.	calc.
AHM_calcined	-	< 1		-	2.8				0.024 ± 0.003
FSP_MoO3	43	16		45.6	1.6				n.d.
FSP_MoO3_HNO3									< 0.01
MoO3·2H2O_HOAc _treated in NH3									0.049 ± 0.001
MoO3·2H2O_HOAc	11	9	2		8.4	1.4	13	16	< 0.01
MoO3·2H2O_HNO3	7	4		11.7	12.0	2.1	16	18	< 0.01
AHM_pH2_24h	< 1	< 1			4.7				n.d
AHM_pH1_24h	< 1	< 1			3.0		16	17	0.011 ± 0.001
AHM_pH0_24h		10	4		10.2	8.1		16	< 0.01

This is in agreement with literature [11], reporting that weak organic acids leads to particles of nanoscale diameter, whereas strong inorganic acids support the formation of rods in the microscale. The rod-like morphology (Figure 3.4a and b) and α-MoO_3 phase could again be retained after calcination but for both samples the surface area decreased (4 m²/g and 9 m²/g respectively, cf. Table 3-1). Flame spray pyrolysis also led to the formation of pure α-

MoO_3. Calcination at 550 °C in air did not have an influence on the phase composition (Figure 3.5), but the surface area decreased from 43 m²/g to 16 m²/g for the as-prepared and calcined sample, respectively. The flame made sample featured a relatively large surface area also after calcination (16 m²/g), compared to the other unsupported molybdenum trioxides (≤ 10 m²/g). The particles were relatively small (25-50 nm length) and showed a slab-like morphology (Figure 3.4c).

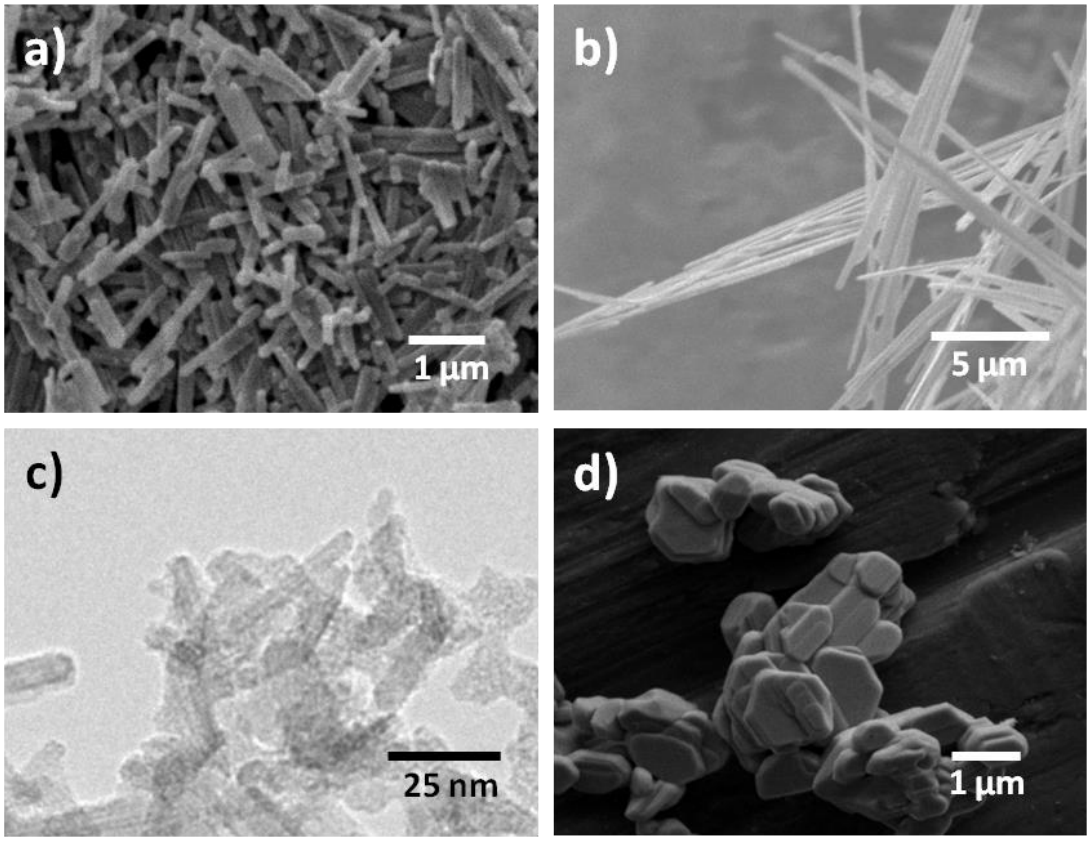

Figure 3.4: SEM images of a) MoO3·2H2O_HOAc_calc, b) MoO3·2H2O_HNO3_calc and d) AHM_calcined. TEM images of the flame made sample FSP_MoO3 (c).

Ammonium heptamolybdate was completely decomposed to α-MoO_3 after calcination at 550 °C for 10 h according to the diffraction pattern and Raman spectrum shown in Figure 3.5, but quantitative nitrogen analysis indicated relatively high nitrogen content in this sample. Only α-MoO_3 prepared by hydrothermal synthesis from $MoO_3 \cdot 2H_2O$ and acetic acid treated in ammonia ($MoO_3 \cdot 2H_2O$_HOAc_treated in NH_3_calc) contained more nitrogen than AHM_calcined.

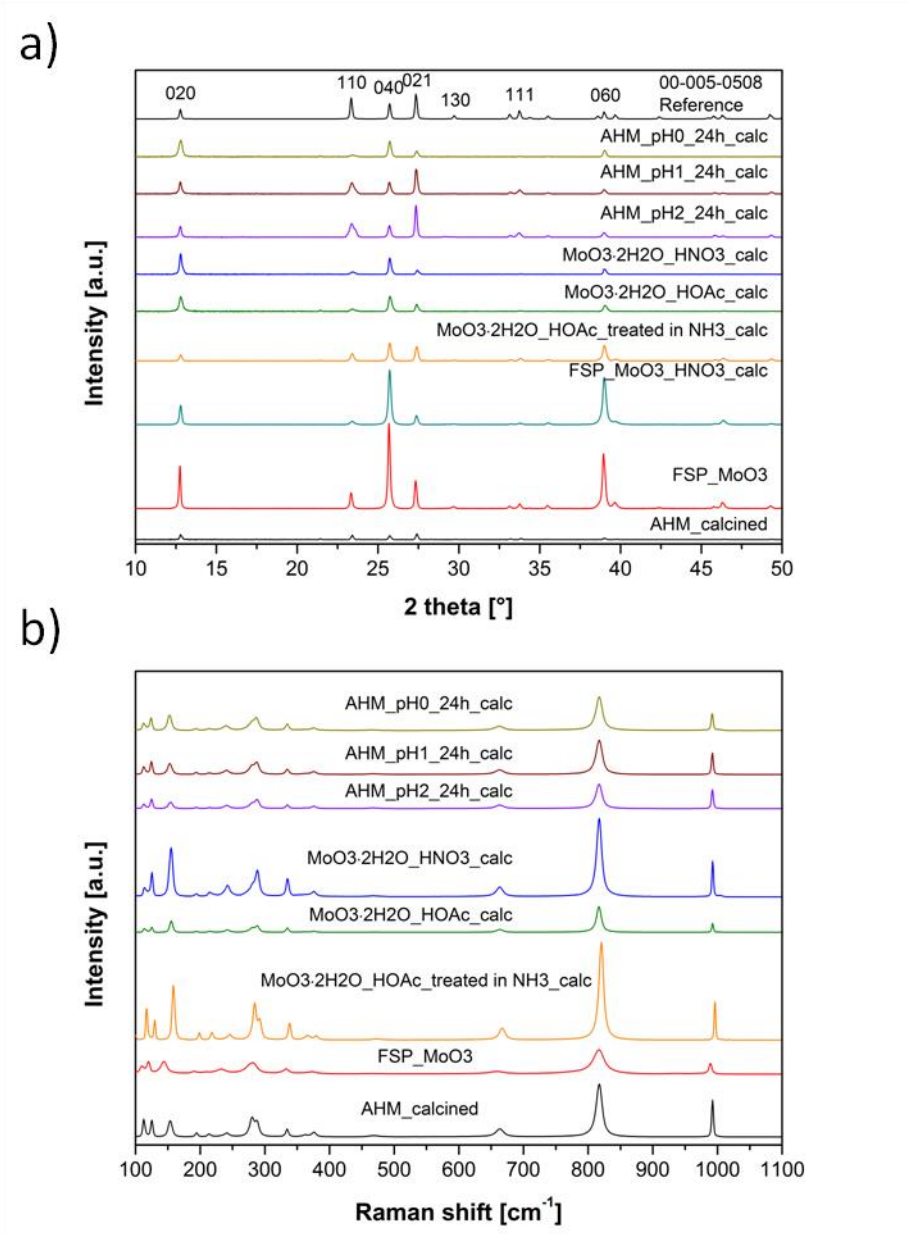

Figure 3.5: X-ray diffraction patterns (a) and Raman spectra (b) of the differently prepared samples after calcination at 550 °C. All samples showed pure α-MoO_3 but with distinct intensity variation of the reflections.

All calcined samples consisted of pure α-MoO_3 and no contributions of other crystalline phases such as β-MoO_3 or impurities could be detected in the diffraction pattern or the Raman spectra (Figure 3.5). All the Raman spectra (Figure 3.5b) show the characteristic bands at 992, 817, 288, 280, 154, 126 and 112 cm^{-1} (attribution see [202]). Comparing the X-ray diffraction pattern of the prepared samples with the reference pattern (JCPDS no. 5-508) evidenced, that the relative intensities of the different reflections varied for the different samples. Each reflection can be assigned to an exposed lattice plane. In the

reference pattern (JCPDS no. 5-508) the reflection at 27.3° (021) had the highest intensity and also the reflection at 23.3° (110) was relatively intense.

Table 3-2: Morphology, particle size and calculated ratios of the intensities of the reflections in the X-ray diffraction pattern in Figure 3.5a.

Sample	Morphology	Particle size		$I_{(020)}/\sum I_{(hkl)}$ [a]	$I_{(040)}/\sum I_{(hkl)}$ [a]	$I_{(021)}/\sum I_{(hkl)}$ [a]
		width	length	%	%	%
AHM_calcined	stacked plates	1-2 µm	1-2 µm	17	10	31
AHM_calcined_used	stacked plates	1-2 µm	1-2 µm	13	13	40
FSP_MoO3	rods and plates	10-25 nm	25-50 nm	18	36	12
FSP_MoO3_used	n.d.			8	26	6
FSP_MoO3_HNO3_calc	n.d.			14	40	7
FSP_MoO3_HNO3_calc_used	n.d.			7	32	14
MoO3·2H2O_HOAc_treated in NH3_calc	n.d.			9	27	22
MoO3·2H2O_HOAc_treated in NH3_used	n.d.			21	38	7
MoO3·2H2O_HOAc_calc	rods	200 nm	up to 1 µm	33	33	16
MoO3·2H2O_HOAc_calc_used	plates	2-5 µm	4-8 µm	32	32	15
MoO3·2H2O_HNO3_calc	rods	600 nm	10-20 µm	43	34	8
MoO3·2H2O_HNO3_calc_used	rods and plates	600-800 nm	10 µm	45	36	3
AHM_pH2_24h_calc	irregular	2 µm	7 µm	14	15	41
AHM_pH2_24h_calc_used	stacked plates	1 µm	2 µm	20	20	30
AHM_pH1_24h_calc	hexagonal prismatic rods	d = 9-11 µm	50-60 µm	18	17	36
AHM_pH1_24h_calc_used	stacked plates	2-3 µm	~3 µm	29	16	34
AHM_pH0_24h_calc	rods	200 nm	1-2 µm	37	34	12
AHM_pH0_24h_calc_used	rods	300 nm	2-3 µm	32	31	17

a: $\sum I_{(hkl)}$ was calculated for the reflections between 10 and 50°; $\sum I_{(hkl)} = I_{(020)} + I_{(110)} + I_{(040)} + I_{(021)} + I_{(111)} + I_{(060)} + I_{(021)}$

This is in line with the samples prepared from ammonium heptamolybdate by calcination or by hydrothermal synthesis at pH = 1 and pH = 2. All other samples showed a rod-like morphology in the SEM images and consequently in the diffraction pattern the (0k0) reflections (12.7, 25.7 and 38.9°) were more intense than the other reflections.

In Table 3-2 the particle morphology of the calcined samples are summarized as well as the relative intensities for different reflections ((020) at 12.7°, (040) at 25.7° and (021) at 27.3°). The intensity of the corresponding reflections was divided by the sum of the intensities of all reflections between 10 and 50°. High values for $I_{(020)}/\sum I_{(hkl)}$ and $I_{(040)}/\sum I_{(hkl)}$ imply the preferred exposure of the (0k0) facets and the presence of α-MoO_3 in the form of rods/fibers or plates. All other samples, which had a irregular, stacked plate-like or hexagonal prismatic morphology, reached additionally high values for $I_{(021)}/\sum I_{(hkl)}$, whereas only in the diffraction pattern of the calcined ammonium heptamolybdate the reflection at 27.3° (021) showed the highest intensity, which agrees well with the reference pattern. Comparison of the different X-ray diffraction pattern already gives an insight into the product morphology of the corresponding α-MoO_3. Higher intensities of (0k0) planes compared to other (hkl) planes are an indication for the anisotropic growth of MoO_3 as well as the preferred orientation of the rods. [14] This can also be seen in the Raman spectra.

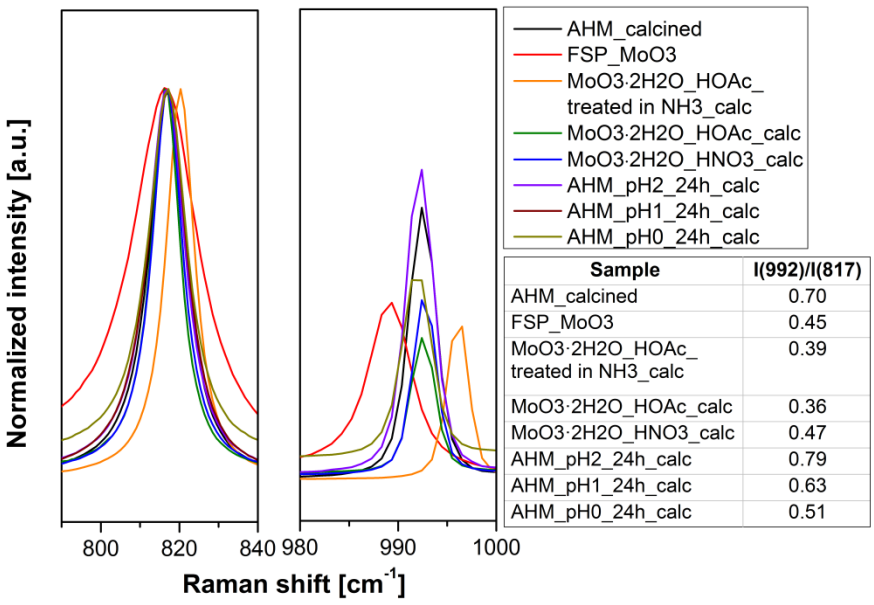

Sample	I(992)/I(817)
AHM_calcined	0.70
FSP_MoO3	0.45
MoO3·2H2O_HOAc_ treated in NH3_calc	0.39
MoO3·2H2O_HOAc_calc	0.36
MoO3·2H2O_HNO3_calc	0.47
AHM_pH2_24h_calc	0.79
AHM_pH1_24h_calc	0.63
AHM_pH0_24h_calc	0.51

Figure 3.6: Raman spectra of the calcined samples in the energy range 790 – 840 cm^{-1} and 980 – 1000 cm^{-1}. The spectra are normalized to the highest intensity band at 817 cm^{-1} and the relative intensity of the band at 992 cm^{-1} of the various samples is given in the table.

According to Dieterle et al. [202] the bands at 992 cm^{-1} and 817 cm^{-1} can both be assigned to terminal Mo=O stretching vibrations, whereas the band at 992 cm^{-1} corresponds to the asymmetric stretching vibrations along the a axis and the band at 817 cm^{-1} is attributed to the Mo=O bond vibrations along the b axis. The Raman intensities were normalized to the band with the highest intensity at 817 cm^{-1} and the normalized spectra are depicted in Figure 3.6 in the energy range 790 – 840 cm^{-1} and 980 – 1000 cm^{-1}. A low normalized intensity for the band at 992 cm^{-1} and a low value for the calculated relative intensity $I_{(992)}/I_{(817)}$ indicates the preferred growth along the b axis ([010]), which is typical for MoO_3 rods.

In addition to X-ray diffraction and Raman spectroscopy the three samples, which showed the rod-like morphology (AHM_pH0_24h_calc, MoO3·2H2O_HNO3_calc, MoO3·2H2O_HOAc_calc), were analyzed by X-ray absorption spectroscopy (XAS). Strong backscattering of the Mo second shell neighbors in the Fourier-transformed Extended X-ray Absorption Fine Structure (EXAFS) spectra confirmed, that exclusively α-MoO_3 was prepared which has an almost linear Mo-O-Mo geometry ("focusing effect" for backscattering see Figure 3.7 and [7]).

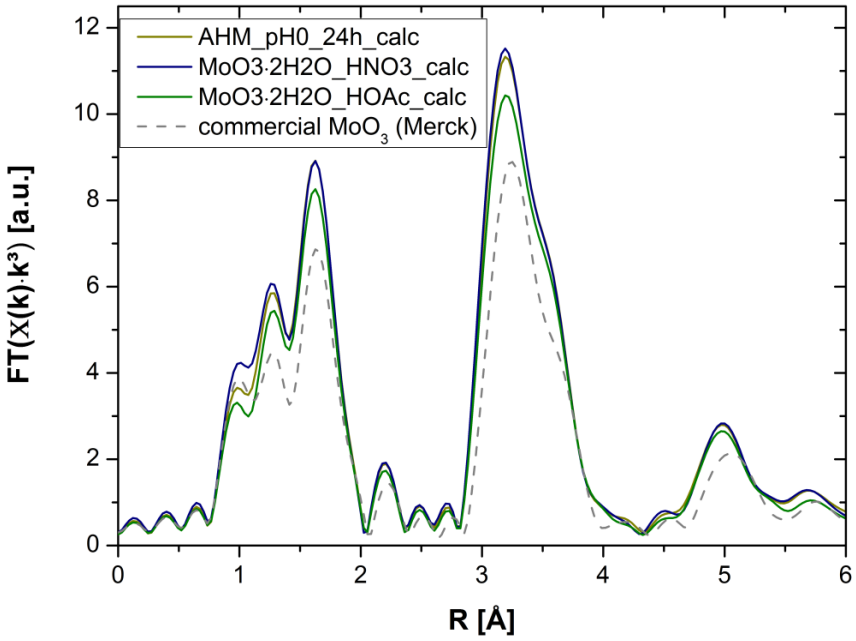

Figure 3.7: Fourier transformed k^3-weighted EXAFS spectra measured at the Mo K edge of differently prepared α-MoO_3 supporting PXRD and Raman spectroscopy results that the samples are structurally the same.

3.3.2. Reducibility and acidity of α-MoO_3 samples

Since both redox-activity of α-MoO_3 and its acidity play an important role for the catalytic performance [203], temperature programmed reduction (TPR) and ammonia adsorption were used for further characterization. In Figure 3.8a the TPR results are displayed plotting the H_2 consumption as a function of the temperature. The spectra can be divided in two regions: a low temperature region showing the reduction of MoO_3 to MoO_2 and a high temperature region, where MoO_2 is further reduced to Mo. At 1000 °C all samples were completely reduced to metallic Mo, which was proven by X-ray diffraction measurements (cf. Figure 3.8b). The samples synthesized from $MoO_3 \cdot 2H_2O$ were reduced at lower temperature than the samples prepared from ammonium heptamolybdate. Calcination of the sample prepared from $MoO_3 \cdot 2H_2O$ and HNO_3 led to a shift in reduction temperature by 30 K to higher temperature (704 °C) compared to the as-prepared sample (674 °C). The amount of hydrogen consumed per catalyst mass ($n(H_2)/m(cat)$) (Table 3-1) was the same for all measured samples (13 – 18 mmol H_2 /$g_{catalyst}$), showing that the as-prepared samples were completely oxidized.

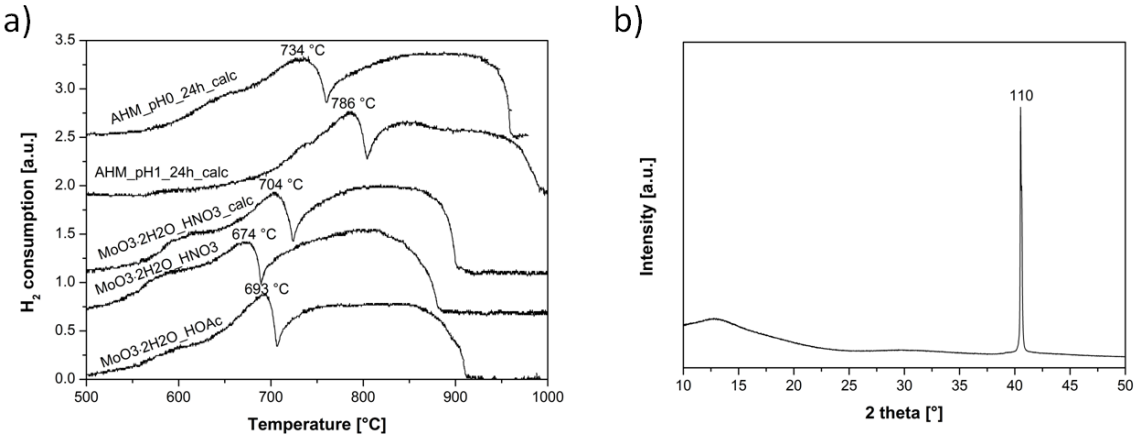

Figure 3.8: H_2-TPR of differently prepared α-MoO_3 (100 mg catalyst, 5 K/min from room temperature to 1000 °C, flow of 96 ml/min, 5% H_2 in argon) (a) and the X-ray diffraction pattern of AHM_pH1_24h_calc after reduction, which showed only the presence of Mo.

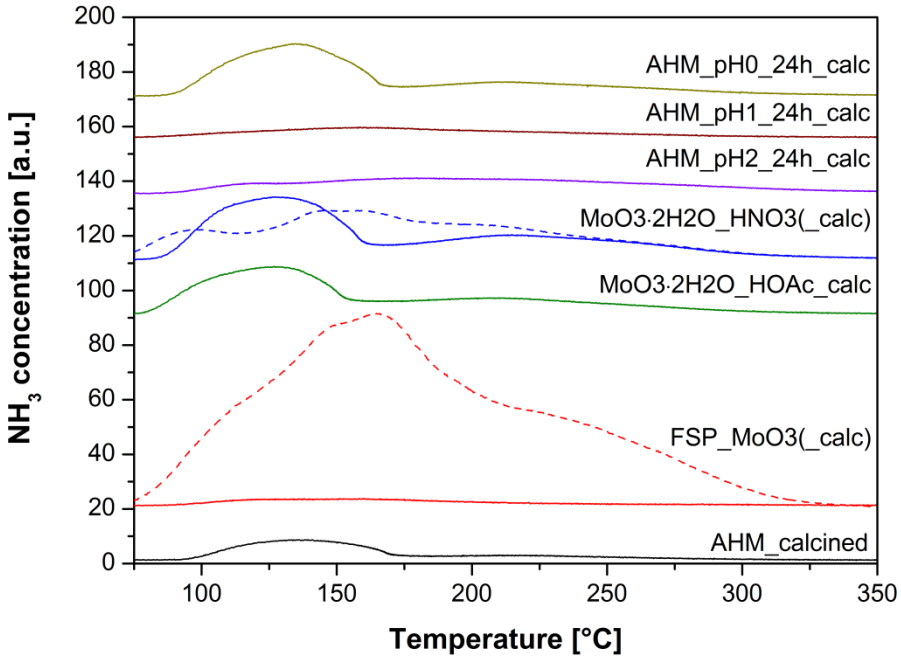

Figure 3.9: NH_3-TPD of differently prepared α-MoO_3 (400 mg catalyst, 1000 ppm NH_3 in N_2, 500 ml/min). The dotted lines indicate the results for the as-prepared samples, full lines belong to calcined samples.

Temperature programmed desorption of ammonia was performed for different as-prepared and calcined samples and the desorbed NH_3 concentration was plotted as a function of the temperature in Figure 3.9. All samples showed relatively low acidity. The calculated amounts of desorbed ammonia per gram of catalyst (Table 3-1) were lower than the values for supported MoO_3-catalysts or potassium doped unsupported MoO_3 studied by Bian et al. [204]. The only exception was the flame made sample, which showed a large amount of ammonia adsorption sites; however, the acidity strongly decreased after calcination at 550 °C. One of the reasons for the decrease in acidity is probably the decrease in surface area (from 43 m^2/g to 16 m^2/g) but the amount of ammonia desorption sites decreased stronger than the surface area (cf. Table 3-1). Calcination of MoO3·2H2O_HNO3 did not reduce the amount of NH_3 adsorption sites on the catalyst surface (Table 3-1), but the as-prepared sample showed two desorption peaks whereas the calcined sample showed only one. In contrast to our results, Oyama [205] reported that MoO_3 needles had a single desorption peak and two desorption peaks were found for powders. Generally, NH_3 is also completely desorbed at temperatures below 350 °C, indicating exclusively the presence of weak acidic sites (Lewis-acid sites). AHM_pH0_24h_calc was more acidic than the samples

synthesized at pH = 1 and pH= 2 and showed similar acidity as MoO3·2H2O_HNO3_calc. Using acetic acid led to less acidic materials compared to the sample synthesized from $MoO_3 \cdot 2H_2O$ and HNO_3.

3.3.3. Effect of morphology on the catalytic activity and selectivity

All samples, except the flame made sample FSP_MoO3_calc and the hydrothermally prepared sample MoO3·2H2O_HOAc_calc, revealed significant catalytic activity towards the partial and total oxidation of propylene under the applied conditions. Figure 3.10 demonstrates that all samples exhibited different catalytic activity and selectivity although they contained the same phase (α-MoO_3). Calcined ammonium heptamolybdate showed low propylene conversion (maximum 5% at 50 Nml/min), whereas the hydrothermally synthesized samples AHM_pH1_24h_calc and AHM_pH2_24h_calc reached a propylene conversion of 15%. AHM_pH0_24h_calc converted more propylene (10 – 40%) than the other catalysts. MoO3·2H2O_HNO3_calc converted between 8% and 30% propylene under the applied conditions at 460 °C. For the four most active catalysts in Figure 3.10 the selectivity to acrolein was higher than 15%, the main undesired product for all samples was CO_2, followed by CO, acetaldehyde and propanal. The selectivity to acetaldehyde and propanal was about 1 - 9% and 0 - 2%, respectively, where selectivity decreased with increasing propylene conversion. Also at low propylene conversion the selectivity to acrolein did not exceed 32%.

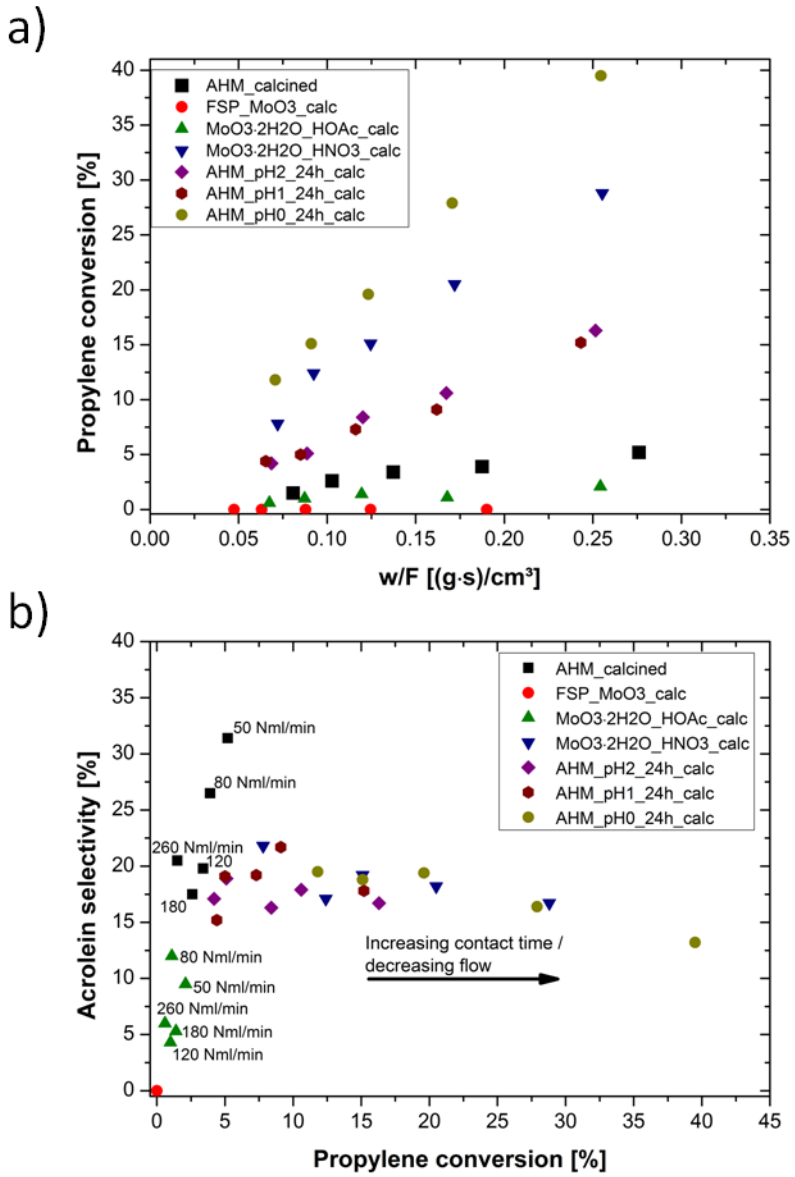

Figure 3.10: Catalytic performance of α-MoO_3 prepared by different methods and with various morphologies at 460 °C: propylene conversion as a function of contact time w/F, which was calculated at reaction temperature and pressure (a) and acrolein selectivity as a function of propylene conversion (b). ($C_3H_6/O_2/N_2$ = 5/25/70, flows 50, 80, 120, 180, 260 Nml/min, 500 mg of catalyst).

Comparison of the results in Figure 3.10 with Table 3-2 and the SEM images in Figure 3.2, Figure 3.3 and Figure 3.4 reveals that the catalytic performance of the catalysts may be determined by the morphology considering the low activity of FSP_MoO3_calc and AHM_calcined. The two samples, which exhibited the highest propylene conversion, both showed a rod-like morphology suggesting that rods were more active than the hexagonal prismatic particles (AHM_pH1_24h_calc) or particles with an irregular morphology (AHM_pH2_24h_calc or AHM_calcined). However, the sample prepared by hydrothermal

synthesis from $MoO_3 \cdot 2H_2O$ and acetic acid also showed a rod-like morphology, but the activity for propylene oxidation was negligible (Figure 3.10a, maximum 2% propylene conversion). Also the surface area and the acidity of MoO3·2H2O_HOAc_calc and AHM_pH0_24h_calc differed only slightly as well as the particle size.

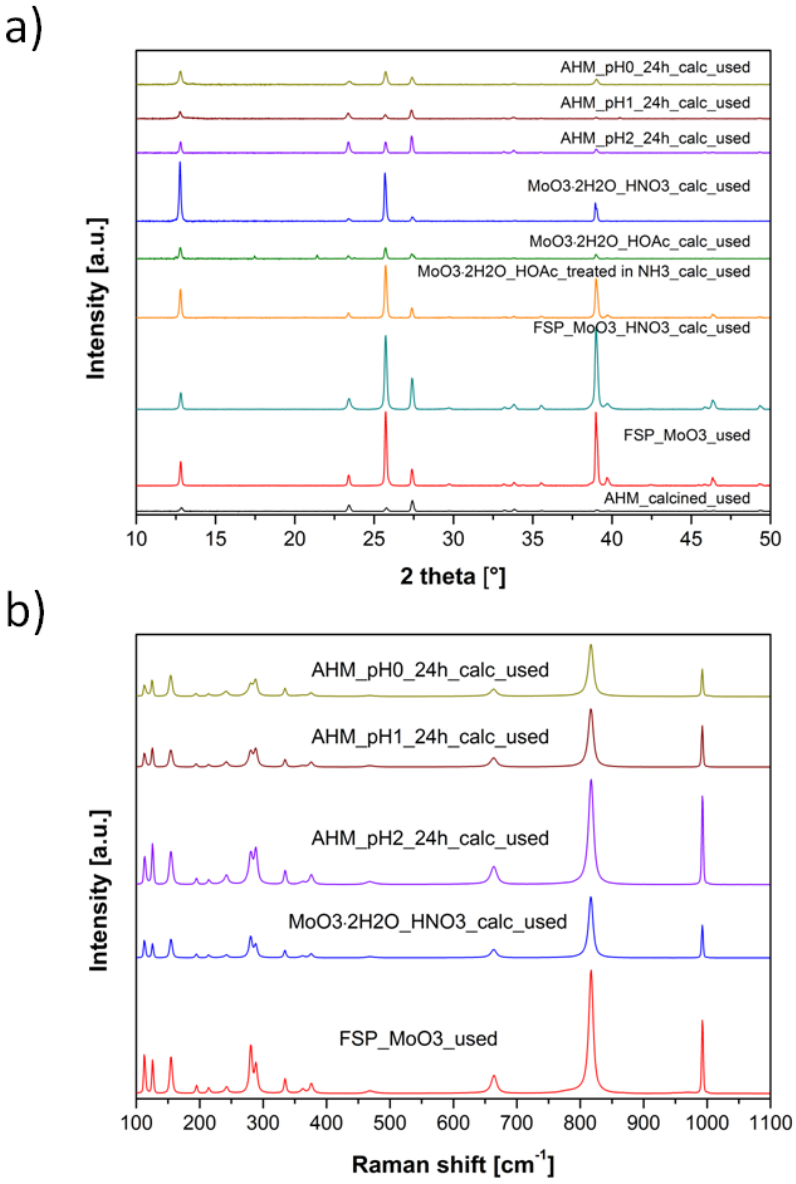

Figure 3.11: X-ray diffraction patterns (a) and Raman spectra (b) of differently prepared samples after the use in propylene oxidation at 420 - 520 °C.

Generally, the surface area did not have a strong influence on the catalytic activity of α-MoO_3: the flame made material exhibiting the highest surface area was completely inactive, whereas the hydrothermally synthesized samples from ammonium

heptamolybdate at pH = 1 and pH = 2 showed a medium activity compared to the other tested samples in Figure 3.10, although their surface areas were low (< 1m²/g).

To understand, why the hydrothermally synthesized sample prepared from $MoO_3 \cdot 2H_2O$ and acetic acid showed lower catalytic activity than the other rod-like materials and whether a change in phase or morphology during time on stream occurred, the catalysts were also characterized after application in propylene oxidation up to 520 °C. According to X-ray diffraction measurements (Figure 3.11a) and Raman spectroscopy (Figure 3.11b) the phases did not change during the catalytic test reaction and all the samples still consisted of pure α-MoO_3 after use. The relative intensities of the reflections in the diffraction pattern were hardly altered for the respective samples (compare Figure 3.5 and Figure 3.11).

Figure 3.12 shows the SEM images of these MoO_3-samples after use in propylene oxidation and in Table 3-2 morphologies and particle sizes before and after use are compared. For ammonium heptamolybdate after calcination (AHM_calcined) the particles did not grow during time on stream and also the steps and edges on the surface of the plate-like particles are still visible in Figure 3.12a. The samples synthesized from ammonium heptamolybdate at pH = 1 and pH = 2, which exhibited a medium catalytic activity (5-16% propylene conversion) both strongly changed their morphology and agglomerated plates formed during propylene oxidation (Figure 3.12d, e). This may be due to the fact that MoO_3 under reaction conditions is slightly reduced [129] and – if catalytically active – also prone to structural changes. The particles formed for AHM_pH1_24h_calc_used were slightly larger (thicker and longer) than AHM_pH2_24h_calc_used. MoO3·2H2O_HOAc_calc, MoO3·2H2O_HNO3_calc and AHM_pH0_24h_calc all showed a rod-like morphology (Figure 3.2, Figure 3.3b, c), but of different particle size. The particles of the sample prepared with acetic acid were thinner and shorter than the particles of MoO3·2H2O_HNO3_calc. MoO3·2H2O_HOAc_calc and AHM_pH0_24h_calc formed particles of similar size with a width of 200 nm and up to 2 µm length (see Table 3-2).

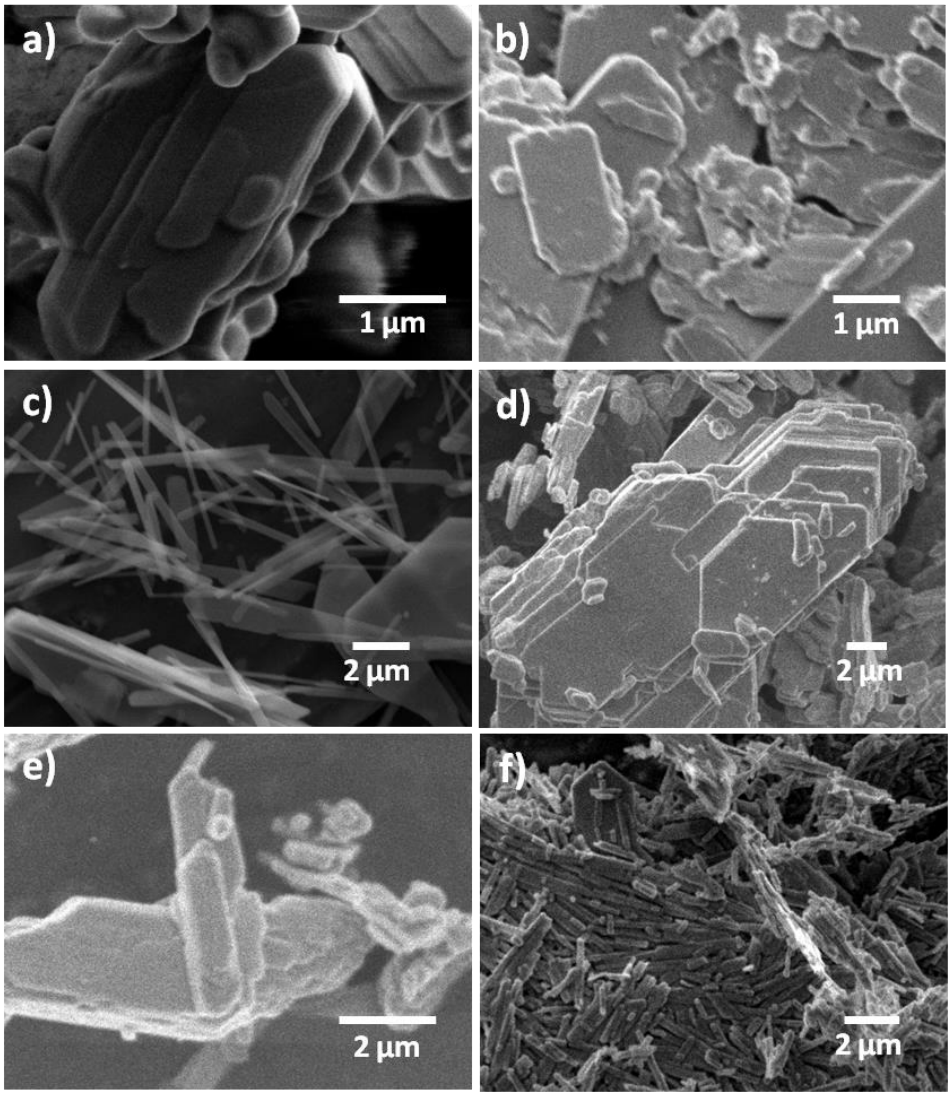

Figure 3.12: SEM images of different MoO_3-samples after use in propylene oxidation at 420 - 520 °C a) AHM_calcined_used, b) MoO3·2H2O_HOAc_calc_used, c) MoO3·2H2O_HNO3_calc_used, d) AHM_pH2_24h_calc_used, e) AHM_pH1_24h_calc_used and f) AHM_pH0_24h_calc_used.

The aspect ratio of the particles of MoO3·2H2O_HOAc_calc changed during the time on stream and plate-like particles were formed from the α-MoO_3-rods (Figure 3.12b), growing in the [001] and [100] direction. MoO3·2H2O_HNO3_calc partly preserved its morphology (Figure 3.12c) and only a few of the particles grew to plates, whereas AHM_pH0_24h_calc completely maintained its rod-like morphology (Figure 3.12f) slightly increasing in width and length (Table 3-2). Nitric acid seemed to stabilize the morphology of α-MoO_3 during catalytic application or heat treatment compared to acetic acid. In this way, a correlation of morphology of the samples after use (Figure 3.12) and the catalytic performance of the samples (Figure 3.10) can be established: α-MoO_3 reached the highest propylene conversion if the rod-like morphology was preserved during the

activity measurement (AHM_pH0_24h_calc and MoO3·2H2O_HNO3_calc), while all the other samples had lower activity for propylene oxidation (Figure 3.10a). A morphology change from rod-like particles to plate-like particles led to lower propylene conversion. Although the rate was dependent on the average morphology throughout the catalytic activity measurements, the selectivity to acrolein was not influenced by the particle morphology (Figure 3.10b). Rods feature relatively large (100) and (010) facets whereas plates only contain large (010) facets. If the (010) facet was responsible for propylene activation, plates would be as active as rods. These results suggest that propylene activation preferentially took place on the (100) facet, which means that propylene is adsorbed, hydrogen is abstracted and a surface complex of an allylic intermediate is formed [138, 206]. Brückman et al. [138] also found that the (100) facet was responsible for propylene activation, testing four MoO_3 samples synthesized at different temperatures. So far, this has been demonstrated as well for two commercial samples with needle or plate crystals [207] and for MoO_3 supported on silica [206]. Propylene activation (α-H abstraction and formation of an allyl intermediate) was observed to be the rate limiting step. [206] The (100) facets of α-MoO_3 consist of a double layer of oxygen atoms bound to molybdenum atoms, thus containing the highest Mo density. The C=C double bond is attracted by these electrophilic centers and propylene is adsorbed on the superficial molybdenum. [133] These Mo-centers on the (100) facet act as Lewis-acid sites [135-136], which were mostly preserved for AHM_pH0_24h_calc. Hence, NH_3-TPD measurements were not only performed on the fresh catalysts (Figure 3.9) but also on the used samples (see Figure 3.13). The number of NH_3 desorption sites for MoO3·2H2O_HOAc_calc, MoO3·2H2O_HNO3_calc and AHM_pH2_24h_calc strongly decreased after catalytic activity measurements (Table 3-2). Only AHM_pH0_24h_calc, which showed the best catalytic performance, still showed relatively high acidity after use in propylene oxidation.

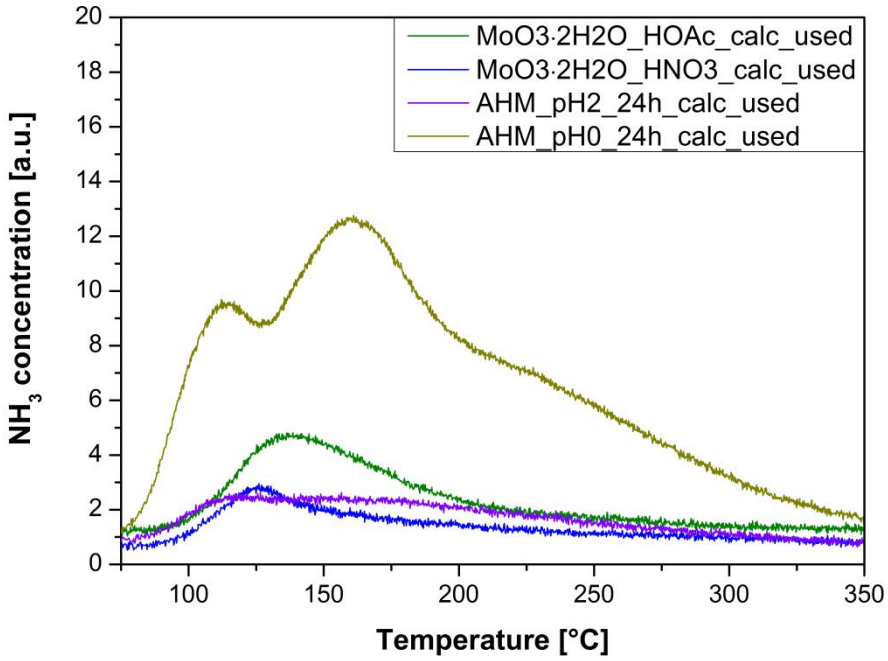

Figure 3.13: Temperature programmed desorption of ammonia of various MoO_3 after application in propylene oxidation at temperatures up to 520 °C.

3.3.4. Effect of nitrogen incorporation on the catalytic activity and selectivity

The results of the catalytic performance tests in Figure 3.10 also indicate that samples prepared using HNO_3 were more active than the other samples, which may suggest that nitrogen incorporation into α-MoO_3 occurred during hydrothermal synthesis, thus increasing the catalytic activity for propylene oxidation. Therefore the hydrothermally prepared sample from $MoO_3 \cdot 2H_2O$ and acetic acid, which did not contain nitrogen, was treated in ammonia. Additionally the flame made sample was treated hydrothermally in the presence of nitric acid. Quantitative nitrogen analysis of the samples implied that no nitrogen was incorporated from HNO_3 into the samples during hydrothermal synthesis with nitric acid. For FSP_MoO3_HNO3_calc, AHM_pH0_24h_calc and MoO3·2H2O_HNO3_calc no nitrogen was detected, whereas 0.01 wt.% N was found for AHM_pH1_24h_calc. In this case ammonium heptamolybdate could be the nitrogen source and thermal transformation of the hydrothermally prepared ammonium molybdenum oxide phase led to α-MoO_3 with remaining traces of nitrogen not detected by X-ray diffraction or Raman spectroscopy. MoO3·2H2O_HOAc treated in NH_3 showed the

highest concentration of nitrogen followed by calcined ammonium heptamolybdate (see Table 3-1).

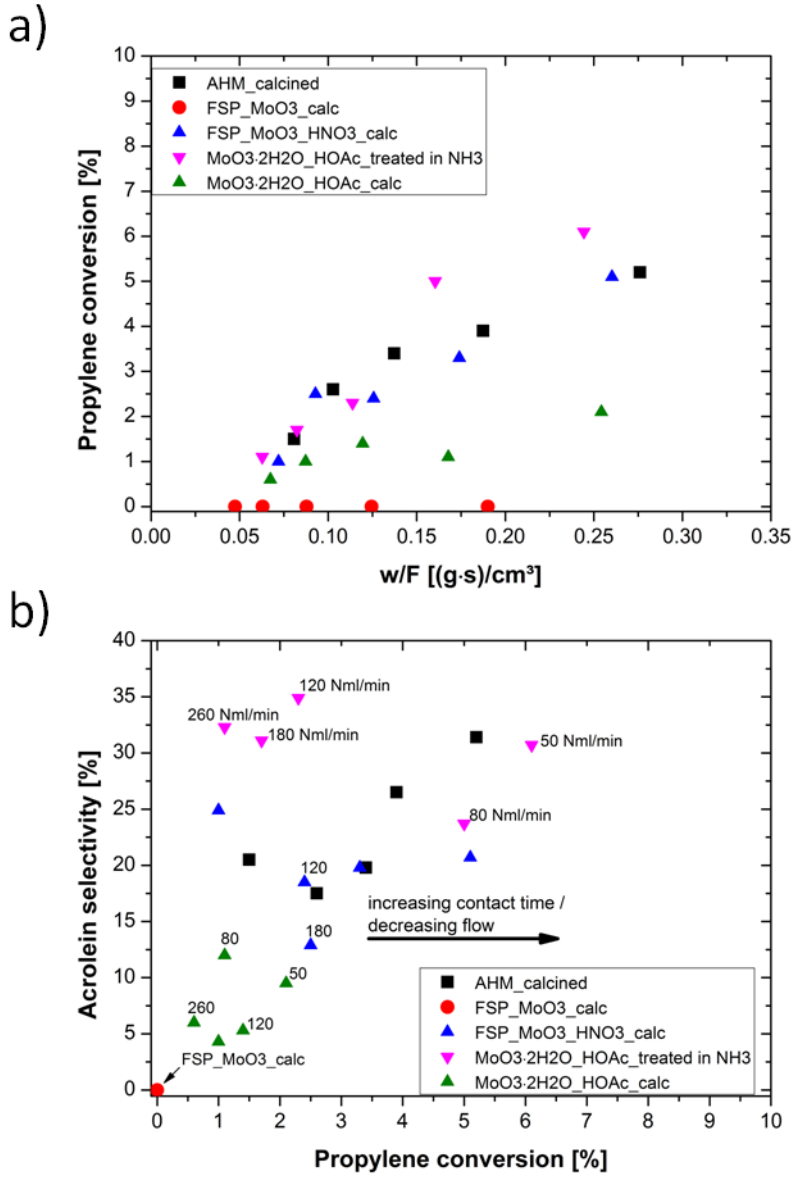

Figure 3.14: Propylene conversion as a function of contact time, w/F (a) and acrolein selectivity as a function of propylene conversion (b) for various samples to determine the influence of the nitrogen incorporation into MoO_3 ($C_3H_6/O_2/N_2$ = 5/25/70, flows 50, 80, 120, 180, 260 Nml/min, 460 °C, 500 mg of catalyst).

The measurements of the catalytic performance depicted in Figure 3.14 indicate that nitrogen incorporation into MoO_3 slightly increased the catalytic activity for propylene oxidation. Treatment of MoO3·2H2O_HOAc_calc in NH_3 resulted in a nitrogen content of 0.049 wt.% and increased the propylene conversion from 2% to 6% at 50 Nml/min (Figure 3.14a) as well as the acrolein selectivity (Figure 3.14b). A similar experiment was

performed by Kuehn et al. [199], who treated commercial α-MoO_3 at 275 °C in ammonia resulting in a nitrogen content of 0.41 wt.%. However, in this study α-MoO_3 and α-MoO_3 after ammonolysis (treatment in NH_3) showed similar catalytic activity in propylene oxidation. Hydrothermal treatment of FSP_MoO3 in HNO_3 also improved the catalytic activity (Figure 3.14) of α-MoO_3, although no nitrogen was detected in both samples and FSP_MoO3_HNO3 achieved similar propylene conversion as calcined ammonium heptamolybdate containing 0.024 wt.% N.

Generally the activities displayed in Figure 3.14 were low and the values measured for propylene conversion below 5% including the corresponding acrolein selectivity are relatively inaccurate. This implied only a minor enhancement of the catalytic performance as consequence of the nitrogen incorporation into α-MoO_3. Nitrogen incorporation could thus be excluded as the reason for the differing activities found for the distinct samples prepared by hydrothermal synthesis and flame spray pyrolysis.

3.3.5. Catalyst deactivation

The reusability as well as the deactivation of the MoO_3 model catalysts was also tested. The samples synthesized from ammonium heptamolybdate and nitric acid at pH = 0 and pH = 2 were used three times in the same cycle i.e. after the catalyst was tested in propylene oxidation at 420 – 520 °C using flows of 50, 80, 120, 180, 260 Nml/min it was applied at the same temperatures and flows again. Figure 3.15 depicts the propylene conversion as a function of the contact time w/F at 460 °C indicating the deactivation for both samples during each cycle. The sample synthesized at pH = 0 with the rod-like morphology deactivated stronger than the sample synthesized at pH = 2 (40% propylene conversion in first cycle to 22% in the third cycle and 16% propylene conversion in first cycle to 13% in the third cycle, respectively). However, also in the third cycle AHM_pH0_24h_calc exhibited higher activity than AHM_pH2_24h_calc in the first cycle.

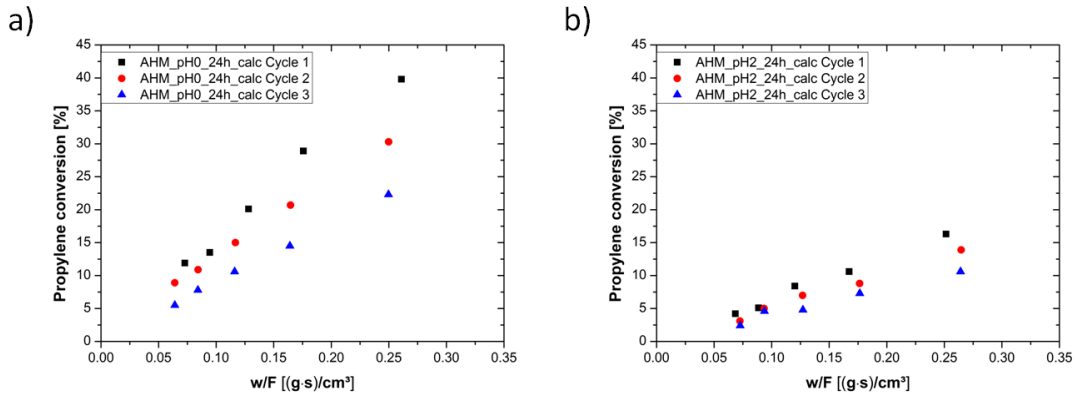

Figure 3.15: Testing the reusability of the catalysts: Propylene conversion at 460 °C of AHM_pH0_24h_calc (a) and AHM_pH2_24h_calc (b) tested three times in the same cycle at three different temperatures (420 - 520 °C) and five different flows (50, 80, 120, 180, 260 Nml/min) with a gas composition of $C_3H_6/O_2/N_2$ = 5/25/70.

To analyze the deactivation of α-MoO_3 at a certain temperature MoO3·2H2O_HNO3_calc was tested for 70 hours at 500 °C using 50 Nml/min and a gas composition of $C_3H_6/O_2/N_2$ = 5/25/70. Propylene conversion as well as oxygen conversion decreased strongly from 44% after 39 h to 27% after 70 h and 26% after 39 h to 15% after 70 h, respectively. Acrolein selectivity slightly increased from 16% to 20% as depicted in Figure 3.16.

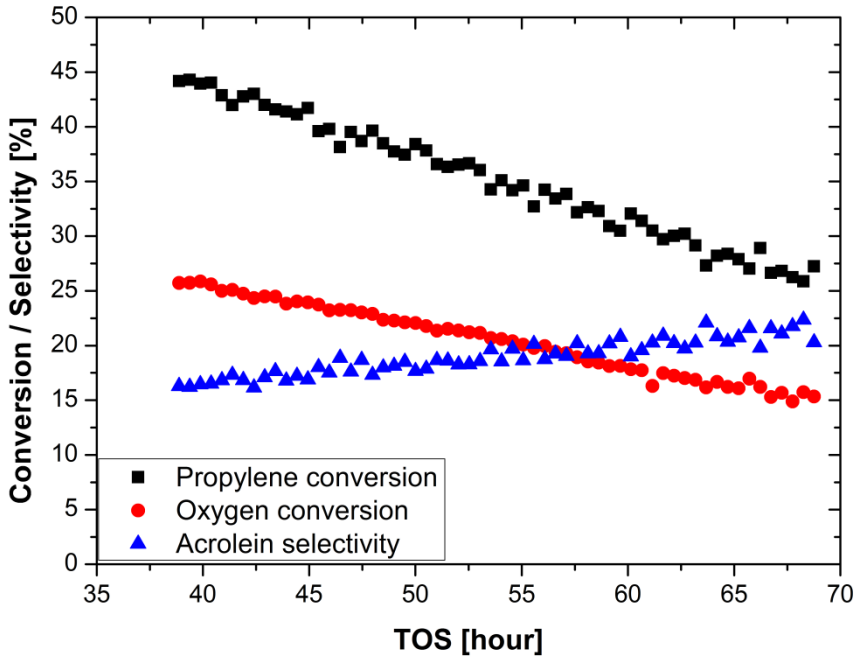

Figure 3.16: Catalytic performance of MoO3·2H2O_HNO3_calc during 70 hours at 500 °C with $C_3H_6/O_2/N_2$ = 5/25/70 and 50 Nml/min.

3.4. Conclusions

A variety of morphologically different α-MoO_3 samples could be prepared by hydrothermal synthesis, well-suited as model systems for the selective oxidation of propylene to acrolein. Variation of the pH value of the initial solution strongly influenced the product phase obtained from ammonium heptamolybdate and nitric acid under hydrothermal conditions, due to the dependence of the present polymolybdate species present in the solution at different pH values. After calcination all samples were transformed into pure α-MoO_3. $MoO_3 \cdot 2H_2O$ in the presence of acetic acid or nitric acid at 180 °C or ammonium heptamolybdate with nitric acid at pH = 0 directly resulted in α-MoO_3 rods in one step. The different relative intensities of the characteristic reflections in the diffraction pattern confirmed the anisotropic growth of these MoO_3 rods preferentially growing along the [010] direction. For comparison high surface area α-MoO_3 was successfully prepared by flame spray pyrolysis and plate-like α-MoO_3 was obtained by calcination of ammonium heptamolybdate. They were catalytically inactive and, obviously, rod-like structures with a relatively high amount of (100) facets seem to be important for the catalytic activity.

The study shows, however, that additional factors have to be considered: The morphology of the samples needs to be stabilized during the catalytic activity measurements, which was particularly observed for the samples prepared with nitric acid during synthesis. This preservation of the rod-like morphology during heat treatment and propylene oxidation resulted in high propylene conversion (10-40% conversion depending on the contact time). A morphology change to plates or stacked plates during propylene oxidation resulted in lower propylene conversion. This suggested, that the (100) facet was responsible for propylene activation due to a high Mo density. These electrophilic centers attract the C=C double bond, so that propylene is adsorbed and oxygen can be inserted forming acrolein. If the adsorption of propylene is too strong, C-C and/or C=C bond cleavage and CO_2 formation is favored. On the (100) plane each active Mo-site is surrounded by two active lattice oxygen atoms [137] so that the selectivity for the total combustion products is higher (~60%) than the selectivity for acrolein (~20%). The morphology of the samples did not have a significant effect on the selectivity to acrolein, but on the propylene conversion. Incorporation of nitrogen slightly improved the catalytic performance of α-MoO_3, but was not a decisive factor.

3 MoO_3 as model catalyst in the selective oxidation of propylene

Although MoO_3 is an easy model system correlation of the particle morphology and the catalytic activity and selectivity in propylene oxidation already requires a detailed characterization of the materials before and after the catalytic test reaction. This may be further developed by extending the present study to operando characterization studies as performed previously by Ressler et al. [129] on samples comparable to AHM_calcined. The catalytic activity in propylene oxidation and especially the selectivity for acrolein was low on α-MoO_3 and more realistic information will be obtained by extension of the strategy of this study to mixed transition molybdates resulting in higher propylene conversion and improved selectivity. Thus bismuth molybdates were prepared by hydrothermal synthesis leading to various phases and phase mixtures, which exhibited higher activity and selectivity in propylene oxidation to acrolein.

4 Bismuth molybdates for selective oxidation of propylene[2]

4.1. Introduction

Since the development of bismuth molybdate catalysts for the oxidation and ammoxidation of propylene to acrolein or acrylonitrile [88-89] by Sohio in 1959, this type of materials have received large attention and various researchers have studied their catalytic properties in considerable detail [91-100] (cf. 1.2.1). Despite extensive preceding studies, there is an ongoing debate in literature about the relative catalytic activity of the different bismuth molybdate phases. [98, 113] In the previous chapter the influence of the morphology of α-MoO_3 on the catalytic activity in propylene oxidation was studied in detail and the (100) facets were suggested to be responsible for propylene activation. The investigation of the influence of the particle morphology along with the relative activity of the different phases is also of great interest for more realistic systems like bismuth molybdates. According to the study in chapter 3 bismuth molybdates were prepared by mild hydrothermal synthesis applying nitric and acetic acid, variation of the pH value and variation of the Bi/Mo ratio. In addition, flame spray pyrolysis (FSP) was applied as an alternative novel method. The influence of calcination on the phase composition and the catalytic activity for propylene oxidation to acrolein has been studied in detail. Phase composition, particle morphology, surface Bi/Mo ratio and overall surface area were correlated to the catalytic performance in propylene oxidation to acrolein. The controlled preparation of unsupported bismuth molybdates exposing high surface area by flame spray pyrolysis or under mild conditions

[2] 4.3.1, 4.3.2, and part of 4.3.3 is planned to be published: Selective oxidation of propylene to acrolein by hydrothermally synthesized bismuth molybdates by Kirsten Schuh, Wolfgang Kleist, Martin Høj, Vanessa Trouillet, Pablo Beato, Anker Degn Jensen, Greta R. Patzke and Jan-Dierk Grunwaldt; 4.3.4 will be published as: Influence of the pH value during hydrothermal synthesis on the catalytic performance in selective oxidation of propylene by Kirsten Schuh, Wolfgang Kleist, Martin Høj, Vanessa Trouillet, Pablo Beato, Anker Degn Jensen and Jan-Dierk Grunwaldt. The FSP part in 4.3.3 is going to be published as a short communication.

by hydrothermal synthesis seems very attractive for selective oxidation of olefins and in the following, we compare the properties of catalysts emerging from these flexible synthetic routes to samples synthesized by conventional co-precipitation.

4.2. Catalyst preparation

The bismuth molybdate materials were synthesized by hydrothermal synthesis and flame spray pyrolysis, while reference samples were obtained from conventional co-precipitation. In a typical hydrothermal synthesis 10 mmol $Bi(NO_3)_3 \cdot 5H_2O$ (Sigma Aldrich, ACS reagent ≥ 98.0%) and the stoichiometric amount of $(NH_4)_6Mo_7O_{24} \cdot 4H_2O$ (VWR AnalaR NORMAPUR) with Bi/Mo ratios in the range of 0.5 – 3 were dissolved in 100 ml deionized water. These samples will be referred to here as HT_BixMoy with x/y being the Bi/Mo-molar ratio. Additionally for a ratio of Bi/Mo = 1:1 the pH was adjusted from 0.9 to 4 by addition of ammonium nitrate solution (HT_Bi1Mo1_pH4). 5 ml of nitric acid was added to the solution containing a Bi/Mo ratio of 1:1 and 2:1 referred to as HT_BixMoy_HNO3. Precursors with a Bi/Mo = 2:1 ratio were moreover dissolved in 80 ml of 25 vol.% acetic acid to lower the pH value from 0.8 to 0.2 (HT_Bi2Mo1_HOAc). The resulting solutions were heated at 180 °C for 24 h in an oven (details of the preparation and description of equipment see chapter 2.1.1). After cooling to room temperature, the solid product was separated by filtration, washed with water, ethanol and finally with acetone. The resulting powder was dried at room temperature and ambient pressure. The samples prepared with a Bi/Mo ratio in the range 0.5 – 2 in water were also calcined at 550 °C for 4 h.

Bismuth molybdate materials exhibiting relatively high surface areas were synthesized under hydrothermal conditions adapting a procedure of Li et al. [34], who synthesized relatively small amounts of sample for photocatalysis. Therefore, 10 mmol $Bi(NO_3)_3 \cdot 5H_2O$ and stoichiometric amounts of $(NH_4)_6Mo_7O_{24} \cdot 4H_2O$ were dissolved in 20 ml 2.0 M nitric acid solution and 20 ml deionized water respectively (for Bi/Mo = 1:1). The two solutions were mixed under vigorous stirring and the pH of the resulting mixture was adjusted to values from 1 to 9 with an aqueous solution of 25 vol.% ammonia. For all samples addition of ammonia solution was necessary due to the low initial pH value. After

stirring for 30 minutes the resulting solutions were heated in sealed autoclaves at 180 °C for 24 h in an oven. After cooling to room temperature, the solid product was separated by filtration, washed with 100 ml deionized water, 40 ml ethanol and finally with 40 ml acetone. The resulting powder was dried at room temperature and ambient pressure. Additionally, the Bi/Mo ratio was changed from Bi/Mo = 1:1 to 2:3 and 2:1. The resulting products are referred to as BixMoy_pH.

To obtain high surface area samples bismuth molybdates with Bi/Mo ratios of 1:1, 2:1 and 2:3 were prepared by one-step flame spray pyrolysis (FSP) from Bi(III)- and Mo(VI)-2-ethylhexanoate dissolved in xylene (total concentration of 0.15 mol/l). The precursor solution was pumped with a speed of 5 ml/min (for details see 2.1.2). The resulting powders were used as-prepared and are denoted as followed: FSP_Bi1Mo1, FSP_Bi2Mo1 and FSP_Bi2Mo3.

For comparison, co-precipitated samples were synthesized according to Carrazán et al. [208] using $(NH_4)_6Mo_7O_{24} \cdot 4H_2O$ dissolved in ammonia solution and $Bi(NO_3)_3 \cdot 5H_2O$ dissolved in nitric acid at pH = 7. The resulting solid material was calcined at 450 °C to yield the α-$Bi_2Mo_3O_{12}$ and γ-Bi_2MoO_6 and at 680 °C to obtain the β-$Bi_2Mo_2O_9$. Experiments are referred to as CP_BixMoy_CT where CT is the calcination temperature in °C.

The structure of the samples was characterized by PXRD, Raman spectroscopy and *ex situ* XAS. The surface area was determined by nitrogen physisorption, the particle morphology was identified by SEM and TEM (for the hydrothermally synthesiezed and flame made samples, respectively). The composition in the bulk and on the surface was analyzed by ICP-OES, quantitative nitrogen analysis and XPS. Details are given in chapter 2.2. The samples were tested in selective oxidation of propylene as described in chapter 2.3.1.

4.3. Results and Discussion

4.3.1. Hydrothermal synthesis in water with Bi/Mo = 0.5 – 3

4.3.1.1. Characterization of the as-prepared bismuth molybdates

At first, several samples were prepared under hydrothermal conditions in pure water with Bi/Mo ratios from 0.5 – 3 and their phase composition was analyzed by powder X-ray

diffraction (PXRD) and Raman spectroscopy. Only two different bimetallic phases could be found in the five different samples with varying Bi/Mo ratio summarized in Table 4-1: α-$Bi_2Mo_3O_{12}$ and γ-Bi_2MoO_6.

Table 4-1: Characterization of hydrothermally prepared samples with different Bi/Mo ratios before and after the catalytic tests by PXRD, Raman spectroscopy and BET (main phases in bold letters).

Sample	Phases according to PXRD		Phases according to Raman spectroscopy		Specific surface area (BET) [m^2/g]
	as-prepared	after use	as-prepared	after use	as-prepared
HT_Bi3Mo1	**γ-Bi_2MoO_6**, cubic BiO_{2-x}	**γ-Bi_2MoO_6**, $Bi_8Mo_3O_{21}$	**γ-Bi_2MoO_6**	**γ-Bi_2MoO_6**, γ´-Bi_2MoO_6	30
HT_Bi2Mo1	**γ-Bi_2MoO_6**, α-$Bi_2Mo_3O_{12}$, $Bi_6O_6(OH)_3(NO_3)_3 \cdot 1.5H_2O$	**γ-Bi_2MoO_6**	**γ-Bi_2MoO_6**, presence of NO_3^-	**γ-Bi_2MoO_6**	6
HT_Bi1Mo1	**γ-Bi_2MoO_6** and **α-$Bi_2Mo_3O_{12}$**	**γ-Bi_2MoO_6** and **α-$Bi_2Mo_3O_{12}$**	**α-$Bi_2Mo_3O_{12}$**	n.d.	8
HT_Bi2Mo3	**α-$Bi_2Mo_3O_{12}$**, cubic $H_{0.68}(NH_4)_2Mo_{14.16}O_{4.34} \cdot 6.92H_2O$	**α-$Bi_2Mo_3O_{12}$**	**α-$Bi_2Mo_3O_{12}$**, MoO_3	**α-$Bi_2Mo_3O_{12}$**	7
HT_Bi1Mo2	**α-$Bi_2Mo_3O_{12}$**, hexagonal $NH_3(MoO_3)_3$	**α-$Bi_2Mo_3O_{12}$**, α-MoO_3	**α-$Bi_2Mo_3O_{12}$**, $NH_3(MoO_3)_3$	**α-$Bi_2Mo_3O_{12}$**, MoO_3	6

Application of a high Bi/Mo ratio led to the formation of the bismuth-rich phase, γ-Bi_2MoO_6. Decreasing the initial bismuth contents increased the amounts of α-$Bi_2Mo_3O_{12}$ in the as-prepared samples. The diffraction pattern of the sample prepared with a high excess of bismuth (Bi/Mo = 3:1) displays characteristic reflections at 2θ = 28.3, 23.7 and 46.9 ° which can be assigned to γ-Bi_2MoO_6 (PDF 21-102 [209]) [210] and cubic BiO_{2-x} (PDF 47-1057) [211]. The crystallinity of HT_Bi3Mo1 was lower than the crystallinity of the other four samples, as indicated by the broader reflections in the diffraction pattern (Figure 4.1a). This goes hand in hand with a significantly higher surface area than observed for the other four samples (30 m^2/g compared to 6 - 8 m^2/g).

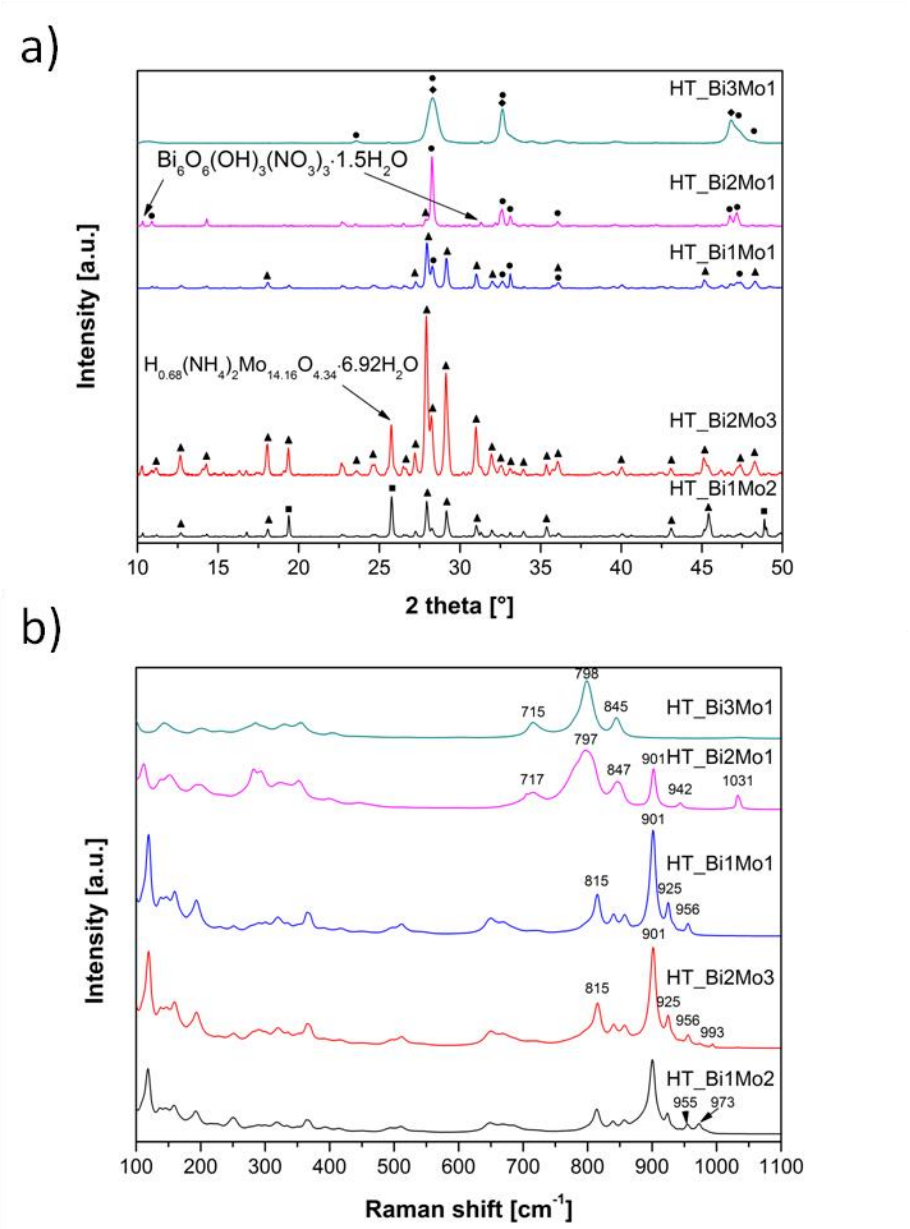

Figure 4.1: Characterization of the samples prepared with different Bi/Mo ratio under hydrothermal conditions without calcination by X-ray diffraction (a) and Raman spectroscopy (b). The different phases in the diffraction pattern (a) are indicated as follows: α-$Bi_2Mo_3O_{12}$ (triangles), γ-Bi_2MoO_6 (circles), $NH_3(MoO_3)_3$ (squares), BiO_{2-x} (diamond).

The diffraction pattern of the sample synthesized with Bi/Mo = 2:1 (Figure 4.1a) indicates γ-Bi_2MoO_6 as the main phase and additionally the presence of α-$Bi_2Mo_3O_{12}$ (low intensity reflection at 27.9°) and $Bi_6O_6(OH)_3(NO_3)_3 \cdot 1.5H_2O$ (10.3° and 31.3°, PDF 53-1038) [212]. The corresponding Raman spectrum of this sample depicted in Figure 4.1b confirmed the presence of γ-Bi_2MoO_6 as the main phase in this sample. The observed Raman bands at 848, 808, 792 and 714 cm^{-1} were assigned as Mo-O stretching frequencies of the distorted MoO_6 octahedra of the Aurivillius layered structure [210, 213]. Additionally, bands at 352,

323, 294 and 282 cm^{-1} were also found, which correspond well to those reported for γ-Bi_2MoO_6 in the literature. [214] The presence of α-$Bi_2Mo_3O_{12}$ was evident from the band at 901 cm^{-1}. The band at 1031 cm^{-1} could be assigned to a nitrate containing phase. This nitrate containing phase also led to a broader band at 782 – 808 cm^{-1}. [215] Quantitative nitrogen analysis yielded 0.36 wt.% (± 0.02 wt.%) N in this sample, which agrees well with the presence of a nitrate phase. The ICP-OES measurement of HT_Bi2Mo1 showed that the product contained bismuth and molybdenum in the ratio 2:1, which equals the applied ratio.

Whereas distinction of the three different phases may be difficult with PXRD methods due to their adjacent main reflections (α: 27.9 °, β: 27.8 °, γ: 28.3 °) and the formation of the β-phase is easily overlooked, Raman spectra permit a better identification of these three different bismuth molybdate phases.

The sample prepared with Bi/Mo = 1:1 contained a mixture of γ-Bi_2MoO_6 and α-$Bi_2Mo_3O_{12}$ according to PXRD measurements, whereas the Raman spectrum only displayed the α-phase. While X-ray diffraction measurements provide information of quantitative phase composition of larger particles, Raman spectra often only show the strongest bands which may overlap with bands of other phases. The Raman spectrum of α-$Bi_2Mo_3O_{12}$ exhibited six bands between 1000 – 800 cm^{-1} which can be attributed to the Mo-O stretching modes of different tetrahedral species, i.e. 955 cm^{-1} (a_3), 925 cm^{-1} (a_1), 906 cm^{-1} (a_2), 856 cm^{-1} (a_1), 840 cm^{-1} (a_2) and 816 cm^{-1} (a_3). All of these six bands were present in the spectra of HT_Bi1Mo1 as well as in the spectra of the samples synthesized with a Bi/Mo ratio below 1:1 (Figure 4.1b). The X-ray diffraction pattern and the Raman spectrum of the sample with an initial Bi/Mo ratio of 2:3 showed the characteristic features of α-$Bi_2Mo_3O_{12}$ and indicated in addition the presence of a bismuth-free molybdenum oxide side phase (reflection at 25.7 °, Raman shift: 993 cm^{-1}). Calculation of the Bi/Mo ratio from the values obtained from ICP-OES measurements yielded to 0.7 (± 10%), corresponding to the Bi/Mo ratio in the α-phase. This indicates that, additionally to α-$Bi_2Mo_3O_{12}$ and an ammonium-containing molybdenum oxide phase, another bismuth oxide phase should be present which could not be detected by PXRD or Raman spectroscopy. Generally, such small amounts of bismuth oxides are difficult to identify from diffraction patterns due to the overlap of some of their reflections with those of bismuth molybdates. van Well et al. [124] also claimed that excess bismuth in form of β-Bi_2O_3 or β-$Bi_2Mo_2O_9$

cannot be seen by X-ray diffraction when the samples were calcined at temperatures lower than 500 °C.

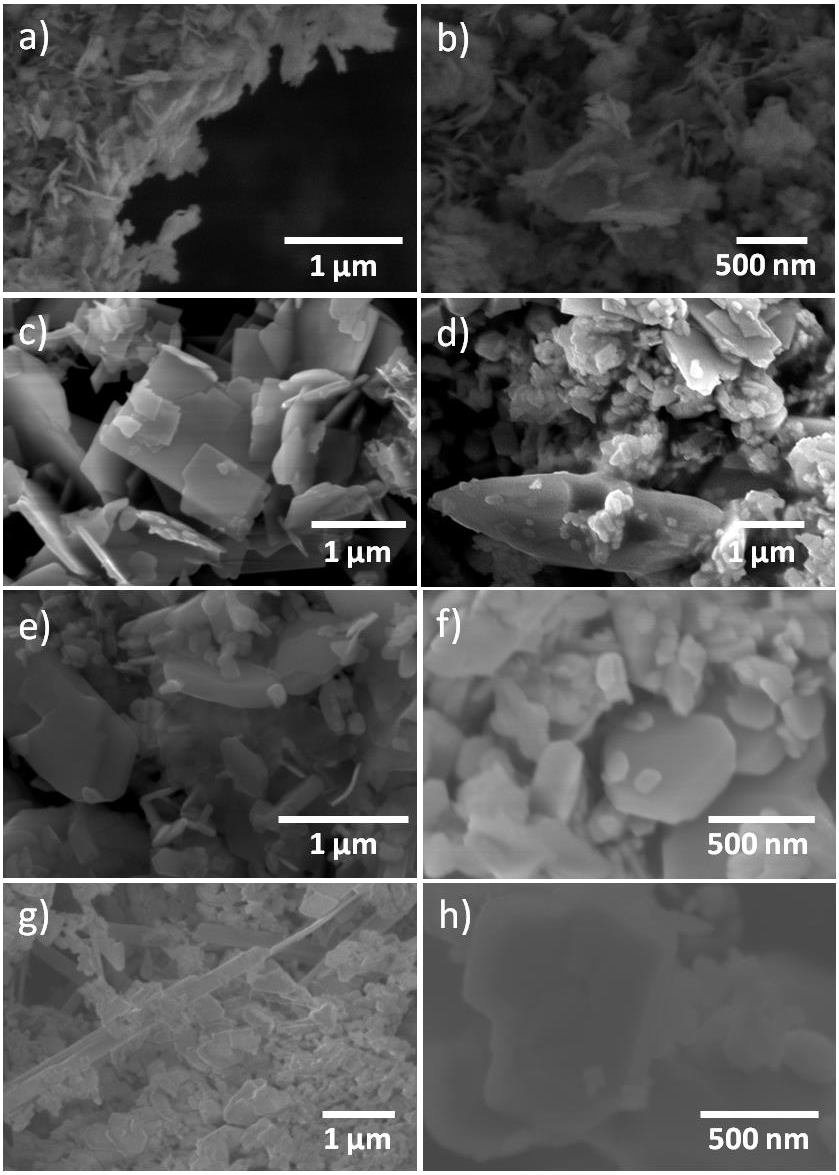

Figure 4.2: SEM images of hydrothermally synthesized samples with different Bi/Mo ratio without further calcination a-b) HT_Bi3Mo1, c) HT_Bi2Mo1, d) HT_Bi1Mo2, e-f) HT_Bi1Mo1, g-h) HT_Bi2Mo3.

The Raman spectrum of the sample synthesized with a high excess of molybdenum (HT_Bi1Mo2) illustrates the presence of the main γ-phase along with a band at 973 cm^{-1} which corresponds well to $NH_3(MoO_3)_3$ in agreement with PXRD data (reflections at 19.4 and 25.7°).

SEM images of all samples showed a plate-like morphology (Figure 4.2) with variations in aspect ratio and size. Synthesis with a large excess of bismuth led to the smallest particle size (Figure 4.2a and b), resulting in a relatively high specific surface area (30 m^2/g). The particles of sample HT_Bi2Mo1 were rectangular with a side length of 1 - 2.5 µm and a thickness of ca. 200 nm (Figure 4.2c). Synthesis with Bi/Mo = 1:1 led to smaller plates (500 nm) with rounded edges (Figure 4.2e and f). SEM images of HT_Bi2Mo3 (Figure 4.2g and h) revealed a mixture of plates with a side length around 1 µm and larger needles / rods. HT_Bi1Mo2 (Figure 4.2d) also displays two types of morphology: the plate-like α-$Bi_2Mo_3O_{12}$ (400 nm – 1 µm in size) and the wedge-like / rod-like ammonium molybdenum oxide phase visible at the bottom of the image.

4.3.1.2. Catalytic performance of the as-prepared bismuth molybdates

The catalytic activity measurements for propylene oxidation of the as-prepared samples are depicted in Figure 4.3. At 360 °C all samples showed very similar activities resulting in a propylene conversion between 10% and 22% depending on the flow and accordingly on the contact time. Besides acrolein (60 - 90%) only CO_x (mainly CO_2) and traces of acetaldehyde were formed. The sample prepared with a large excess of bismuth (HT_Bi3Mo1) converted less propylene than the other four samples at 360 °C and was almost inactive for propylene oxidation. This sample was also not selective for acrolein and mainly produced hexadiene and CO_x. This agrees well with previous literature reports on the formation of hexadiene in the presence of Bi_2O_3. [102, 216] HT_Bi2Mo1 also contained a bismuth oxide phase but its concentration may be too low to influence the catalytic activity of the sample. The presence of γ-Bi_2MoO_6 as main product goes hand in hand with a slightly higher selectivity at lower conversion compared to the samples synthesized with lower Bi/Mo ratio.

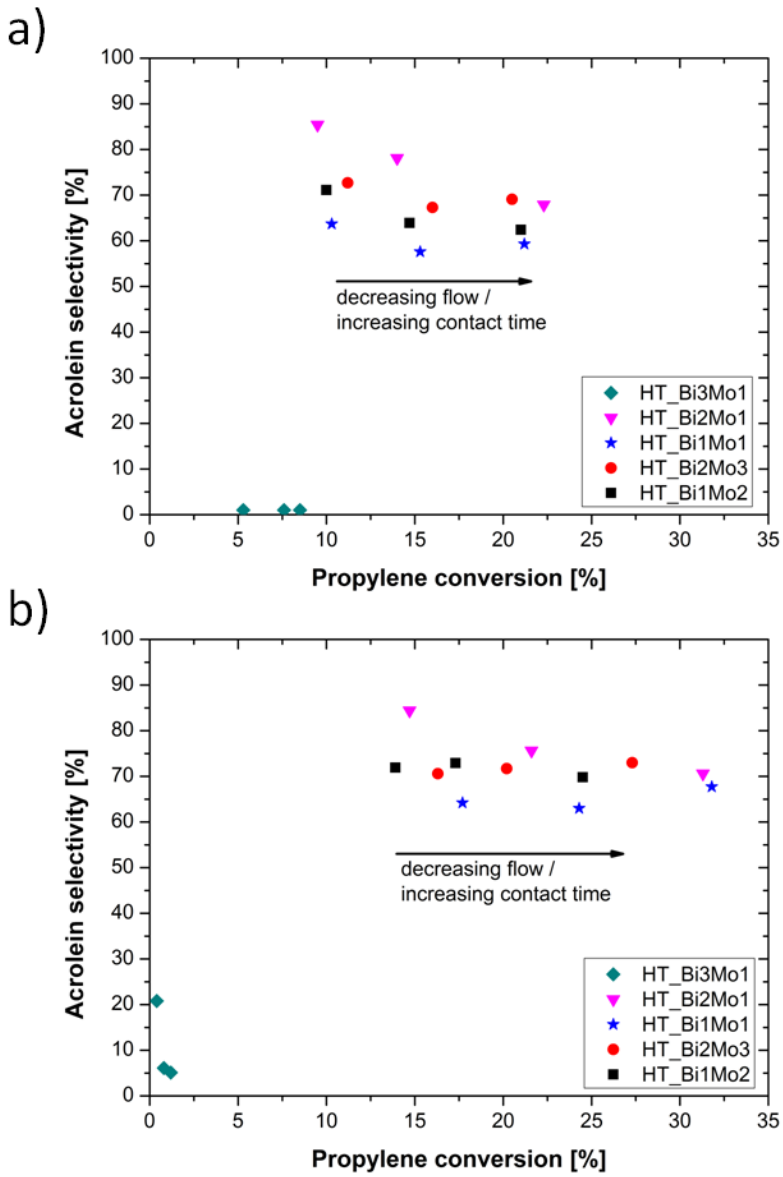

Figure 4.3: Catalytic performance of hydrothermally prepared samples with different Bi/Mo ratios at 360 °C (a) and 400 °C (b) without calcination. 500 mg of the as-prepared samples (150 – 300 µm) were pre-treated in the reactor in synthetic air at 300 °C and the catalytic performance was measured using a gas composition of $C_3H_6/O_2/N_2$ = 5/25/70 and flows of 50, 80, 120 Nml/min.

At higher temperature (400 °C) the propylene conversion increased up to 32% and the difference between the measurement points for each sample at similar conditions also raised (Figure 4.3b). The sample prepared with Bi/Mo = 1:1 was slightly more active than HT_Bi2Mo1 and their catalytic activity deteriorated with decreasing Bi/Mo ratio. The selectivity for acrolein was never below 60% and stayed relatively constant with increasing propylene conversion indicating that acrolein further reacted to CO_x only very slowly on these catalysts.

Note that as for most transition metal oxide catalysts the initial phase probably changed during the catalytic activity measurements from 320 – 520 °C, so that the phases summarized in the second column of Table 4-1 ("as-prepared") are not those actually present in the reactor during propylene conversion. We thus investigated the phase composition after the catalytic process as well.

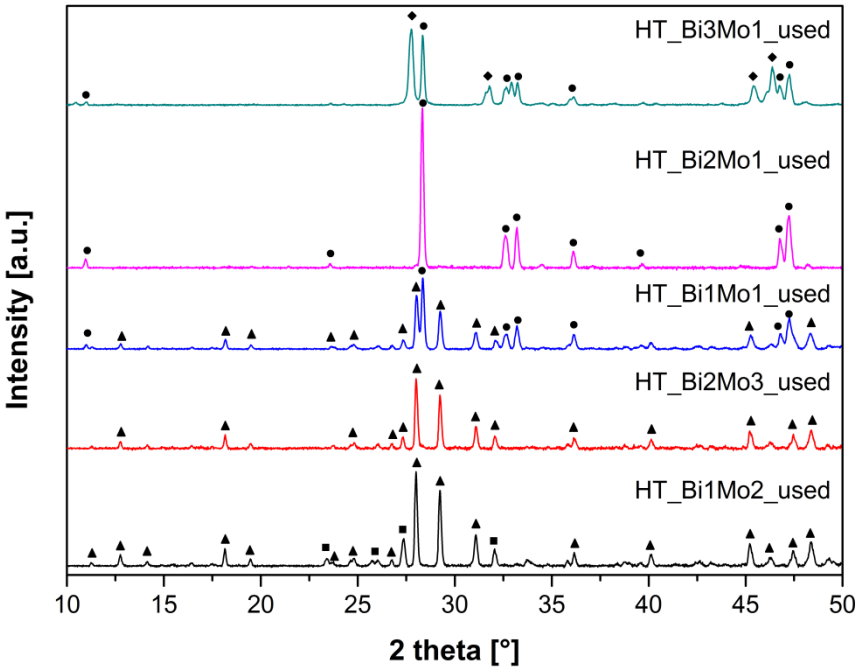

Figure 4.4: PXRD pattern of hydrothermally synthesized samples after propylene oxidation at temperatures up to 520 °C, illustrating that no major changes occurred in the main phase after catalysis; α-$Bi_2Mo_3O_{12}$ (triangles), γ-Bi_2MoO_6 (circles), α-MoO_3 (squares) and $Bi_8Mo_3O_{21}$ (diamond).

Figure 4.4 shows the powder diffraction pattern of the hydrothermally synthesized samples after catalytic tests at temperatures up to 520 °C. Comparison of the diffraction pattern and also of the Raman spectra of fresh and used catalysts indicate that the main phase of the catalysts did not change during the application in selective oxidation of propylene. After application in propylene oxidation, HT_Bi3Mo1 consisted of γ-Bi_2MoO_6 and $Bi_8Mo_3O_{21}$, which is orthorhombic and presents a basic fluorite-type structure. [217-218] The minor phases in samples HT_Bi2Mo1 and HT_Bi2Mo3 indicated by only one or two low intensity reflections disappeared, whereas for the sample synthesized with a high excess of molybdenum (HT_Bi1Mo2) the hexagonal $NH_3(MoO_3)_3$-phase was transformed into α-MoO_3. SEM images in Figure 4.5 revealed that the plate-like morphology of the samples

could not be preserved during the application for selective oxidation of propylene at 320 – 520 °C. Only the sample synthesized with the Bi/Mo ratio 2:1 partly retained its plate-like morphology (Figure 4.5d). All samples exhibited similar morphologies after the catalytic tests, whereas their particle sizes decreased with increasing bismuth content. Generally, thermal treatment led to particle agglomeration and a significant loss of surface area (< 1 m^2/g). The used samples only contained α-$Bi_2Mo_3O_{12}$ and / or γ-Bi_2MoO_6, except for sample HT_Bi1Mo2, where an excess of Mo led to the additional formation of α-MoO_3.

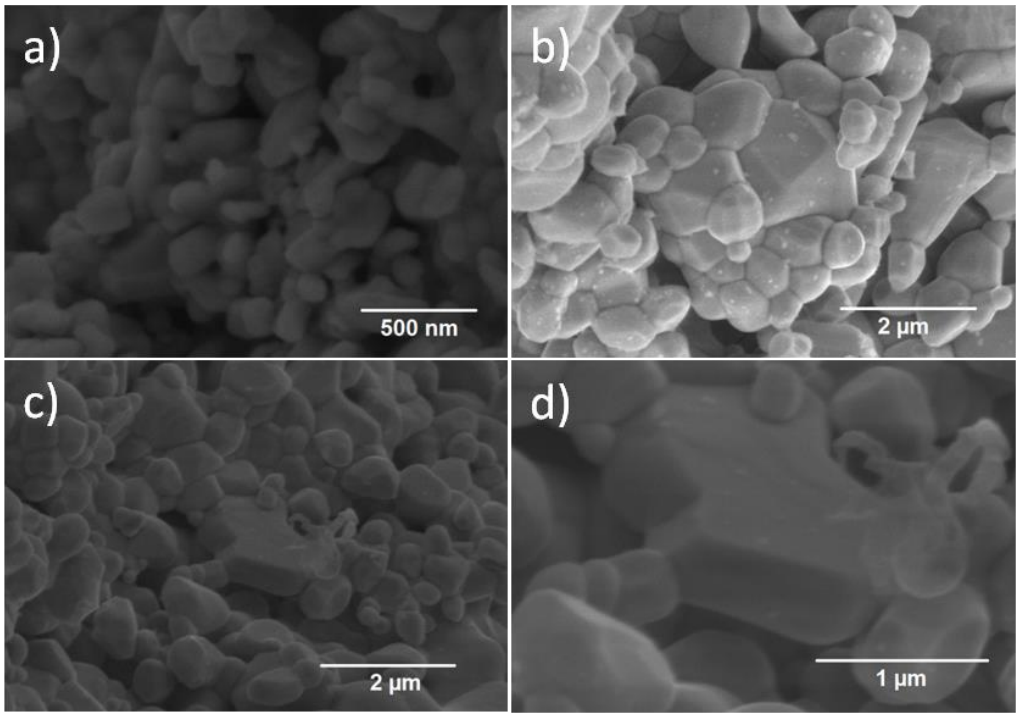

Figure 4.5: SEM images of a) HT_Bi3Mo1, b) HT_Bi2Mo3 and c-d) HT_Bi2Mo1 after catalytic propylene oxidation at temperatures up to 520 °C.

4.3.2. Influence of the calcination procedure on catalyst properties and activity

4.3.2.1. Characterization of the calcined samples

Hydrothermally synthesized samples with Bi/Mo ratios 0.5 – 2.0 (pure water) were calcined at 550 °C for 4 h to increase the phase purity of the products and to evaluate the transformation of the phases at elevated temperatures. Figure 4.6a depicts the PXRD patterns of the four calcined samples, and the corresponding phase composition as well as the Bi/Mo ratios determined by ICP-OES and XPS are summarized in Table 4-2.

Table 4-2: Characterization of hydrothermally prepared samples before and after calcination at 550 °C for 4 h. Phases were identified by PXRD, the ratio of bismuth to molybdenum in the bulk and on the surface were calculated from ICP-OES (atom %) and XPS analysis.

Sample	Phases according to PXRD			Bi/Mo ratio bulk		Bi/Mo ratio surface	
	as-prepared	Calcined at 550 °C for 4 h	Calcined and used	as-prep	calc	as-prep	calc
HT_Bi2Mo1	**γ-Bi_2MoO_6**, α-$Bi_2Mo_3O_{12}$, $Bi_6O_6(OH)_3(NO_3)_3 \cdot 1.5H_2O$	**γ-Bi_2MoO_6**, some β-$Bi_2Mo_2O_9$	**γ-Bi_2MoO_6**	2.0	2.0	3.0	1.9
HT_Bi1Mo1	**γ-Bi_2MoO_6** and **α-$Bi_2Mo_3O_{12}$**	**γ-Bi_2MoO_6** and **α-$Bi_2Mo_3O_{12}$**	**γ-Bi_2MoO_6** and **α-$Bi_2Mo_3O_{12}$**	n.d.	n.d.	1.3	n.d.
HT_Bi2Mo3	**α-$Bi_2Mo_3O_{12}$**, cubic $H_{0.68}(NH_4)_2Mo_{14.16}O_{4.34} \cdot 6.92H_2O$	**α-$Bi_2Mo_3O_{12}$**	**α-$Bi_2Mo_3O_{12}$**	0.7	0.7	0.8	0.7
HT_Bi1Mo2	**α-$Bi_2Mo_3O_{12}$**, hexagonal $NH_3(MoO_3)_3$	**α-$Bi_2Mo_3O_{12}$**, MoO_3	**α-$Bi_2Mo_3O_{12}$**, MoO_3	0.5	n.d.	n.d.	n.d.

For the sample synthesized with a Bi/Mo ratio of 2:1 additionally to γ-Bi_2MoO_6 the β-phase was formed during calcination at 550 °C. The presence of β-$Bi_2Mo_2O_9$ is indicated by characteristic reflections at 27.9° and 31.8° in the diffraction pattern in Figure 4.6a and by the band at 885 cm^{-1} in the Raman spectrum (Figure 4.6b). As the β-phase is considered stable between 540 and 665 °C, formation of β-$Bi_2Mo_2O_9$ was also expected for the calcined sample emerging from Bi/Mo = 1:1. Surprisingly, calcination of HT_Bi1Mo1 only improved the crystallinity of the α- and γ-bismuth molybdate mixture, but did not lead to the formation of β-$Bi_2Mo_2O_9$. This suggests that higher calcination temperatures or longer treatment times should have been applied. Li et al. [34] could not synthesize the β-phase directly by hydrothermal synthesis but after calcination at 560 °C. Beale and Sankar [8] showed by combined EDXRD/XAS that phase-pure β-$Bi_2Mo_2O_9$ could be produced

from a hydrothermally synthesized precursor material by heat treatment at temperatures above 500 °C.

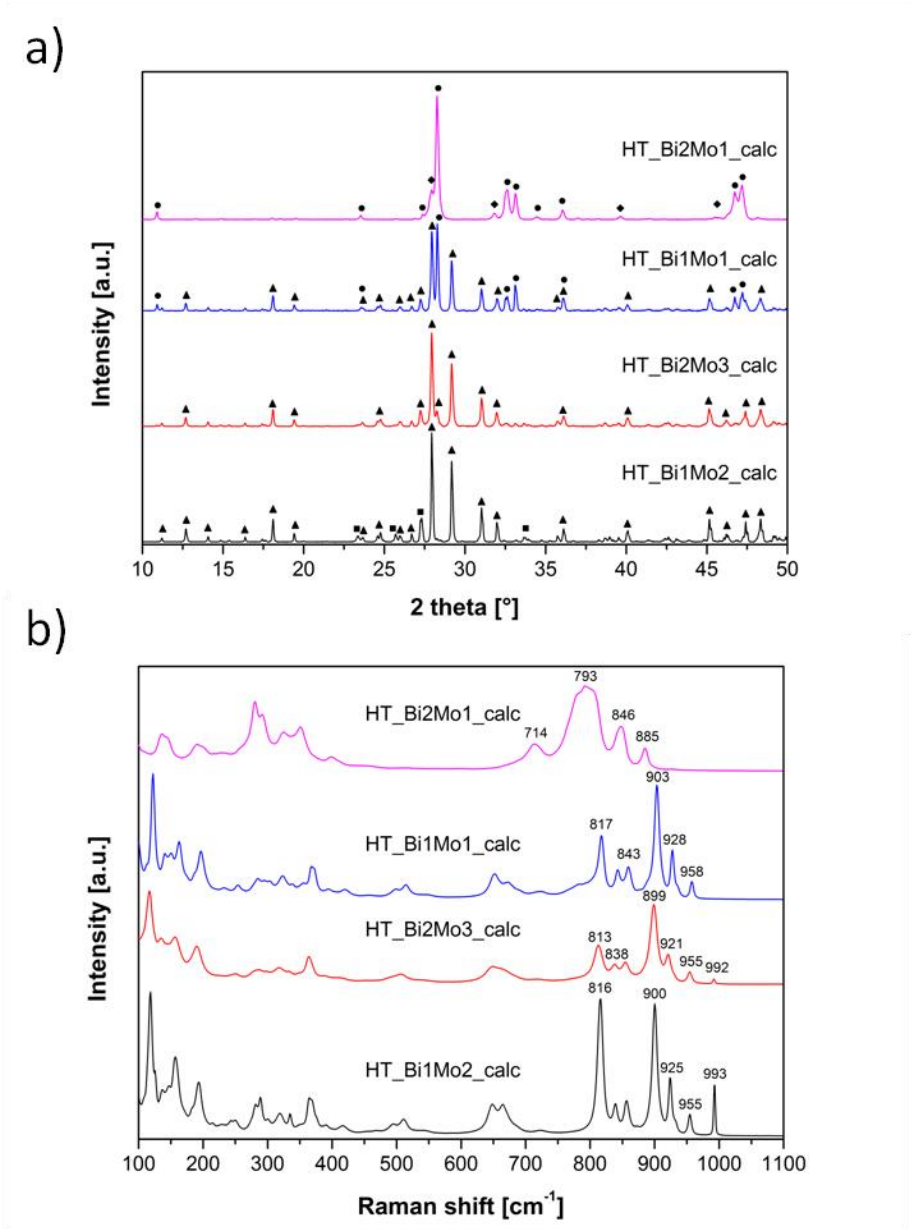

Figure 4.6: Characterization of the hydrothermally synthesized samples after calcination at 550 °C by X-ray diffraction (a) and Raman spectroscopy (b). γ-Bi_2MoO_6 (circles), β-$Bi_2Mo_2O_9$ (diamond), α-$Bi_2Mo_3O_{12}$ (triangle) and α-MoO_3 (993 cm^{-1}, squares).

After calcination at 550 °C for 4 h the sample synthesized from a Bi/Mo ratio 2:3 only contained α-$Bi_2Mo_3O_{12}$. HT_Bi1Mo2_calc containing a larger excess of molybdenum additionally showed characteristic features of α-MoO_3 in the diffraction pattern (Figure 4.6a; reflections at 23.3°, 25.7°, 27.3°, 33.7°) and in the Raman spectra (Figure 4.6b; 993 cm^{-1}). Bi/Mo ratios found in the bulk of the products synthesized with Bi/Mo = 2:1 and 2:3

was consistent with the applied ratio and did not change during calcination (Table 4-2), thereby indicating that no molybdenum or bismuth losses occurred during thermal treatment. Comparison of the metal ratio in the bulk determined by ICP-OES and on the surface (XPS) showed both values were practically identical after calcination. The surface composition of the catalyst was determined from the peak areas of Mo $3d_{5/2}$ = 232.7 eV and Bi $4f_{7/2}$ = 159.4 eV. A representative spectrum is shown in Figure 4.7.

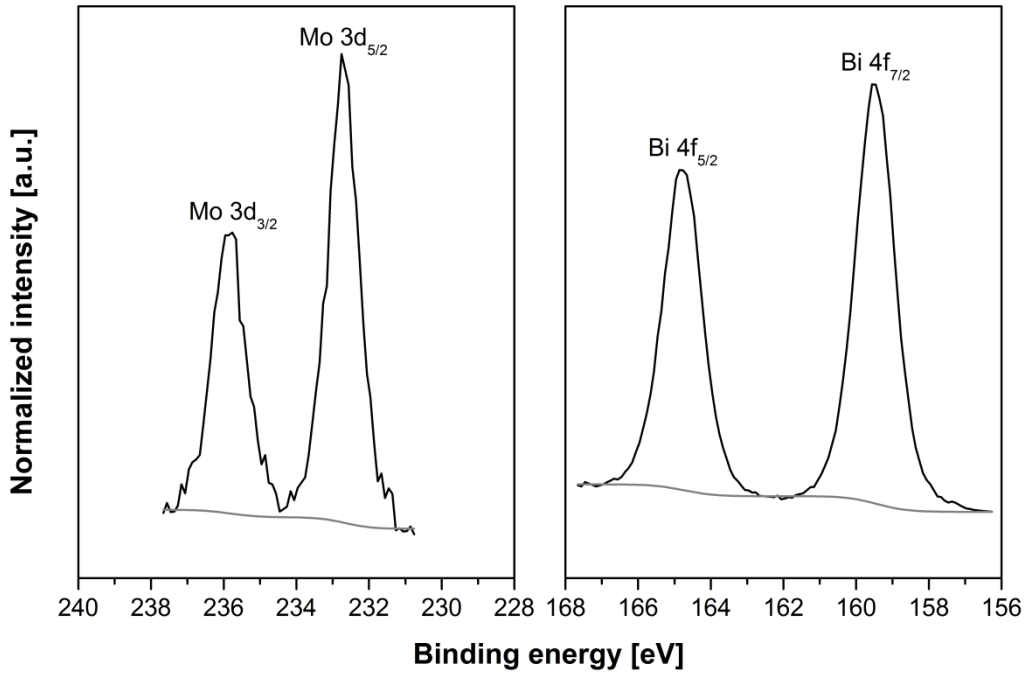

Figure 4.7: Representative XPS of a hydrothermally synthesized sample with Bi/Mo = 2:1 at 180 °C for 24 h without further heat treatment.

XPS measurement of the as-prepared HT_Bi2Mo1 revealed enrichment with bismuth on the surface, which might be due to the presence of $Bi_2O_{3.96}$. However, the activity for propylene conversion was sufficiently high and no formation of hexadiene due to the presence of Bi_2O_3 could be observed. [102, 216] Hence, it is more likely that the γ-bismuth molybdates have an excess of superficial bismuth, which is in line with literature. [121, 219] Bing et al. [98] also observed a decrease of the surface Bi/Mo ratio for γ-Bi_2MoO_6 prepared by co-precipitation during calcination at 420 °C. van Well et al. [124] calcined spray dried and co-precipitated samples with a theoretical Bi/Mo ratio of 2.0 at 550 °C and determined similar surface ratios to the values found for our hydrothermally synthesized samples: the

high Bi/Mo ratio of 3.0 determined for the as-prepared HT_Bi2Mo1 and the value of 1.9 for the calcined sample diluted by the β-phase (see Table 4-2).

4.3.2.2. Catalytic performance before and after calcination

Next, the four calcined samples HT_Bi2Mo1_calc, HT_Bi1Mo1_calc, HT_Bi2Mo3_calc and HT_Bi1Mo2_calc were applied in the catalytic oxidation of propylene where they exhibited a lower propylene conversion and, accordingly, a lower acrolein yield than the non-calcined samples under the same conditions (flow range 50 – 260 Nml/min, 460 – 520 °C). Figure 4.8 compares the acrolein yield and the propylene conversion of the as-prepared and calcined catalysts at 480 °C and 80 Nml/min. The acrolein yield for the calcined samples decreased with increasing molybdenum content to 1.0% at corresponding propylene conversion of 1.7% for HT_Bi1Mo2_calc.

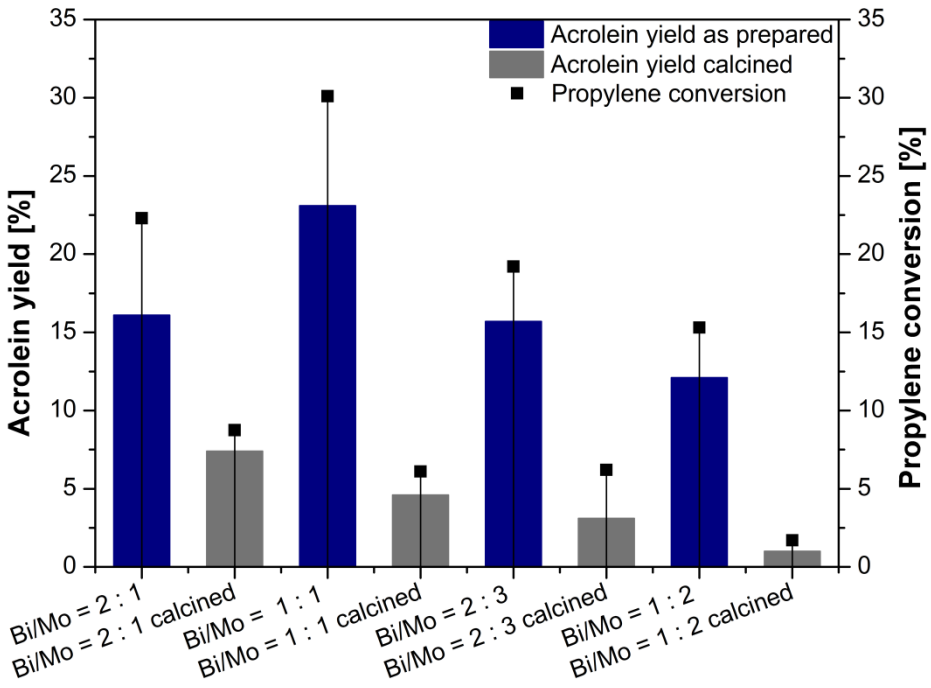

Figure 4.8: Catalytic performance of the hydrothermally synthesized samples with Bi/Mo ratios 2.0 – 0.5 at 480 °C with 80 Nml/min and a contact time of 0.16 (g·s)/ml (calculated at reaction temperature and pressure); black squares: propylene conversion, bars: acrolein yield (as-prepared materials = blue, calcined samples = grey). For each sample the propylene conversion and the acrolein yield decreased after calcination.

For HT_Bi2Mo3 propylene conversion decreased from 19.2% to 6.2% due to calcination and the acrolein selectivity decreased from 82% to 51%. Comparing the phase composition

of this sample before and after calcination suggests that the phase change was responsible for the deactivation. During calcination the ammonium molybdenum oxide phase in HT_Bi2Mo3 disappeared and phase pure α-$Bi_2Mo_3O_{12}$ was obtained (Table 4-2). This ammonium molybdenum phase should have a lower catalytic activity in propylene oxidation and a lower selectivity to acrolein than α-$Bi_2Mo_3O_{12}$. [220] Therefore the mixture of ammonium molybdenum oxide and α-$Bi_2Mo_3O_{12}$ should be less active and less selective than pure α-$Bi_2Mo_3O_{12}$. But also for the other three samples, calcination led to a deactivation in propylene oxidation. For HT_Bi2Mo1 the β-phase was formed and for HT_Bi1Mo2 hexagonal $NH_3(MoO_3)_3$ was changed to orthorhombic MoO_3. HT_Bi1Mo1 did not undergo phase changes during calcination but the deactivation by calcination was more significant than for the other three samples. Although propylene conversion decreased for the calcined samples compared to the as-prepared materials, the selectivity decreased as well for all samples except HT_Bi2Mo1. Here, acrolein selectivity increased due to thermal treatment from 69.2% to 85.2% at a propylene conversion of 22.3% and 8.7% respectively. van Well et al. [124] reported that calcination time and temperature strongly influenced the activity of the bismuth molybdenum catalysts. They suggested that this was due to a surface enrichment with bismuth after calcination at higher temperature or longer time. This could not be confirmed here, as the bismuth concentration on the surface decreased during calcination (see Table 4-2). But a possible explanation could be the decrease of the surface area, which was ≤ 1 m²/g for all calcined samples. The surface area of the calcined samples was very low and therefore propylene conversion was also low.

Comparison of SEM images in Figure 4.9 and Figure 4.2 revealed that the particles sinter and agglomerate during calcination. Only the sample prepared from an initial Bi/Mo ratio 2:1 retained a plate-like morphology, but the thickness increased during calcination and the aspect ratio changed from rectangular to quadratic (Figure 4.9a). In summary only HT_Bi2Mo1 partially preserved its morphology during calcination and this sample showed the best catalytic performance compared to the other three calcined materials.

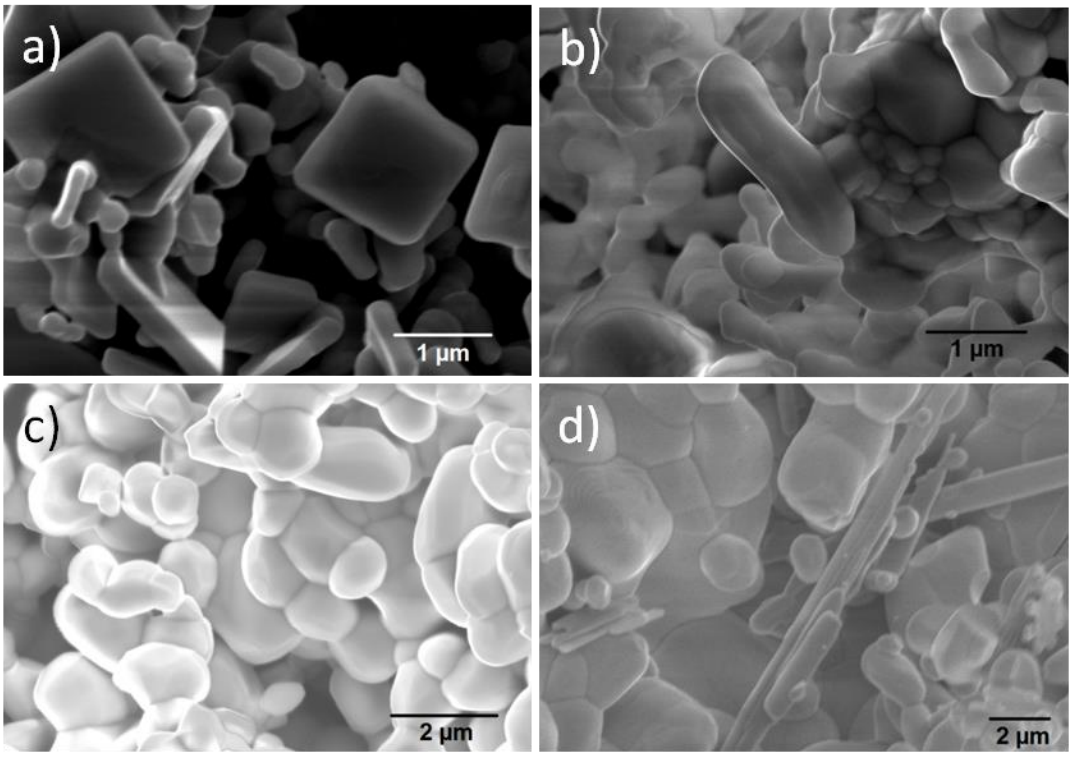

Figure 4.9: SEM images of samples synthesized with different Bi/Mo ratio after calcination at 550 °C a) HT_Bi2Mo1_calc, b) HT_Bi1Mo1_calc, c) HT_Bi2Mo3_calc and d) HT_Bi1Mo2_calc.

4.3.3. Comparison of hydrothermally synthesized catalysts with flame made materials

4.3.3.1. Characterization of the samples synthesized by different preparation methods

The diffraction pattern of the bismuth molybdates prepared with different Bi/Mo ratios by flame spray pyrolysis, hydrothermal synthesis or co-precipitation are shown in Figure 4.10. All samples prepared with a Bi/Mo ratio 2:1 contained mainly γ-Bi_2MoO_6 except for the co-precipitated sample calcined at 680 °C, which consisted of γ”-Bi_2MoO_6, whereas α-$Bi_2Mo_3O_{12}$ was the main phase for Bi/Mo = 2:3. The majority of the samples prepared with Bi/Mo = 1:1 consisted of a mixture of the α-phase with either β- or γ-bismuth molybdate. Flame spray synthesis led to the formation of β-$Bi_2Mo_2O_9$.

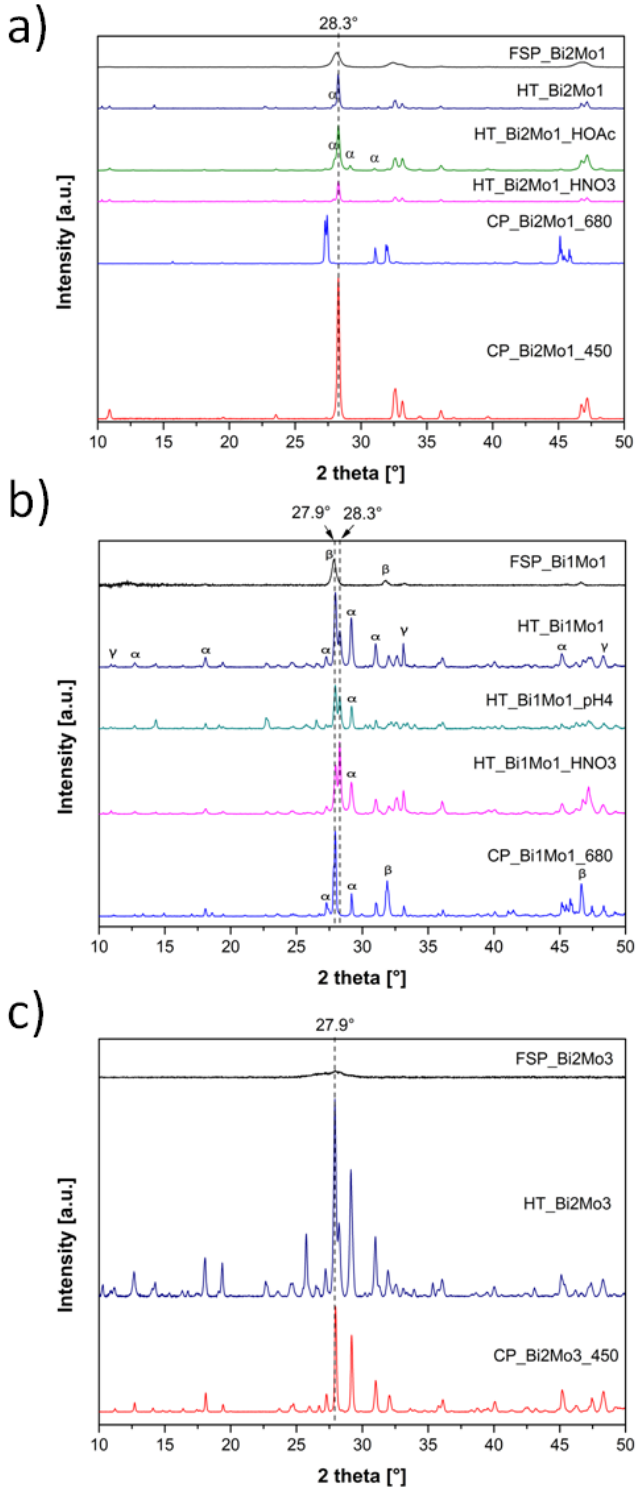

Figure 4.10: X-ray diffraction pattern of different samples prepared by flame spray pyrolysis (FSP), co-precipitation (CP) and hydrothermal synthesis (HT) synthesized with Bi/Mo = 2:1 (a), Bi/Mo = 1:1 (b) and Bi/Mo = 2:3 (c).

As already discussed in chapter 4.3.1., hydrothermal synthesis at 180 °C with Bi/Mo = 2:1 prepared in pure water led to the formation of γ-Bi_2MoO_6 with some other Mo- or Bi-

containing phases as impurity. Addition of acetic acid did also result in γ-Bi_2MoO_6, but with α-$Bi_2Mo_3O_{12}$ as a side product. This sample featured agglomerates of flat plates with round-shaped edges illustrated in Figure 4.11a and b. Phase pure γ-Bi_2MoO_6 was obtained from synthesis in the presence of nitric acid. The plates of HT_Bi2Mo1_HNO3 (Figure 4.11c) were rectangular with well defined steps and edges on the surface, which may be beneficial for the selectivity of the catalytic reaction.

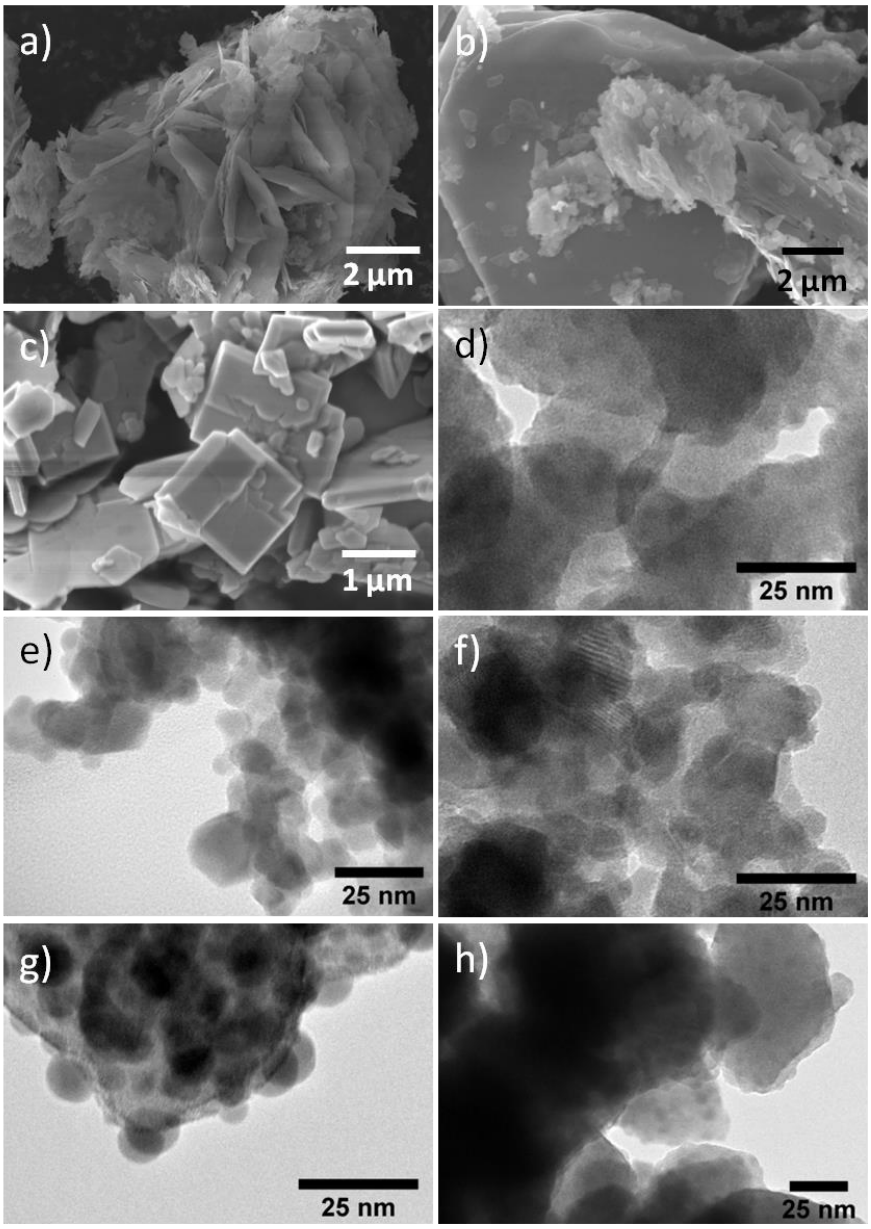

Figure 4.11: SEM images of a-b) HT_Bi2Mo1_HOAc and c) HT_Bi2Mo1_HNO3, TEM images of the three different flame made materials: d) FSP_Bi2Mo3, e-f) FSP_Bi2Mo1, g-h) FSP_Bi1Mo1.

Table 4-3: Characterization and catalytic data of the differently prepared samples. All samples are as-prepared and non-calcined except the co-precipitated samples (calcination temperature is included in the sample name).

Sample	Max. yield (C_3H_4O) %	Corresponding conversion (C_3H_6) %	T °C	Specific surface area (BET) [m²/g]	Bi/Mo ratio bulk [a] [at.%/at.%]	Bi/Mo ratio surface [b] [at.%/at.%]
FSP_Bi2Mo1	22.2	26.1	484	45	1.9	2.3
CP_Bi2Mo1_450	25.3	33.9	491	6	2.0	2.3
CP_Bi2Mo1_680	5.8	7.3	482	< 1	n.d.	n.d.
HT_Bi2Mo1_HNO3	33.6	41.2	450	6	1.8	2.8
HT_Bi2Mo1_HOAc	20.1	26.8	405 [c]	5	n.d.	n.d.
HT_Bi2Mo1	23.1	33.3	445	6	2.0	3.0
FSP_Bi1Mo1	30.3	37.4	451	19	n.d.	1.1
CP_Bi1Mo1_680	3.6	4.3	521	< 1	n.d.	n.d.
HT_Bi1Mo1_HNO3	38.4	43.8	486	9	n.d.	1.2
HT_Bi1Mo1_pH4 [d]	36.6	45.5	489	7	n.d.	n.d.
HT_Bi1Mo1	31.0	39.9	493	8	n.d.	1.3
FSP_Bi2Mo3	6.1	7.4	484	18	n.d.	n.d.
CP_Bi2Mo3_450	15.3	18.8	483	1	0.7	n. d.
HT_Bi2Mo3	21.9	28.9	443	7	0.7	0.8

a: The calculated error accounts to around 10%.

b: Average of two XPS measurements at different spots.

c: Maximum test temperature 400 °C for HT_Bi2Mo1_HOAc.

d: pH value adjusted with NH_3.

Co-precipitation followed by calcination at 450 °C yielded pure γ-Bi_2MoO_6 as well, whereas during calcination at 680 °C γ"-Bi_2MoO_6 (PDF No. 33-208 [209]) [31] was formed as indicated by the reflections at 27.4, 31.1, 31.9 and 45.1° (cf. Figure 4.10a). Similarly the flame made material FSP_Bi2Mo1 exclusively contained the γ-phase according to its diffraction pattern. Hydrothermal synthesis with Bi/Mo = 1:1 did not lead to the formation of the β-phase but to a mixture of α- and γ-phase for all three samples. Co-precipitation of bismuth molybdates with Bi/Mo = 1:1 and calcination at 680 °C resulted in a mixture of β-

$Bi_2Mo_2O_9$ and α-$Bi_2Mo_3O_{12}$. As mentioned above, only flame spray pyrolysis afforded pure β-$Bi_2Mo_2O_9$ at a Bi/Mo ratio of 1:1. The flame made material synthesized with Bi/Mo = 2:3 was highly amorphous. In Table 4-3 the results of the N_2 physisorption measurements are summarized. The co-precipitated samples and the hydrothermally synthesized samples had similar surface area (6 - 9 m²/g) whereas the flame made materials always exhibited higher surface areas (18 – 45 m²/g). FSP_Bi2Mo1 (45 m²/g) reached the highest specific surface area. Whereas the spherical particles of this sample were approximately 25 nm in size (Figure 4.11e-f), FSP_Bi2Mo3 and FSP_Bi1Mo1 retained larger particles with smaller spherical particles with a diameter < 10 nm on top (TEM images in Figure 4.11). The obtained surface area of these two samples was identical (Table 4-3).

To identify the coordination number of Mo and the structure of the materials, the samples were also analyzed by X-ray absorption spectroscopy (XAS) at the Mo K edge. The X-ray absorption near edge structure (XANES) spectra are depicted in Figure 4.12. $Na_2MoO_4 \cdot 2H_2O$ (tetrahedral Mo) and α-MoO_3 (octahedral Mo) were used as references. According to Reilly et al. [221] the features A and B correspond to 1s-4d (A) and 1s-5p (B) transitions, respectively. [222] The pre-edge feature A is larger for sodium molybdate containing tetrahedrally coordinated Mo(VI) compared to orthorhombic MoO_3, which incorporates Mo(VI) in an octahedral environment, because the 1s-4d transition is more allowed in tetrahedral symmetry. XANES spectra of FSP_Bi1Mo1 agreed well with those of $Na_2MoO_4 \cdot 2H_2O$ indicating that β-$Bi_2Mo_2O_9$ was formed by flame spray pyrolysis, given that the β-phase contains tetrahedral Mo(VI) species. For comparison the spectra measured for FSP_Bi2Mo1, HT_Bi2Mo1 and HT_Bi2Mo1_HNO3 (Figure 4.12) exhibited a stronger peak in the B region sensitive for octahedral Mo(VI) and lower intensity for A. The remaining spectra agreed well with reference data for octahedrally coordinated Mo (reference here α-MoO_3). This hints at the presence of γ-Bi_2MoO_6 for these three samples. Extended X-ray absorption fine structure (EXAFS) spectra mainly constituted the Mo-O backscattering. Due to the corner shared octahedra in γ-Bi_2MoO_6 also some Mo-Mo contribution was found for these samples (lowest for FSP_Bi2Mo1 because of the small particle size).

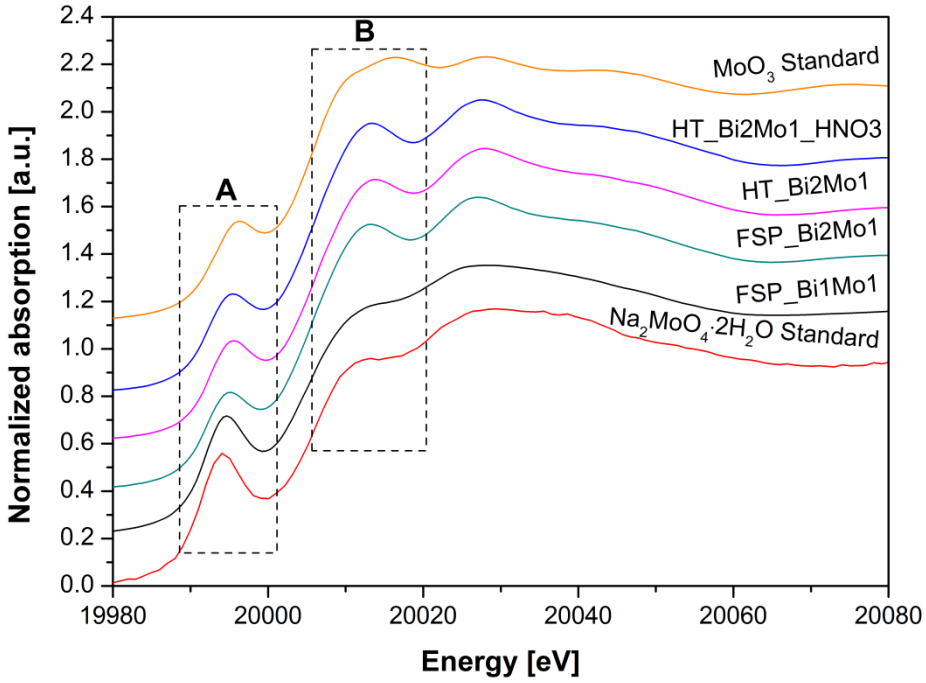

Figure 4.12: Mo K-edge XANES spectra of two flame made and two hydrothermally synthesized samples as well as two standards: $Na_2MoO_4 \cdot 2H_2O$ and α-MoO_3. The pre-edge feature A dominates the spectra of tetrahedrally coordinated Mo(VI) centers whereas the B-region is more prominent for symmetric six-fold coordinated Mo.

X-ray diffraction and absorption measurements both confirmed that flame spray pyrolysis led to the formation of β-$Bi_2Mo_2O_9$ and γ-Bi_2MoO_6 applying the corresponding Bi/Mo ratios. The β-phase is only considered stable at temperatures between 540 and 665 °C. A recent study [223] showed that the located maximum flame temperature is generally above 700 °C at 20 mm above the nozzle with oxygen as the dispersion gas, and continuously decreases with increasing distance from the nozzle. Studies on SiO_2 synthesis suggested that all reaction and particle formation processes take place in the gas phase. [64] Kho et al. [73] found that the residence time in the flame (millisecond range) is insufficient to induce crystallization within the flame. They suggested that the degree of crystallization is a function of the filter temperature (cf. chapter 1.1.2). In the present work the temperature of the filter did not exceed 200 °C, which is insufficient for the formation of β-$Bi_2Mo_2O_9$ so that phase formation probably occurred in the flame. For FSP_Bi2Mo1 the presence of the high temperature form γ´-Bi_2MoO_6, which is stable at temperatures higher than 640 °C, was detected neither by PXRD nor by XAS.

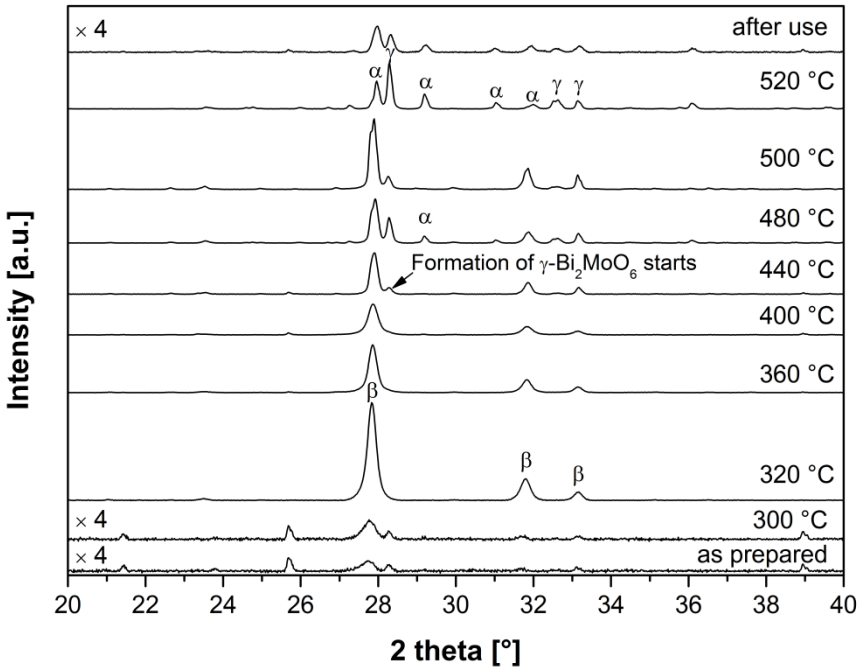

Figure 4.13: PXRD analysis of the stability of FSP_Bi1Mo1 after calcination at different temperatures. The formation of γ-Bi_2MoO_6 from β-$Bi_2Mo_2O_9$ sets in at 440 °C. At 480 °C and 500 °C α-, β- and γ- phase were present, whereas at 520 °C β-$Bi_2Mo_2O_9$ was below the detection limit.

As the β-phase is a metastable phase and thus raises questions about the true catalyst phase present in the reactor, the stability of the flame made material synthesized with Bi/Mo = 1:1 (FSP_Bi1Mo1) was analyzed. Fresh FSP_Bi1Mo1-samples were calcined at various temperatures for 4 h and after cooling down to room temperature they were analyzed by X-ray diffraction. Figure 4.13 displays the diffraction pattern of fresh, used and stepwise calcined FSP_Bi1Mo1. The formation of γ-Bi_2MoO_6 set in at 440 °C and is indicated by its characteristic reflection with the highest intensity at 28.3°. The decomposition into α-$Bi_2Mo_3O_{12}$ and γ-Bi_2MoO_6 was completed at 520 °C, when no more β-bismuth molybdate could be detected by X-ray diffraction. This suggested that at 360 °C, where the catalytic activity of the different samples was compared, FSP_Bi1Mo1 still consisted only of β-$Bi_2Mo_2O_9$.

The Bi/Mo ratios determined by ICP-OES and XPS are summarized in Table 4-3. For all three preparation methods the applied ratio corresponded to the bulk concentration actually present in the prepared catalyst. A loss of molybdenum, which was found by van Well et al. [124] during precipitation, could not be confirmed here, probably because higher pH values were applied in the present study. Comparison of the ICP-OES results with the

corresponding ratios calculated from XPS evidenced, that the samples containing γ-Bi_2MoO_6 exhibited an excess of bismuth on the surface. HT_Bi2Mo1 displayed the highest Bi excess, whereas heat treatment (e.g. calcination of the co-precipitated samples) or the use of a high temperature method like flame spray pyrolysis led to a reduced Bi/Mo ratio on the surface (Table 4-3). FSP_Bi1Mo1 composed of β-$Bi_2Mo_2O_9$ resulted in Bi/Mo = 1.1 which agrees well with the results reported for β-$Bi_2Mo_2O_9$ by Matsuura et al. [224] and Soares et al. [117].

4.3.3.2. Catalytic performance of differently synthesized bismuth molybdates

The catalytic performance of all materials during the selective oxidation of propylene to acrolein at 360 °C is summarized in Figure 4.14. Comparison of the samples synthesized with the ratio Bi/Mo = 2:1 (Figure 4.14a) evidenced that the samples HT_Bi2Mo1_HNO3 and CP_Bi2Mo1_450, both synthesized using nitric acid and consisting of pure γ-Bi_2MoO_6 showed the highest activity, whereas the co-precipitated sample was less selective than the hydrothermally synthesized sample. This difference in selectivity could be associated with the morphology, which was well defined for HT_Bi2Mo1_HNO3 but random for co-precipitated samples [117, 225]. Despite of a high surface area, the flame made sample of pure γ-Bi_2MoO_6 was less active than HT_Bi2Mo1_HNO3 and CP_Bi2Mo1_450. The samples synthesized under hydrothermal conditions with acetic acid, which partially led to the formation of α-$Bi_2Mo_3O_{12}$, showed relatively low activity in propylene oxidation and low selectivity for acrolein. In general the γ-phase was more active than the α-phase, which can be seen comparing Figure 4.14a and c.

Both samples calcined at 680 °C (CP_Bi2Mo1_680 and CP_Bi1Mo1_680) were inactive for propylene oxidation, due to the high temperature treatment and the very low surface area (< 1 m^2/g). As calcination at 550 °C strongly decreased the surface area and the activity of the prepared samples without affording β-$Bi_2Mo_2O_9$, prolonged calcination at higher temperatures would probably not exert a productive influence either. Whereas direct hydrothermal synthesis of β-$Bi_2Mo_2O_9$ without calcination was not possible, the obtained mixtures (HT_Bi1Mo1, HT_Bi1Mo1_HNO3, HT_Bi1Mo1_pH4, see Table 4-3) still exhibited relatively high activity at 360 °C.

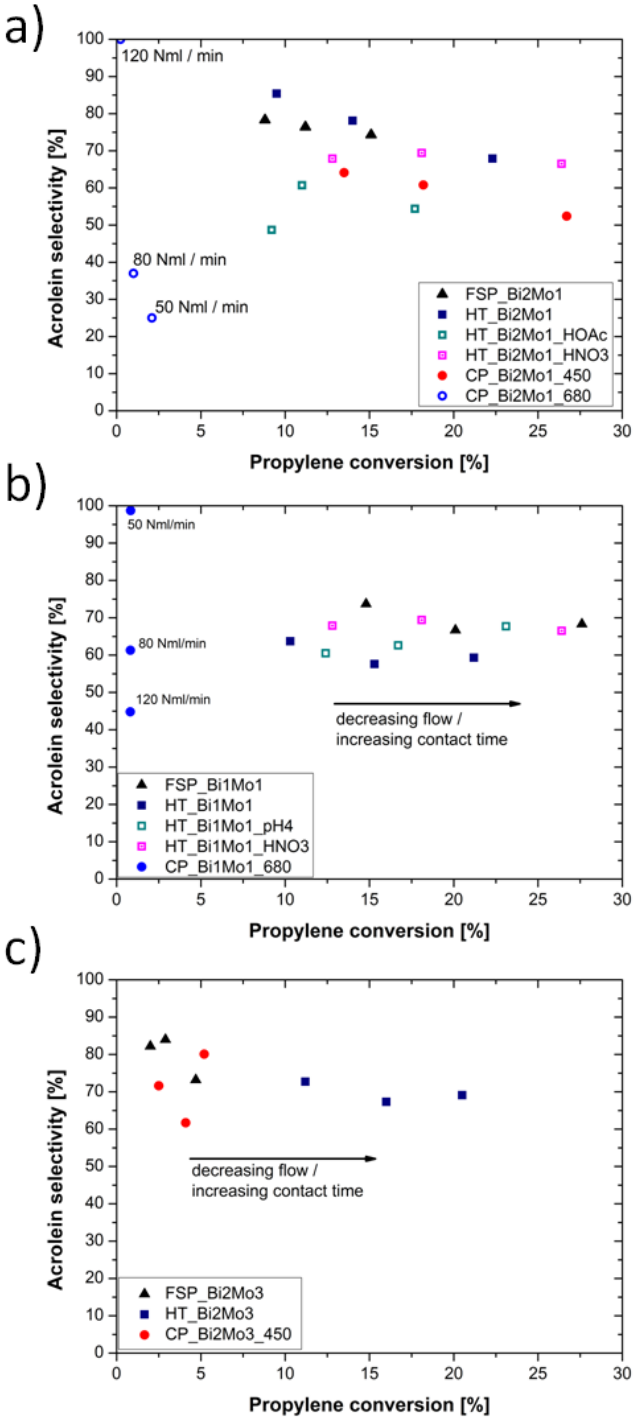

Figure 4.14: Catalytic performance of samples prepared by different methods with various Bi/Mo ratios (Bi/Mo = 2:1 (a), 1:1 (b) and 2:3 (c)) at 360 °C with $C_3H_6/O_2/N_2$ = 5/25/70 applying total flows of 50, 80 and 120 Nml/min. HT_Bi2Mo1_HNO3, HT_Bi1Mo1_HNO3 and FSP_Bi1Mo1 were comparably active and selective.

According to Table 4-3, where the maximum acrolein yield for each sample and the corresponding propylene conversion are summarized, HT_Bi1Mo1_pH4, HT_Bi1Mo1_HNO3 and HT_Bi2Mo1_HNO3, i.e. the samples synthesized under

hydrothermal conditions with nitric acid or ammonia, were the most active catalysts. One reason could be the incorporation of nitrogen in the catalyst, but the analysis of the nitrogen content of the samples HT_Bi2Mo1, HT_Bi2Mo1_HOAc and HT_Bi2Mo1_HNO3 resulted in 0.4 wt.%, 0.1 wt.% and 0.1 wt.% N and does not correlate with the catalytic performance. The highest nitrogen content was found for the sample synthesized in the absence of acid, probably due to the presence of a nitrate phase, which disappeared during calcination. HT_Bi2Mo1_HOAc, which is composed of γ-Bi_2MoO_6 and α-$Bi_2Mo_3O_{12}$, also contained nitrogen. This indicated that either the Mo or the Bi precursor or both acted as main nitrogen source instead of HNO_3 or NH_3. The increased activity of the samples synthesized with nitric acid could not be explained in terms of nitrogen incorporation. This agrees well with the results for α-MoO_3 reported in chapter 3.3.

Comparison of the samples HT_Bi2Mo1_HNO3 and HT_Bi1Mo1_HNO3 demonstrated that the catalytic performance of these two samples was identical at 360 °C although they showed different phase composition. A synergistic effect between the α- and the γ-phase could not be confirmed comparing HT_Bi1Mo1_HNO3 to HT_Bi2Mo1_HNO3, which only contained γ-Bi_2MoO_6. The flame made material with Bi/Mo = 1:1 which gave access to β-$Bi_2Mo_2O_9$ showed higher activity at 360 °C than the phase mixtures synthesized by hydrothermal synthesis (Figure 4.14b). FSP_Bi1Mo1 was also more active and led to a higher acrolein yield than FSP_Bi2Mo1 and FSP_Bi2Mo3 (Table 4-3). Comparison of the catalytic performance of the co-precipitated samples calcined at 450 °C showed that γ-Bi_2MoO_6 (CP_Bi2Mo1_450) converted more propylene and yielded more acrolein than α-$Bi_2Mo_3O_{12}$ (CP_Bi2Mo3_450). Generally, comparison of catalysts prepared under the same conditions shows that the activity decreased in the following order: β-$Bi_2Mo_2O_9$ > γ-Bi_2MoO_6 > α-$Bi_2Mo_3O_{12}$. However, a different order of activity has been suggested in preceding studies, namely: β-$Bi_2Mo_2O_9$ ≥ α-$Bi_2Mo_3O_{12}$ > γ-Bi_2MoO_6. [92, 115, 224, 226] Krenzke and Keulks [96] as well as Batist et al. [227] observed yet another trend (γ-Bi_2MoO_6 ≥ β-$Bi_2Mo_2O_9$ > α-$Bi_2Mo_3O_{12}$), confirming the α-phase as the least active phase. For FSP_Bi1Mo1 the acrolein yield did not exceed 30% at a propylene conversion of 37% at 450 °C, whereas HT_Bi1Mo1_HNO3 and HT_Bi1Mo1_pH4 enhanced propylene conversion up to 44% and 46%, respectively. The fact that FSP_Bi1Mo1 showed the highest propylene conversion of the tested samples at 360 °C suggested a deactivation of the flame made material due to decomposition of the β-phase.

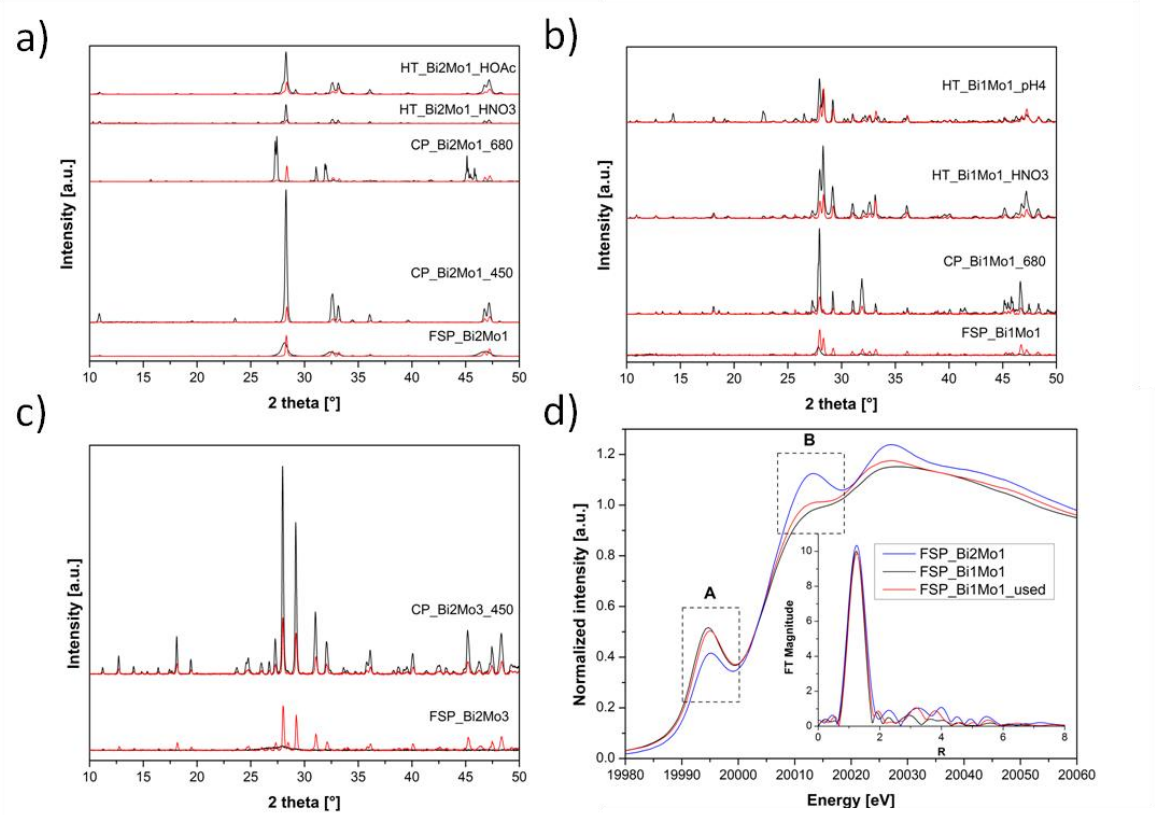

Figure 4.15: Comparison of the PXRD pattern before (black) and after (red) application in catalytic oxidation of propylene at temperatures from 320 °C to 520 °C with Bi/Mo = 2:1 (a) Bi/Mo = 1:1 (b) and Bi/Mo = 2:3 (c). Characterization of the flame made samples by X-ray absorption spectroscopy (d).

Characterization of the used samples by PXRD confirmed that the majority of the samples did not change their phase composition during the application in propylene oxidation at temperatures up to 520 °C (cf. Figure 4.15). One exception was CP_Bi2Mo1_680, which changed its phase composition from metastable γ”-Bi_2MoO_6 to a mixture of orthorhombic γ´-Bi_2MoO_6 and γ-Bi_2MoO_6. This transformation usually occurs between 550 and 640 °C. [31, 228] During phase transformation of β-$Bi_2Mo_2O_9$ in FSP_Bi1Mo1 into α-$Bi_2Mo_3O_{12}$ and γ-Bi_2MoO_6 the Bi/Mo ratio on the surface did not change and remained around 1.1 according to XPS measurements. Figure 4.15d shows XANES obtained after normalization of FSP_Bi2Mo1, which contained γ-Bi_2MoO_6 (i.e. octahedral Mo(VI)) resulting in a spectra with high intensity in region B but low intensity in region A. The spectrum for FSP_Bi1Mo1 is more dominant in the region A but the intensity is less in the region B, which is in well agreement with β-$Bi_2Mo_2O_9$, containing tetrahedral Mo(VI) species. The spectrum of the used sample (FSP_Bi1Mo1_used) lies in between, which fits well with the results obtained from the powder X-ray diffraction pattern suggesting the presence of a mixture of α- and γ-bismuth molybdate. This observation on FSP_Bi1Mo1 agrees well

with studies of Batist et al. [227] and Jung et al. [229], who reported that 55% of the co-precipitated β-$Bi_2Mo_2O_9$ was decomposed into α- and γ-bismuth molybdate after 24 h at 420 °C. The results in Table 4-3 suggest that the transformation occurred between 440 and 460 °C. However, calcination and analysis by X-ray diffraction discussed earlier (Figure 4.13) showed that the decomposition in air already starts at temperatures between 400 and 440 °C. Except for FSP_Bi1Mo1, CP_Bi2Mo1_680, HT_Bi2Mo1 and HT_Bi2Mo3 all other samples were stable during the activity measurements up to 520 °C.

4.3.4. Hydrothermally synthesized bismuth molybdates at various pH values

The samples synthesized with Bi/Mo = 1:1 and addition of nitric acid or ammonia solution exhibited high catalytic activity in selective oxidation of propylene, although the formation of β-$Bi_2Mo_2O_9$ was not observed. Bismuth molybdates with relatively high surface areas could be prepared by hydrothermal synthesis using nitric acid and ammonia solution by variation of the pH value. [34] High surface areas in combination with the application of nitric acid and ammonia may result in improved catalytic activity. Therefore bismuth molybdates were synthesized with Bi/Mo = 1:1 varying the pH value from 1 to 9.

4.3.4.1. Characterization of the samples synthesized with Bi/Mo = 1:1

The X-ray diffraction pattern and Raman spectra of the samples synthesized with Bi/Mo = 1:1 at pH = 1 – 9 in Figure 4.16 show the effects of the pH on the structure under hydrothermal conditions. At high pH values (pH ≥ 6) γ-Bi_2MoO_6 was formed, which is indicated by the reflections at 2θ = 28.3, 32.6, 33.1, 36.1, 46.7, 47.2° in the PXRD pattern (Figure 4.16a; JCPDS card no. 77-1246). The corresponding Raman spectra showed bands at 848 cm^{-1} and 807 cm^{-1} as well as at 719 cm^{-1} which were ascribed to γ-bismuth molybdate. [34, 214] Analysis of the bismuth and molybdenum concentration of the products by ICP-OES led to a Bi/Mo bulk ratio of 1.8 – 2.1 for pH = 6 – 9 (Table 4-4) suggesting that molybdenum partly remained in solution and did not completely precipitate at high pH values. At pH > 6 the molybdenum anion assumed to be present in solution is $(MoO_4)^{2-}$. [35] In weakly acidic or basic aqueous solutions bismuth nitrate is "hydrolyzed" resulting in the formation of BiO^+. [230] These bismuthyl subunits react with $(MoO_4)^{2-}$ and precipitate as γ-Bi_2MoO_6. [34, 231]

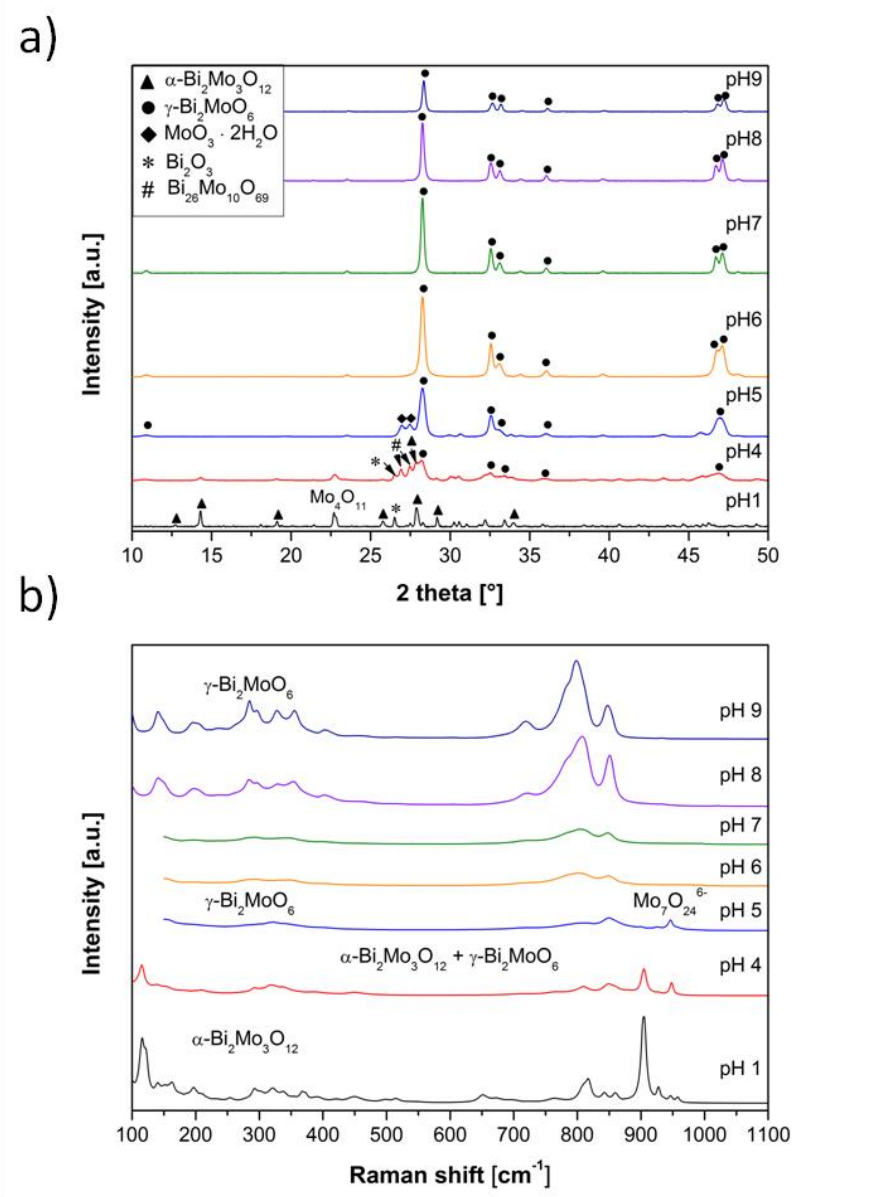

Figure 4.16: PXRD pattern (a) and Raman spectra (b) of the samples synthesized with ratio Bi/Mo = 1:1 at different pH values.

With decreasing pH value additionally to the γ-phase a bismuth free molybdenum oxide phase was formed at pH = 5 indicated by the reflections at 26.9 and 27.5°, which could be assigned to $MoO_3 \cdot 2H_2O$ (JCPDS no. 39-363), and by the Raman band at 947 cm^{-1} pointing out the presence of $Mo_7O_{24}^{6-}$. At pH = 3 – 6 the stable polymolybdate species in aqueous solution is $Mo_7O_{24}^{6-}$ [14, 35] which agrees well with the Raman spectrum for the sample synthesized at pH = 5. Bi1Mo1_pH5 exhibited a Bi/Mo ratio of 1.1, which equaled the applied ratio (see Table 4-4) and α-$Bi_2Mo_3O_{12}$ could not be detected by X-ray diffraction (main reflection at 27.9°) or Raman spectroscopy (main band at 904 cm^{-1}).

Table 4-4: Characterization of samples prepared by hydrothermal synthesis with different Bi/Mo ratios and at various pH values by X-ray diffraction measurements and Raman spectroscopy as well as nitrogen physisorption measurements (BET), ICP-OES and XPS.

Sample	Phases according to PXRD	Phases according to Raman	Surface area (BET)	Bi/Mo ratio bulk[a]	Bi/Mo ratio surface[b]
initial ratio Bi/Mo = 2:1					
Bi2Mo1_pH7	γ-Bi_2MoO_6		13		
Bi2Mo1_pH8	γ-Bi_2MoO_6		7		
initial ratio Bi/Mo = 1:1					
Bi1Mo1_pH1	α-$Bi_2Mo_3O_{12}$, Mo_4O_{11}, Bi_2O_3	α-$Bi_2Mo_3O_{12}$	3	1.0	
Bi1Mo1_pH4	γ-Bi_2MoO_6, α-$Bi_2Mo_3O_{12}$, Bi_2O_3,	α-$Bi_2Mo_3O_{12}$, γ-Bi_2MoO_6, β-	18	0.9	1.1
Bi1Mo1_pH5	γ-Bi_2MoO_6, $MoO_3 \cdot 2H_2O$	γ-Bi_2MoO_6, $Mo_7O_{24}^{6-}$ or $MoO_3(H_2O)_2$	32	1.1	1.1
Bi1Mo1_pH6	γ-Bi_2MoO_6	γ-Bi_2MoO_6	26	1.8	1.7
Bi1Mo1_pH7	γ-Bi_2MoO_6	γ-Bi_2MoO_6	17	1.8	1.8
Bi1Mo1_pH8	γ-Bi_2MoO_6	γ-Bi_2MoO_6	10	1.9	2.5
Bi1Mo1_pH9	γ-Bi_2MoO_6	γ-Bi_2MoO_6	4	2.1	
initial ratio Bi/Mo = 2:3					
Bi2Mo3_pH1	α-$Bi_2Mo_3O_{12}$, $H_{0.68}(NH_4)_2$	α-$Bi_2Mo_3O_{12}$	5		
Bi2Mo3_pH4	γ-Bi_2MoO_6, $MoO_3 \cdot 2H_2O$, $Bi_5O_7NO_3$	γ-Bi_2MoO_6, $Mo_7O_{24}^{6-}$ or $MoO_3(H_2O)_2$, NO_3^-	17		
Bi2Mo3_pH9	γ-Bi_2MoO_6	γ-Bi_2MoO_6	5		

a: The calculated error accounts to around 10%.

b: Average of two XPS measurements at different spots.

The formation of the α-phase was observed at pH ≤ 4 and additionally to α- and γ-bismuth molybdate minor contributions of other phases were detected. Further decrease in pH to 1 led to the disappearance of γ-Bi_2MoO_6 in the product and α-$Bi_2Mo_3O_{12}$ was the main phase found in the X-ray diffraction pattern (Figure 4.16a). Additionally to the reflections at

14.1, 18.1, 25.9, 27.9 and 29.2° assigned to α-$Bi_2Mo_3O_{12}$ (JCPDS no. 21-103) two reflections at 22.7° and 26.5° were observed in the diffraction pattern of the sample synthesized at pH = 1. The reflection at 22.7° could be assigned to Mo_4O_{11} (JCPDS no. 86-1269), whereas the correlation of the reflection at 26.5° was not possible. The corresponding Raman spectra (Figure 4.16b) showed the characteristic bands of α-$Bi_2Mo_3O_{12}$ (928, 904, 861, 843 and 817 cm^{-1}). For all samples synthesized with a Bi/Mo ratio 1:1 β-$Bi_2Mo_2O_9$ was detected neither by X-ray diffraction (27.8°) nor Raman spectroscopy (884 cm^{-1}), which agrees with literature [8, 34] where calcination at 560 °C was required to form the β-phase. The samples synthesized at pH = 1 - 5 contained bismuth and molybdenum in the ratio 1:1 in the bulk (Table 4-4), corresponding to the initially applied ratio.

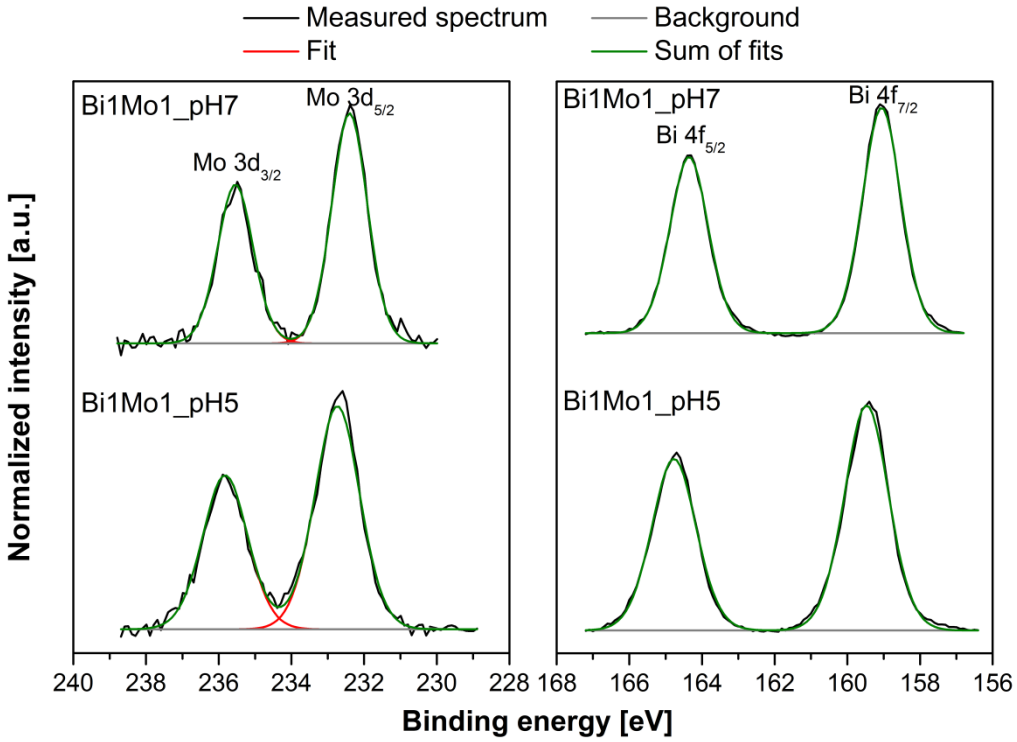

Figure 4.17: XP spectra of Bi1Mo1_pH7 and Bi1Mo1_pH5 with the corresponding Voigt fits around the Mo 3d and Bi 4f region. For a better visualization all spectra are normalized to maximum intensity.

In addition to the characterization of the phase composition and the resulting Bi/Mo ratio in the bulk, the specific surface area and the Bi/Mo ratio on the surface of the products were determined (see Table 4-4). The surface composition of the catalyst was calculated using the peak areas of Mo $3d_{5/2}$ = 232.7 eV and Bi $4f_{7/2}$ = 159.4 eV in the XPS (representative spectra see Figure 4.17). At pH = 4 - 7 the Bi/Mo ratio on the surface

equaled the ratio in the bulk (Bi/Mo ≈ 1 for pH = 4 and 5, Bi/Mo ≈ 2 for pH = 6 and 7), whereas at pH = 8 a surface enrichment of bismuth (Bi/Mo = 2.5) was detected by XPS. High Bi/Mo surface ratios were also reported in the literature for γ-Bi_2MoO_6 prepared by different methods (spray dried: 2.4 [121], co-precipitated: 2.6 [98, 219]) and for the samples synthesized by hydrothermal synthesis and co-precipitation in chapter 4.3.3 (Bi/Mo = 2.3 - 3.0). The presence of surface Bi_2O_3 was not found neither in literature nor in the present work. The sample synthesized at pH = 5 featured the highest specific surface area (32 m²/g), whereas with increasing and decreasing pH value the surface area of the resulting product was reduced (Table 4-4) to 4 m²/g and 3 m²/g for pH = 9 and pH = 1, respectively. The product composition does not seem to be a determining factor for the specific surface area, as the two samples with the highest surface area showed different phases resulting in a different Bi/Mo ratio in the bulk and on the surface (Bi/Mo =1.1 for pH = 5 with 32 m²/g and Bi/Mo =1.8 for pH = 6 with 26 m²/g).

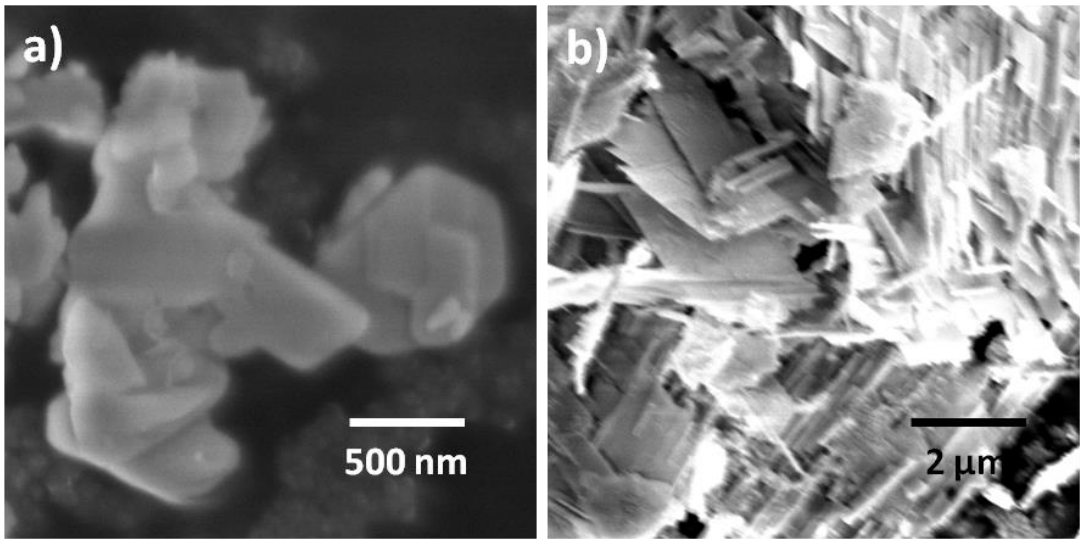

Figure 4.18: SEM images of the products obtained from hydrothermal synthesis with Bi/Mo = 1:1 at pH = 1 (a) and pH = 4 (b).

SEM images of the samples prepared at pH = 1 and pH = 4 are shown in Figure 4.18. The sample synthesized at lower pH value (pH = 1) evidenced a plate-like morphology (400 - 650 nm x 700 – 800 nm) with defined steps on the surface (Figure 4.18a). At pH = 4 sheets are seen in the image (Figure 4.18b), which agrees well with the particles prepared by Li et al. [34], although the particle size of their samples is smaller than the particles obtained here (700 nm x 2 µm). Accordingly, the surface areas obtained for our samples in the present

work were lower (compare Table 4-4 with 39 m²/g for α-$Bi_2Mo_3O_{12}$ and 58 m²/g for γ-Bi_2MoO_6).

4.3.4.2. Influence of the pH at lower and higher Bi/Mo ratio

To elucidate the influence of the applied Bi/Mo ratio on the phases the amount of molybdenum was increased to Bi/Mo = 2:3. At pH = 9 only γ-Bi_2MoO_6 with a high crystallinity was formed as proven by X-ray diffraction (Figure 4.19a) and Raman spectroscopy (Figure 4.19b). This indicated that also at low Bi/Mo ratio (i.e. with an excess of molybdenum) bismuth-rich γ-Bi_2MoO_6 was formed at high pH values, which agrees with the results of Li et al. [34]. The specific surface areas of the two samples synthesized at pH = 9 (Bi1Mo1_pH9 and Bi2Mo3_pH9) were similar (4 m²/g and 5 m²/g). Decreasing the pH to 4 led to the same phase composition as in sample Bi1Mo1_pH4 (γ-Bi_2MoO_6 and $MoO_3 \cdot 2H_2O$), but additionally a nitrate containing phase was found as indicated by the Raman band at 1047 cm^{-1} (Figure 4.19b). The reflections in the X-ray diffraction pattern (Figure 4.19a) at 27.6°, 30.7° and 45.7° could be assigned to $Bi_5O_7NO_3$ (JCPDS no. 51-525). Further decrease of the pH to 1 did not result in the formation of pure α-$Bi_2Mo_3O_{12}$, but additionally an ammonium containing molybdenum oxide phase was formed (see Figure 4.19 and Table 4-4). The applied pH value and therefore the different (poly)molybdate anions in the aqueous solution seems to have a stronger impact on the resulting phase than the applied Bi/Mo ratio. For all three samples synthesized with Bi/Mo = 2:3 the surface area determined by nitrogen physisorption was identical to the samples synthesized with Bi/Mo = 1:1 at the same pH value (Table 4-4).

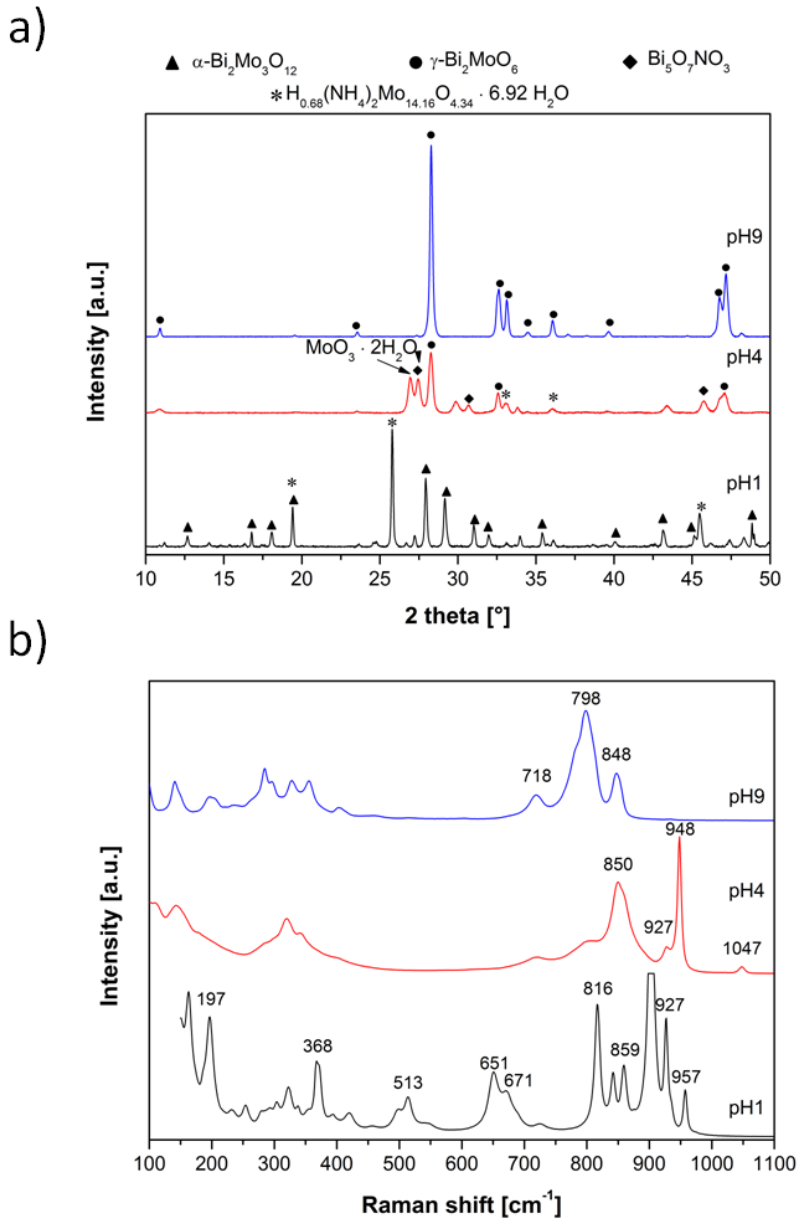

Figure 4.19: PXRD patterns (a) and Raman spectra (b) of the samples with ratio Bi/Mo = 2:3 at different pH values.

Using an excess of bismuth and applying the initial ratio Bi/Mo = 2:1 at pH = 7 and pH = 8 led to the formation of highly crystalline γ-Bi_2MoO_6 (see PXRD pattern in Figure 4.20). Li et al. [34] and Zhang et al. [28] already reported that hydrothermal synthesis with Bi/Mo = 2:1 always resulted in γ-Bi_2MoO_6 independent of the pH value (pH = 1 – 13).

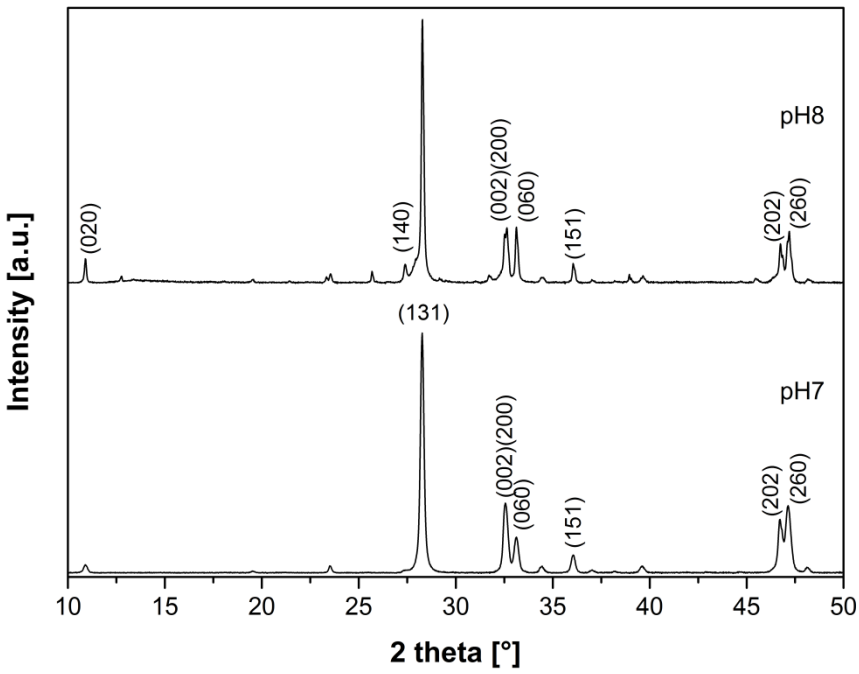

Figure 4.20: PXRD pattern of γ-Bi_2MoO_6 prepared with Bi/Mo = 2:1 at pH = 7 and 8.

4.3.4.3. Catalytic performance in propylene oxidation to acrolein

The samples synthesized with Bi/Mo = 1:1 were tested in propylene oxidation at 320 – 520 °C to study the influence of the preparation parameters such as the pH value and the corresponding structural properties on the catalytic performance of the hydrothermally synthesized bismuth molybdates. Figure 4.21 depicts the acrolein selectivity as a function of the propylene conversion at three different flows (50, 80 and 120 Nml/min) leading to different catalyst contact times and therefore to a different propylene conversion and / or acrolein selectivity. At 320 °C (Figure 4.21a) the sample synthesized at pH = 6 showed the highest propylene conversion (19 and 31% propylene conversion, 73 and 79% acrolein selectivity for 120 Nml/min and 50 Nml/min respectively), followed by the samples synthesized at pH = 7 (27% $X_{propylene}$ and 73% $S_{acrolein}$ for 50 Nml/min) and pH = 8 (25% $X_{propylene}$ and 60% $S_{acrolein}$ for 50 Nml/min). The samples synthesized at pH = 4 and pH = 5, which additionally to γ-Bi_2MoO_6 contained minor phases, converted less propylene (6-16% $X_{propylene}$ and 10-21% $X_{propylene}$ respectively).

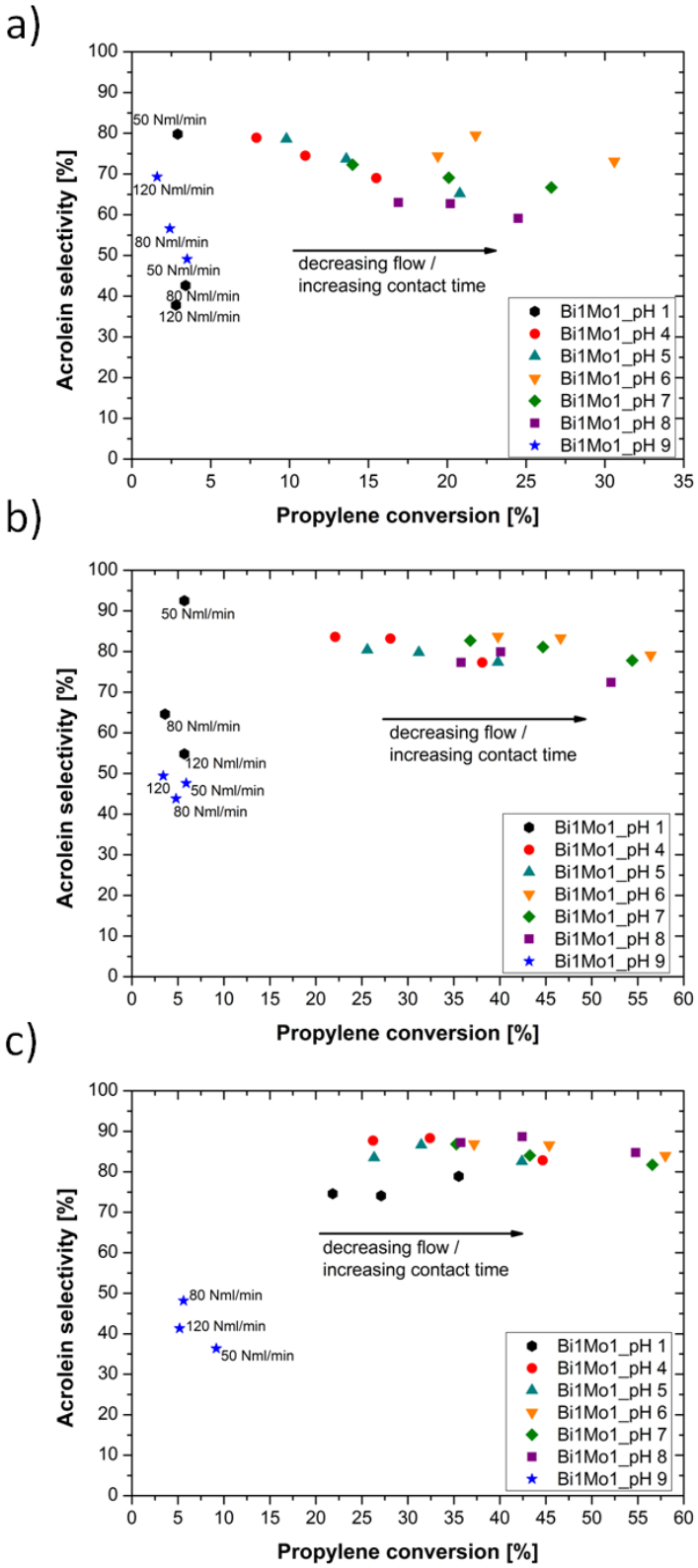

Figure 4.21: Catalytic performance of samples prepared with Bi/Mo = 1:1 at 320 °C (a), 360 °C (b) and 400 °C (c). The samples were dried in air at room temperature, crushed and sieved and pre-treated in the reactor in synthetic air at 300 °C. Reaction conditions: 500 mg catalyst; $C_3H_6/O_2/N_2$ = 5/25/70; 50, 80 and 120 Nml/min.

This indicates that the samples which contained only γ-Bi_2MoO_6 were more active than the other samples. However, the sample synthesized at pH = 9 also composed of γ-Bi_2MoO_6 but with smaller surface area reached propylene conversions of only 2-4% at acrolein selectivities of 70-50%. The sample synthesized at pH = 1 exhibiting small surface area (3 m^2/g) was also nearly inactive, where the propylene conversion remained around 3% for 120 – 50 Nml/min total flow, but acrolein selectivity strongly decreased from 80% to 40% with increasing flow. The main by-products were CO_2 (selectivities around 10-20%), acetaldehyde (7-8%) and CO (1-5%). Ethylene and hexadiene were only detected in very small amounts for sample Bi1Mo1_pH9 at temperatures above 440 °C.

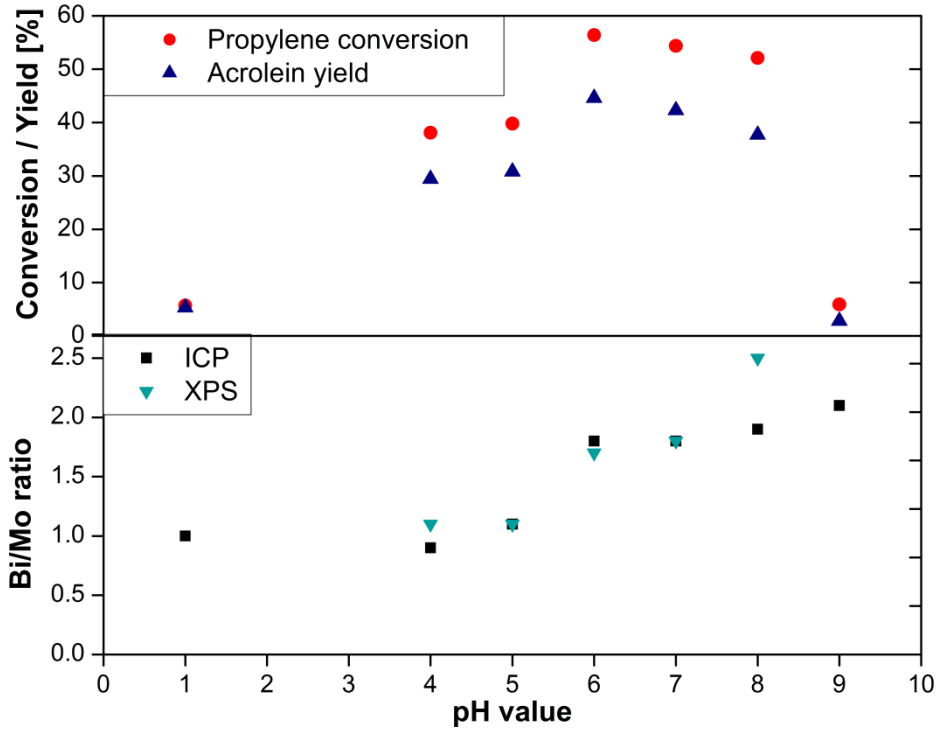

Figure 4.22: Correlation between the pH value in the initial solution, the Bi/Mo ratio determined in the bulk and on the surface and the catalytic performance at 360 °C using a flow of 50 Nml/min with a composition of $C_3H_6/O_2/N_2$ = 5/25/70.

At 360 °C the difference in activity between the various samples decreased, but the samples synthesized at pH = 6 and pH = 7 still showed the best catalytic performance (propylene conversion of 40-56% and 37-54% respectively) followed by the sample at pH = 8, which was slightly less selective (acrolein selectivity of 72-79% compared to 79-83%). In general all the samples synthesized at pH = 4 – 8 yielded relatively high propylene conversion compared to the hydrothermally synthesized samples presented in section 4.3.1 and 4.3.3 (cf. Figure 4.14 and Figure 4.21b) along with acrolein selectivities

of 70–85%. In Figure 4.22 the propylene conversion as well as the acrolein yield measured at 360 °C was correlated to the pH values during hydrothermal synthesis. Propylene conversion and acrolein yield showed volcano-like curves with respect to pH with a maximum at pH = 6. The samples at pH = 6 and pH = 7 featured a Bi/Mo ratio of ca. 2 both in the bulk and on the surface (Figure 4.22) and Bi1Mo1_pH6 additionally exhibited a relatively large surface area (26 m²/g, Table 4-4). Comparison of Table 4-4 with Figure 4.22 evidenced that a combination of the right bismuth molybdate phase (γ-Bi_2MoO_6) and a high surface area are important for high propylene conversion. The sample synthesized at pH = 8 showing a smaller surface area (10 m²/g) and bismuth excess on the surface led to lower acrolein selectivity at 360 °C (Figure 4.21b). Also at 360 °C propylene conversion of the bismuth molybdates prepared at pH = 1 and pH = 9 did not exceed 6%. The sample synthesized at pH = 9 showed low propylene conversion at 400 °C (5-9%) at acrolein selectivities below 50% and CO_2 selectivities of around 50% (Figure 4.21c), whereas the catalytic performance of the sample synthesized at pH = 1 increased strongly to propylene conversions of 22-35% at acrolein selectivities of 75-80%. For all the other samples the catalytic performance in propylene oxidation was only slightly increased when the temperature changed from 360 °C to 400 °C. The three samples synthesized at pH = 6 – 8 still exhibited the highest propylene conversion (35-58%) of the tested samples at acrolein selectivities up to 92% and acrolein yields of 46-49% at 400 °C. The sample synthesized at pH = 8, which was slightly less selective at 360 °C, gave the same acrolein selectivity as the samples synthesized at pH = 6 – 7 at 400 °C (Figure 4.21c). A further increase in process temperature above 400 °C did not result in an improvement of the catalytic activity (cf. Figure 4.23), where propylene conversion and acrolein selectivities are displayed for process temperatures from 320 °C to 520 °C using the samples synthesized at pH = 5 (highest surface area) and pH = 6 (highest activity) as representative examples. An increase in temperature from 320 °C to 400 °C resulted in a better catalytic performance, whereas the activity at 440 °C was very similar to the one at 400 °C. At temperatures higher than 440 °C the catalytic activity started to decrease and at 520 °C propylene conversion was similar to the values at 320 °C but with higher acrolein selectivities. The decrease in activity at temperatures higher than 440 °C was probably caused by a decrease in surface area for all samples. After application in propylene oxidation at 320 - 520 °C the surface area of all used samples was ≤ 1 m²/g, whereas after 8 h of calcination at 360°C the samples synthesized at pH = 5 and pH = 6 still exhibited surface areas of 15 m²/g and 16

m^2/g, respectively. The decrease in surface area already started at 360 °C but the decrease was more significant between 400 and 440 °C when catalyst deactivation started. Figure 4.24 shows the X-ray diffraction pattern of the samples after their application in the selective oxidation of propylene at 320 – 520 °C. According to PXRD the phase composition of the samples synthesized at pH = 6 – 9 (γ-Bi_2MoO_6) did not change during the catalytic activity tests, but the hydrothermally prepared materials synthesized at pH = 1 – 5 were all composed of a mixture of α-$Bi_2Mo_3O_{12}$ and γ-Bi_2MoO_6 after use. This indicates that rather the reduced surface area instead of the phase change was the reason for the decreasing propylene conversion at temperatures above 440 °C. Consequently a combination of the desired phase and a high surface area seemed to be crucial for propylene oxidation.

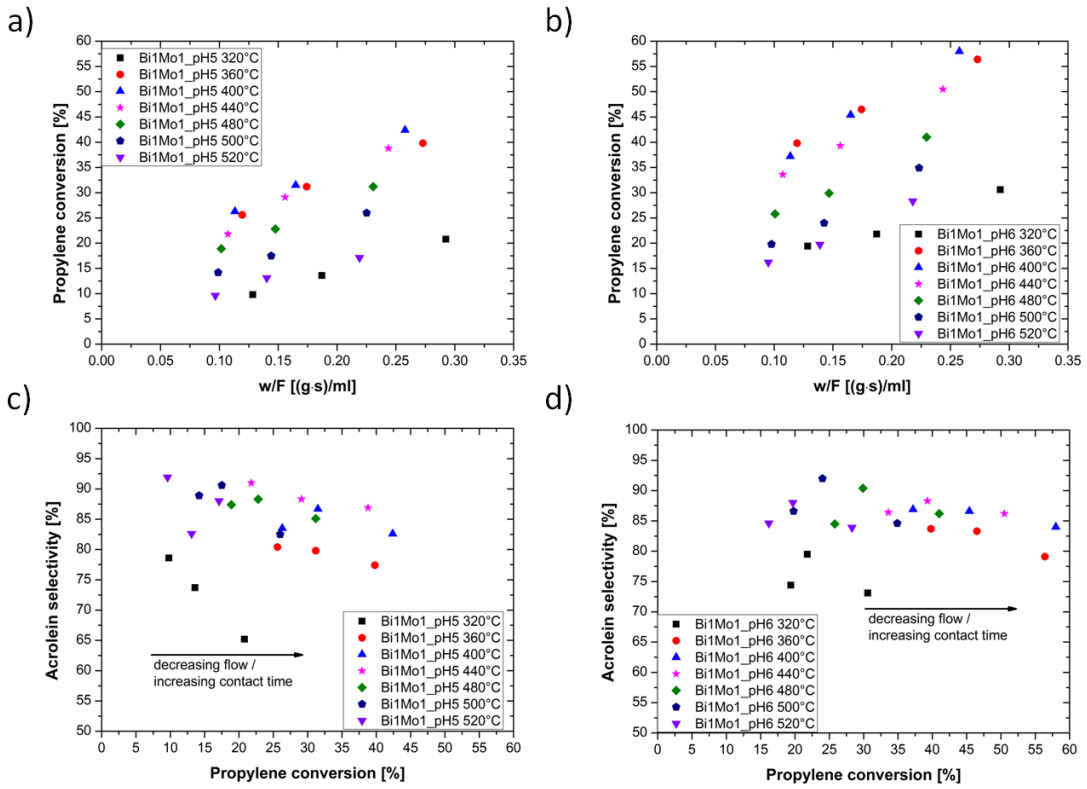

Figure 4.23: Catalytic performance of the high surface area sample synthesized at pH = 5 (a, c) and the highly active sample synthesized at pH = 6 (b, d) at various temperatures between 320 °C and 520 °C at 50, 80 and 120 Nml/min and with $C_3H_6/O_2/N_2$ = 5/25/70.

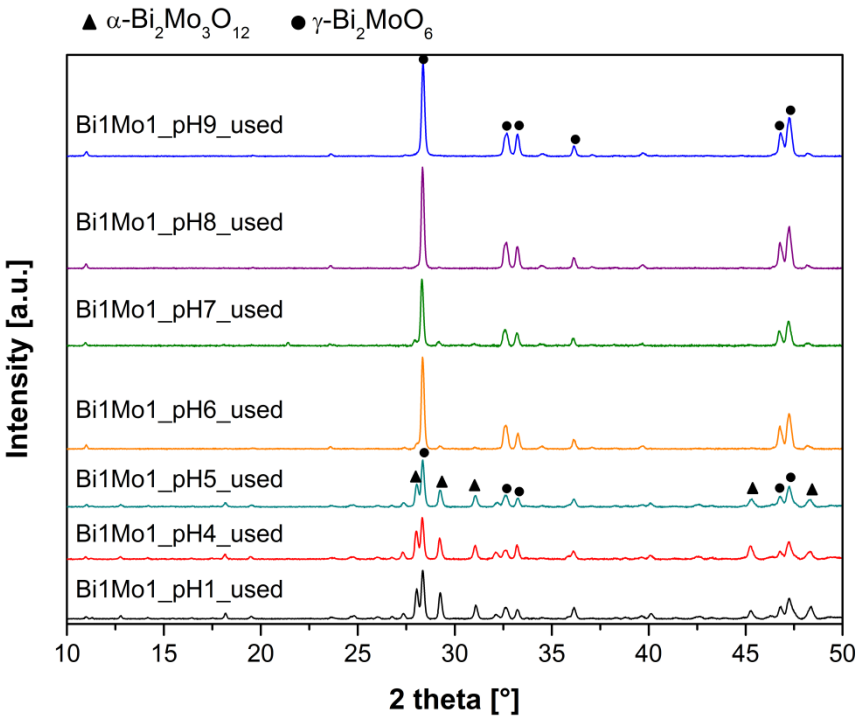

Figure 4.24: PXRD patterns of the samples synthesized with Bi/Mo = 1:1 at different pH values after application in catalytic oxidation of propylene at temperatures up to 520 °C.

Jung et al. [232] tested the influence of the pH value during co-precipitation of γ-Bi_2MoO_6 (initial ratio Bi/Mo = 2:1) on the oxidative dehydrogenation of n-butene and discovered that the sample synthesized at pH = 3 showed both the highest butene conversion and 1,3-butadiene yield due to a high oxygen mobility of this sample. According to the group of Keulks [96, 113] re-oxidation of the catalyst is the rate-determining step at temperatures below 400 °C whereas abstraction of an α-hydrogen atom to form an allylic intermediate is the rate determining step at higher temperatures (> 400 °C). This could be confirmed by testing HT_Bi2Mo1_HNO3 (contains γ-Bi_2MoO_6) and changing the oxygen concentration from C_3H_6/O_2 = 1:5 to C_3H_6/O_2 = 1:1 (see Figure 4.25). At T ≥ 440 °C propylene conversion as well as acrolein selectivity is independent of the O_2 concentration, whereas at 400 °C a higher oxygen concentration slightly improved the acrolein selectivity but not the propylene conversion. The hydrothermally synthesized samples at pH = 4 – 8 exhibited high propylene conversion and also relatively high acrolein selectivities already at 360 °C. Therefore, oxygen mobility is considered not to be the decisive factor for the varying catalytic performance of the different samples depicted in Figure 4.21. The oxygen concentration used for the catalytic activity tests in this study was relatively high (C_3H_6/O_2 = 1:5) to guarantee a complete re-oxidation of the bismuth molybdate catalysts.

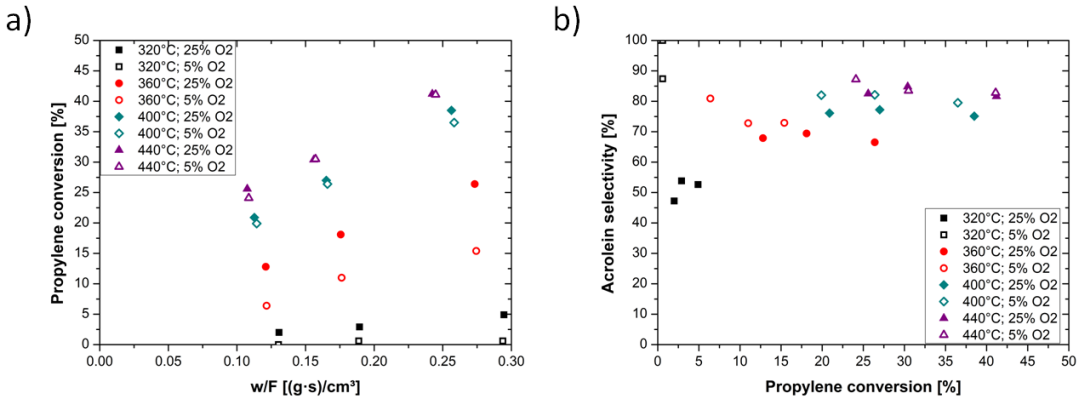

Figure 4.25: Influence of the oxygen concentration during propylene oxidation at different temperatures representative for sample HT_Bi2Mo1_HNO3 (cf. 4.3.3.1).

Aleshina et al. [120] prepared bismuth molybdates by co-precipitation with Bi/Mo = 2 at pH values between 0 and 7 and with surface areas of 1 – 3 m²/g and tested them in propylene oxidation in the presence of steam. They detected Bi_2O_3 in the sample prepared at pH = 7 and claimed that with increasing pH value molybdenum dissolved and remained in solution leading to a bismuth rich product (mixture of Bi_2O_3 and γ-Bi_2MoO_6), which showed lower propylene conversion (73% compared to 86%) and very low acrolein selectivity compared to the sample containing only γ-Bi_2MoO_6. In contrast to that in the present work, Bi_2O_3 was not detected in the samples containing mainly γ-Bi_2MoO_6 neither by PXRD nor by Raman spectroscopy and also the formation of hexadiene during propylene conversion was hardly observed, although in the literature it was reported that hexadiene is formed in the presence of Bi_2O_3 [102, 216]. Thus, the reason for the low activity of Bi1Mo1_pH9 and the lower selectivity of Bi1Mo1_pH8 is not contamination of the product with bismuth oxide but rather the lower surface area compared to the samples synthesized at pH values of 6 and 7.

4.4. Conclusions

The catalytic performance of bismuth molybdates strongly depends on the crystalline phases present in the catalysts, their specific surface areas and their morphologies which emerge from the selected synthetic method. During hydrothermal synthesis application of a high Bi/Mo ratio led mainly to the formation of γ-Bi_2MoO_6, while applying a Bi/Mo ratio < 1 resulted in α-$Bi_2Mo_3O_{12}$ as the main phase. A mixture of α- and γ-phase was obtained

with precursor ratios of Bi/Mo = 1:1. As hydrothermal synthesis did not provide access to the one-step formation of β-$Bi_2Mo_2O_9$ under the parameters applied in the present study, the materials synthesized in pure water were furthermore calcined at 550 °C. Even these harsh conditions resulted only in partial formation of the β-phase, and the process can probably be driven to completion only at the expense of considerable loss of surface area and catalytic performance. Generally, the plate-like morphology of the as-prepared hydrothermal samples could only partly be retained during calcination. Applying Bi/Mo in the ratio 1:1 along with variation of the pH value from 1 to 9 gave access to bismuth molybdates with a relatively large surface area (at pH = 4 – 7) compared to unsupported bismuth molybdates reported in the literature (1 – 4 m^2/g), which was beneficial for the catalytic activity in selective oxidation of propylene under the applied conditions. At high pH values γ-Bi_2MoO_6 was formed and the Bi/Mo ratio in the product was 2, indicating that molybdenum partly stayed in solution in the form of $[MoO_4]^{2-}$ and did not precipitate. With decreasing pH values the amount of α-$Bi_2Mo_3O_{12}$ in the product increased additionally to the presence of bismuth free and molybdenum free phases. At pH values below 6 the products obtained a ratio of Bi/Mo = 1, which equaled the applied Bi/Mo ratio. The samples synthesized at pH = 6 – 7, which according to PXRD and Raman spectroscopy contained only γ-Bi_2MoO_6 and which exhibited high specific surface areas, yielded high propylene conversion at high acrolein selectivities.

The catalytic activity of the freshly hydrothermally prepared catalysts was significantly higher than after their calcination at 550 °C. Furthermore, the obtained acrolein yield decreased regardless of the phase composition. Generally, for the investigation of the relative activities of the different bismuth molybdate phases, catalysts should be prepared under the same conditions including pre-conditioning of the precursor materials. Therefore we used as-prepared materials or applied the same thermal treatment to compare the catalytic performance of the different bismuth molybdate phases.

Strikingly, one-step flame spray pyrolysis for Bi/Mo = 1:1 resulted in the formation of pure β-$Bi_2Mo_2O_9$. This catalyst was stable at temperatures up to 400 °C and exhibited good activity and selectivity. This selective one-step synthetic access to the Bi-Mo-oxide system nicely illustrates the great potential of flame spray pyrolysis for catalyst synthesis. At temperatures above 400 °C decomposition into α-$Bi_2Mo_3O_{12}$ and γ-Bi_2MoO_6 started,

leading to deactivation of the catalyst. The activity of the different bismuth molybdate phases prepared by flame spray pyrolysis decreased in the following order: $\beta > \gamma > \alpha$.

Although the β-phase was not observed during hydrothermal synthesis under the parameters applied in the present study, highly active catalysts could be prepared under hydrothermal conditions applying initial Bi/Mo ratios of 1:1 or 2:1 with nitric acid or ammonia as additives. The hydrothermally synthesized samples containing mainly α- or γ-bismuth molybdate were more active than the according flame made materials, whereas direct synthesis of β-$Bi_2Mo_2O_9$ under hydrothermal conditions without further calcination still remains a challenge and may require much higher temperatures during synthesis. An increase in process temperature between 320 °C and 400 °C resulted in improved catalytic performance (propylene conversion and acrolein selectivity), whereas at temperatures above 440 °C the catalyst started to deactivate probably due to a reduction in surface area. Hydrothermally synthesized bismuth molybdates with high surface area showed high potential in the selective oxidation of propylene, but stabilization of the surface area during catalytic tests especially at higher temperatures remains a key issue. Therefore, the incorporation of further elements, which are also included in industrial multicomponent bismuth molybdates e.g. Co, Fe or V, during hydrothermal synthesis, could be beneficial for the stability of the prepared catalysts relating their surface area and the overall catalytic performance.

5 Cobalt molybdates as hydrotreating catalysts

5.1. Introduction

Mo-oxide based materials synthesized by novel preparation routes such as hydrothermal synthesis or flame spray pyrolysis are not only attractive in selective oxidation reactions which was the topic of chapter 3 and 4 but also in other areas e.g. hydrotreating. The preparation method for hydrotreating catalysts based on Co-Mo or Ni-Mo strongly influence their catalytic performance. [140] Alternative preparation methods such as chemical vapor deposition (CVD) was applied to synthesize designed catalysts and to understand the nature of the support and the active site. [233] A lot of research effort was spent to understand the nature of the active sites in sulfided hydrotreating catalysts, due to the need to improve industrial hydrodesulfurization (HDS) catalysts (see also 1.2.2). Bulk MoS_2 has a layered structure in which S-Mo-S layers so called slabs are stacked on top of each other. Based on studies of structural-reactivity relationships, the catalytic activity was associated with the edges of these MoS_2 nanoclusters. The promoter atoms (e.g. Co) decorate the edges of MoS_2 and form the CoMoS phase. An increase in edge atoms leads to higher HDS activity. Therefore a higher number of edge and corner sites due to small slabs are beneficial for hydrotreating activity. [142] In the past, it has been suggested that coordinative unsaturated sites (CUS) are created in a reaction with hydrogen at the MoS_2 edges and that these sulfur vacancies have a high affinity to form bonds with the hetero-atoms in the organic molecules. Incorporation of transition metal atoms leads to a lower metal-sulfur binding energy and thereby provides more active sites. [234-236] The dispersion and the degree of stacking were considered to be important in the activity and selectivity of hydrodesulfurization. According to the “rim-edge” model the top and the bottom of the stacked MoS_2 crystallites can perform hydrogenation and C-S cleavage whereas the edges

in the intermediate slabs are only active in direct desulfurization. [237] Scanning tunneling microscopy (STM) of MoS_2 supported on Au(111) revealed the presence of the so called "brim" sites at the edges of the MoS_2 clusters having metallic character [162-163] and in combination with DFT calculation it was demonstrated that these sites can adsorb thiophene [168, 238]. Addition of cobalt changes the shape of the MoS_2 slabs from triangular to hexagonal. [166]

Unsupported molybdenum sulfide catalysts have often been used as model catalysts for hydrotreating reactions to exclude the influence of a support effect on the activity and to study the nature of the catalytic function in the sulfide systems. [239-241] These model systems were mainly prepared by homogeneous sulfide precipitation (HSP) [161, 242-243] and impregnated-thiosalt decomposition (ITD) [240-241, 244] but also hydrothermal synthesis starting from sulfur containing molybdenum precursors e.g. ammonium tetrathiomolybdate (ATTM) was applied [23-24, 245]. The preparation methods strongly influenced the catalytic properties of bulk sulfides. [23, 244] Hydrothermal synthesis of MoS_2 from ATTM led to the formation of needle like MoS_2 and this morphological difference compared to the samples obtained from thermal decomposition of the same precursor influenced the ratio of activity in hydrogenation of tetralene to hydrodesulfurization of thiophene. [23] Commercial catalysts are obtained by *in situ* sulfidation of the oxidic precursor prepared by impregnation of pre-shaped alumina support with aqueous solutions of molybdenum and cobalt compounds with subsequent calcination. The conditions during activation of unsupported HDS catalysts strongly influenced the catalytic properties. [246] Therefore in this work Co-Mo-oxides were prepared under hydrothermal conditions as precursors for unsupported Co-Mo-S model systems in hydrotreating reactions. The influence of the preparation conditions (pH, Mo precursor, synthesis time, Co/Mo ratio) on the phase composition of the product and on the surface area was studied in detail. Flame spray pyrolysis and co-precipitation were applied for comparison. Selected materials were sulfided *in situ* before they were tested in hydrotreating of a model oil. To elucidate preparation-structure-activity correlations they were characterized after catalytic application.

5.2. Catalyst precursor preparation

Similar to the high surface area bismuth molybdates synthesized under hydrothermal conditions at various pH values with Bi/Mo = 1:1 (cf. 4.2 and 4.3.4), a series of cobalt molybdates was prepared by hydrothermal synthesis from cobalt nitrate and ammonium heptamolybdate or sodium molybdate. The influence of pH value, preparation time and applied Co/Mo ratio were studied in detail. For comparison four unsupported cobalt molybdates were prepared by flame spray pyrolysis with Co/Mo = 1:1 – 1:4 and two co-precipitated samples with Co/Mo = 1:1 and 1:3 were synthesized.

Hydrothermal synthesis with ammonium heptamolybdate: Typically 1.77 g ammonium heptamolybdate (AHM; $(NH_4)_6Mo_7O_{24} \cdot 4H_2O$, VWR AnalaR NORMAPUR) and 2.9 g cobalt nitrate (10 mmol Co; $Co(NO_3)_2 \cdot 6H_2O$, Fluka, > 99.0%, p.a.) were dissolved in 100 ml deionized water. The precursors dissolved completely and the pH value of the resulting solution was 4.4 - 4.5. The pH of the solution was adjusted either with nitric acid (2.2 M HNO_3) or an ammonia solution (25 vol.%) to values between 1 and 10. The resulting solution was stirred with a magnetic stirrer for 30 minutes and subsequently transferred into the Teflon-lined stainless steel autoclave. The autoclave was sealed and heated for 24 h at 180 °C in an oven. During hydrothermal synthesis of the cobalt molybdates the pH value of the solution decreased. After cooling to room temperature the solid product was separated by filtration, washed with water, ethanol and acetone. The resulting powder was dried at room temperature and ambient pressure. The resulting samples are referred to as Co1Mo1_AHM_pHx where x indicated the pH value (see Table 5-1).

Table 5-1: Hydrothermally synthesized samples at various pH values (10 mmol Co and 10 mmol Mo). All samples were prepared at 180 °C for 24 h.

Sample	Co precursor	Mo precursor	Acid or base	pH	Phases acc. to PXRD	BET [m²/g]	Co/Mo ratio
Co1Mo1_AHM_pH1	$Co(NO_3)_2 \cdot 6H_2O$	$(NH_4)_6Mo_7O_{24} \cdot 4H_2O$	7.7 ml 2.2M HNO_3	1	α-MoO_3, $NH_4Mo_5O_{15}(OH) \cdot 2H_2O$	7	0.01[a]
Co1Mo1_AHM_pH2	$Co(NO_3)_2 \cdot 6H_2O$	$(NH_4)_6Mo_7O_{24} \cdot 4H_2O$	3.83 ml 2.2M HNO_3	2	$CoMo_4O_{13} \cdot 2H_2O$	1	0.3[a]
Co1Mo1_AHM_pH3	$Co(NO_3)_2 \cdot 6H_2O$	$(NH_4)_6Mo_7O_{24} \cdot 4H_2O$	2.09 ml 2.2M HNO_3	3	$CoMo_4O_{13} \cdot 2H_2O$	< 1	0.3[a]
Co1Mo1_AHM_pH4	$Co(NO_3)_2 \cdot 6H_2O$	$(NH_4)_6Mo_7O_{24} \cdot 4H_2O$	0.56 ml 2.2M HNO_3	4	$CoMo_4O_{13} \cdot 2H_2O$, ($CoMoO_4 \cdot 0.75H_2O$)	1	0.4[a]
Co1Mo1_AHM_pH5	$Co(NO_3)_2 \cdot 6H_2O$	$(NH_4)_6Mo_7O_{24} \cdot 4H_2O$	0.17 ml 25% NH_3	5	$CoMo_4O_{13} \cdot 2H_2O$, $CoMoO_4 \cdot 0.75H_2O$	1	0.7[b]
Co1Mo1_AHM_pH6	$Co(NO_3)_2 \cdot 6H_2O$	$(NH_4)_6Mo_7O_{24} \cdot 4H_2O$	0.92 ml 25% NH_3	6	$CoMoO_4$	11	n.d.
Co1Mo1_AHM_pH7	$Co(NO_3)_2 \cdot 6H_2O$	$(NH_4)_6Mo_7O_{24} \cdot 4H_2O$	1.02 ml 25% NH_3	7	$Co_{1.2}MoO_{4.2} \cdot 1.3H_2O$	11	n.d.
Co1Mo1_AHM_pH8	$Co(NO_3)_2 \cdot 6H_2O$	$(NH_4)_6Mo_7O_{24} \cdot 4H_2O$	1.49 ml 25% NH_3	8	unknown	n.d.	2.0[a]
Co1Mo1_AHM_pH9	$Co(NO_3)_2 \cdot 6H_2O$	$(NH_4)_6Mo_7O_{24} \cdot 4H_2O$	2.66 ml 25% NH_3	9	unknown	37	2.0[a]
Co1Mo1_AHM_pH10	$Co(NO_3)_2 \cdot 6H_2O$	$(NH_4)_6Mo_7O_{24} \cdot 4H_2O$	3.65 ml 25% NH_3	10	unknown	23	n.d.

a: determined by ICP-OES
b: average value from EDX

Hydrothermal synthesis with sodium molybdate: Alternatively, cobalt molybdates were prepared from 2.4 g sodium molybdate (10 mmol Mo; $Na_2MoO_4 \cdot 2H_2O$, Alfa Aesar, 99.5 – 103.0%) and 10 mmol cobalt nitrate resulting in an aqueous solution (100 ml deionized water) with pH = 5.9 – 6.0. The obtained samples are denoted Co1Mo1_NaMo_pHx. A full list of samples is given in Table 5-2.

Table 5-2: Hydrothermally synthesized samples at various pH values (10 mmol Co and 10 mmol Mo). All samples were prepared at 180 °C for 24 h.

Sample	Co precursor	Mo precursor	Acid or base	pH	Phases acc. to PXRD	BET [m²/g]	Co/Mo ratio
Co1Mo1_NaMo_pH1	$Co(NO_3)_2 \cdot 6H_2O$	$Na_2MoO_4 \cdot 2H_2O$	12.73 ml 2.2M HNO_3	1	α-MoO_3	18	0.01[a]
Co1Mo1_NaMo_pH2	$Co(NO_3)_2 \cdot 6H_2O$	$Na_2MoO_4 \cdot 2H_2O$	6.95 ml 2.2M HNO_3	2	$CoMo_4O_{13} \cdot 2H_2O$	n.d.	n.d.
Co1Mo1_NaMo_pH3	$Co(NO_3)_2 \cdot 6H_2O$	$Na_2MoO_4 \cdot 2H_2O$	6.03 ml 2.2M HNO_3	3	$CoMo_4O_{13} \cdot 2H_2O$	1	n.d.
Co1Mo1_NaMo_pH4	$Co(NO_3)_2 \cdot 6H_2O$	$Na_2MoO_4 \cdot 2H_2O$	5.14 ml 2.2M HNO_3	4	$CoMoO_4 \cdot 0.75H_2O$, ($CoMo_4O_{13} \cdot 2H_2O$)	3	n.d.
Co1Mo1_NaMo_pH5	$Co(NO_3)_2 \cdot 6H_2O$	$Na_2MoO_4 \cdot 2H_2O$	3.45 ml 2.2M HNO_3	5	$CoMoO_4 \cdot 0.75H_2O$	6	n.d.
Co1Mo1_NaMo_pH6	$Co(NO_3)_2 \cdot 6H_2O$	$Na_2MoO_4 \cdot 2H_2O$	0.09 ml 2.2M HNO_3	6	$CoMoO_4$	15	0.8[b]
Co1Mo1_NaMo_pH7	$Co(NO_3)_2 \cdot 6H_2O$	$Na_2MoO_4 \cdot 2H_2O$	0.07 ml 25% NH_3	7	$NaCo_2(OH)(MoO_4)_2 \cdot 2H_2O$	16	1.1[a]
Co1Mo1_NaMo_pH8	$Co(NO_3)_2 \cdot 6H_2O$	$Na_2MoO_4 \cdot 2H_2O$	0.55 ml 25% NH_3	8	$NaCo_2(OH)(MoO_4)_2 \cdot 2H_2O$	n.d.	1.3[a]
Co1Mo1_NaMo_pH9	$Co(NO_3)_2 \cdot 6H_2O$	$Na_2MoO_4 \cdot 2H_2O$	1.34 ml 25% NH_3	9	unknown	36	n.d.
Co1Mo1_NaMo_pH10	$Co(NO_3)_2 \cdot 6H_2O$	$Na_2MoO_4 \cdot 2H_2O$	2.06 ml 25% NH_3	10	unknown	22	n.d.
Co1Mo1_NaMo_pH11	$Co(NO_3)_2 \cdot 6H_2O$	$Na_2MoO_4 \cdot 2H_2O$	6 ml 25% NH_3	11	unknown	42	1.7[b]

a: determined by ICP-OES
b: average value from EDX

In addition the preparation procedure was varied: Ammonium heptamolybdate and cobalt nitrate were dissolved in 50 ml deionized water and the pH was adjusted to pH = 7 and pH = 8 with 5 vol.% ammonia solution. This procedure is denoted as P1, whereas preparation from two separate solutions is denoted as P2, which is described in the following: Ammonium heptamolybdate was dissolved in 40 ml 5 vol.% ammonia solution and cobalt nitrate was dissolved in 40 ml nitric acid. The cobalt solution was added slowly to the

molybdenum solution and the pH was adjusted with 5 vol.% ammonia solution. The resulting liquid was transferred into a Teflon-lined autoclave and heated at 180 °C for 24 h.
One-step flame spray pyrolysis (FSP): As an alternative route Co-Mo samples were prepared by FSP. Precursor solutions were prepared by dissolving the required amounts of Co(II)-2-ethylhexanoate ($Co[OOCCH(C_2H_5)C_4H_9]_2$; Sigma Aldrich, 65 wt.% in mineral spirits) and Mo(VI)-2-ethylhexanoate ($Mo[OOCCH(C_2H_5)C_4H_9]_x$; Strem Chemicals, 15% Mo) in xylene to a total concentration of 0.4 mol/l, applying Co/Mo ratios of 1:1, 1:2, 1:3 and 1:4. Details of the preparation and the equipment were already described in chapter 2.1.2. The flame made samples are denoted as follows: FSP_Co1Mo1, FSP_Co1Mo2, FSP_Co1Mo3 and FSP_Co1Mo4.
Conventional co-precipitation: For comparison, co-precipitated Co-Mo samples (Co/Mo = 1:1 and 1:3) were synthesized according to Carrazán et al. [208] using $(NH_4)_6Mo_7O_{24} \cdot 4H_2O$ and $Co(NO_3)_2 \cdot 6H_2O$ in deionized water. After heating the solution to 80 °C the resulting precipitate was filtrated, dried at 100 °C and subsequently calcined at 500 °C for 2 h. These materials are referred to as CP_Co1Mo1_500 and CP_Co1Mo3_500.

The samples were characterized by PXRD, Raman spectroscopy, nitrogen physisorption measurements, SEM and ICP-OES. Details of the characterization have already been described in 2.2. Catalytic activity measurements for hydrotreating were performed at Haldor Topsøe A/S using the experimental set-up described in 2.3.2. The used samples were analyzed by TEM measurements at Haldor Topsøe A/S according to 2.2.5.

5.3. Results and Discussion

5.3.1. Influence of the pH value during hydrothermal synthesis using two different Mo precursors

Cobalt molybdates were prepared hydrothermally at 180 °C and 24 h from cobalt nitrate and either ammonium heptamolybdate or sodium molybdate as Mo precursors in a Co/Mo ratio of 1. The synthetic parameters along with the product phases identified by PXRD, the specific surface area and the Co/Mo ratio in the product determined by ICP-OES or EDX

are summarized in Table 5-1 and Table 5-2. Figure 5.1 shows the powder X-ray diffraction pattern and selected Raman spectra of the solid products obtained from ammonium heptamolybdate and cobalt nitrate at pH = 1 – 10. The pH value has a strong influence on the phase formed during hydrothermal synthesis. At low pH value (pH = 1) only orthorhombic α-MoO_3 (JCPDS no. 05-508) and an ammonium molybdenum oxide phase was found in the diffraction pattern (Figure 5.1a), which could be hexagonal $NH_4Mo_5O_{15}(OH) \cdot 2H_2O$ (JCPDS no. 40-671) or cubic $H_{0.68}(NH_4)_2Mo_{14.16}O_{4.34} \cdot 6.92H_2O$ (JCPDS no. 46-100) both assigned to the reflections at 16.8° and 19.4°. No cobalt containing phase was observed. The ICP-OES measurements revealed a cobalt content of only 0.6 mol% (Co/Mo = 0.01) in sample Co1Mo1_AHM_pH1 in accordance with the Raman spectrum in Figure 5.1b which showed the characteristic features of α-MoO_3 (995, 820, 667 and 292 cm^{-1})[247]. Under acidic conditions cobalt remained in solution and did not precipitate. The product composition corresponds well to the composition found in the sample synthesized without cobalt nitrate (see 3.3.1). With increasing pH value the cobalt content of the products increased (see Table 5-1). At pH = 2 and pH = 3 a red/brown precipitate was formed, which could be identified as $CoMo_4O_{13} \cdot 2H_2O$, a molybdenum rich phase with a pillared structure recently discovered by Eda et al. [40]. Especially the sample at pH = 2 was highly crystalline as shown by PXRD (Figure 5.1a) and accordingly exhibited a very small surface area (< 1 m^2/g; see Table 5-2). The Raman spectrum of $CoMo_4O_{13} \cdot 2H_2O$ has not yet been measured and analyzed; hence it was measured here and is shown in Figure 5.1b. It revealed several bands between 800 and 1000 cm^{-1}. In this region the bands attributed to stretching modes of Mo-O vibrations are typically observed [247], whereas features arising from the shorter Mo-O bonds appear at relatively high wave numbers [248]. $CoMo_4O_{13} \cdot 2H_2O$ forms a pillared layer structure, where corner-sharing Z-shaped units, which consist of two MoO_6 and two MoO_5OH_2 octahedra sharing edges, built ribbons, which are connected to sheets. [40] The band at 817 cm^{-1} is related to asymmetric vibration of Mo-O-Mo bridges in the octahedra [249], whereas the band at 928 cm^{-1} can be ascribed to Mo-O-Co stretching vibrations [249-250]. The band at 955 cm^{-1} arises from the presence of terminal Mo=O in MoO_x clusters and the band at 989 cm^{-1} can be assigned to MoO_5OH_2 octahedra [248]. It was also suggested that the band at 985 cm^{-1} corresponds to a loss of oxygen in octahedral molybdenum oxide [251] or to polymolybdate aggregates [252-253].

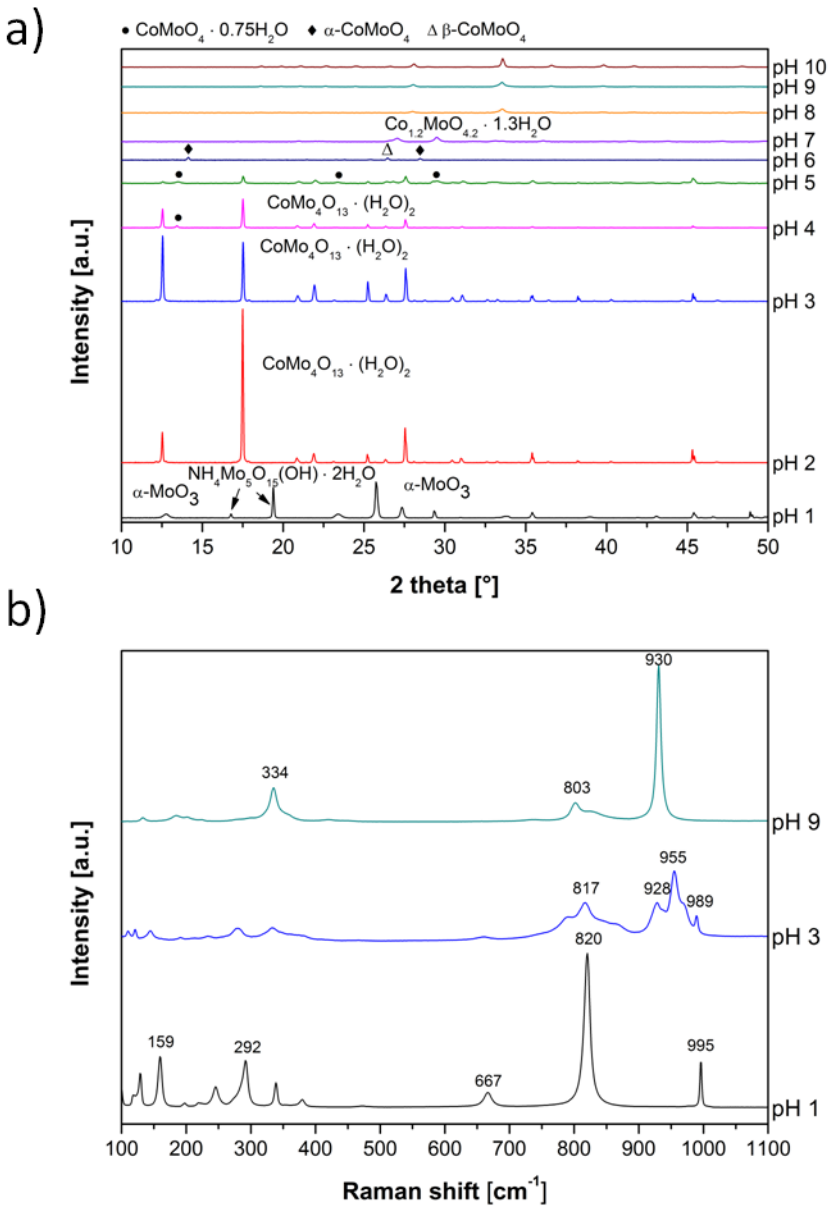

Figure 5.1: Powder X-ray diffraction pattern (a) and selected Raman spectra (b) of hydrothermally prepared samples from cobalt nitrate and ammonium heptamolybdate with Co/Mo = 1 at pH = 1 - 10. The Raman spectra indicate the presence of α-MoO_3 (pH = 1) and β-$CoMoO_4$ (pH = 9). At pH = 3 pure $CoMo_4O_{13} \cdot 2H_2O$ was obtained.

Here we successfully prepared chlorine and alkali free $CoMo_4O_{13} \cdot 2H_2O$ from ammonium heptamolybdate, cobalt nitrate and nitric acid, whereas Eda et al. [40] used cobalt chloride as a precursor, which can lead to chlorine residues in the product. The applied pH values leading to $CoMo_4O_{13} \cdot 2H_2O$ were similar (pH = 1.5 to 4 in [40] and pH = 2 – 4 in the present work), indicating the importance of the pH value during hydrothermal synthesis.

The formation of $CoMoO_4 \cdot 0.75H_2O$ (CSD no. 415282)[38] started at pH = 4, as indicated by the reflection at 13.4° in the PXRD. Preparation at pH = 5 resulted in a mixture of

$CoMo_4O_{13} \cdot 2H_2O$[40] and $CoMoO_4 \cdot 0.75H_2O$[38], whereas at pH = 6 $CoMoO_4$ was obtained. The reflections in the powder X-ray diffraction pattern of Co1Mo1_AHM_pH6 could be attributed to the strongest reflections in the diffraction pattern of α-$CoMoO_4$ (2θ = 26.5°; JCPDS no. 21-868) and β-$CoMoO_4$ (2θ = 14.2°, 28.4°; JCPDS no. 25-1434). At or above pH = 7 the intensity of the reflections in the diffraction pattern was low. For Co1Mo1_AHM_pH7 the reflections at 2θ = 27.1°, 29.2° may indicate the presence of $Co_{1.2}MoO_{4.2} \cdot 1.3H_2O$ (JCPDS no. 14-087). Under more basic conditions none of the diffraction pattern could be matched with cobalt molybdate phases, although the Raman spectrum of Co1Mo1_AHM_pH9 showed the characteristic features of β-$CoMoO_4$[254]. However, the Co/Mo ratio determined from ICP-OES in this sample synthesized at pH = 9 was 2.0, indicating that β-$CoMoO_4$ could not be the only phase present in the product. Ding et al. [44] synthesized cobalt molybdate from ammonium heptamolybdate and cobalt nitrate at pH = 9 and obtained $Co(OH)_2$ at 140 °C after 12 h. The presence of a cobalt hydroxide phase in Co1Mo1_AHM_pH9 could not be detected by powder X-ray diffraction or Raman spectroscopy and ICP-OES measurements indicated the presence of molybdenum excluding the formation of pure cobalt hydroxides at high pH values. Interestingly the specific surface area increased at higher pH value (Table 5-1).

An increase in the applied pH value from 1 to 9 increased the cobalt content from Co/Mo = 0.01 at pH = 1 to Co/Mo = 2.0 at pH = 9 (Table 5-1) indicating that cobalt partly remained in solution under acidic conditions, in accordance with the red color of the filtrate. Under basic conditions molybdenum did not completely precipitate. At low pH values mainly layered structures containing octahedrally coordinated molybdenum were formed (α-MoO_3, $CoMo_4O_{13} \cdot 2H_2O$), whereas at higher pH values also phases with tetrahedral molybdenum were found ($CoMoO_4 \cdot 0.75H_2O$, β-$CoMoO_4$). This agrees well with the stability of molybdenum species in an aqueous ammonium heptamolybdate solution at different pH values, which was discussed in 1.1.1 and in literature [14] ($Mo_7O_{24}^{6-}$ at pH = 2.9 – 6 and MoO_4^{2-} at pH > 6).

Figure 5.2 depicts the powder X-ray diffraction pattern of the samples synthesized from sodium molybdate and cobalt nitrate under hydrothermal conditions at pH = 1 – 10 and 180 °C for 24 h. Analog to the samples prepared from ammonium heptamolybdate there is no evidence for a cobalt containing phase in the sample synthesized at pH = 1 and very low

cobalt content (Co/Mo = 0.01, 0.6 mol% Co, see Table 5-2) with α-MoO_3 (JCPDS no. 05-508) were identified by ICP-OES and PXRD.

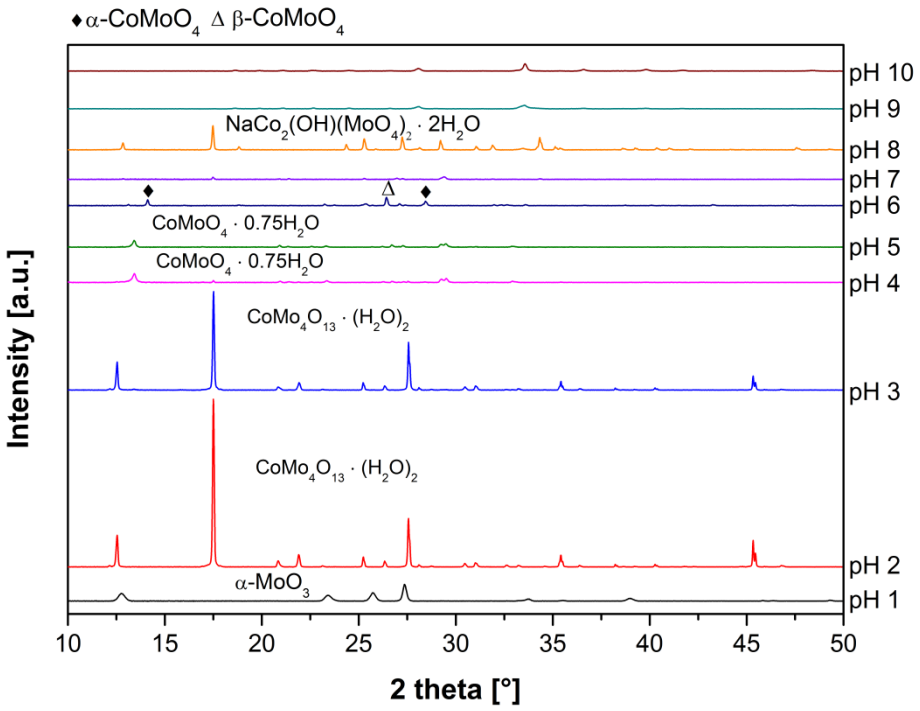

Figure 5.2: Powder X-ray diffraction pattern of hydrothermally synthesized samples from $Na_2MoO_4 \cdot 2H_2O$ and $Co(NO_3)_2 \cdot 6H_2O$ at various pH values at 180 °C for 24 h (applied Co/Mo in solution equaled 1).

At pH = 2 and pH = 3 highly crystalline $CoMo_4O_{13} \cdot 2H_2O$[40] was detected by PXRD (see Figure 5.2), which agrees with the samples synthesized from ammonium heptamolybdate. In contrast to preparation with ammonium heptamolybdate, already at pH = 4 $CoMoO_4 \cdot 0.75H_2O$ was detected beside some residual $CoMo_4O_{13} \cdot 2H_2O$. At pH = 5 only $CoMoO_4 \cdot 0.75H_2O$[38] is found and the sample was violet. The diffraction pattern of sample Co1Mo1_NaMo_pH6 (Figure 5.2) resembled the diffraction pattern of sample Co1Mo1_AHM_pH6 (Figure 5.1a) indicating the presence of α- and β-$CoMoO_4$. Cobalt molybdates were also prepared from sodium molybdate and cobalt nitrate in deionized water by Rico et al. [43] without the addition of an acid or base, which should correspond to a pH value around 6. Their hydrothermal route at 160 °C and 200 °C for 15 h and subsequent calcination at 500 °C for 5 h resulted in β-$CoMoO_4$. Note that phase identification was performed without a calcination step here. A similar approach without calcination yielded $CoMoO_4 \cdot nH_2O$ after hydrothermal synthesis at 180 °C for 15 h. [45]

The shorter reaction time compared to this work (24 h) could be the reason that the hydrate instead of α- and β-$CoMoO_4$ was obtained.

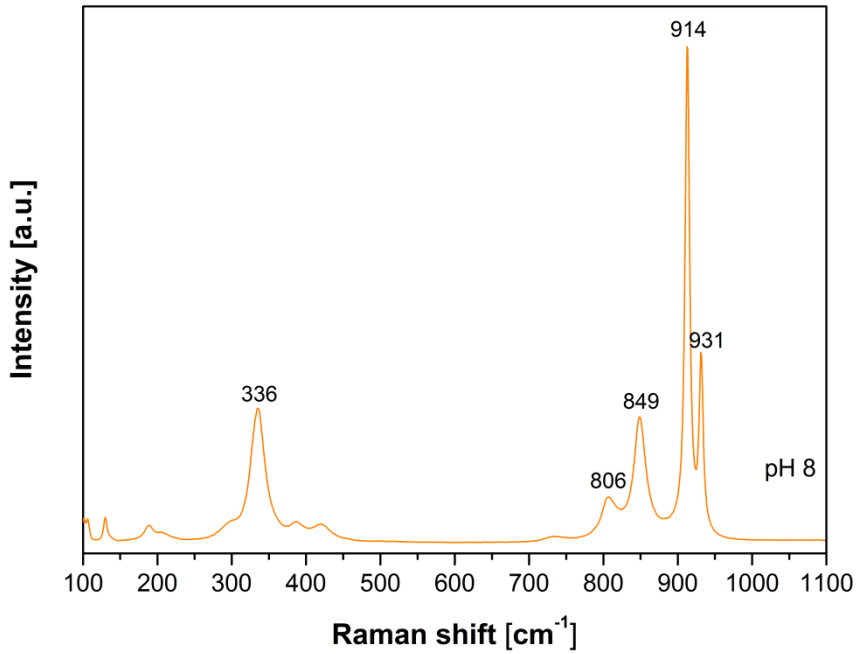

Figure 5.3: Raman spectrum of Co1Mo1_NaMo_pH8 consisting of $NaCo_2(OH)(MoO_4)_2 \cdot 2H_2O$ according to PXRD in Figure 5.2.

According to powder X-ray diffraction measurements the sample synthesized at neutral conditions (pH = 7) contained $NaCo_2(OH)(MoO_4)_2 \cdot 2H_2O$ (JCPDS no. 74-2876)[255], which consists of tetrahedral MoO_4 and octahedral CoO_6. In contrast to the samples synthesized from ammonium heptamolybdate at pH = 8, where phase identification by PXRD was not possible, Co1Mo1_NaMo_pH8 contained crystalline $NaCo_2(OH)(MoO_4)_2 \cdot 2H_2O$ which could easily be detected in the diffraction pattern. In the corresponding Raman spectrum of sample Co1Mo1_NaMo_pH8 in Figure 5.3 two strong bands at 931 cm^{-1} and 914 cm^{-1} as well as weaker bands at 849 cm^{-1}, 806 cm^{-1} and 336 cm^{-1} were detected. The only reference spectrum for $NaCo_2(OH)(MoO_4)_2 \cdot 2H_2O$ found in the literature was of lower quality, but showed bands with shifts at 925, 804 and 673 cm^{-1} assigned to different Mo-O bonds [47]. The two bands at 931 and 914 cm^{-1} in Figure 5.3 may correspond to the band at 925 cm^{-1}, which is split due to a shift of the Mo-O bond in the presence of water or sodium. Under basic conditions the PXRDs of the hydrothermally synthesized products could not be analyzed but they were identical to the according

diffraction pattern of the samples synthesized with ammonium heptamolybdate at pH = 9 and 10. For sodium molybdate the pH value was increased to pH = 11 but the PXRD equaled the diffraction pattern of the samples prepared at pH = 9 and 10, thus it was not depicted in Figure 5.2.

The samples synthesized from $Na_2MoO_4 \cdot 2H_2O$ followed the same trend as the samples prepared from $(NH_4)_6Mo_7O_{24} \cdot 4H_2O$: The cobalt content increased with increasing pH value and the sample prepared at pH = 9 exhibited the highest surface area (36 m²/g for sodium molybdate and 37 m²/g for ammonium heptamolybdate).

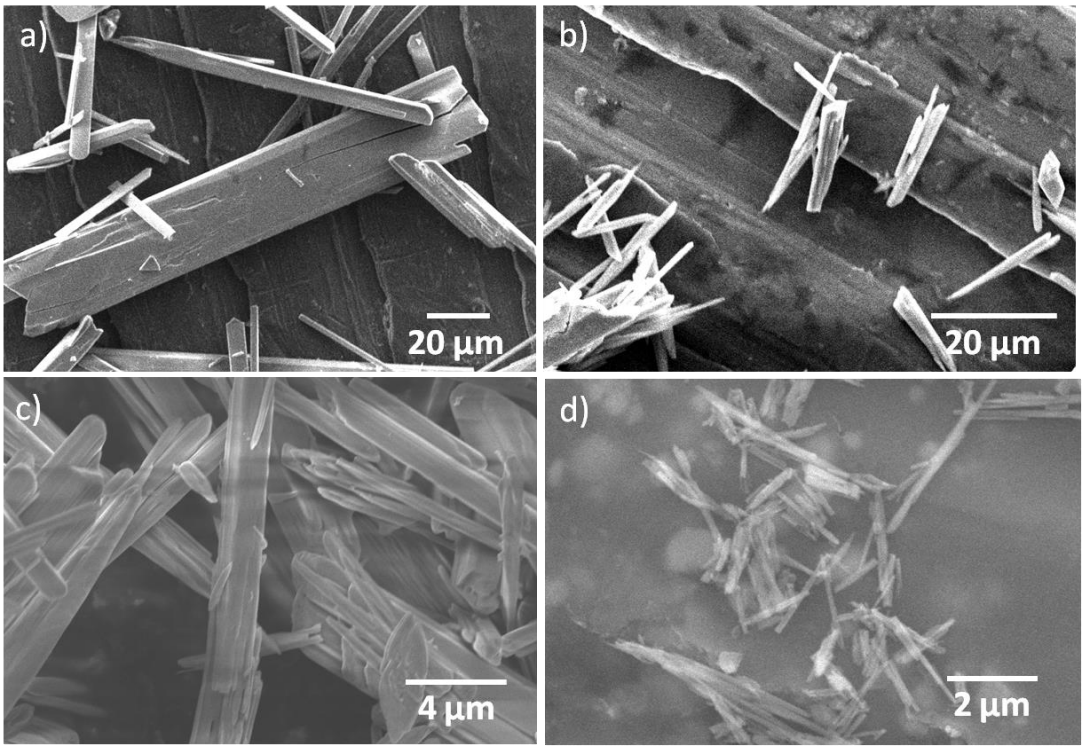

Figure 5.4: SEM images of the hydrothermally synthesized samples synthesized from ammonium heptamolybdate or sodium molybdate with cobalt nitrate at various pH values: a) Co1Mo1_AHM_pH2, b) Co1Mo1_AHM_pH4, c) Co1Mo1_AHM_pH5 and d) Co1Mo1_NaMo_pH6.

Figure 5.4 displays the SEM images of several samples prepared from ammonium heptamolybdate and sodium molybdate showing a rod-like morphology for all samples but with different particle sizes and aspect ratios. The particles of sample Co1Mo1_AHM_pH2 were of inhomogeneous size and ranged from 5 µm x 100 µm to 30 µm x 150 µm with a height of 1.5 – 3 µm. The samples synthesized at pH = 4 and pH = 5 were smaller with a particle size of 2 µm x 25 µm - 4 µm x 50 µm and 1.2 - 1.3 µm x 10 - 15 µm, respectively.

The sample synthesized with sodium molybdate at pH = 6 (Figure 5.4d) formed relatively small rods which were around 500 nm x 5 µm in size.

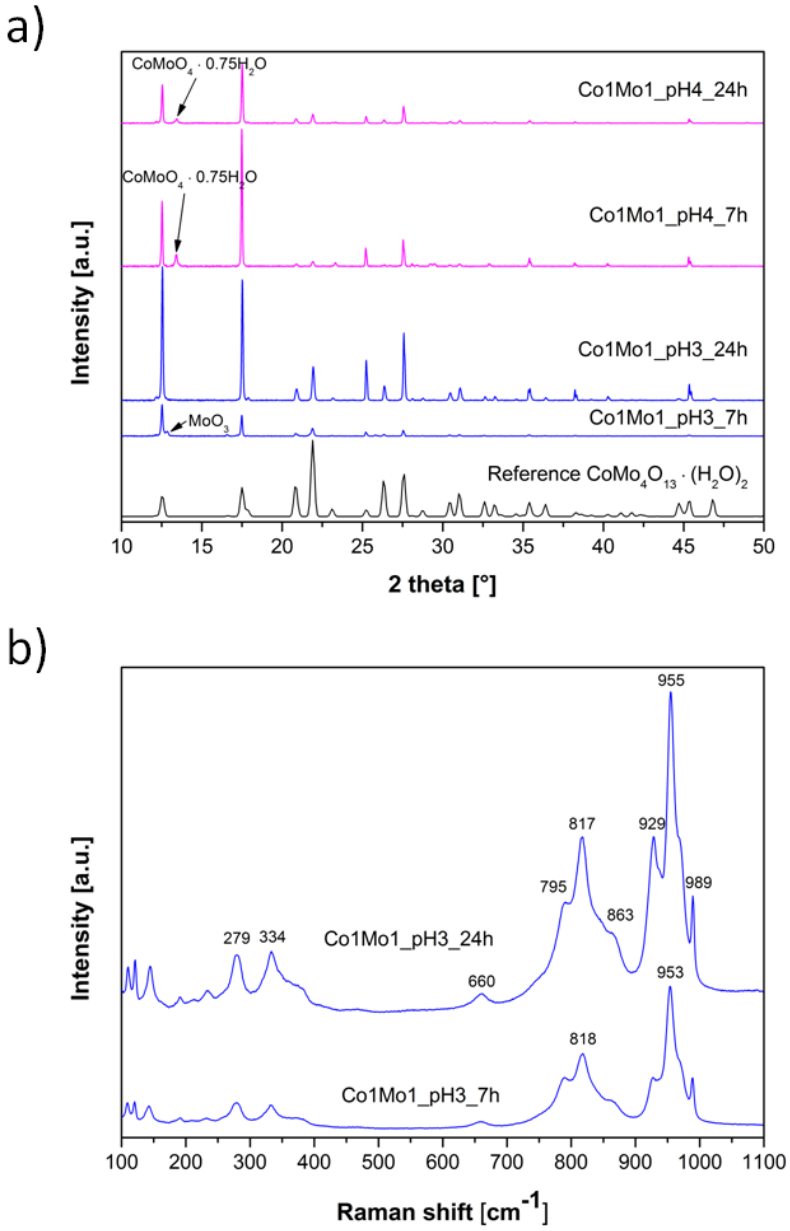

Figure 5.5: Powder X-ray diffraction pattern (a) and Raman spectra (b) of hydrothermally synthesized samples from ammonium heptamolybdate and cobalt nitrate at 180 °C for 7 h and 24 h.

5.3.2. Effect of synthesis time during hydrothermal synthesis

In a next step the influence of the synthesis time on the product phase was studied at pH = 3 and pH = 4. Hydrothermal synthesis from ammonium heptamolybdate and cobalt nitrate was performed for only 7 h and the resulting powder X-ray diffraction patterns of the

products are depicted in Figure 5.5. The diffraction pattern of the products prepared for 7 h and their corresponding samples synthesized for 24 h matched the reference pattern of $CoMo_4O_{13} \cdot 2H_2O$ [40]. The sample synthesized at pH = 3 for 7 h additionally contained impurities of MoO_3, which was only detected by PXRD and not by Raman spectroscopy (see Figure 5.5b). The Co/Mo ratios of these two samples were identical (Co/Mo = 0.3) according to ICP-OES. The sample synthesized at pH = 4 for 7 h did not contain any additional phases compared to the sample synthesized for 24 h. This indicates that already after 7 h crystalline materials with relatively high phase purity can be obtained.

Additionally three samples from sodium molybdate and cobalt nitrate were synthesized for 72 h to analyze the influence of synthesis time on the crystalline products as well as on the Co/Mo ratios in the resulting samples. The powder X-ray diffraction pattern in Figure 5.6 suggest that an increase in synthesis time from 1 day to 3 days did not influence the phase composition at low pH value (pH = 1 – 2). According to ICP-OES the sample synthesized at pH = 1 contained slightly more cobalt after 72 h compared to the sample synthesized for 24 h (0.9 mol% Co and 0.6 mol% Co), which indicated that longer reaction times led to an increase in cobalt under acidic conditions. At higher pH value (pH = 5) the product was composed of $CoMoO_4 \cdot 0.75H_2O$ after 24 h and contains a mixture of $CoMoO_4 \cdot 0.75H_2O$ and $CoMo_4O_{13} \cdot 2H_2O$ after 72 h. A high concentration of protons during hydrothermal synthesis or a relatively long synthesis time was beneficial for the formation of $CoMo_4O_{13} \cdot 2H_2O$, which was already indicated by the results of Eda et al. [40] who obtained pure $CoMo_4O_{13} \cdot 2H_2O$ at pH = 3.5 – 3.7 after 3 days from an insoluble Mo source or at pH = 1.5 - 1.6 after 1 day from a soluble Mo source, respectively. They suggested that this was due to solubility of the different precursors but the main reason could be the different acidity of the Mo source as in the present study initially the precursors were all completely dissolved at pH < 7.

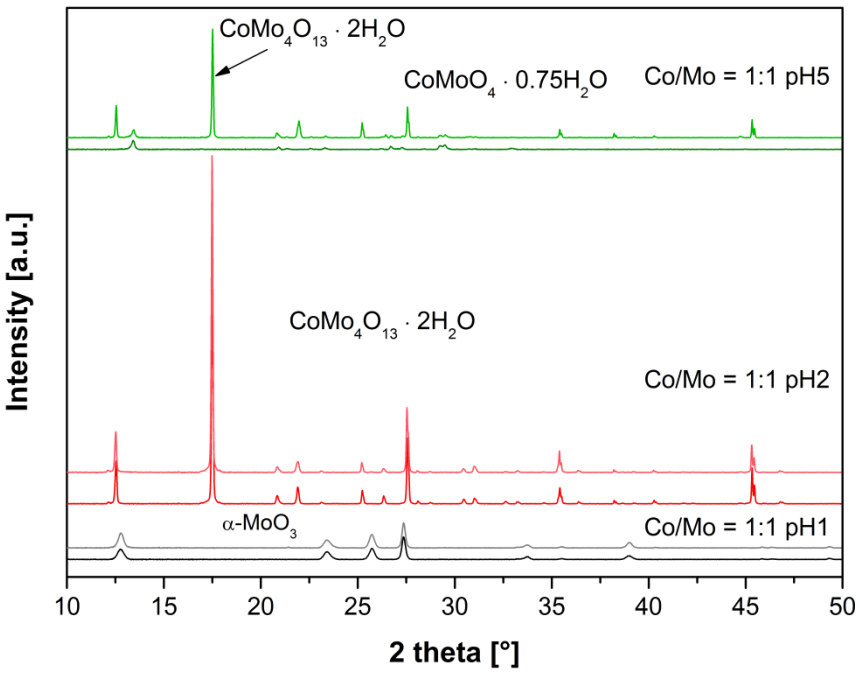

Figure 5.6: Powder X-ray diffraction pattern of samples prepared from sodium molybdate and cobalt nitrate at 180 °C for 24 h and 72 h at pH = 1, pH = 2 and pH = 5. The darker line corresponds to 24 h and the lighter colored line to 72 h.

5.3.3. Influence of the Co/Mo ratio and synthesis procedure

The influence of the Co/Mo ratio on the product phase and surface area were studied to enable the preparation of pure phases with relatively high surface area. The cobalt to molybdenum ratio was varied between Co/Mo = 1:1 to 1:3 using ammonium heptamolybdate and cobalt nitrate as precursors, which were dissolved in 100 ml water. The pH value was adjusted to pH = 6 or pH = 7 with diluted ammonia solution (5 vol.%). Additionally at pH = 7 and pH = 8 the samples were prepared by two different procedures: Dissolving the precursor in 50 ml deionized water and adjustment of pH value with 5 vol.% ammonia solution (P1) and separate dissolution of the cobalt and the molybdenum precursor in nitric acid and ammonia solution, respectively, with subsequent mixing (P2). The details of the preparation as well as the product phases determined by PXRD and the specific surface areas are summarized in Table 5-3.

Table 5-3: Hydrothermally synthesized samples prepared from ammonium heptamolybdate and cobalt nitrate at different pH values and with various Co/Mo ratios.

Sample	Preparation	Co [mmol]	Mo [mmol]	pH	Phase according to PXRD	BET [m²/g]
Co1Mo1_pH6	100 ml deionized water	10	10	6	$CoMoO_4 \cdot 0.75H_2O$	7
Co1Mo2_pH6	100 ml deionized water	10	20	6	$CoMoO_4 \cdot 0.75H_2O$	n.d.
Co1Mo3_pH6	100 ml deionized water	10	30	6	$CoMoO_4 \cdot 0.75H_2O$, α-MoO_3	3
Co1Mo1_pH7	100 ml deionized water	10	10	7	$CoMoO_4 \cdot 0.75H_2O$	11
Co1Mo2_pH7	100 ml deionized water	10	20	7	$CoMoO_4 \cdot 0.75H_2O$	n.d.
Co1Mo3_pH7	100 ml deionized water	10	30	7	$CoMoO_4 \cdot 0.75H_2O$	16
Co1Mo1_pH7_P2	$Co(NO_3)_2 \cdot 6H_2O$ in 40 ml HNO_3 and $(NH_4)_6Mo_7O_{24} \cdot 4H_2O$ in NH_4OH; mixing	10	10	7	β-$CoMoO_4$, $Co_{1.2}MoO_{4.2} \cdot 1.3H_2O$, $Mo_{17}O_{47}$	< 1
Co1Mo3_pH7_P2	$Co(NO_3)_2 \cdot 6H_2O$ in 40 ml HNO_3 and $(NH_4)_6Mo_7O_{24} \cdot 4H_2O$ in NH_4OH; mixing	10	30	7	β-$CoMoO_4$, $Co_{1.2}MoO_{4.2} \cdot 1.3H_2O$, $Mo_{17}O_{47}$	< 1
Co1Mo1_pH7_P1	50 ml deionized water	10	10	7	$CoMoO_4 \cdot 0.75H_2O$	9
Co1Mo3_pH7_P1	50 ml deionized water	10	30	7	$CoMoO_4 \cdot 0.75H_2O$	8
Co1Mo1_pH8_P2	$Co(NO_3)_2 \cdot 6H_2O$ in 40 ml HNO_3 and $(NH_4)_6Mo_7O_{24} \cdot 4H_2O$ in NH_4OH; mixing	10	10	8	β-$CoMoO_4$, $Co_{1.2}MoO_{4.2} \cdot 1.3H_2O$, $Mo_{17}O_{47}$	2
Co1Mo3_pH8_P2	$Co(NO_3)_2 \cdot 6H_2O$ in 40 ml HNO_3 and $(NH_4)_6Mo_7O_{24} \cdot 4H_2O$ in NH_4OH; mixing	10	30	8	β-$CoMoO_4$, $Co_{1.2}MoO_{4.2} \cdot 1.3H_2O$, $Mo_{17}O_{47}$	1
Co1Mo1_pH8_P1	50 ml deionized water	10	10	8	$CoMoO_4 \cdot 0.75H_2O$	1
Co1Mo3_pH8_P1	50 ml deionized water	10	30	8	β-$CoMoO_4$, $Co_{1.2}MoO_{4.2} \cdot 1.3H_2O$, $Mo_{17}O_{47}$	9

According to PXRD all three samples synthesized with Co/Mo = 1:1 to 1:3 at pH = 6 contained $CoMoO_4 \cdot 0.75H_2O$ (see Figure 5.7) except the sample with the highest molybdenum content (Co/Mo = 1:3), where additionally α-MoO_3 (JCPDS no. 05-508) was

found (additional reflection at 2θ = 12.7° and reflections with increased intensity at 25.7° and 27.3°).

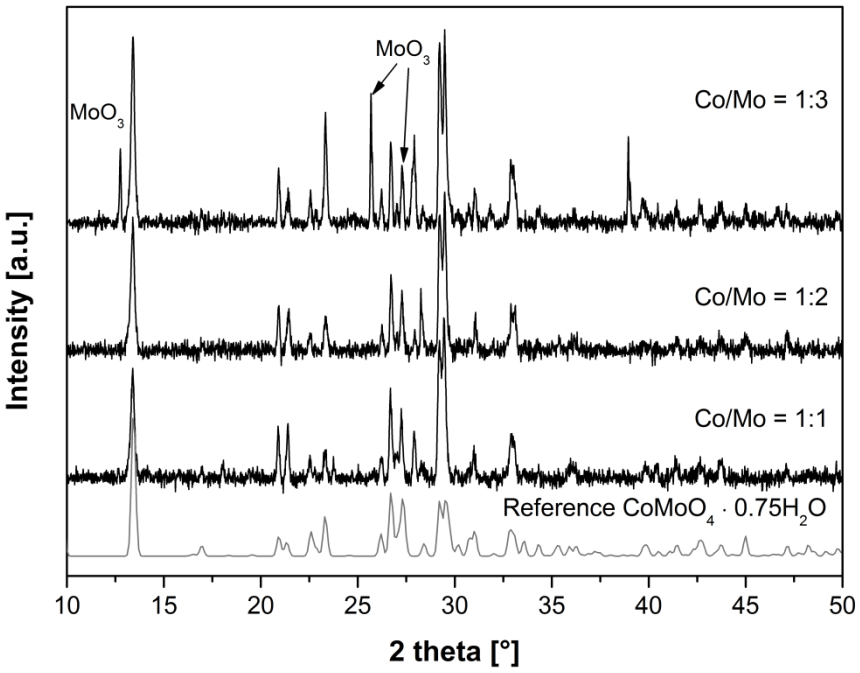

Figure 5.7: Powder X-ray diffraction pattern of samples synthesized from ammonium heptamolybdate and cobalt nitrate at pH = 6 with Co/Mo = 1:1, 1:2 and 1:3.

The corresponding Raman spectrum of Co1Mo3_pH6 in Figure 5.8 showed the characteristic features of β-$CoMoO_4$ with bands at 935, 851, 815, 358 and 331 cm^{-1} indicating tetrahedral MoO_4. [254] The Raman spectrum of the sample synthesized at pH = 6 with Co/Mo = 1:1 resembled the spectrum of the material synthesized from sodium molybdate and cobalt nitrate at pH = 8 (compare Figure 5.3), which contained $NaCo_2(OH)(MoO_4)_2 \cdot 2H_2O$ according to X-ray diffraction measurements. The band at 930 cm^{-1} could be assigned to Co-O-Mo stretching vibrations, which are similar in α- and β-$CoMoO_4$ as well as $CoMoO_4 \cdot 0.75H_2O$ and $NaCo_2(OH)(MoO_4)_2 \cdot 2H_2O$. The band at 912 cm^{-1} could result from an elongation of the Mo-O bond due to the presence of coordinated water. The band at 848 cm^{-1} is characteristic for asymmetric deformation vibrations of Mo-O-Mo polymolybdate species, whereas the band at 807 cm^{-1} could be assigned to Mo-O stretching vibrations and the band at 333 cm^{-1} to Mo-O bending vibrations.

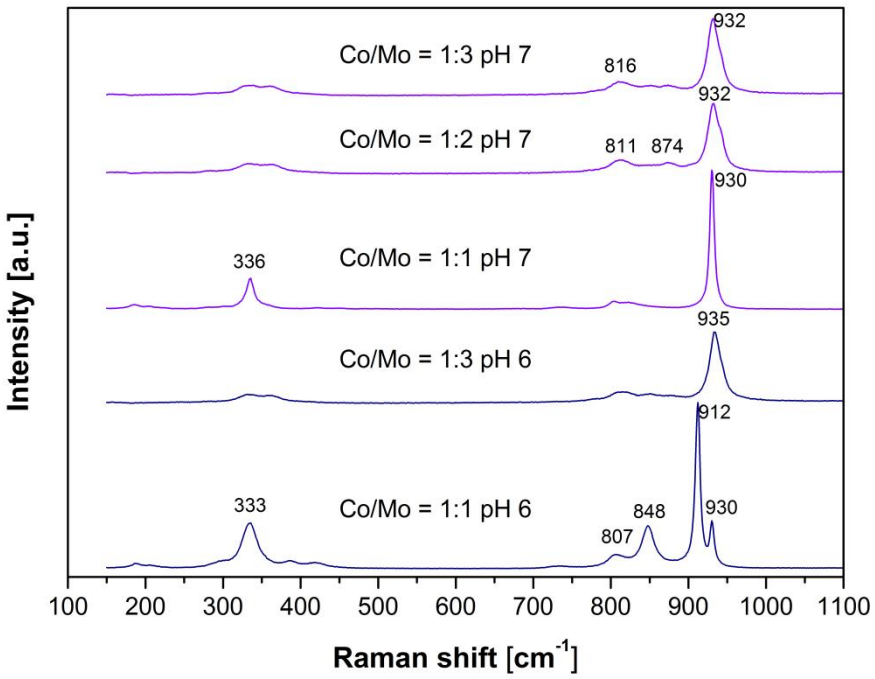

Figure 5.8: Raman spectra of hydrothermally synthesized samples from ammonium heptamolybdate and cobalt nitrate at pH = 6 and pH = 7 with different Co/Mo ratios.

All Raman spectra of the samples synthesized at pH = 7 with Co/Mo = 1:1 to 1:3 (Figure 5.8) were similar to the Raman spectra of Co1Mo3_pH6 and indicate the presence of $CoMoO_4 \cdot 0.75H_2O$, which has the β-$CoMoO_4$ structure ("hydrated β-$CoMoO_4$"). The corresponding X-ray diffraction pattern in Figure 5.9 matched the reference pattern of $CoMoO_4 \cdot 0.75H_2O$ [38]. This implied that $CoMoO_4 \cdot 0.75H_2O$ could easily be prepared from ammonium heptamolybdate and cobalt nitrate at pH = 6 and pH = 7. In contrast to Eda et al. [38] who used CoO and MoO_3 as precursors for the preparation of $CoMoO_4 \cdot 0.75H_2O$ and added NaCl to increase the ionic strength, this route allows preparation of a chlorine free cobalt molybdate. If cobalt nitrate and ammonium heptamolybdate were dissolved separately in diluted nitric acid and diluted ammonia solution, respectively, and the pH value was subsequently adjusted to pH = 7, a mixture of phases was obtained according to PXRD in Figure 5.9 ($Mo_{17}O_{47}$, β-$CoMoO_4$ and $Co_{1.2}MoO_{4.2} \cdot 1.3H_2O$). Furthermore the specific surface area of these samples was low (< 1 m²/g; Table 5-3) compared to the samples prepared at pH = 7, where both precursors were dissolved in water (11 m²/g for Co1Mo1_AHM_pH7, 9 m²/g for Co1Mo1_pH7_P1).

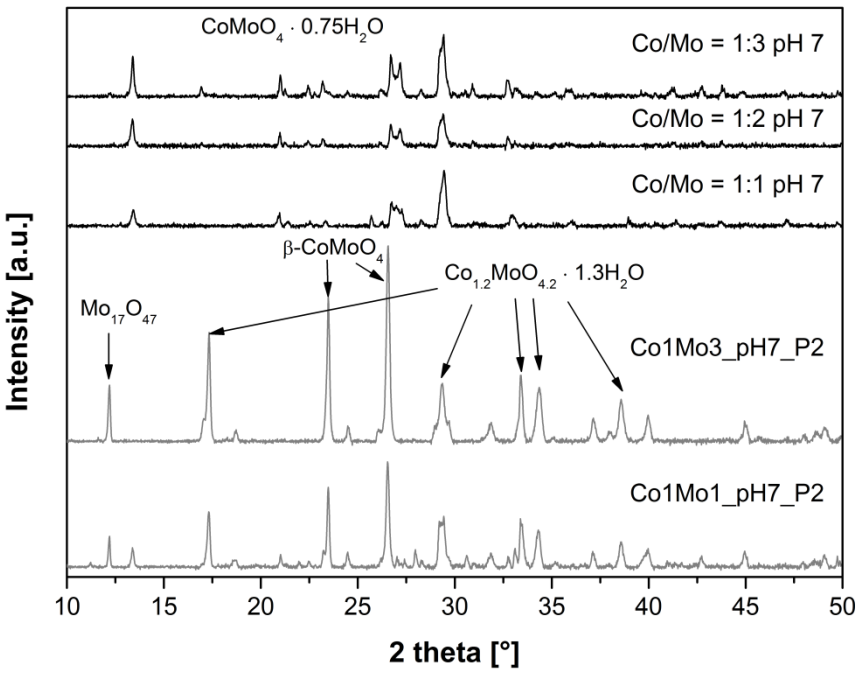

Figure 5.9: Powder X-ray diffraction pattern of hydrothermally synthesized samples from ammonium heptamolybdate and cobalt nitrate at pH = 7 with different Co/Mo ratios. In the preparation procedure P2 cobalt nitrate was dissolved in nitric acid solution and ammonium heptamolybdate in ammonia solution and the two separate solutions were mixed.

The diffraction pattern of the samples synthesized from two separate precursor solutions at pH = 8 could be assigned to the same phase mixture and showed the same reflections as Co1Mo1_pH7_P2 and Co1Mo3_pH7_P2 (see Figure 5.10). The surface areas of these samples were also relatively low (2 m²/g and 1 m²/g for Co:Mo = 1:1 and 1:3 respectively). Figure 5.10 shows the diffraction pattern of the samples synthesized by dissolving ammonium heptamolybdate and cobalt nitrate in the ratio Co/Mo = 1:1 or 1:3 in 50 ml deionized water and adjusting the pH value with 5 vol.% ammonia solution to pH = 8. The PXRD of Co1Mo3_pH8_P1 resembled the diffraction pattern of Co1Mo3_pH8_P2 and Co1Mo1_pH8_P2, whereas the application of Co:Mo = 1:1 in 50 ml water (P1) led to the formation of $CoMoO_4 \cdot 0.75H_2O$. ICP-OES measurements of Co1Mo1_pH8_P1 and Co1Mo3_pH8_P1 resulted in a product Co/Mo ratio of 1.2 and 1.0, respectively, indicating that the cobalt and molybdenum content depended rather on the pH value than on the initial Co/Mo ratio. The pH value determined the solubility of cobalt and molybdenum as well as the stability of different species in the aqueous solution. Comparison with sample Co1Mo1_AHM_pH8 for which a Co/Mo ratio of 2.0 was found by ICP-OES suggested

that a concentrated ammonia solution was required to achieve high cobalt content in the hydrothermally synthesized product.

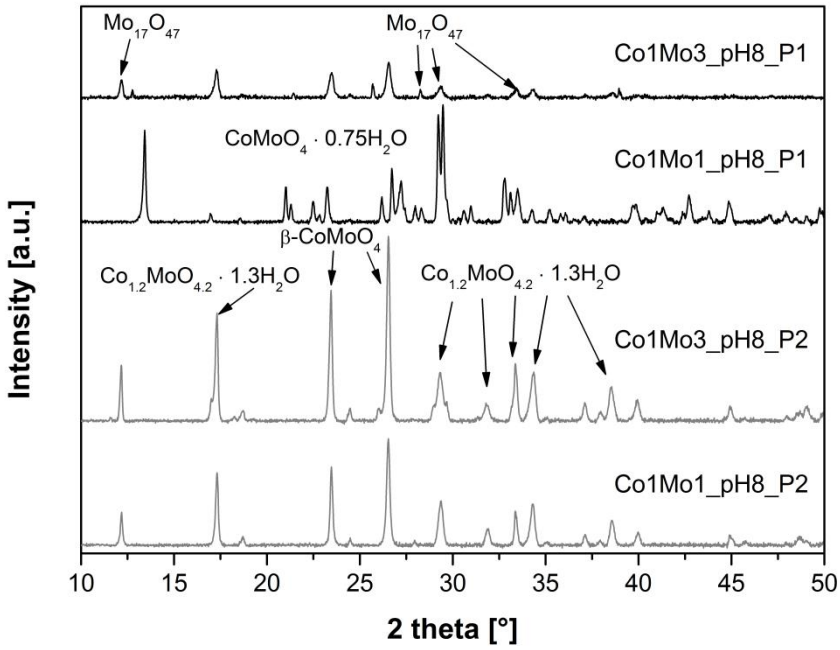

Figure 5.10: Powder X-ray diffraction pattern of hydrothermally synthesized samples from ammonium heptamolybdate and cobalt nitrate at pH = 8 at 180 °C for 24 h by different preparation routes.

5.3.4. Characterization of the samples prepared by flame spray pyrolysis and co-precipitation

For comparison four Co-Mo-oxides with Co/Mo = 1:1, 1:2, 1:3 and 1:4 were prepared by flame spray pyrolysis and the corresponding X-ray diffraction pattern are depicted in Figure 5.11. In contrast to the hydrothermally synthesized samples which contained a large variety of different phases and formed mainly cobalt molybdate hydrate (as described in 5.3.1, 5.3.2 and 5.3.3), flame spray pyrolysis led to the formation of β-$CoMoO_4$ and also α-MoO_3 in the case of the samples synthesized with an excess of molybdenum. Flame spray pyrolysis gives access to nanocrystalline particles and the powder X-ray diffraction pattern in Figure 5.11 suggest the formation of small particles or an amorphous phase. The reflection with the highest intensity for β-$CoMoO_4$ (JCPDS no. 21-868) is at $2\theta = 26.5°$, which is also the most intense reflection in the diffraction pattern of the four flame made samples. The sample synthesized with Co/Mo = 1:2 showed also reflections at 12.8° and

23.3°, where the reflections of β-$CoMoO_4$ and α-MoO_3 overlap. The shoulder at 27.3° clearly indicated the presence of α-MoO_3 and the intensity of this reflection at 27.3° increased for the samples prepared with higher molybdenum content.

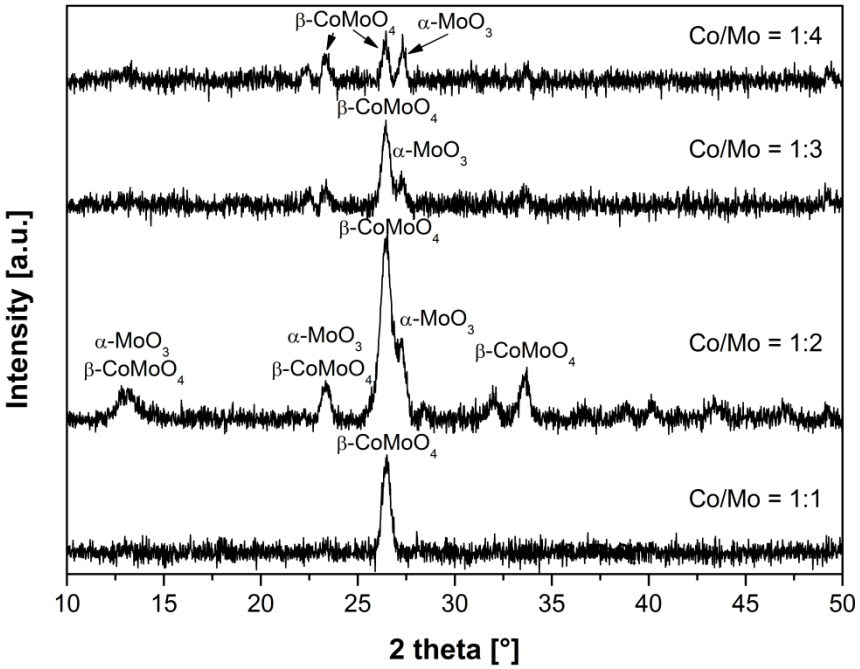

Figure 5.11: Powder X-ray diffraction pattern of flame made samples with different Co/Mo ratios.

In comparison with the hydrothermally synthesized samples the unsupported cobalt molybdates prepared by FSP exhibited relatively high specific surface areas, which decreased with increasing molybdenum content from 92 m^2/g (Co/Mo = 1:1) to 68 m^2/g (Co/Mo = 1:4). Recently unsupported cobalt molybdate was synthesized with Co/Mo = 1:3 by flame spray pyrolysis and the product had a specific surface area of 90 m^2/g, which is in the same range as for the sample obtained in this work (74 m^2/g) despite a different solvent (toluene instead of xylene), feed flow and gas flow. [76]

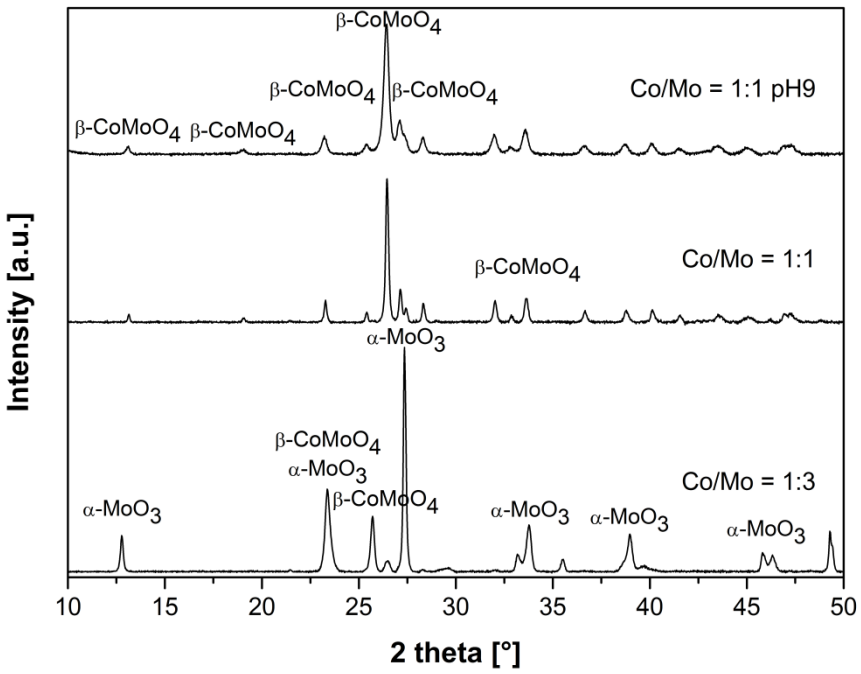

Figure 5.12: Powder X-ray diffraction pattern of co-precipitated samples with Co/Mo = 1:1 and 1:3.

Co-precipitation was used to prepare cobalt molybdates with Co/Mo ratios of 1:1 and 1:3. In the literature impregnated-thiosalt decomposition was mainly used for the preparation of unsupported Co-Mo-S [239-241, 244] but co-precipitation resembles hydrothermal synthesis using S-free precursors and obtaining an oxidic product. The PXRD of the sample synthesized with Co/Mo = 1:1 showed the characteristic features of β-$CoMoO_4$, whereas preparation with an excess of molybdenum (Co/Mo = 1:3) resulted also in the formation of α-MoO_3 (Figure 5.12). The surface area of both co-precipitated samples was low with 6 m^2/g for Co/Mo = 1:1 and 8 m^2/g for Co/Mo = 1:3. An increase of the pH value during co-precipitation to pH = 9 did not result in a change of the product phase.

5.3.5. Performance in hydrotreating and characterization of the spent catalysts

A selection of the hydrothermally synthesized samples at various pH values as well as the four flame made samples and the two co-precipitated materials were tested in hydrodesulfurization (HDS), hydrodenitrogenation (HDN) and hydrogenation (HYD) after *in situ* sulfidation with dimethyldisulfide (DMDS) at 350 °C.

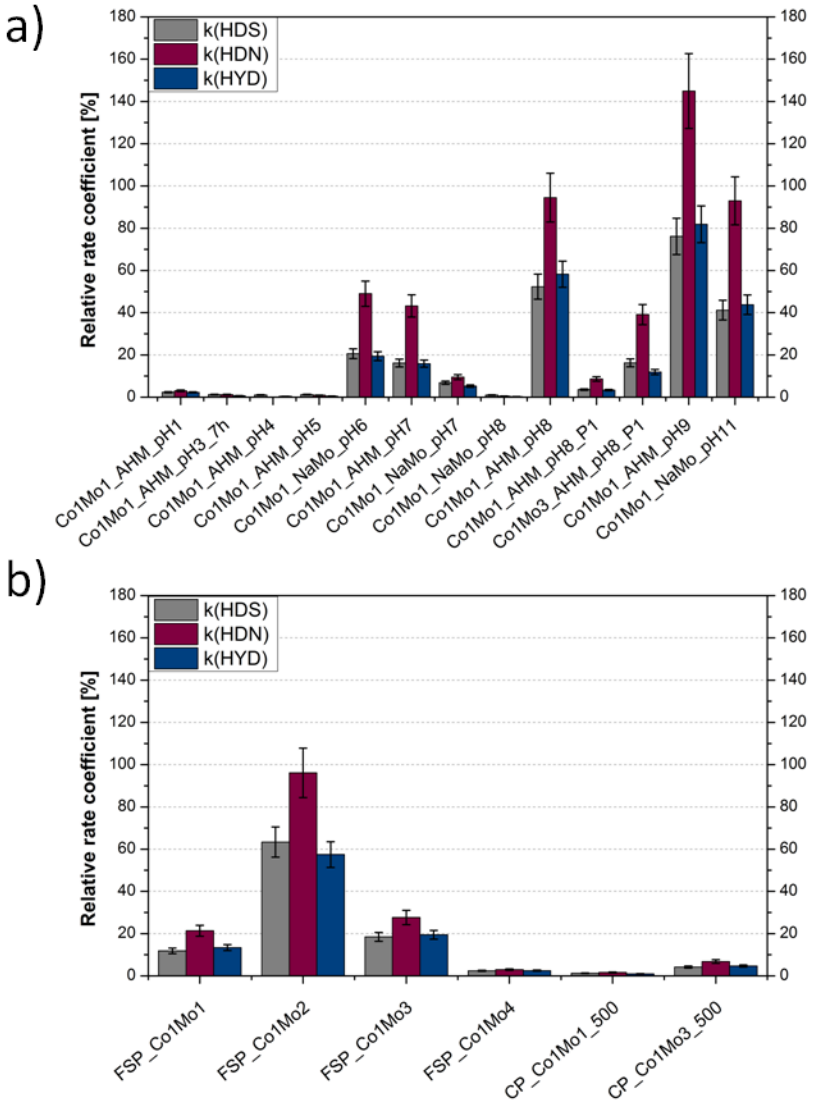

Figure 5.13: Experimentally determined pseudo first order rate constants in relation to an industrial Co-Mo reference catalyst ($k/k_{reference}$) for conversion of dibenzothiophene (HDS), indole (HDN) and naphthalene (HYD) for the hydrothermally synthesized samples (a) as well as the flame made and co-precipitated samples (b) (Reference: $k_{reference}$(HDS) = 90 h^{-1}, $k_{reference}$(HDN) = 44 h^{-1} and $k_{reference}$(HYD) = 32 h^{-1}). The error bars are calculated from the standard deviation determined from several k-values for the reference catalyst. The catalytic activity tests were performed at 350 °C at p(total) = 50 atm and $p(H_2)$ = 38 atm with a hydrogen flow rate of 250 Nml/min and 300 mg catalyst.

For comparison of the rates for HDS, HDN and HYD a model diesel feed containing dibenzothiophene, indole and naphthalene in n-heptane was used. The resulting performance for each reaction was compared to an industrial reference catalyst based on cobalt and molybdenum. The results of the activity measurements for the three reactions are reported relative to the reference (k/k_{ref}) and are depicted in Figure 5.13. The standard

deviation of the calculated pseudo first order rate constants was determined from several catalytic activity measurements of the reference and is given by the error bars. In Figure 5.13a the relative rate coefficients for the hydrothermally synthesized samples are shown and the samples are arranged according to the pH value during synthesis with low pH value and accordingly low Co-content on the left side. The samples synthesized at pH values below 6 were inactive for HDS, HDN and HYD, as well as the sample Co1Mo1_NaMo_pH8, Co1Mo1_AHM_pH8_P1. Co1Mo1_NaMo_pH6, Co1Mo1_AHM_pH7 and Co1Mo3_AHM_pH8_P1 showed medium activity with 16 - 20% activity for hydrodesulfurization, 40 - 50% activity for hydrodenitrogenation and 16 - 20% activity for hydrogenation compared to the industrial reference catalyst. The samples synthesized from ammonium heptamolybdate and cobalt nitrate at pH = 8 and from sodium molybdate and cobalt nitrate at pH = 11 reached almost the same activity for HDN as the reference catalyst but only 50% and 40% for HDS, respectively. Co1Mo1_AHM_pH9 obtained around 75% HDS activity related to the industrial reference catalyst, whereas the relative rate coefficient for HDN was higher and reached 140%.

In Table 5-4 the phase composition of the as-prepared and the spent catalysts according to X-ray diffraction are summarized. The samples are arranged according to their catalytic activity. In general, it was not possible to correlate the initial phases of the Co-Mo-O materials and the relative catalytic activity. For example Co1Mo1_AHM_pH7 and Co1Mo1_AHM_pH8_P1 consisted of $CoMoO_4 \cdot 0.75H_2O$, but the corresponding hydrotreating activity was different (relative rate coefficients: 16.2% and 3.6% respectively with a standard deviation of 11%). However, the samples prepared at low pH value containing a low Co content exhibited significantly lower catalytic activity than those prepared at neutral or basic pH values. Of particular interest are some of the samples synthesized at pH > 7 where the phase of the as-prepared materials could not be identified in the PXRD. The diffraction pattern of the spent catalysts (Figure 5.14) showed almost all the characteristic features of Co_9S_8 (JCPDS no. 56-002) and no evidence of MoS_2 with reflections at 2θ = 14.4°, 32.7°, 39.5°, 49.8° or any mixed phase. The hydrothermally synthesized samples with the highest catalytic activities exhibited relatively high surface areas (37 m²/g for Co1Mo1_AHM_pH9, 39 m²/g for Co1Mo1_AHM_pH8 and 42 m²/g for Co1Mo1_NaMo_pH11) along with a high cobalt content (Co/Mo = 2.0, 2.0 and 1.7 respectively). This supports the proposal in the literature that Co can not only act as a promoter in MoS_2 hydrotreating catalysts but Mo can also act as a promoter in Co_9S_8. [245,

[256-257] Supported hydrotreating catalysts usually consist mainly of MoS_2 on alumina and cobalt is added as a promoter decorating the edges of MoS_2 and increasing catalytic activity. It was demonstrated, that the promotion effect increases with increasing Co content until a maximum is reached, which lies typically between Co/Mo ratios of 0.1 – 0.3 for supported catalysts. Further addition of cobalt results in Co_9S_8 segregation leading to coexistence of both bulk phases, Co_9S_8 and MoS_2. This region was called "synergy by contact region" by the group of Chianelli [245, 257] and these two immiscible phases interact by forming surface phases or surface complexes [256]. However, in the region with excess molybdenum a Mo-Co-S phase can exist where Mo promotes the HDS activity of Co_9S_8. Bulk Co_9S_8 can be surface enriched with MoS_2 and the extent of this enrichment depends on the surface area of the material. [257]

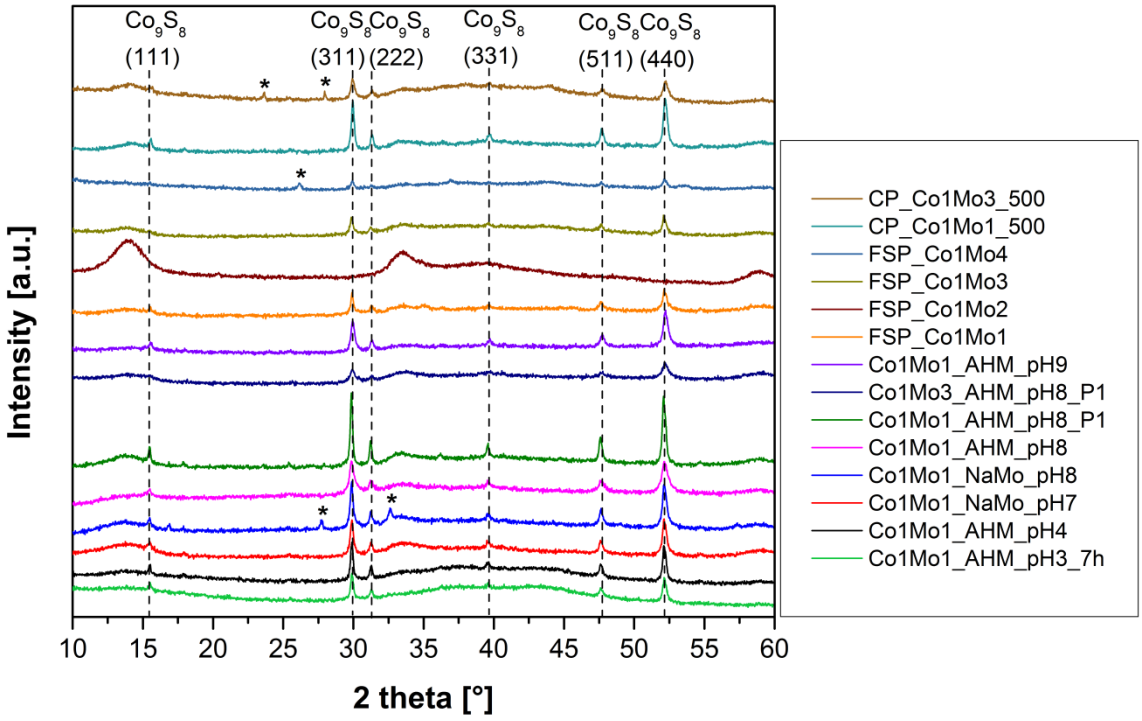

Figure 5.14: X-ray diffraction pattern of the sulfided catalysts after test reaction, where the stars indicate reflections which could not be assigned to a phase from the database.

Table 5-4: Phase composition of the oxidic precursor and the spent sulfidic catalyst as detected by powder X-ray diffraction, specific surface area of the as-prepared, crushed and spent catalysts and Co/Mo ratio of the oxidic material determined by ICP-OES or EDX. The catalytic hydrotreating activity was demonstrated by the relative rate coefficient ($k/k_{reference}$) for hydrodesulfurization (HDS) of DBT with $k_{reference}(HDS) = 90\ h^{-1}$ as well as the ratio of pre-hydrogenation (HYD) pathway (k(CHB)) to direct desulfurization (DDS) pathway (k(BP)) for the unsupported cobalt molybdate catalysts (cf. Figure 2.7).

Sample	**Phases according to PXRD**		**Surface area [m²/g]**			**Co/Mo ratio as-prep.**	**k/ k_{ref} (HDS)**	**k(CHB)/ k(BP)**
	as-prepared	**spent**	**as-prep.**	**crushed**	**spent**		**%**	
Co1Mo1_NaMo_pH8	$NaCo_2(OH)(MoO_4)_2 \cdot H_2O$	Co_9S_8 (+ 27.2°, 32.6°)	n.d.	11	2	1.3	1.0	0
Co1Mo1_AHM_pH4	$CoMo_4O_{13} \cdot 2H_2O$, ($CoMoO_4 \cdot 0.75H_2O$)	Co_9S_8	1	n.d.	3	0.4	1.0	0
Co1Mo1_AHM_pH5	$CoMo_4O_{13} \cdot 2H_2O$, $CoMoO_4 \cdot 0.75H_2O$	n.d.	1	n.d.	n.d.	0.7	1.3	0
Co1Mo1_AHM_pH3_7h	$CoMo_4O_{13} \cdot 2H_2O$	Co_9S_8	< 1	n.d.	2	0.3	1.3	0.08
CP_Co1Mo1_500	β-$CoMoO_4$	Co_9S_8	6	8	1	0.4	1.3	0.03
Co1Mo1_AHM_pH1	α-MoO_3, $NH_4Mo_5O_{15}(OH) \cdot 2H_2O$	n.d.	7	8	n.d.	0.01	2.3	0.03
FSP_Co1Mo4	β-$CoMoO_4$, α-MoO_3	Co_9S_8 (+ 26.1°)	68	n.d.	7	0.3	2.4	0.07
Co1Mo1_AHM_pH8_P1	$CoMoO_4 \cdot 0.75H_2O$	Co_9S_8	< 1	n.d.	1	1.2	3.6	0.24
CP_Co1Mo3_500	β-$CoMoO_4$, α-MoO_3	Co_9S_8 (+ 23.7°, 27.9°)	8	7	7	0.3	4.2	0.07
Co1Mo1_NaMo_pH7	$NaCo_2(OH)(MoO_4)_2 \cdot 2H_2O$	Co_9S_8	16	11	3	1.1	6.9	0.15
FSP_Co1Mo1	β-$CoMoO_4$	Co_9S_8	92	n.d.	27	1.1	11.9	0.28
Co1Mo1_AHM_pH7	$CoMoO_4 \cdot 0.75H_2O$	n.d.	11	n.d.	n.d.	n.d.	16.2	0.25
Co1Mo3_AHM_pH8_P1	$Co_{1.2}MoO_{4.2} \cdot 1.3H_2O$, β-$CoMoO_4$, $Mo_{17}O_{47}$	Co_9S_8	9	10	6	1.0	16.3	0.19
FSP_Co1Mo3	β-$CoMoO_4$, α-MoO_3	Co_9S_8	74	n.d.	5	n.d.	18.4	0.16
Co1Mo1_NaMo_pH6	$CoMoO_4$ (α+β)	n.d.	15	n.d.	n.d.	0.8	20.6	0.24
Co1Mo1_NaMo_pH11	Not identified reflections	n.d.	42	n.d.	n.d.	1.7	41.2	0.30
Co1Mo1_AHM_pH8	Not identified reflections	Co_9S_8	n.d.	39	17	2.0	52.3	0.38
FSP_Co1Mo2	β-$CoMoO_4$, α-MoO_3	amor-phous	81	n.d.	42	n.d.	63.4	0.25
Co1Mo1_AHM_pH9	Not identified reflections	Co_9S_8	37	n.d.	10	2.0	76.1	0.37

Inamura and Prins [240] studied unsupported Co-Mo-S catalysts prepared by impregnation of MoS_2 with cobalt nitrate and reported that Co situated at MoS_2 crystallites promote the activity in HDS. Further addition of cobalt resulted in the segregation of Co_9S_8 during the catalytic activity tests, which can act as a support for Co-promoted MoS_2 crystallites resulting in better accessibility of these MoS_2 crystallites and thus improved catalytic activity. This segregation of Co from CoMoS followed by formation of Co_9S_8 was also observed by Karroua et al. [161], who prepared unsupported Co-Mo-S materials by homogeneous sulfide precipitation. This CoMoS decomposition was accompanied by sintering of the MoS_2 crystallites. In the early works of the group of Topsøe [146] it was demonstrated that Co-Mo-S catalysts showed maximum activity when segregated CoS_x was detected. Furthermore it has been observed for unsupported Ni/MoS_2 or Ni/WS_2 systems, which have similar structural properties than Co-Mo-S materials, that active catalysts for HDS were obtained when MoS_2 or WS_2 slabs are dispersed on nickel sulfide bulk particles (NiS or Ni_7S_6). [258-259] Farag et al. [260] showed for unsupported MoS_2 catalysts that the sample with the highest surface area also exhibited the highest activity for hydrodesulfurization of DBT.

The oxidic precursors Co1Mo1_NaMo_pH11, Co1Mo1_AHM_pH8 and Co1Mo1_AHM_pH9 leading to highly active unsupported hydrotreating catalysts contained an excess of cobalt combined with a relatively high specific surface area (~40 m^2/g). On the one hand, the high Co-content could result in segregated Co_9S_8 supporting active Co-promoted MoS_2. On the other hand, the unknown phase or phase mixture of the as-prepared materials may be beneficial for the formation of a close contact between Co_9S_8 and MoS_2 during sulfidation. The presence of MoS_2 was not detected by X-ray diffraction (cf. Figure 5.14) neither for the samples with a high cobalt content nor for the samples with a high amount of molybdenum. This could be explained by an amorphous character of MoS_2 and MoS_2 acting as a support for Co_9S_8 for the samples containing small amounts of cobalt. It has been demonstrated that MoS_2 can support Co_9S_8 [261-263] and maximum activity results when Co_9S_8 is optimally dispersed on MoS_2. [261] In this work the Co_9S_8 crystallites are large enough to be detected in the diffraction pattern resulting in low catalytic activity. In the cobalt rich samples Co_9S_8 can act as support for highly dispersed MoS_2, which cannot be detected in PXRD.

For comparison, unsupported cobalt molybdates prepared by co-precipitation and flame spray pyrolysis were tested in hydrotreating and the results of the activity measurements are depicted in Figure 5.13b. The co-precipitated sample synthesized with a ratio of Co/Mo = 1:1 was inactive with respect to HDS, HDN and HYD, whereas an increase in molybdenum content from Co/Mo = 0.4 to 0.3 for CP_Co1Mo3_500 resulted in very low catalytic activity with relative rate coefficients for HDS, HDN and HYD of 4%, 7% and 5%, respectively. This indicates that the co-precipitated samples follow the opposite trend compared to the hydrothermally prepared samples where a higher cobalt content led to higher activity. However, the overall hydrotreating activity of the co-precipitated samples as well as their surface areas were low (< 10 m^2/g). The flame made samples exhibiting relatively high surface areas (92 – 68 m^2/g) reached maximum activity for HDS, HDN and HYD with Co/Mo = 1:2 (relative rate coefficients 63%, 96% and 57%), whereas the flame made sample with Co/Mo = 1:4 was almost inactive and hardly showed the formation of cobalt sulfides in the diffraction pattern of the spent catalysts (Figure 5.14). The activity results of the flame made Co-Mo-O samples assist the conclusion for the hydrothermally synthesized samples that low cobalt content (Co/Mo < 0.3) leads to inactive unsupported hydrotreating catalysts. Obviously the ratio Co/Mo = 1:2 is beneficial for the hydrotreating activity of unsupported flame made cobalt molybdates. The effect of different Co/Mo ratios on the hydrotreating activity of unsupported and supported catalysts was studied before. [146, 243, 264] Wivel et al. [146] found that maximum activity can be achieved with Co/Mo = 1.0 for supported Co-Mo/Al_2O_3. In general they detected three different Co-species: Co located in the alumina support, Co_9S_8 and cobalt in the Co-Mo-S surface (cf. Figure 1.11), whereas Co_9S_8 was only present in catalysts with Co/Mo > 0.4. Unsupported Co-Mo-S samples prepared by homogeneous sulfide precipitation showed maximum activity with Co/Mo = 0.5 [243] which agrees with the flame made samples studied in the present work. Zabala et al. [264] demonstrated for reduced and sulfided mixtures of Co_3O_4 and MoO_3 that their catalytic activity in HDS depends on the sulfidation temperatures with H_2S: sulfidation at 800 °C resulted in a maximum activity for Co/(Co+Mo) = 0.5 whereas at 400 °C the sulfided samples exhibited maximum activity with Co/(Co+Mo) = 0.67. After the catalytic test all samples with Co/(Co+Mo) = 0.05 – 0.85 contained MoS_2 and Co_9S_8 according to the X-ray diffraction measurements, whereas in the present work only Co_9S_8 was detected by PXRD (cf. Figure 5.14). In a previous study unsupported cobalt molybdate with Co/Mo = 1:3 and supported Co-Mo-oxides prepared by flame spray

pyrolysis were studied. [76] The unsupported catalyst with a surface area of 90 m²/g composed of a mixture of β-$CoMoO_4$ and MoO_3 exhibited higher activity than the corresponding sample synthesized in the present work (FSP_Co1Mo3) but lower activity than FSP_Co1Mo2. The supported catalysts were prepared with Co/Mo = 1:3 by FSP and it may be worth to study these supported flame made catalysts with Co/Mo = 1:2 in the future.

Hydrodesulfurization can proceed via two different routes: the direct desulfurization route (DDS) and the pre-hydrogenation route (see Figure 2.7). The selectivity of HDS to biphenyl (BP) or cyclohexyl benzene (CHB) provides information about the favored pathway on the corresponding catalysts and on its hydrogenation ability, which was additionally determined by HYD of naphthalene. Industrial Co-Mo/Al_2O_3 catalysts typically yield a ratio of k(CHB)/k(BP) of 0.15 [194] showing that the direct desulfurization pathway is favored. The commercial Co-Mo-S catalyst tested in the present study exhibited a selectivity of k(CHB)/k(BP) = 0.19. For all catalysts the selectivity for BP was higher than for CHB and the direct desulfurization pathway was preferred (Table 5-4), but the ratios for the active catalysts Co1Mo1_NaMo_pH11, Co1Mo1_AHM_pH8 and Co1Mo1_AHM_pH9 were relatively high compared to the commercial Co-Mo-S reference catalyst and resembled the values for supported nickel catalysts (NiMo/Al_2O_3: k(CHB)/k(BP) ≈ 0.35 [194]). MoS_2 particles are organized into stacked slabs consisting of Mo sandwiched between two S, which appear as dark lines in TEM images. It is generally accepted that the active sites on external layers of these stacked slabs perform both DBT hydrogenation steps and desulfurization, whereas the edge sites located on internal slabs will only be able to perform direct desulfurization. Therefore stacking height can directly influence HDS selectivity. [237] Hence, high selectivity towards CHB implies the presence of a high ratio of external slabs due to a low amount of stacking. Herbst et al. [194] observed that short single layered MoS_2 showed the highest activity in hydrotreating. Co1Mo1_AHM_pH9 and Co1Mo1_AHM_pH8 resulted in k(CHB)/k(BP) = 0.37 and 0.38 compared to 0.19 for the industrial reference catalyst suggesting that these materials show MoS_2 layers of low stacking degree giving access to the pre-hydrogenation route and to a relatively high overall activity. Therefore, three hydrothermally synthesized samples with different activity were characterized by transmission electron microscopy (TEM) after application in hydrotreating i.e. after sulfidation and the distribution of number of slabs and slab length were determined. TEM characterization of Co1Mo1_NaMo_pH11,

Co1Mo1_NaMo_pH6 and Co1Mo1_NaMo_pH11 (k/k_{ref}(HDS) = 41.2%, 20.6% and 16.2%, respectively) revealed the characteristic dark lines indicating the presence of MoS_2 (see Figure 5.15).These MoS_2 slabs formed also curved morphologies leading to defect sites on these curved basal planes which are considered to be active in HDS. [239, 265] Figure 5.15 c, f and i show the statistical distribution of the number of slabs and slab length obtained from various TEM images, which suggest a small shift to single, double and triple layered slabs along with shorter length for Co1Mo1_NaMo_pH11. This may explain the higher catalytic activity in combination with the increased cobalt content.

For hydrodenitrogenation (HDN) the direct denitrogenation pathway is inhibited by H_2S [266], which is formed during hydrodesulfurization, hence pre-hydrogenation takes place i.e. in the first step indole is hydrogenated and in the second step N is removed [267-268]. Therefore a low stacking degree of MoS_2 slabs is also crucial for the activity in HDN and sample Co1Mo1_AHM_pH9 which exhibited relatively high activity for hydrogenation of naphthalene also showed high HDN activity. Jian and Prins [269-270] found that hydrogenolysis for HDN requires highly unsaturated molybdenum atoms, which could also be present in Co1Mo1_AHM_pH9.

Preparation of cobalt molybdates by different methods led to sulfided hydrotreating catalysts, which showed different activity. Characterization of the sulfided, spent samples did not clearly elucidate the reason for the differing catalytic performances. Therefore, it is important to identify the initial phase composition of the more active samples synthesized by hydrothermal synthesis under basic condition e.g. by means of X-ray absorption spectroscopy. X-ray absorption spectroscopy could also be used to analyze the state of molybdenum in the sulfided samples, because the X-ray diffraction pattern gave no information about the molybdenum phase. For a detailed understanding of the formation of the active sites and their characteristics, the sulfidation process needs to be investigated e.g. by *in situ* Raman spectroscopy.

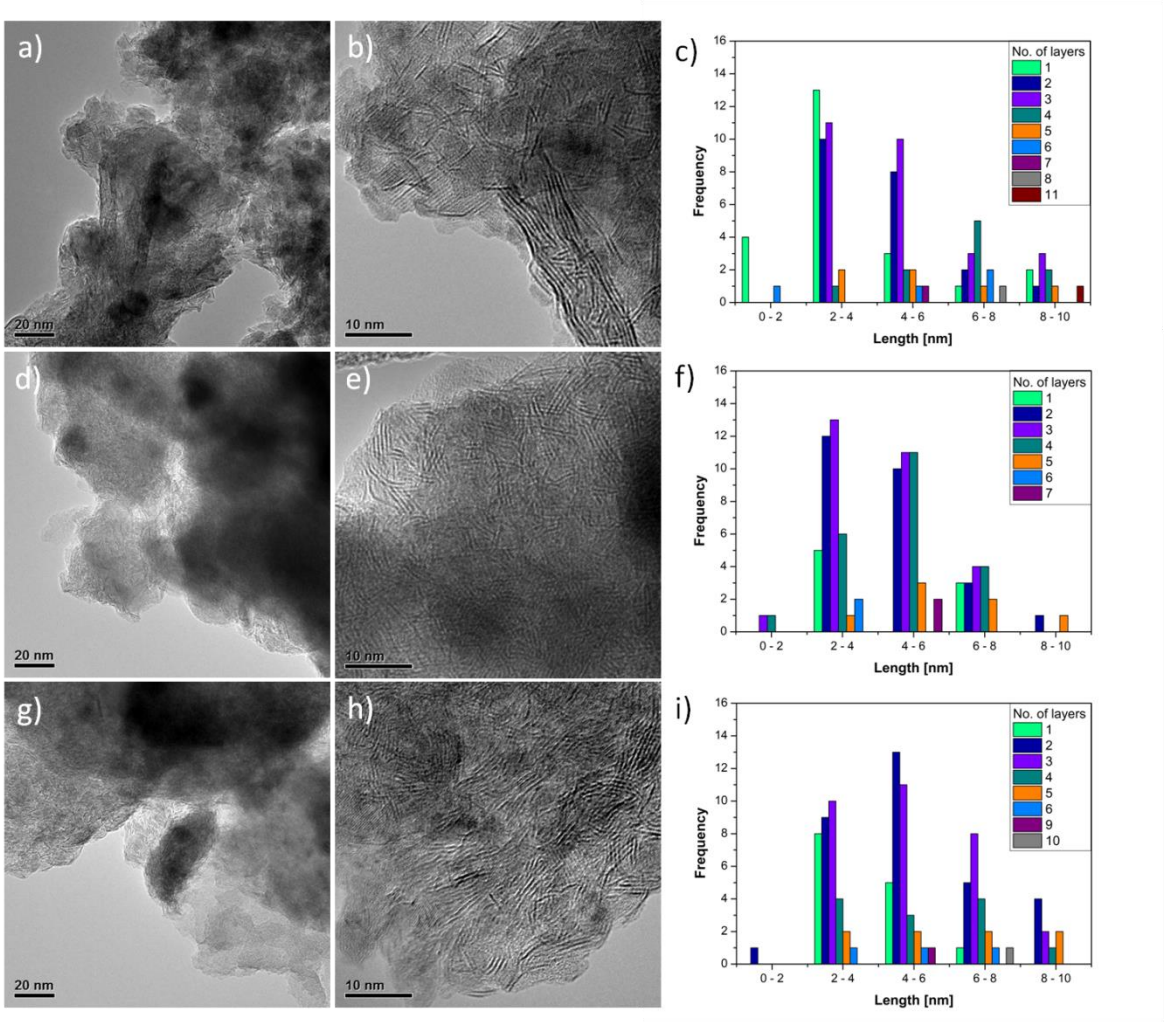

Figure 5.15: Transmission electron microscopy (TEM) images of three sulfidic catalysts after catalytic activity measurements with corresponding statistical distributions of the MoS_2 slab number and length a – c) Co1Mo1_NaMo_pH11, d – f) Co1Mo1_NaMo_pH6 and g – i) Co1Mo1_AHM_pH7.

5.4. Conclusions

The hydrothermal synthesis of cobalt molybdates was systematically studied as a function of pH and Co/Mo ratio applying two molybdenum precursors. This gave access to a large variety of phases mainly influenced by the pH value and the precursor. Under acidic conditions cobalt was not sufficiently incorporated and molybdenum rich phases such as α-MoO_3 or $CoMo_4O_{13} \cdot 2H_2O$ were formed. At pH = 5 – 7 $NaCo_2(OH)(MoO_4)_2 \cdot 2H_2O$, $CoMoO_4$ and $CoMoO_4 \cdot 0.75H_2O$ were obtained. At high pH values (pH = 8 – 10), higher cobalt contents were detected in the products but the determination of the phase composition was not possible by means of X-ray diffraction. The solubility of the

precursors under ambient and under hydrothermal conditions was strongly dependent on the pH value, thus a change in the initial Co/Mo ratio only slightly influenced the phase composition and Co/Mo ratio of the product.

The Mo-rich phases of the samples synthesized at low pH values under hydrothermal conditions were inactive for hydrotreating. A higher Co-concentration in the product applying higher pH values in combination with a relatively high surface area (for unsupported catalysts) resulted in much higher HDS, HDN and HYD activity, probably due to the promotion effect of Co_9S_8 with Mo or Co_9S_8 serving as a support for highly dispersed Co-promoted MoS_2. The catalyst with the best catalytic performance additionally exhibited relatively high selectivity for the pre-hydrogenation pathway, suggesting the presence of MoS_2 slabs with low degree of stacking and short length exhibiting mainly external slabs. Hence, hydrothermal synthesis is a very interesting route for the preparation of unsupported hydrotreating catalysts.

Flame spray pyrolysis led to β-$CoMoO_4$ and additionally to MoO_3 when an excess of molybdenum was applied showing relatively high surface areas. The hydrotreating activity for the flame made materials could be optimized by using a variation of Co/Mo ratios and was found to be best for the sample synthesized with Co/Mo = 1:2.

Cobalt molybdates are also attractive in selective oxidation reactions e.g. in oxidative dehydrogenation of propane. They could also be studied in connection with bismuth molybdates for example by mechanical mixing of cobalt and bismuth molybdate and application in propylene oxidation.

6 Final remarks and Outlook

The present work shows that hydrothermal synthesis is a well suited method for the preparation of model catalysts for various applications. As an example for a relatively easy model system α-MoO_3 with different morphologies could be successfully prepared and correlations of the reactivity with the exposed surface were found using propylene oxidation as a model reaction. Extension of this study towards more complex mixed molybdates resulted in a large variety of phases. Hence, the correlation between the morphology and the catalytic activity is more challenging in this case. On the other hand the preparation of different phases under comparable reaction conditions offers new possibilities giving access to a variety of model systems.

The pH value during hydrothermal synthesis strongly influences the phase composition, the morphology and the surface area. Variation of the pH value results in a change of the polymolybdate species in the aqueous solution and therefore different phases are formed. At low pH values molybdenum rich phases were found, whereas at high pH values phases with a high amount of the other transition metal (Bi, Co, ..) were obtained. The pH value of the initial solution also influenced the surface area and the composition at the surface.

Addition of nitric acid and / or ammonia solution during hydrothermal synthesis resulted in higher catalytic activity probably due to the stabilization of the morphology. The influence of nitrogen incorporation could be excluded. Calcination of the bismuth molybdates had a negative effect on the catalytic performance in propylene oxidation independent of the phase change. These results indicate the importance to prepare catalysts under the same conditions or applying the same thermal treatment to compare their catalytic performance.

In the selective oxidation of propylene a relatively large amount of (100) facets seems to be crucial for high propylene conversion, whereas the morphology had no influence on the selectivity to acrolein. The relative activity of bismuth molybdates decreased in the following order: β > γ > α. One-step flame spray pyrolysis enabled the preparation of β-$Bi_2Mo_2O_9$ which however decomposed into α-$Bi_2Mo_3O_{12}$ and γ-Bi_2MoO_6 at temperatures above 400 °C thereby deactivating. Hydrothermal synthesis gave access to γ-Bi_2MoO_6 with relatively high surface area which showed high propylene conversion at high acrolein selectivity but deactivated at T ≥ 400 °C probably due to a loss in surface area. γ-Bi_2MoO_6 with different morphologies using Bi/Mo = 2:1 was successfully synthesized in literature at various pH values [28] and similar samples could be tested in selective oxidation of propylene investigating the influence of the particle morphology on the catalytic activity and selectivity of γ-Bi_2MoO_6. Hydrothermal synthesis of more complex systems e.g. addition of Co or Fe may result in more stable catalysts especially at higher temperatures and may also result in higher surface area. However, addition of other transition metals will also lead to a larger variety of phases along with more complex phases so that phase identification will be a great challenge. The catalytic performance of these complex materials could be compared to the performance of samples synthesized by physically mixing the corresponding bi-metallic oxides e.g. hydrothermally synthesized Bi-Co-Mo-O could be compared to a physical mixture of hydrothermally synthesized Bi-Mo-O and hydrothermally synthesized Co-Mo-O. All structures and compositions should be studied in detail before and after the catalytic activity measurements. A corresponding study should be performed for flame made samples.

Hydrothermal synthesis of cobalt molybdates at high pH values gave access to Co-rich products with a relatively high surface area resulting in relatively high activity for hydrodesulfurization, hydrodenitrogenation and hydrogenation. The precursor phases of these hydrothermally synthesized samples at high pH value should be identified e.g. by X-ray absorption spectroscopy (XAS). This will help to understand the nature of the varying activities. Additionally to cobalt molybdates the corresponding nickel molybdates can be synthesized by hydrothermal synthesis although their preparation is more challenging and for several pH values in first preparation experiments only small amounts of product were formed. Several samples based on nickel and molybdenum have already been synthesized but the preparation needs to be optimized. Flame spray pyrolysis of nickel molybdates should be avoided due to the toxicity of nickel.

One selected hydrothermally synthesized sample of each cobalt molybdate and nickel molybdate was additionally tested in selective oxidation of propylene but the resulting pressure drop over the catalyst bed was too high. High temperatures arose due to the exothermic reaction and high activity of these samples. Adequate test conditions need to be identified and the cobalt and nickel molybdates should be diluted in the reactor for the selective oxidation of propylene. Both materials, cobalt and nickel molybdate, are also attractive materials for oxidative dehydrogenation of propane, as propane is more difficult to activate than propylene.

As a next step, *in situ* methods e.g. *in situ* Raman spectroscopy, X-ray diffraction or X-ray absorption spectroscopy should be applied to elucidate the active phase in selective oxidation of propylene under reaction conditions. Observation of the sulfidation process of the active cobalt molybdate catalysts e.g. by Raman spectroscopy will give new insight in the formation of the active sites and the reorganization in the structure during reduction and sulfur incorporation.

The crystallization and growth mechanism of bismuth molybdates during hydrothermal synthesis were already studied in the literature but hydrothermal synthesis of cobalt and nickel molybdates has not yet been investigated by *in situ* methods. In situ X-ray absorption spectroscopy (XAS) measurements could be applied to study the nucleation, crystallization and particle growth during hydrothermal synthesis of cobalt and nickel molybdates under various reaction conditions. Thereby knowledge of the processes inside the autoclave can be generated which will lead one step further towards the rational design of hydrothermally synthesized materials. The information on the particle growth and crystallization of bismuth molybdates and cobalt molybdates can be further applied to the preparation of more complex multicomponent molybdates and the preparation of Bi-Co-Mo-O should also be followed by *in situ* XAS measurements.

With respect to flame spray pyrolysis bismuth, cobalt and molybdenum precursors as well as spray conditions should be varied to synthesize samples with different particle size, surface area and possibly also phase composition. Maybe more stable β-$Bi_2Mo_2O_9$ or β-$Bi_2Mo_2O_9$ with a higher surface area resulting in increased catalytic performance can be prepared. Stabilization of β-$Bi_2Mo_2O_9$ e.g. by addition of cobalt or iron should be investigated to obtain highly active and selective catalysts for the selective oxidation of propylene.

References

[1] K. Byrappa and M. Yoshimura *Handbook of hydrothermal technology*; Noyes Publications: NJ, USA, 2001.

[2] J. S. O. Evans, R. J. Francis, D. Ohare, S. J. Price, S. M. Clark, J. Flaherty, J. Gordon, A. Nield and C. C. Tang *An apparatus for the study of the kinetics and mechanism of hydrothermal reactions by in-situ energy-dispersive X-ray diffraction*, Rev. Sci. Instrum. **1995**, *66*, 2442-2445.

[3] M. Yoshimura and K. Byrappa *Hydrothermal processing of materials: past, present and future*, J. Mater. Sci. **2008**, *43*, 2085-2103.

[4] J. Gopalakrishnan *Chimie douce approaches to the synthesis of metastable oxide materials*, Chem. Mater. **1995**, *7*, 1265-1275.

[5] A. Clearfield *Hydrothermal synthesis of selected phosphates and molybdates*, Prog. Crystal Growth Charact. **1990**, *21*, 1-28.

[6] M. S. Whittingham, J. D. Guo, R. J. Chen, T. Chirayil, G. Janauer and P. Zavalij *The hydrothermal synthesis of new oxide materials*, Solid State Ionics **1995**, *75*, 257-268.

[7] A. Michailovski, J.-D. Grunwaldt, A. Baiker, R. Kiebach, W. Bensch and G. R. Patzke *Studying the solvothermal formation of MoO_3 fibers by complementary in situ EXAFS/EDXRD techniques*, Angew. Chem. Int. Edit. **2005**, *44*, 5643-5647.

[8] A. M. Beale and G. Sankar *In situ study of the formation of crystalline bismuth molybdate materials under hydrothermal conditions*, Chem. Mater. **2003**, *15*, 146-153.

[9] C. V. Ramana, V. V. Atuchin, I. B. Troitskaia, S. A. Gromilov, V. G. Kostrovsky and G. B. Saupe *Low-temperature synthesis of morphology controlled metastable hexagonal molybdenum trioxide (MoO_3)*, Solid State Comm. **2009**, *149*, 6-9.

[10] X. W. Lou and H. C. Zeng *Hydrothermal synthesis of alpha-MoO_3 nanorods via acidification of ammonium heptamolybdate tetrahydrate*, Chem. Mater. **2002**, *14*, 4781-4789.

[11] G. R. Patzke, A. Michailovski, F. Krumeich, R. Nesper, J.-D. Grunwaldt and A. Baiker *One-step synthesis of submicrometer fibers of MoO_3*, Chem. Mater. **2004**, *16*, 1126-1134.

[12] K. Dewangan, S. S. Patil, D. S. Joag, M. A. More and N. S. Gajbhiye *Topotactical Nitridation of alpha-MoO_3 Fibers to gamma-Mo_2N Fibers and Its Field Emission Properties*, J. Phys. Chem. C **2010**, *114*, 14710-14715.

[13] A. Chithambararaj and A. C. Bose *Hydrothermal synthesis of hexagonal and orthorhombic MoO_3 nanoparticles*, J. Alloys Compd. **2011**, *509*, 8105-8110.

[14] K. Dewangan, N. N. Sinha, P. K. Sharma, A. C. Pandey, N. Munichandraiah and N. S. Gajbhiye *Synthesis and characterization of single-crystalline alpha-MoO_3 nanofibers for enhanced Li-ion intercalation applications*, Cryst.Eng. Comm **2011**, *13*, 927-933.

[15] H. Sinaim, D. J. Ham, J. S. Lee, A. Phuruangrat, S. Thongtem and T. Thongtem *Free-polymer controlling morphology of alpha-MoO_3 nanobelts by a facile hydrothermal synthesis, their electrochemistry for hydrogen evolution reactions and optical properties*, J. Alloys Compd **2012**, *516*, 172-178.

[16] Z. Li, Y. Li, E. Zhan, N. Ta and W. Shen *Morphology-controlled synthesis of alpha-MoO_3 nanomaterials for ethanol oxidation*, J. Mater. Chem. A **2013**, *1*, 15370-15376.

[17] S. T. Wang, Y. G. Zhang, X. C. Ma, W. Z. Wang, X. B. Li, Z. D. Zhang and Y. T. Qian *Hydrothermal route to single crystalline alpha-MoO_3 nanobelts and hierarchical structures*, Solid State Comm. **2005**, *136*, 283-287.

[18] L. Zheng, Y. Xu, D. Jin and Y. Xie *Novel Metastable Hexagonal MoO_3 Nanobelts: Synthesis, Photochromic, and Electrochromic Properties*, Chem. Mater. **2009**, *21*, 5681-5690.

[19] A. Chithambararaj, N. S. Sanjini, A. C. Bose and S. Velmathi *Flower-like hierarchical h-MoO_3: new findings of efficient visible light driven nano photocatalyst for methylene blue degradation*, Catal. Sci. Technol. **2013**, *3*, 1405-1414.

[20] Y. Xu, L. Xie, Y. Zhang and X. Cao *Hydrothermal synthesis of hexagonal MoO_3 and its reversible electrochemical behavior as a cathode for Li-ion batteries*, Electron. Mater. Lett. **2013**, *9*, 693-696.

[21] T. A. Xia, Q. Li, X. D. Liu, J. A. Meng and X. Q. Cao *Morphology-controllable synthesis and characterization of single-crystal molybdenum trioxide*, J. Phys. Chem. B **2006**, *110*, 2006-2012.

[22] F. Paraguay-Delgado, M. A. Albiter, R. Huirache-Acuña, Y. Verde and G. Alonso-Nuñez *Optimization of the Synthesis of α-MoO_3 Nanoribbons and Hydrodesulfurization (HDS) Catalyst Test*, J. Nanosci. Nanotechno. **2007**, *7*, 3677-3683.

[23] E. Devers, P. Afanasiev, B. Jouguet and M. Vrinat *Hydrothermal syntheses and catalytic properties of dispersed molybdenum sulfides*, Catal. Lett. **2002**, *82*, 13-17.

[24] B. Yoosuk, J. H. Kim, C. Song, C. Ngamcharussrivichai and P. Prasassarakich *Highly active MoS_2, $CoMoS_2$ and $NiMoS_2$ unsupported catalysts prepared by hydrothermal synthesis for hydrodesulfurization of 4,6-dimethyldibenzothiophene*, Catal. Today **2008**, *130*, 14-23.

[25] Y. Shi, S. Feng and C. Cao *Hydrothermal synthesis and characterization of Bi_2MoO_6 and Bi_2WO_6*, Mater. Lett. **2000**, *44*, 215-218.

[26] C. Xu, D. Zou, L. Wang, H. Luo and T. Ying *γ-Bi_2MoO_6 nanoplates: Surfactant-assisted hydrothermal synthesis and optical properties*, Ceram. Int. **2009**, *35*, 2099-2102.

[27] M. Maczka, L. Macalik, K. Hermanowicz, L. Kepinski and J. Hanuza *Synthesis and phonon properties of nanosized Aurivillius phase of Bi_2MoO_6*, J. Raman Spectrosc. **2010**, *41*, 1289-1296.

[28] L. Zhang, T. Xu, X. Zhao and Y. Zhu *Controllable synthesis of Bi_2MoO_6 and effect of morphology and variation in local structure on photocatalytic activities*, Appl. Catal., B **2010**, *98*, 138-146.

[29] J. Q. Yu and A. Kudo *Hydrothermal synthesis and photocatalytic property of 2-dimensional bismuth molybdate nanoplates*, Chem. Lett. **2005**, *34*, 1528-1529.

[30] A. Phuruangrat, P. Jitrou, P. Dumrongrojthanath, N. Ekthammathat, B. Kuntalue, S. Thongtem and T. Thongtem *Hydrothermal Synthesis and Characterization of Bi_2MoO_6 Nanoplates and Their Photocatalytic Activities*, J. Nanomater. **2013**.

[31] D. J. Buttrey, T. Vogt, U. Wildgruber and W. R. Robinson *Structural refinement of the high temperature form of Bi_2MoO_6*, J. Solid State Chem. **1994**, *111*, 118-127.

[32] D. J. Buttrey, D. A. Jefferson and J. M. Thomas in *The structural relationships between the various phases of bismuth molybdates with special reference to their catalytic activity*, **1986**.

[33] J. Ren, W. Wang, M. Shang, S. Sun and E. Gao *Heterostructured Bismuth Molybdate Composite: Preparation and Improved Photocatalytic Activity under Visible-Light Irradiation*, ACS Appl. Mater. Interfaces **2011**, *3*, 2529-2533.

[34] H. Li, K. Li and H. Wang *Hydrothermal synthesis and photocatalytic properties of bismuth molybdate materials*, Mater. Chem. Phys. **2009**, *116*, 134-142.

[35] C. Kongmark, R. Coulter, S. Cristol, A. Rubbens, C. Pirovano, A. Loefberg, G. Sankar, W. van Beek, E. Bordes-Richard and R.-N. Vannier *A Comprehensive Scenario of the Crystal Growth of gamma-Bi_2MoO_6 Catalyst during Hydrothermal Synthesis*, Cryst. Growth Des. **2012**, *12*, 5994-6003.

[36] A. R. Landa-Canovas, E. Vila, J. Hernandez-Velasco, J. Galy and A. Castro *Structural elucidation of the $Bi_{2(n+2)}Mo_nO_{6(n+1)}$ (n=3, 4, 5 and 6) family of fluorite superstructures by transmission electron microscopy*, Acta Crystallogr., Section B: Struct. Sci. **2009**, *65*, 458-466.

[37] R. Gruar, C. J. Tighe, L. M. Reilly, G. Sankar and J. A. Darr *Tunable and rapid crystallisation of phase pure Bi_2MoO_6 (koechlinite) and $Bi_2Mo_3O_{12}$ via continuous hydrothermal synthesis*, Solid State Sci. **2010**, *12*, 1683-1686.

[38] K. Eda, Y. Uno, N. Nagai, N. Sotani and M. S. Whittingham *Crystal structure of cobalt molybdate hydrate $CoMoO_4 \cdot nH_2O$*, J. Solid State Chem. **2005**, *178*, 2791-2797.

[39] K. Eda, Y. Kato, Y. Ohshiro, T. Sugitani and M. S. Whittingham *Synthesis, crystal structure, and structural conversion of Ni molybdate hydrate $NiMoO_4 \cdot nH_2O$*, J. Solid State Chem. **2010**, *183*, 1334-1339.

[40] K. Eda, Y. Ohshiro, N. Nagai, N. Sotani and M. S. Whittingham *Transition metal tetramolybdate dihydrates $MMo_4O_{13} \cdot 2H_2O$(M = Co,Ni) having a novel pillared layer structure*, J. Solid State Chem. **2009**, *182*, 55-59.

[41] K. Eda, Y. Uno, N. Nagai, N. Sotani, C. Chen and M. S. Whittingham *Structure-inheriting solid-state reactions under hydrothermal conditions*, J. Solid State Chem. **2006**, *179*, 1453-1458.

[42] J. A. Rodriguez, S. Chaturvedi, J. C. Hanson and J. L. Brito *Reaction of H_2 and H_2S with $CoMoO_4$ and $NiMoO_4$: TPR, XANES, time-resolved XRD, and molecular-orbital studies*, J. Phys. Chem. B **1999**, *103*, 770-781.

[43] J. L. Rico, M. Avalos-Borja, A. Barrera and J. S. J. Hargreaves *Template-free synthesis of $CoMoO_4$ rods and their characterization*, Mater. Res. Bull. **2013**, *48*, 4614-4617.

[44] Y. Ding, Y. Wan, Y.-L. Min, W. Zhang and S.-H. Yu *General synthesis and phase control of metal molybdate hydrates $MMoO_4 \cdot nH_2O$ (M = Co, Ni, Mn, n=0, 3/4, 1) nano/microcrystals by a hydrothermal approach: Magnetic, photocatalytic, and electrochemical properties*, Inorg. Chem. **2008**, *47*, 7813-7823.

[45] W. Xiao, J. S. Chen, C. M. Li, R. Xu and X. W. Lou *Synthesis, Characterization, and Lithium Storage Capabitity of $AMoO_4$ (A = Ni, Co) Nanorods*, Chem. Mater. **2010**, *22*, 746-754.

[46] Y. Kong, J. Peng, Z. Xin, B. Xue, B. Dong, F. Shen and L. Li *Selective synthesis and novel properties of single crystalline alpha-$CoMoO_4$ nanorods/nanowhiskers*, Mater. Lett. **2007**, *61*, 2109-2112.

[47] L. A. Palacio, A. Echavarria, L. Sierra and E. A. Lombardo *Cu, Mn and Co molybdates derived from novel precursors catalyze the oxidative dehydrogenation of propane*, Catal. Today **2005**, *107-08*, 338-345.

[48] M. Salamanca, Y. E. Licea, A. Echavarria, A. C. Faro, Jr. and L. A. Palacio *Hydrothermal synthesis of new wolframite type trimetallic materials and their use in oxidative dehydrogenation of propane*, Phys. Chem. Chem. Phys. **2009**, *11*, 9583-9591.

[49] B. Yoosuk, C. Song, J. H. Kim, C. Ngamcharussrivichai and P. Prasassarakich *Effects of preparation conditions in hydrothermal synthesis of highly active unsupported NiMo sulfide catalysts for simultaneous hydrodesulfurization of dibenzothiophene and 4,6-dimethyldibenzothiophene*, Catal. Today **2010**, *149*, 52-61.

[50] W. Ueda and K. Oshihara *Selective oxidation of light alkanes over hydrothermally synthesized Mo-V-M-O (M=Al, Ga, Bi, Sb, and Te) oxide catalysts*, Appl. Catal. A - General **2000**, *200*, 135-143.

[51] P. Botella, B. Solsona, A. Martinez-Arias and J. M. L. Nieto *Selective oxidation of propane to acrylic acid on MoVNbTe mixed oxides catalysts prepared by hydrothermal synthesis*, Catal. Lett. **2001**, *74*, 149-154.

[52] P. Botella, J. M. L. Nieto, B. Solsona, A. Mifsud and F. Marquez *The preparation, characterization, and catalytic behavior of MoVTeNbO catalysts prepared by hydrothermal synthesis*, J. Catal. **2002**, *209*, 445-455.

[53] D. Vitry, Y. Morikawa, J. L. Dubois and W. Ueda *Mo-V-Te-(Nb)-O mixed metal oxides prepared by hydrothermal synthesis for catalytic selective oxidations of propane and propene to acrylic acid*, Appl. Catal. A -General **2003**, *251*, 411-424.

[54] A. C. Sanfiz, T. W. Hansen, F. Girgsdies, O. Timpe, E. Roedel, T. Ressler, A. Trunschke and R. Schloegl *Preparation of Phase-Pure M1 MoVTeNb Oxide Catalysts by Hydrothermal Synthesis-Influence of Reaction Parameters on Structure and Morphology*, Top. Catal. **2008**, *50*, 19-32.

[55] A. C. Sanfiz, T. W. Hansen, D. Teschner, P. Schnoerch, F. Girgsdies, A. Trunschke, R. Schloegl, M. H. Looi and S. B. A. Hamid *Dynamics of the MoVTeNb Oxide M1 Phase in Propane Oxidation*, J. Phys. Chem. C **2010**, *114*, 1912-1921.

[56] M. Sadakane, N. Watanabe, T. Katou, Y. Nodasaka and W. Ueda *Crystalline Mo_3VO_x mixed-metal-oxide catalyst with trigonal symmetry*, Angew. Chem. Int. Edit. **2007**, *46*, 1493-1496.

[57] G. Jin, W. Weng, Z. Lin, N. F. Dummer, S. H. Taylor, C. J. Kiely, J. K. Bartley and G. J. Hutchings *$Fe_2(MoO_4)_3/MoO_3$ nano-structured catalysts for the oxidation of methanol to formaldehyde*, J. Catal. **2012**, *296*, 55-64.

[58] A. M. Beale, S. D. M. Jacques, E. Sacaliuc-Parvalescu, M. G. O'Brien, P. Barnes and B. M. Weckhuysen *An iron molybdate catalyst for methanol to formaldehyde conversion prepared by a hydrothermal method and its characterization*, Appl. Catal., A **2009**, *363*, 143-152.

[59] W. Y. Teoh, R. Amal and L. Mädler *Flame spray pyrolysis: An enabling technology for nanoparticles design and fabrication*, Nanoscale **2010**, *2*, 1324-1347.

[60] R. Strobel, A. Baiker and S. E. Pratsinis *Aerosol flame synthesis of catalysts*, Adv. Powder Technol. **2006**, *17*, 457-480.

[61] K. Wegner and S. E. Pratsinis *Scale-up of nanoparticle synthesis in diffusion flame reactors*, Chem. Eng. Sci. **2003**, *58*, 4581-4589.

[62] M. Sokolowski, A. Sokolowska, A. Michalski and B. Gokieli *The "in-flame-reaction" method for Al_2O_3 aerosol formation*, J. Aerosol Sci. **1977**, *8*, 219-230.

[63] C. R. Bickmore, K. F. Waldner, D. R. Treadwell and R. M. Laine *Ultrafine spinel powders by flame spray pyrolysis of a magnesium aluminum double alkoxide*, J. Am. Ceram. Soc. **1996**, *79*, 1419-1423.

[64] L. Mädler, H. K. Kammler, R. Müller and S. E. Pratsinis *Controlled synthesis of nanostructured particles by flame spray pyrolysis*, J. Aerosol Sci. **2002**, *33*, 369-389.

[65] A. Williams *Combustion of liquid fuel sprays*; Butterworth&Co Ltd.: London, 1990.

[66] D. Li, W. Y. Teoh, C. Selomulya, R. C. Woodward, P. Munroe and R. Amal *Insight into microstructural and magnetic properties of flame-made gamma-Fe_2O_3 nanoparticles*, J. Mater. Chem. **2007**, *17*, 4876-4884.

[67] G. L. Chiarello, I. Rossetti and L. Forni *Flame-spray pyrolysis preparation of perovskites for methane catalytic combustion*, J. Catal. **2005**, *236*, 251-261.

[68] R. Strobel, L. Mädler, M. Piacentini, M. Maciejewski, A. Baiker and S. E. Pratsinis *Two-nozzle flame synthesis of Pt/Ba/Al_2O_3 for NO_x storage*, Chem. Mater. **2006**, *18*, 2532-2537.

[69] R. A. Dobbins and C. M. Megaridis *Morphology of flame-generated soot as determined by thermophorectic sampling*, Langmuir **1987**, *3*, 254-259.

[70] S. E. Pratsinis, W. H. Zhu and S. Vemury *The role of gas mixing in flame synthesis of titania powders*, Powder Technol. **1996**, *86*, 87-93.

[71] R. Mueller, L. Mädler and S. E. Pratsinis *Nanoparticle synthesis at high production rates by flame spray pyrolysis*, Chem. Eng. Sci. **2003**, *58*, 1969-1976.

[72] W. Y. Teoh, R. Setiawan, L. Mädler, J.-D. Grunwaldt, R. Amal and S. E. Pratsinis *Ru-doped cobalt-zirconia nanocomposites by flame synthesis: Physicochemical and catalytic properties*, Chem. Mater. **2008**, *20*, 4069-4079.

[73] Y. K. Kho, W. Y. Teoh, A. Iwase, L. Mädler, A. Kudo and R. Amal *Flame Preparation of Visible-Light-Responsive $BiVO_4$ Oxygen Evolution Photocatalysts with Subsequent Activation via Aqueous Route*, ACS Appl. Mater. Interfaces **2011**, *3*, 1997-2004.

[74] L. Mädler and S. E. Pratsinis *Bismuth oxide nanoparticles by flame spray pyrolysis*, J. Am. Ceram. Soc. **2002**, *85*, 1713-1718.

[75] D. P. Debecker, B. Schimmoeller, M. Stoyanova, C. Poleunis, P. Bertrand, U. Rodemerck and E. M. Gaigneaux *Flame-made MoO_3/SiO_2-Al_2O_3 metathesis catalysts with highly dispersed and highly active molybdate species*, J. Catal. **2011**, *277*, 154-163.

[76] M. Høj, K. Linde, T. K. Hansen, M. Brorson, A. D. Jensen and J.-D. Grunwaldt *Flame spray synthesis of CoMo/Al_2O_3 hydrotreating catalysts*, Appl. Catal., A **2011**, *397*, 201-208.

[77] M. Høj, D. K. Pham, M. Brorson, L. Mädler, A. D. Jensen and J.-D. Grunwaldt *Two-Nozzle Flame Spray Pyrolysis (FSP) Synthesis of CoMo/Al_2O_3 Hydrotreating Catalysts*, Catal. Lett. **2013**, *143*, 386-394.

[78] R. K. Grasselli *Fundamental principles of selective heterogeneous oxidation atalysis*, Top. Catal. **2002**, *21*, 79-88.

[79] U. S. Ozkan and R. B. Watson *The structure-function relationships in selective oxidation reactions over metal oxides*, Catal. Today **2005**, *100*, 101-114.

[80] M. M. Bettahar, G. Costentin, L. Savary and J. C. Lavalley *On the partial oxidation of propane and propylene on mixed metal oxide catalysts*, Appl. Catal. A General **1996**, *145*, 1-48.

[81] P. Mars and D. W. van Krevelen *Oxidations carried out by means of vanadium oxide catalysts*, Chem. Eng. Sci **1954**, 3.

[82] J. L. Callahan and R. K. Grasselli *A selectivity factor in vapor-phase hydrocarbon oxidation catalysis*, AIChE Journal **1963**, *9*, 755-760.

[83] R. Schlögl, A. Knop-Gericke, M. Havecker, U. Wild, D. Frickel, T. Ressler, R. E. Jentoft, J. Wienold, G. Mestl, A. Blume, O. Timpe and I. Uchida *In situ analysis of metal-oxide systems used for selective oxidation catalysis: how essential is chemical complexity?*, Top. Catal. **2001**, *15*, 219-228.

[84] B. Grzybowska-Swierkosz *Thirty years in selective oxidation on oxides: what have we learned ?*, Top. Catal. **2000**, *11*, 23-42.

[85] B. Delmon and P. Ruiz *Synergy in selective catalytic oxidation*, React. Kinet. Catal. Lett. **1987**, *35*, 303-314.

[86] I. E. Wachs and K. Routray *Catalysis Science of Bulk Mixed Oxides*, ACS Catal. **2012**, *2*, 1235-1246.

[87] G. W. Hearns and M. L. Adams, U.S. Patent 2,451,485 (1948).

[88] J. D. Idol, U.S. Patent 2,904,580 (1959).

[89] J. L. Callahan, R. W. Foreman and F. Veatch, U.S. Patent 3,044,966 (1962).

[90] Y. Morooka and W. Ueda *Multicomponent bismuth molybdate catalyst: A highly functionalized catalyst system for the selective oxidation of olefin*, Adv. Catal. **1994**, *40*, 233-273.

[91] T. P. Snyder and C. G. Hill *The mechanism of the partial oxidation of propylene over bismuth molybdate catalysts*, Catal. Rev. **1989**, *31*, 43-95.

[92] R. K. Grasselli and J. D. Burrington *Selective oxidation and ammoxidation of propylene by heterogeneous catalysis*, Adv. Catal. **1981**, *30*, 133-163.

[93] E. V. Hoefs, J. R. Monnier and G. W. Keulks *Investigation of the type of active oxygen for the oxidation of propylene over bismuth molybdate catalysts using Infrared and Raman spectroscopy*, J. Catal. **1979**, *57*, 331-337.

[94] P. A. Batist *Bismuth molybdates - Preparation and catalysis*, J. Chem. Technol. Biotechnol. **1979**, *29*, 451-466.

[95] K. German, Grzybows.B and J. Haber *Active centers for oxidation of propylene on Bi-Mo-O catalysts*, B. Acad. Pol. Sci. Chim. **1973**, *21*, 319-325.

[96] L. D. Krenzke and G. W. Keulks *Catalytic oxidation of propylene. 6. Mechanistic studies utilizing isotopic tracers*, J. Catal. **1980**, *61*, 316-325.

[97] D. Carson, G. Coudurier, M. Forissier, J. C. Védrine, A. Laarif and F. Theobald *Synergy effects in the catalytic properties of bismuth molybdates*, J. Chem. Soc., Faraday Trans. 1 **1983**, *79*, 1921-1929.

[98] Z. Bing, S. Pei, S. Shishan and G. Xiexian *Cooperation between the alpha and gamma phases of bismuth molybdate in the selective oxidation of propene*, J. Chem. Soc., Faraday Trans. **1990**, *86*, 3145-3150.

[99] M. T. Le, W. J. M. van Well, P. Stoltze, I. van Driessche and S. Hoste *Synergy effects between bismuth molybdate catalyst phases (Bi/Mo from 0.57 to 2) for the selective oxidation of propylene to arcrolein*, Appl. Catal., A **2005**, *282*, 189-194.

[100] A. Ayame, K. Uchida, M. Iwataya and M. Miyamoto *X-ray photoelectron spectroscopic study on alpha- and gamma-bismuth molybdate surfaces exposed to hydrogen, propene and oxygen*, Appl. Catal., A **2002**, *227*, 7-17.

[101] C. R. Adams and T. J. Jennings *Investigation of the mechanism of catalytic oxidation of propylene to acrolein and acrylonitrile*, J. Catal. **1963**, *2*, 63-68.

[102] B. Grzybowska, J. Haber and J. Janas *Interaction of allyl iodide with molybdate catalysts for selective oxidation of hydrocarbons*, J. Catal. **1977**, *49*, 150-163.

[103] T. Ono and N. Ogata *Raman band shifts of gamma-Bi_2MoO_6 and alpha-$Bi_2Mo_3O_{12}$ exchanged ^{18}O tracer at active sites for reoxidation*, J. Chem. Soc., Faraday Trans. **1994**, *90*, 2113-2118.

[104] W. Ueda, Y. Moro-Oka and T. Ikawa *^{18}O tracer study of the active species of oxygen on Bi_2MoO_6 catalyst*, J. Chem. Soc., Faraday Trans. 1 **1982**, *78*, 495-500.

[105] A. Ayame, M. Iwataya, K. Uchida, N. Igarashi and M. Miyamoto *X-ray photoelectron spectroscopic study on gamma-bismuth molybdate surfaces on exposure to propene and oxygen*, Jpn. J. Appl. Phys. Part 1 **2000**, *39*, 4335-4339.

[106] D. Arntz, M. Höpp, S. Jacobi, J. Sauer, T. Ohara, T. Sato, N. Shimizu, G. Prescher, H. Schwind and O. Weiberg *Ullmann´s Encyclopedia chapter Acrolein and Methacrolein*; 2005.

[107] H. Redlingshöfer, O. Krocher, W. Bock, K. Huthmacher and G. Emig *Catalytic wall reactor as a tool for isothermal investigations in the heterogeneously catalyzed oxidation of propene to acrolein*, Ind. Eng. Chem. Res. **2002**, *41*, 1445-1453.

[108] J. D. Burrington, C. T. Kartisek and R. K. Grasselli *Mechanism of nitrogen insertion in ammoxidation catalysis*, J. Catal. **1983**, *81*, 489-498.

[109] Y. H. Jang and W. A. Goddard *Selective oxidation and ammoxidation of propene on bismuth molybdates, ab initio calculations*, Top. Catal. **2001**, *15*, 273-289.

[110] R. K. Grasselli, J. D. Burrington, D. J. Buttrey, P. DeSanto, C. G. Lugmair, A. F. Volpe and T. Weingand *Multifunctionality of active centers in (amm)oxidation catalysts: from Bi-Mo-O-x to Mo-V-Nb-(Te, Sb)-O-x*, Top. Catal. **2003**, *23*, 5-22.

[111] J. B. Wagner, D. S. Su, S. A. Schunk, H. Hibst, J. Petzoldt and R. Schlögl *Structural characterization of high-performance catalysts for partial oxidation-the high-resolution and analytical electron microscopy approach*, J. Catal. **2004**, *224*, 28-35.

[112] L. D. Krenzke and G. W. Keulks *The catalytic oxidation of propylene. 8. An investigation of kinetics over $Bi_2Mo_3O_{12}$, Bi_2MoO_6 and $Bi_3FeMo_2O_{12}$,* J. Catal. **1980**, *64*, 295-302.

[113] J. R. Monnier and G. W. Keulks *The catalytic oxidation of propylene. 9. The kinetics and mechanism over beta-$Bi_2Mo_2O_9$,* J. Catal. **1981**, *68*, 51-66.

[114] Z. Zhai, A. B. Getsoian and A. T. Bell *The kinetics of selective oxidation of propene on bismuth vanadium molybdenum oxide catalysts*, J. Catal. **2013**, *308*, 25-36.

[115] J. F. Brazdil, D. D. Suresh and R. K. Grasselli *Redox kinetics of bismuth molybdate ammoxidation catalysts*, J. Catal. **1980**, *66*, 347-367.

[116] D. Carson, M. Forissièr and J. C. Védrine *Kinetic study of the partial oxidation of propene and 2-methylpropene on different bismuth molybdate and on a bismuth iron molybdate phase,* J. Chem. Soc., Faraday Trans. I **1984**, *80*, 1017-1028.

[117] A. P. V. Soares, L. D. Dimitrov, M. de Oliveira, L. Hilaire, M. F. Portela and R. K. Grasselli *Synergy effects between beta and gamma phases of bismuth molybdates in the selective catalytic oxidation of 1-butene,* Appl. Catal., A **2003**, *253*, 191-200.

[118] T. P. Snyder and C. G. Hill *Stability of bismuth molybdate catalysts at elevated temperatures in air under reaction conditions*, J. Catal. **1991**, *132*, 536-555.

[119] A. M. Beale and G. Sankar in *In Situ Study of the Formation of Crystalline Bismuth Molybdate Materials under Hydrothermal Conditions*, **2003**.

[120] G. I. Aleshina, C. Joshi, D. V. Tarasova, G. N. Kustova and T. A. Nikoro *Catalytic properties of Bi/Mo oxide catalysts prepared via precipitation*, React. Kinet. Catal. Lett. **1984**, *26*, 203-208.

[121] M. T. Le, J. Van Craenenbroeck, I. Van Driessche and S. Hoste *Bismuth molybdate catalysts synthesized using spray drying for the selective oxidation of propylene*, Appl. Catal., A **2003**, *249*, 355-364.

[122] R. P. Rastogi, A. K. Singh and C. S. Shukla *Kinetics and mechanism of solid-state reaction between bismuth(III) oxide and molybdenum(VI) oxide*, J. Solid State Chem. **1982**, *42*, 136-148.

[123] L. M. Thang, L. H. Bac, I. van Driessche, S. Hoste and W. J. M. van Well *The synergy effect between gamma and beta phase of bismuth molybdate catalysts: Is there any relation between conductivity and catalytic activity?*, Catal. Today **2008**, *131*, 566-571.

[124] W. J. M. van Well, M. T. Le, N. C. Schiodt, S. Hoste and P. Stoltze *The influence of the calcination conditions on the catalytic activity of Bi_2MoO_6 in the selective oxidation of propylene to acrolein*, J. Mol. Catal. A: Chem. **2006**, *256*, 1-8.

[125] W. Ueda, Y. Morooka, T. Ikawa and I. Matsuura *Promotion effect of iron for the multicomponent bismuth molybdate catalysts as revealed by $^{18}O_2$ tracer,* Chem. Lett. **1982**, 1365-1368.

[126] B. Delmon and G. F. Froment *Remote control of catalytic sites by spillover species: A chemical reaction engineering approach,* Catal. Rev. **1996**, *38*, 69-100.

[127] D. H. He, W. Ueda and Y. Morooka *Promotion effect of molybdate supported in $Bi_2Mo_3O_{12}$ catalyst in the selective oxidation of propylene,* Catal. Lett. **1992**, *12*, 35-44.

[128] J. B. Wagner, S. B. Abd Hamid, D. Othman, O. Timpe, S. Knobl, D. Niemeyer, D. S. Su and R. Schlögl *Nanostructuring of binary molybdenum oxide catalysts for propene oxidation,* J. Catal. **2004**, *225*, 78-85.

[129] T. Ressler, J. Wienold, R. E. Jentoft and F. Girgsdies *Evolution of defects in the bulk structure of MoO_3 during the catalytic oxidation of propene,* Eur. J. Inorg. Chem. **2003**, 301-312.

[130] R. L. Smith and G. S. Rohrer *An atomic force microscopy study of the morphological evolution of the MoO_3 (010) surface during reduction reactions,* J. Catal. **1996**, *163*, 12-17.

[131] R. L. Smith and G. S. Rohrer *Scanning probe microscopy of cleaved molybdates: alpha-MoO_3(010), $Mo_{18}O_{52}$(100), Mo_8O_{23}(010), and eta-Mo_4O_{11}(100),* J. Solid State Chem. **1996**, *124*, 104-115.

[132] J. C. Volta and B. Moraweck *Specificity of MoO_3 crystalline faces in propene oxidation,* J. Chem. Soc., Chem. Comm. **1980**, 338-339.

[133] J. C. Volta, M. Forissier, F. Theobald and T. P. Pham *Dependence of selectivity on surface-structure of MoO_3 catalysts,* Faraday Discuss. **1981**, *72*, 225.

[134] J. C. Volta and J. M. Tatibouet *Structure sensitivity of MoO_3 in mild oxidation of propylene* J. Catal. **1985**, *93*, 467-470.

[135] M. Abon, J. Massardier, B. Mingot, J. C. Volta, N. Floquet and O. Bertrand *New unsupported 100-oriented MoO_3 catalysts 2. Catalytic properties in propylene oxidation,* J. Catal. **1992**, *134*, 542-548.

[136] B. Mingot, N. Floquet, O. Bertrand, M. Treilleux, J. J. Heizmann, J. Massardier and M. Abon *New unsupported 100-oriented MoO_3 catalysts. 1. Preparation and characterization,* J. Catal. **1989**, *118*, 424-435.

[137] J. Ziolkowski *Catalytic anisotropy of MoO_3 in oxidation reactions in the light of bond-strength model of active sites,* J. Catal. **1983**, *80*, 263-273.

[138] K. Brückman, R. Grabowski, J. Haber, A. Mazurkiewicz, J. Słoczyński and T. Wiltowski *The role of different MoO_3 crystal faces in elementary steps of propene oxidation,* J. Catal. **1987**, *104*, 71-79.

[139] P. Grange and X. Vanhaeren *Hydrotreating catalysts, an old story with new challenges,* Catal. Today **1997**, *36*, 375-391.

[140] F. Besenbacher, M. Brorson, B. S. Clausen, S. Helveg, B. Hinnemann, J. Kibsgaard, J. V. Lauritsen, P. G. Moses, J. K. Nørskov and H. Topsøe *Recent STM, DFT and HAADF-STEM studies of sulfide-based hydrotreating catalysts: Insight into mechanistic, structural and particle size effects*, Catal. Today **2008**, *130*, 86-96.

[141] K. G. Knudsen, B. H. Cooper and H. Topsøe *Catalyst and process technologies for ultra low sulfur diesel*, Appl. Catal., A **1999**, *189*, 205-215.

[142] H. Topsøe, B. S. Clausen and F. E. Massoth in J. R. Anderson and M. Boudart (Eds.), *Catalysis: Science and Technology* Springer-Verlag, Berlin, **1996**.

[143] R. Prins in G. Ertl, H. Knözinger, F. Schüth and J. Weitkamp (Eds.), *Handbook of Heterogeneous Catalysis* **2008**.

[144] N. Y. Topsøe and H. Topsøe *Characterization of the structures and active-sites in sulfided Co-Mo/Al_2O_3 and Ni-Mo/Al_2O_3 catalysts by NO chemisorption*, J. Catal. **1983**, *84*, 386-401.

[145] B. S. Clausen, B. Lengeler, R. Candia, J. Alsnielsen and H. Topsøe *EXAFS studies of calcined and sulfided Co-Mo HDS catalysts*, Bull. Soc. Chim. Belg. **1981**, *90*, 1249-1259.

[146] C. Wivel, R. Candia, B. S. Clausen, S. Mørup and H. Topsøe *On the catalytic significance of a Co-Mo-S phase in Co-Mo-Al_2O_3 hydrodesulfurization catalysts - Combined in situ Mössbauer emission-spectroscopy and activity studies*, J. Catal. **1981**, *68*, 453-463.

[147] I. Alstrup, I. Chorkendorff, R. Candia, B. S. Clausen and H. Topsøe *A combined X-ray photoelectron and Mössbauer emission-spectroscopy study of the state of cobalt in sulfided, supported and unsupported Co-Mo Catalysts*, J. Catal. **1982**, *77*, 397-409.

[148] N. Y. Topsøe, H. Topsøe, O. Sorensen, B. S. Clausen and R. Candia *IR and AEM evidence for the edge location of the promoter atoms in Co-Mo-S type structures*, B. Soc. Chim. Belg. **1984**, *93*, 727-733.

[149] J. Ladrière, S. Göböls, F. Delannay and B. Delmon *Mössbauer emission-spectroscopy of an unsupported cobalt-molybdenum hydrodesulfurization catalyst*, J. Radioan. Nucl. Ch. Ar. **1987**, *109*, 213-222.

[150] B. Delmon *New hypothesis explaining synergy between 2 phases in heterogeneous catalysis - Case of hydrodesulfurization catalysts*, Bull. Soc. Chim. Belg. **1979**, *88*, 979-987.

[151] B. Delmon *New mechanistic model explaining synergy in hydrotreating catalysts*, Cr. Acad. Sci. C Chim. **1979**, *289*, 173-176.

[152] B. Delmon *A new concept explaining catalysis synergy between 2 solid phases*, React. Kinet. Catal. Lett. **1980**, *13*, 203-208.

[153] X. Chu and L. D. Schmidt *Process in MoS_2 gasification*, J. Catal. **1993**, *144*, 77-92.

[154] K. Inamura and R. Prins in The Role of Co in Unsupported Co-Mo Sulfides in the Hydrodesulfurization of Thiophene, Y. Izumi, H. Arai and M. Iwamoto (Eds.), *Science and Technology in Catalysis 1994* **1995**, pp. 401-404.

[155] S. Eijsbouts, L. C. A. van den Oetelaar and R. R. van Puijenbroek *MoS_2 morphology and promoter segregation in commercial Type 2 Ni-Mo/Al_2O_3 and Co-Mo/Al_2O_3 hydroprocessing catalysts*, J. Catal. **2005**, *229*, 352-364.

[156] S. Eijsbouts, S. W. Mayo and K. Fujita *Unsupported transition metal sulfide catalysts: From fundamentals to industrial application*, Appl. Catal. A **2007**, *322*, 58-66.

[157] T. C. Ho, A. J. Jacobson, R. R. Chianelli and C. R. F. Lund *Hydrodenitrogenation selective catalysts. 1. Fe promoted Mo/W sulfides*, J. Catal. **1992**, *138*, 351-363.

[158] T. C. Ho, R. R. Chianelli and A. J. Jacobson *Promotion effects in bulk metal sulfide catalysts*, Appl. Catal. A **1994**, *114*, 127-139.

[159] J. Y. Koo and T. C. Ho *Characterization of fresh and lined-out bulk FeMo sulfide catalysts*, Catal. Lett. **1994**, *28*, 99-108.

[160] M. Karroua, J. Ladriere, H. Matralis, P. Grange and B. Delmon *Characterization of unsupported FeMoS catalysts - Stability during reaction and effect of the sulfiding temperature*, J. Catal. **1992**, *138*, 640-658.

[161] M. Karroua, H. Matralis, E. Sham, P. Grange and B. Delmon *Synergy between the CoMoS phase and supported or unsupported cobalt sulfide - Existence of remote-control effect*, Bull. Chem. Soc. Jpn **1995**, *68*, 107-119.

[162] S. Helveg, J. V. Lauritsen, E. Laegsgaard, I. Stensgaard, J. K. Nørskov, B. S. Clausen, H. Topsøe and F. Besenbacher *Atomic-scale structure of single-layer MoS_2 nanoclusters*, Phys. Rev. Lett. **2000**, *84*, 951-954.

[163] M. V. Bollinger, J. V. Lauritsen, K. W. Jacobsen, J. K. Nørskov, S. Helveg and F. Besenbacher *One-dimensional metallic edge states in MoS_2*, Phys. Rev. Lett. **2001**, *87*.

[164] C. Kisielowski, Q. M. Ramasse, L. P. Hansen, M. Brorson, A. Carlsson, A. M. Molenbroek, H. Topsøe and S. Helveg *Imaging MoS_2 Nanocatalysts with Single-Atom Sensitivity*, Angew. Chem. Int. Edit. **2010**, *49*, 2708-2710.

[165] L. P. Hansen, Q. M. Ramasse, C. Kisielowski, M. Brorson, E. Johnson, H. Topsøe and S. Helveg *Atomic-Scale Edge Structures on Industrial-Style MoS2 Nanocatalysts*, Angew. Chem. Int. Edit. **2011**, *50*, 10153-10156.

[166] J. V. Lauritsen, J. Kibsgaard, G. H. Olesen, P. G. Moses, B. Hinnemann, S. Helveg, J. K. Nørskov, B. S. Clausen, H. Topsøe, E. Lægsgaard and F. Besenbacher *Location and coordination of promoter atoms in Co- and Ni-promoted MoS_2-based hydrotreating catalysts*, J. Catal. **2007**, *249*, 220-233.

[167] H. Topsøe *The role of Co-Mo-S type structures in hydrotreating catalysts*, Appl. Catal. A **2007**, *322*, 3-8.

[168] J. V. Lauritsen, M. Nyberg, J. K. Nørskov, B. S. Clausen, H. Topsøe, E. Lægsgaard and F. Besenbacher *Hydrodesulfurization reaction pathways on MoS_2 nanoclusters revealed by scanning tunneling microscopy*, J. Catal. **2004**, *224*, 94-106.

[169] B. C. Gates and H. Topsøe *Reactivities in deep catalytic hydrodesulfurization: Challenges, opportunities, and the importance of 4-methyldibenzothiophene and 4,6-dimethyldibenzothiophene*, Polyhedron **1997**, *16*, 3213-3217.

[170] S. Mann *The chemistry of form*, Angew. Chem. Int. Edit. **2000**, *39*, 3393-3406.

[171] A. Phuruangrat, J. S. Chen, X. W. Lou, O. Yayapao, S. Thongtem and T. Thongtem *Hydrothermal synthesis and electrochemical properties of alpha-MoO_3 nanobelts used as cathode materials for Li-ion batteries*, Appl. Phys. A - Mater. **2012**, *107*, 249-254.

[172] X. Xie, Y. Li, Z.-Q. Liu, M. Haruta and W. Shen *Low-temperature oxidation of CO catalysed by Co_3O_4 nanorods*, Nature **2009**, *458*, 746-749.

[173] K. B. Zhou, X. Wang, X. M. Sun, Q. Peng and Y. D. Li *Enhanced catalytic activity of ceria nanorods from well-defined reactive crystal planes*, J. Catal. **2005**, *229*, 206-212.

[174] Tana, M. Zhang, J. Li, H. Li, Y. Li and W. Shen *Morphology-dependent redox and catalytic properties of CeO_2 nanostructures: Nanowires, nanorods and nanoparticles*, Catal. Today **2009**, *148*, 179-183.

[175] X. Mou, X. Wei, Y. Li and W. Shen *Tuning crystal-phase and shape of Fe_2O_3 nanoparticles for catalytic applications*, Cryst. Eng. Comm. **2012**, *14*, 5107-5120.

[176] J. C. Védrine, G. J. Hutchings and C. J. Kiely *Molybdenum oxide model catalysts and vanadium phosphates as actual catalysts for understanding heterogeneous catalytic partial oxidation reactions: A contribution by Jean-Claude Volta*, Catal. Today **2013**, *217*, 57-64.

[177] M. Gasior and T. Machej *Morphological aspects in the oxidation of orthoxylene on V_2O_5 catalysts*, J. Catal. **1983**, *83*, 472-476.

[178] A. Baiker and D. Gasser *Influence of the grain morphology of molybdenum trioxide on its catalytic properties - oxidation of methanol to formaldehyde*, Z. Phys. Chem Neue Fol. **1986**, *149*, 119-124.

[179] H. K. Kammler, L. Mädler and S. E. Pratsinis *Flame synthesis of nanoparticles*, Chem. Eng. Technol. **2001**, *24*, 583-596.

[180] T. Tani, L. Mädler and S. E. Pratsinis *Synthesis of zinc oxide/silica composite nanoparticles by flame spray pyrolysis*, J. Mater. Sci. **2002**, *37*, 4627-4632.

[181] W. J. Stark, S. E. Pratsinis and A. Baiker *Heterogeneous catalysis by flame-made nanoparticles*, Chimia **2002**, *56*, 485-489.

[182] M. J. Beier, B. Schimmoeller, T. W. Hansen, J. E. T. Andersen, S. E. Pratsinis and J.-D. Grunwaldt *Selective side-chain oxidation of alkyl aromatic compounds catalyzed by cerium modified silver catalysts*, J. Mol. Catal. A: Chem. **2010**, *331*, 40-49.

[183] D. Chan. *Thermische Alterung von Dieseloxidationskatalysatoren und NO_x-Speicherkatalysatoren: Korrelierung von Aktivität und Speicherfähigkeit mit physikalischen und chemischen Katalysatoreigenschaften.* Dissertation, Karlsruhe Institut für Technologie, Fakultät für Chemie und Biowissenschaften, **2013**.

[184] J. W. Niemantsverdriet *Spectroscopy in Catalysis*; WILEY-VCH: Weinheim, 2000.

[185] J.-D. Grunwaldt, Lectures *Modern concepts and spectroscopic methods in catalysis: Vibrational spectroscopy* **2012**.

[186] R. J. Behm, Lectures of the South German Catalysis Institute *Catalyst Characterization* **2010**.

[187] J.-D. Grunwaldt, Lectures *Spectroscopic Methods, Diffraction and Scattering Techniques using Synchrotron Radiation* **2012**.

[188] B. Ravel and M. Newville *ATHENA, ARTEMIS, HEPHAESTUS: data analysis for X-ray absorption spectroscopy using IFEFFIT*, J. Synchrotron Radiat. **2005**, *12*, 537-541.

[189] K. L. Parry, A. G. Shard, R. D. Short, R. G. White, J. D. Whittle and A. Wright *ARXPS characterisation of plasma polymerised surface chemical gradients*, Surf. Interface Anal. **2006**, *38*, 1497-1504.

[190] J.-D. Grunwaldt, M. D. Wildberger, T. Mallat and A. Baiker *Unusual redox properties of bismuth in sol-gel Bi-Mo-Ti mixed oxides*, J. Catal. **1998**, *177*, 53-59.

[191] J. H. Scofield *Hartree-Slater subshell photoionization cross-sections at 1254 and 1487eV*, J. Electron Spectrosc. Relat. Phenom. **1976**, *8*, 129-137.

[192] M. Høj. *Nanoparticle synthesis using flame spray pyrolysis for catalysis.* Dissertation, Technical University of Denmark, Department of Chemical and Biochemical Engineering, **2012**.

[193] S. L. Ebbehøj. *Synthesis, characterization and testing of mesoporous alumina as a new support for hydrotreating catalysts.* Bachelor Thesis, University of Copenhagen, Nano Science Centre, **2007**.

[194] K. Herbst, M. Brorson and A. Carlsson *Hydrotreating activities of alumina-supported bimetallic catalysts derived from noble metal containing molecular sulfide clusters Mo_3S_4M' (M ' = Ru, Rh, Ir, Pd, Pt)*, J. Mol. Catal. A: Chem. **2010**, *325*, 1-7.

[195] J. M. Tatibouet and J. E. Germain *A structure-sensitive oxidation reaction - Methanol on molybdenum trioxide catalysts*, J. Catal. **1981**, *72*, 375-378.

[196] J. M. Tatibouet *Acido-basicity and structure senstitivity of methanol catalytic-oxidation on crystallized alpha-MoO_3 - Acidic sites*, CR Acad. II C **1983**, *297*, 703.

[197] A. Baiker, P. Dollenmeier and A. Reller *Influence of the grain morphology of molybdenum trioxide on its catalytic properties - reduction of nitric oxide with ammonia*, J. Catal. **1987**, *103*, 394-398.

[198] J. J. Cruywagen and J. B. B. Heyns *Solubility of yellow molybdenum (VI) oxide dihydrate ($MoO_3 \cdot 2H_2O$) in 3.0M sodium perchlorate at 25°C*, S. Afr. J. Chem. **1981**, *34*, 118-120.

[199] S. Kuehn, P. Schmidt-Zhang, A. H. P. Hahn, M. Huber, M. Lerch and T. Ressler *Structure and properties of molybdenum oxide nitrides as model systems for selective oxidation catalysts*, Chem. Cent. J. **2011**, *5*.

[200] J. Guo, P. Zavalij and M. S. Whittingham *Metastable Hexagonal Molybdates: Hydrothermal Preparation, Structure, and Reactivity*, J. Solid State Chem. **1995**, *117*, 323-332.

[201] L. Kihlborg *Least square refinement of crystal structure of molybdenum trioxide*, Arkiv for Kemi **1963**, *21*, 357.

[202] M. Dieterle, G. Weinberg and G. Mestl *Raman spectroscopy of molybdenum oxides - Part I. Structural characterization of oxygen defects in $MoO_{(3-x)}$ by DR UV/VIS, Raman spectroscopy and X-ray diffraction*, Phys. Chem. Chem. Phys. **2002**, *4*, 812-821.

[203] G. Busca, E. Finocchio, G. Ramis and G. Ricchiardi *On the role of acidity in catalytic oxidation*, Catal. Today **1996**, *32*, 133-143.

[204] G. Z. Bian, L. Fan, Y. L. Fu and K. Fujimoto *Mixed alcohol synthesis from syngas on sulfided K-Mo-based catalysts: Influence of support acidity*, Ind. Eng. Chem. Res. **1998**, *37*, 1736-1743.

[205] S. T. Oyama *Crystal-face anisotropy of propylene oxidation on molybdenum trioxide*, Bull. Chem. Soc. Jpn **1988**, *61*, 2585-2594.

[206] R. Grabowski, T. Machej, A. Mazurkiewicz and J. Sloczynski *Morphology of MoO_3 supported on silica and its activity in propene oxidation*, B. Pol. Acad. Sci. - Chem. **1987**, *35*, 141.

[207] J. Haber and E. Serwicka *Surface structure and reactivity of MoO_3*, Polyhedron **1986**, *5*, 107-109.

[208] S. R. G. Carrazán, C. Martin, V. Rives and R. Vidal *Selective oxidation of isobutene to methacrolein on multiphasic molybdate-based catalysts*, Appl. Catal A **1996**, *135*, 95-123.

[209] http://icsd.fiz-karlsruhe.de/ (October 2013).

[210] F. Pertlik and J. Zemann *New determination of the crystal structure of Koechlinite*, Fortschr. Mineral. **1982**, *60*, 162-163.

[211] B. Begemann and M. Jansen *Bi_4O_7, a binary Bismuth (III,V) oxide with definite Bi^{5+} positions*, J. Less Common Met. **1989**, *156*, 123-135.

[212] A. N. Christensen, M.-A. Chevallier, J. Skibsted and B. B. Iversen *Synthesis and characterization of basic bismuth(III) nitrates*, J. Chem. Soc. Dalton **2000**, 265-270.

[213] F. Theobald, A. Laarif and A. W. Hewat *The structure of Koechlinite bismuth molybdate - A controversy resolved by neutron diffraction*, Ferroelectr. **1984**, *56*, 219-237.

[214] F. D. Hardcastle and I. E. Wachs *Molecular structure of molybdenum oxide in bismuth molybdates by Raman spectroscopy*, J. Phys. Chem. **1991**, *95*, 10763-10772.

[215] R. P. Oertel and R. A. Plane *Raman and Infrared study of nitrate complexes of bismuth (3)*, Inorg. Chem. **1968**, *7*, 1192-1196.

[216] H. E. Swift, J. E. Bozik and J. A. Ondrey *Dehydrodimerization of propylene using bismuth oxide as oxidant*, J. Catal. **1971**, *21*, 212.

[217] E. Vila, A. R. Landa-Canovas, J. Galy, J. E. Iglesias and A. Castro *$Bi_{2n+4}Mon O_{6(n+1)}$ with n=3, 4, 5, 6: A new series of low-temperature stable phases in the mBi_2O_3-MoO_3 system (1.0 < m < 1.7): Structural relationships and conductor properties*, J. Solid State Chem. **2007**, *180*, 661-669.

[218] P. J. Bereciartua, F. J. Zuniga, J. M. Perez-Mato, V. Petricek, E. Vila, A. Castro, J. Rodriguez-Carvajal and S. Doyle *Structure refinement and superspace description of the system $Bi_{2(n+2)}Mo_nO6_{(n+1)}$ (n=3, 4, 5 and 6)*, Acta Crystallogr., Sect. B: Struct. Sci. **2012**, *68*, 323-340.

[219] J. M. Herrmann, M. El Jamal and M. Forissier *Evidence by electrical conductivity for an excess of bismuth as Bi^+ interstitial at the surface of gamma-phase Bi_2MoO_6 - Consequence for selectivity in propene catalytic oxidation*, React. Kinet. Catal. Lett. **1988**, *37*, 255-260.

[220] J. D. Burrington and R. K. Grasselli *Aspects of selective oxidation and ammoxidation mechanisms over bismuth molybdate catalysts*, J. Catal. **1979**, *59*, 79-99.

[221] L. M. Reilly, G. Sankar and C. R. A. Catlow *Following the formation of gamma-phase Bi_2MoO_6 catalyst by in situ XRD/XAS and thermogravimetric techniques*, J. Solid State Chem. **1999**, *148*, 178-185.

[222] A. M. Beale, M. T. Le, S. Hoste and G. Sankar *A time resolved in situ investigation into the formation of bismuth molybdate catalysts prepared by spray-dried methods*, Solid State Sci. **2005**, *7*, 1141-1148.

[223] A. J. Gröhn, S. E. Pratsinis and K. Wegner *Fluid-particle dynamics during combustion spray aerosol synthesis of ZrO_2*, Chem. Eng. J. **2012**, *191*, 491-502.

[224] I. Matsuura, R. Schut and K. Hirakawa *The surface-structures of the active bismuth molybdate catalysts*, J. Catal. **1980**, *63*, 152-166.

[225] M. T. Le, W. J. M. van Well, I. van Driessche and S. Hoste *Spray drying, a versatile synthetic method to control purity in single phases and mixed phases of bismuth molybdates*, Can. J. Chem. Eng. **2005**, *83*, 336-343.

[226] E. Godard, E. M. Gaigneaux, P. Ruiz and B. Delmon *New insights in the understanding of the behaviour and performances of bismuth molybdate catalysts in the oxygen-assisted dehydration of 2-butanol*, Catal. Today **2000**, *61*, 279-285.

[227] P. A. Batist, J. F. H. Bouwens and G. C. A. Schuit *Bismuth molybdate catalysts - Preparation, characterization and activity of different compounds in Bi-Mo-O System*, J. Catal. **1972**, *25*, 1.

[228] D. J. Buttrey, D. A. Jefferson and J. M. Thomas *The structural relationships between the various phases of bismuth molybdates with special reference to their catalytic activity*, Philos. Mag. A **1986**, *53*, 897-906.

[229] J. C. Jung, H. Kim, A. S. Choi, Y.-M. Chung, T. J. Kim, S. J. Lee, S.-H. Oh and I. K. Song *Preparation, characterization, and catalytic activity of bismuth molybdate catalysts for the oxidative dehydrogenation of n-butene into 1,3-butadiene*, J. Mol. Catal. A: Chem. **2006**, *259*, 166-170.

[230] G. G. Briand. *Bifunctional Ligands in Discerning and Developing the Fundamental and Medicinal Chemistry of Bismuth (III).* Dissertation, Dalhousie University, **1999**.

[231] F. Trifiro, R. D. Scarle and H. Hoser *Relationships between structure and activity of mixed oxides as oxidation catalyst. 1. Preparation and solid state reactions of Bi-molybdates*, J. Catal. **1972**, *25*, 12.

[232] J. C. Jung, H. Kini, A. S. Choi, Y.-M. Chung, T. J. Kim, S. J. Lee, S.-H. Oh and I. K. Song *Effect of pH in the preparation of gamma-Bi_2MoO_6 for oxidative dehydrogenation of n-butene to 1,3-butadiene: Correlation between catalytic performance and oxygen mobility of gamma-Bi_2MoO_6*, Catal. Comm. **2007**, *8*, 625-628.

[233] Y. Okamoto *A novel preparation-characterization technique of hydrodesulfurization catalysts for cleaner fuels*, Catal. Today **2008**, *132*, 9-17.

[234] J. K. Nørskov, B. S. Clausen and H. Topsøe *Understanding the trends in the hydrodesulfurization activity of the transition metal sulfides*, Catal. Lett. **1992**, *13*, 1-8.

[235] L. S. Byskov, B. Hammer, J. K. Nørskov, B. S. Clausen and H. Topsøe *Sulfur bonding in MoS_2 and Co-Mo-S structures*, Catal. Lett. **1997**, *47*, 177-182.

[236] L. S. Byskov, J. K. Nørskov, B. S. Clausen and H. Topsøe *DFT Calculations of Unpromoted and Promoted MoS_2-Based Hydrodesulfurization Catalysts*, J. Catal. **1999**, *187*, 109-122.

[237] M. Daage and R. R. Chianelli *Structure-function relations in molybdenum sulfide catalysts - The rim-edge model*, J. Catal. **1994**, *149*, 414-427.

[238] J. V. Lauritsen, M. Nyberg, R. T. Vang, M. V. Bollinger, B. S. Clausen, H. Topsøe, K. W. Jacobsen, E. Laegsgaard, J. K. Nørskov and F. Besenbacher *Chemistry of one-dimensional metallic edge states in MoS_2 nanoclusters*, Nanotechnology **2003**, *14*, 385-389.

[239] Y. Iwata, K. Sato, T. Yoneda, Y. Miki, Y. Sugimoto, A. Nishijima and H. Shimada *Catalytic functionality of unsupported molybdenum sulfide catalysts prepared with different methods*, Catal. Today **1998**, *45*, 353-359.

[240] K. Inamura and R. Prins *The Role of Co in Unsupported Co-Mo Sulfides in the Hydrodesulfurization of Thiophene*, J. Catal. **1994**, *147*, 515-524.

[241] A. Daudin, A. F. Lamic, G. Pérot, S. Brunet, P. Raybaud and C. Bouchy *Microkinetic interpretation of HDS/HYDO selectivity of the transformation of a model FCC gasoline over transition metal sulfides*, Catal. Today **2008**, *130*, 221-230.

[242] R. Candia, B. S. Clausen and H. Topsøe *On the role of promoter atoms in unsupported hydrodesulfurization catalysts - Influence of preparation methods*, Bull. Soci. Chim. Belg. **1981**, *90*, 1225-1232.

[243] R. Candia, B. S. Clausen and H. Topsøe *The origin of catalytic synergy in unsupported Co-Mo HDS catalysts*, J. Catal. **1982**, *77*, 564-566.

[244] S. Fuentes, G. Diaz, F. Pedraza, H. Rojas and N. Rosas *The influence of a new preparation method on the catalytic properties of CoMo and NiMo sulfides*, J. Catal. **1988**, *113*, 535-539.

[245] M. Ramos, G. Berhault, D. A. Ferrer, B. Torres and R. R. Chianelli *HRTEM and molecular modeling of the MoS_2-Co_9S_8 interface: understanding the promotion effect in bulk HDS catalysts*, Catal. Sci. Technol. **2012**, *2*, 164-178.

[246] L. Alvarez, J. Espino, C. Ornelas, J. L. Rico, M. T. Cortez, G. Berhault and G. Alonso *Comparative study of MoS_2 and Co/MoS_2 catalysts prepared by ex situ/in situ activation of ammonium and tetraalkylammonium thiomolybdates*, J. Mol. Catal. A: Chem. **2004**, *210*, 105-117.

[247] G. Mestl and T. K. K. Srinivasan *Raman Spectroscopy of Monolayer-Type Catalysts: Supported Molybdenum Oxides*, Catal. Rev. **1998**, *40*, 451-570.

[248] F. D. Hardcastle and I. E. Wachs *Determination of molybdenum oxygen bond distances and bond orders by Raman-spectroscopy*, J. Raman Spectrosc. **1990**, *21*, 683-691.

[249] B. Pawelec, T. Halachev, A. Olivas and T. A. Zepeda *Impact of preparation method and support modification on the activity of mesoporous hydrotreating CoMo catalysts*, Appl. Catal. A **2008**, *348*, 30-41.

[250] J. E. Herrera and D. E. Resasco *Loss of single-walled carbon nanotubes selectivity by disruption of the Co-Mo interaction in the catalyst*, J. Catal. **2004**, *221*, 354-364.

[251] S. L. González-Cortés, T.-C. Xiao, T.-W. Lin and M. L. H. Green *Influence of double promotion on HDS catalysts prepared by urea-matrix combustion synthesis*, Appl. Catal., A **2006**, *302*, 264-273.

[252] V. La Parola, G. Deganello, C. R. Tewell and A. M. Venezia *Structural characterisation of silica supported CoMo catalysts by UV Raman spectroscopy, XPS and X-ray diffraction techniques*, Appl. Catal. A **2002**, *235*, 171-180.

[253] V. La Parola, G. Deganello and A. M. Venezia *CoMo catalysts supported on aluminosilicates: synergy between support and sodium effects*, Appl. Catal. A **2004**, *260*, 237-247.

[254] A. Maione and M. Devillers *Solid solutions of Ni and Co molybdates in silica-dispersed and bulk catalysts prepared by sol-gel and citrate methods*, J. Solid State Chem. **2004**, *177*, 2339-2349.

[255] L. A. Palacio, A. Echavarria and C. Saldarriaga *Crystal structure a cobalt molybdate type phi(x): $NaCo_2OH(H_2O)(MoO_4)_2$*, Int. J. Inorg. Mater. **2001**, *3*, 367-371.

[256] R. W. Phillips and A. A. Fote *New class of models to explain role of promoters in hydrodesulfurization catalysts*, J. Catal. **1976**, *41*, 168-172.

[257] R. R. Chianelli and G. Berhault *Symmetrical synergism and the role of carbon in transition metal sulfide catalytic materials*, Catal. Today **1999**, *53*, 357-366.

[258] Z. Le, P. Afanasiev, D. Li, X. Long and M. Vrinat *Solution synthesis of the unsupported Ni-W sulfide hydrotreating catalysts*, Catal. Today **2008**, *130*, 24-31.

[259] L. Wang, Y. Zhang, Y. Zhang, Z. Jiang and C. Li *Ultra-Deep Hydrodesulfurization of Diesel Fuels on Trimetallic NiMoW Sulfide Catalysts*, Chem. Eur. J. **2009**, *15*, 12571-12575.

[260] H. Farag, K. Sakanishi, M. Kouzu, A. Matsumura, Y. Sugimoto and I. Saito *Dibenzothiophene hydrodesulfurization over synthesized MoS_2 catalysts*, J. Mol. Catal. A: Chem. **2003**, *206*, 399-408.

[261] J. P. R. Vissers, V. H. J. de Beer and R. Prins *The role of Co in sulphidised Co-Mo hydrodesulphurisation catalysts supported on carbon and alumina*, J. Chem. Soc., Faraday Trans. 1 **1987**, *83*, 2145-2155.

[262] A. M. van der Kraan, M. W. J. Craje, E. Gerkema, W. Ramselaar and V. H. J. de Beer *So-called Co-Mo-S phase observed in carbon-supported cobalt sulfide catalysts by Mössbauer emission-spectroscopy*, Appl. Catal. **1988**, *39*, L7-L10.

[263] S. M. A. M. Bouwens, D. C. Koningsberger, V. H. J. De Beer and R. Prins *An Exafs Study on Carbon-Supported Mo and Co-Mo Sulfide Hydrodesulfurization Catalysts*, Bull. Soc. Chim. Belg. **1987**, *96*, 951-960.

[264] J. M. Zabala, M. Mainil, P. Grange and B. Delmon *Synergism between Co_9S_8 and MoS_2 in the hydrogenolysis of thiophene and hydrogenation of cyclohexene*, React. Kin. Catal. Lett. **1975**, *3*, 285-291.

[265] A. Nogueira, R. Znaiguia, D. Uzio, P. Afanasiev and G. Berhault *Curved nanostructures of unsupported and Al_2O_3-supported MoS_2 catalysts: Synthesis and HDS catalytic properties*, Appl. Catal. A **2012**, *429*, 92-105.

[266] J. van Gestel, C. Dujardin, F. Mauge and J. C. Duchet *Direct aromatic C-N bond cleavage evidenced in the hydrodenitrogenation of 2,6-dimethylaniline over cobalt-promoted Mo/Al_2O_3 sulfide catalysts: A reactivity and FTIR study*, J. Catal. **2001**, *202*, 78-88.

[267] M. J. Girgis and B. C. Gates *Reactivities, reaction networks, and kinetics in high-pressure catalytic hydroprocessing*, Ind. Eng. Chem. Res. **1991**, *30*, 2021-2058.

[268] R. Prins, M. Jian and M. Flechsenhar *Mechanism and kinetics of hydrodenitrogenation*, Polyhedron **1997**, *16*, 3235-3246.

[269] M. Jian and R. Prins *Existence of different catalytic sites in HDN catalysts*, Catal. Today **1996**, *30*, 127-134.

[270] M. Jian and R. Prins *Determination of the nature of distinct catalytic sites in hydrodenitrogenation by competitive adsorption*, Catal. Lett. **1998**, *50*, 9-13.

List of Abbreviations

AFM	Atomic force microscopy
AHM	Ammonium heptamolybdate
ATTM	Ammonium tetrathiomolybdate
BET	Brunauer, Emmett and Teller theory for SSA calculation
BP	Biphenyl
CHB	Cyclohexyl benzene
CTAB	Cetyltrimethyl ammonium bromide
CUS	Unsaturated coordination site
CVD	Chemical vapor deposition
DBT	Dibenzothiophene
DDS	Direct desulfurization
DFT	Density functional theory
DMDBT	Dimethyldibenzothiophene
DMDS	Dimethyldisulfide
EDX	Energy dispersive X-ray (spectroscopy)
EDXRD	Energy dispersive X-ray diffraction
EPR	Electron paramagnetic resonance
EXAFS	Extended X-ray absorption fine structure
FASP	Flame assisted spray pyrolysis
FID	Flame ionization detector
FSP	Flame spray pyrolysis
FTIR	Fourier transformed infrared (spectroscopy)
GC	Gas chromatography
HDN	Hydrodenitrogenation
HDS	Hydrodesulfurization
HOAc	Acetic acid
hp	High pressure
HRPD	High resolution powder diffraction
HRTEM	High-resolution transmission electron microscopy
HSP	Homogeneous sulfide precipitation

List of Abbreviations

HYD	Hydrogenation
ICP-OES	Optical emission spectrometry with inductively coupled plasma
IR	Infrared
ITD	Impregnated-thiosalt decomposition
JCPDS	Joint Committee on Powder Diffraction Standards
MO	Molecular orbital
MS	Mass spectrometer
ODH	Oxidative dehydrogenation
PEG	Polyethylene glycol
PVP	Poly(vinyl pyrrolidone)
PXRD	Powder X-ray diffraction
SEM	Scanning electron microscopy
SSA	Specific surface area
STM	Scanning tunneling microscopy
TCD	Thermal conductivity detector
TEM	Transmission electron microscopy
TOS	Time on stream
TPD	Temperature programmed desorption
TPR	Temperature programmed reduction
ULSD	Ultra low sulfur diesel
VAFS	Vapor-fed aerosol flame synthesis
vol.%	Volume percentage
wt.%	Weight percentage
XAS	X-ray absorption spectroscopy
XANES	X-ray absorption near edge structure
XPS	X-ray photoelectron spectroscopy
XRD	X-ray diffraction

List of Symbols

c	Concentration
d	Spacing between atom layers (XRD)
E_B	Binding energy [eV]
E_{kin}	Kinetic energy
F	Volumetric flow rate
h	Planck´s constant
k	Rate constant
n_{ads}	Quantity of adsorbed gas (BET)
n_m	Quantity of monolayer adsorbed gas (BET)
p_0	Saturation pressure of adsorbate (BET)
R	Distance of nearest neighbor (EXAFS)
S	Selectivity
T	Temperature
$w_{catalyst}$	Catalyst mass
X	Conversion
Y	Yield
θ	Angle of incidence of the X-rays
λ	Wavelength
ν	Frequency (for XPS: of excitation radiation)
ρ	Density
X(k)	EXAFS function

List of Publications

Publications

K. Schuh, W. Kleist, M. Høj, A. D. Jensen, P. Beato, G. R. Patzke and J.-D. Grunwaldt *Systematic study on the influence of particle size and morphology of α-MoO_3 for the selective oxidation of propylene*, submitted.

K. Schuh, W. Kleist, M. Høj, V. Trouillet, P. Beato, A.D. Jensen, G.R. Patzke and J.-D. Grunwaldt
Selective oxidation of propylene to acrolein by hydrothermally synthesized bismuth molybdates, Appl. Catal., A 482 (2014) 145.

K. Schuh, W. Kleist, M. Høj, V. Trouillet, A. D. Jensen and J.-D. Grunwaldt
One-step synthesis of bismuth molybdate catalysts via flame spray pyrolysis for the selective oxidation of propylene to acrolein, Chem. Commun., 50 (2014) 15404.

K. Schuh, W. Kleist, M. Høj, V. Trouillet, P. Beato, A.D. Jensen and J.-D. Grunwaldt
Bismuth molybdates obtained by mild hydrothermal synthesis: Influence of preparation parameters on selective oxidation of propylene, to be submitted.

Oral presentations

K. Schuh, W. Kleist, J.-D. Grunwaldt, M. Høj, A. D. Jensen, G. R. Patzke
Hydrothermal Synthesis of Molybdenum-Based Catalysts for Selective Oxidation of C_3 Hydrocarbons
15th Nordic Symposium on Catalysis, 10th – 12th of June 2012, Marienhamn, Finnland

K. Schuh, W. Kleist, J.-D. Grunwaldt, M. Høj, A. D. Jensen, G. R. Patzke
Hydrothermal synthesis and characterization of bismuth molybdate catalysts for the selective oxidation of propene to acrolein
7th World Congress on Oxidation Catalysis, 9th - 12th of June 2013, St. Louis, Missouri, USA

Poster presentations

K. Schuh, J.-D. Grunwaldt, W. Kleist, Y. Zhou, G. R. Patzke
Monitoring the hydrothermal synthesis of molybdenum oxide nanorods for selective oxidation reactions
44. Jahrestreffen Deutscher Katalytiker, 14th – 16th of March 2011, Weimar, Germany

K. Schuh, W. Kleist, J.-D. Grunwaldt, M. Høj, A. D. Jensen, G. R. Patzke
Molybdenum-based catalysts for selective oxidation of propane prepared by hydrothermal synthesis
45. Jahrestreffen Deutscher Katalytiker, 16th – 18th of March 2012, Weimar, Germany

K. Schuh, W. Kleist, J.-D. Grunwaldt, M. Høj, A. D. Jensen, G. R. Patzke
Bismuth molybdate catalysts for the selective oxidation of propylene to acrolein prepared by hydrothermal synthesis
46. Jahrestreffen Deutscher Katalytiker, 13th – 15th of March 2013, Weimar, Germany

K. Schuh, W. Kleist, J.-D. Grunwaldt, M. Høj, A. D. Jensen, G. R. Patzke, M. Brorson
Synthesis of transition metal molybdates and their activity in hydrotreating and partial oxidation of hydrocarbons
11th European Congress on Catalysis, 1st – 6th of September 2013, Lyon, France

Eidesstattliche Erklärung

Hiermit versichere ich, die vorliegende Doktorarbeit selbstständig angefertigt und keine anderen als die von mir angegebenen Quellen und Hilfsmittel verwendet, sowie wörtliche und sinngemäße Zitate als solche gekennzeichnet zu haben. Die Arbeit wurde in gleicher oder anderer Form keiner anderen Prüfungsbehörde zur Erlangung eines akademischen Grades vorgelegt.

Karlsruhe, den _____

Datum und Unterschrift